Master's thesis

NTNU
Norwegian University of Science and Technology
Faculty of Natural Sciences
Department of Physics

Lina Grøvan Johnsen

Controllable Superconducting Phase Transition and Magnetization Reorientation due to Spin-Orbit Interactions

Master's thesis in Physics
Supervisor: Jacob Linder
May 2019

NTNU
Kunnskap for en bedre verden

Lina Grøvan Johnsen

Controllable Superconducting Phase Transition and Magnetization Reorientation due to Spin-Orbit Interactions

Master's thesis in Physics
Supervisor: Jacob Linder
May 2019

Norwegian University of Science and Technology
Faculty of Natural Sciences
Department of Physics

NTNU
Norwegian University of
Science and Technology

ABSTRACT

We consider proximity-effects in two superconducting hybrid structures. The first system consists of a single homogeneous ferromagnet proximity-coupled to a superconducting layer, where an intermediate thin-film heavy normal-metal enhances the interfacial Rashba spin-orbit interaction. We demonstrate a reorientation of the favored magnetization direction driven by the superconducting phase transition. Depending on the intrinsic anisotropy of the ferromagnet, either a reorientation from in-plane to out-of-plane or a $\pi/4$ in-plane rotation is possible. Computation of the superconducting critical temperature in the ballistic limit shows a dependence on the in-plane magnetization direction, in contrast to previous diffusive limit results. The second system consists of a single heavy normal-metal with Rashba spin-orbit coupling, proximity-coupled to a superconducting layer. We predict a suppression of the superconducting critical temperature for in-plane spin-orbit fields, that depends on the in-plane orientation. The main theoretical framework for our numerical treatment is the ballistic-limit tight-binding lattice Bogoliubov-de Gennes framework. We also use a Bogoliubov-de Gennes continuum model for obtaining analytical expressions for the singlet and triplet retarded anomalous Green's functions of our second system.

SAMMENDRAG

Vi undersøker to superledende hybridstrukturer og ser på virkningen av å kombinere ulike materialer. Det første systemet består av en enkelt homogen ferromagnet koblet til en superleder, hvor et tynt lag av tungt normalmetall forsterker Rashba spin-bane-koblingen i grenseskiktet. Vi finner en retningsendring i magnetiseringen drevet av den superledende faseovergangen. Avhengig av den iboende anisotropien til ferromagneten vil vi få en endring i den foretrukne magnetiseringsretningen enten fra i planet til ut av planet eller en $\pi/4$ rotasjon i planet. Beregninger i den ballistiske grensen viser at den kritiske temperaturen varierer under rotasjon av magnetiseringsretingen i planet, i motsetning til invariansen funnet i den diffusive grensen. Det andre systemet består av en superleder og et enkelt tungt normalmetall med Rashba spinn-bane-kobling. Den kritiske temperaturen til den superledende hybridstrukturen er lavere for spinn-bane-felt i planet enn ut av planet, og den er også avhengig av retningen i planet. Hovedrammeverket brukt i våre numeriske beregninger er en Bogoliubov-de Gennes gittermodell for ballistiske materialer hvor det antas at elektronene er tett knyttet til gitterpunktene. Vi introduserer også en Bogoliubov-de Gennes kontinuumsmodell for å kunne utlede analytiske uttrykk for de retarderte, anomale Greensfunksjonene som beskriver singlett- og triplettamplitudene i systemet bestående av en superleder og et tungt normalmetall.

PREFACE

This work was submitted after a two years' Master's degree program in physics at the Norwegian University of Science and Technology (NTNU) under the supervision of Prof. Jacob Linder at the Center for Quantum Spintronics (QuSpin). The work presented in this thesis spanned the final two semesters and amounts to 60 ECTS credits. The thesis work was divided into two parts: We first considered magnetization reorientation driven by the superconducting phase transition, and modulation of the critical temperature under rotation of the magnetization, in a superconductor/heavy-metal/ferromagnet trilayer. Secondly, we considered modulation of the critical temperature under reorientation of the Rashba spin-orbit field in a superconductor/heavy-metal bilayer. The first of these two projects resulted in a paper published in Physical Review B, [L. G. Johnsen, N. Banerjee, and J. Linder, Phys. Rev. B **99**, 134516 (2019)], that is enclosed in this thesis.

First and foremost, I want to thank my supervisor Prof. Jacob Linder for inspiring and helpful discussions over the past two years, and for answering my countless questions. I look forward to our continued collaboration over the next years. I am also grateful to Dr. Niladri Banerjee at Loughborough University for collaboration on the magnetization reorientation project, and for his input and comments on the resulting paper. I also want to thank Prof. Justin W. Wells for discussions regarding the experimental realization of critical temperature modulations under reorientations of the spin-orbit field. In addition, I especially want to thank Dr. Jabir Ali Ouassou for sharing with me his elegant and effective algorithm for computing the superconducting critical temperature, Kristian Svalland for collaboration on symmetrizing the Rashba spin-orbit coupling term in the Hamiltonian, and also Dr. Sol Jacobsen, Atousa Ghanbari Birgani, Vetle Risinggård, and Morten Amundsen for helpful discussions. I am also grateful to Arnau Sala for reading through and helping me improve my thesis. Finally, I would like to thank all the members of QuSpin for making us Master students feel like a part of the group. You have made the last year of my Master's studies truly enjoyable, and I look forward to being your colleague.

Lina Grøvan Johnsen, Trondheim, May 2019

The design of this thesis is based on the LaTeX classic thesis template originally created by André Miede.

CONTENTS

USEFUL IDENTITIES AND NOTATION

In this thesis, the mathematical notation will mostly follow the usual conventions in physics. We write unit vectors with a hat as $\hat{v}$. Other vectors are written in a bold font as $\boldsymbol{v}$. Scalars and matrices are written in a normal font. We will also use a hat for the momentum operator in the n direction, $\hat{p}_n = -i\partial_n$, while the momentum introduced by the spatial Fourier transform is written without a hat as p_n. The partial derivative with respect to n is sometimes written $\partial_n \equiv \partial/\partial n$ for brevity of notation. We use † for the hermitian conjugate, * for the complex conjugate and ^{T} for the transpose of a matrix or vector. Commutators are written with square brackets as $[A, B] \equiv AB - BA$. Anticommutators are written with curly brackets as $\{A, B\} \equiv AB + BA$. We will also use the Kroenecker-δ

$$\delta_{i,j} \equiv \begin{cases} 1, & \text{if } i = j \\ 0, & \text{if } i \neq j, \end{cases} \tag{0.1}$$

as well as the Dirac δ-function $\delta(x - x_0)$ defined by

$$\int_{-\infty}^{\infty} dx f(x)\delta(x - x_0) = f(x_0). \tag{0.2}$$

The Heaviside step function is defined as

$$\theta(x - x_0) \equiv \begin{cases} 1, & \text{if } x > x_0 \\ \frac{1}{2}, & \text{if } x = x_0 \\ 0, & \text{if } x < x_0, \end{cases} \tag{0.3}$$

or in the integral representation as

$$\theta(t - t_0) \equiv -\frac{1}{2\pi i} \int_{-\infty}^{\infty} d\omega \, \frac{1}{\omega + i\delta^+} e^{-i\omega(t-t_0)}, \tag{0.4}$$

where $\delta^+ \to 0^+$.

The Pauli matrices spanning spin space are defined as

$$\sigma_x \equiv \begin{pmatrix} 0 & 1 \\ 1 & 0 \end{pmatrix}, \quad \sigma_y \equiv \begin{pmatrix} 0 & -i \\ i & 0 \end{pmatrix}, \quad \sigma_z \equiv \begin{pmatrix} 1 & 0 \\ 0 & -1 \end{pmatrix}. \tag{0.5}$$

The vector of Pauli matrices is written as $\boldsymbol{\sigma} \equiv \sigma_x\hat{x} + \sigma_y\hat{y} + \sigma_z\hat{z}$, where $\hat{x}$, $\hat{y}$ and $\hat{z}$ are the unit vectors along the Cartesian axes. The Pauli matrices spanning Nambu (particle-hole) space are defined as

$$\tau_1 \equiv \begin{pmatrix} 0 & 1 \\ 1 & 0 \end{pmatrix}, \quad \tau_2 \equiv \begin{pmatrix} 0 & -i \\ i & 0 \end{pmatrix}, \quad \tau_3 \equiv \begin{pmatrix} 1 & 0 \\ 0 & -1 \end{pmatrix}. \tag{o.6}$$

The identity matrices in spin and Nambu space respectively are defined as

$$\sigma_0 \equiv \begin{pmatrix} 1 & 0 \\ 0 & 1 \end{pmatrix}, \quad \tau_0 \equiv \begin{pmatrix} 1 & 0 \\ 0 & 1 \end{pmatrix}. \tag{o.7}$$

From the identity matrix and the Pauli matrices in Nambu and spin space, we construct 4×4 matrices given by the Kronecker product $\tau_i \otimes \sigma_j \equiv \hat{\tau}_i\hat{\sigma}_j$, where $i = \{0, 1, 2, 3\}$ and $j = \{0, x, y, z\}$. Note that we write the Kronecker product $\hat{\tau}_i\hat{\sigma}_j$ with hats to avoid using identical notation to the matrix multiplication $\tau_i\sigma_j$ resulting in a 2×2 matrix. We also define $\tau^{\pm} = (\tau_1 \pm i\tau_2)/2$ in order to simplify the notation.

ABBREVIATIONS

BCS	Bardeen-Cooper-Schrieffer
BdG	Bogoliubov-de Gennes
F	ferromagnet
HM	heavy normal-metal with Rashba spin-orbit coupling
IP	in-plane with respect to the interface
N	normal-metal (without spin-orbit coupling)
OOP	out-of-plane with respect to the interface
S	superconductor

1

INTRODUCTION

1.1 BACKGROUND AND MOTIVATION

In the last years, research within the field of superconducting spintronics has focused on combining superconducting and magnetic materials into hybrid structures. When combining magnetic materials with conventional superconductors, novel phases arise from proximity effects not found in individual materials [1]. Conventional superconductivity is in itself an old field of research, as it was first discovered in 1911 [2, 3] and thoroughly described by the microscopic theories of superconductivity by Bardeen, Cooper and Schrieffer in 1957 [4], Bogoliubov in 1958 [5] and Gor'kov in 1958-59 [6, 7]. In the conventional Bardeen-Cooper-Schrieffer (BCS) description of superconductivity, the electrons inside the superconductor (S) form Cooper pairs bound together by an attractive potential. In conventional superconductors, Cooper pairs exists as spin-singlet pairs, $(\uparrow\downarrow - \downarrow\uparrow)$. Due to the opposite spin of the two electrons, the pair is destroyed when it enters a ferromagnet (F) as the electrons quickly lose their coherence due to the magnetic exchange field [8, 9]. It is therefore clear that a spin-singlet Cooper pair makes for a poor candidate for long-range Cooper pair penetration into ferromagnetic materials.

The early research on proximity effects in superconducting hybrid structures, done by de Gennes [10, 11] and by Werthamer [12, 13] in the 1960's, investigated the coherence of electrons and holes in thin normal-metal (N) films due to the penetration of Cooper pairs. A phenomenon closely related to the proximity effect, Andreev reflection, was discovered by Andreev in 1964 [14] and by de Gennes and Saint-Jaimes in 1963-64 [15]. An electron with an energy ϵ relative to the Fermi energy, but below the superconducting gap, cannot be transmitted from a normal-metal into a superconductor in the form of a single electron. Instead, a quasi-particle state is transmitted. This demands the transmission of two opposite-spin electrons, and therefore an electron with opposite-spin at energy $-\epsilon$ relative to the Fermi energy must disappear at the normal-metal side

of the interface. This is equivalent to the Andreev reflection of a hole with the opposite spin, approximately opposite momentum and energy ϵ relative to the Fermi energy [9, 16]. The coherence length of the electron and hole inside the normal-metal region describes the penetration depth of the singlet Cooper pairs into the normal-metal.

Due to the pair-breaking inside ferromagnetic materials, it may be seen as counter-intuitive that replacing the normal-metal with ferromagnetic (F) films can increase the Cooper pair penetration depth. Interestingly, the spin-splitting of the energy bands of a ferromagnet leads to a transformation of spin-singlet Cooper pairs into spin-zero triplet Cooper pairs ($\uparrow\downarrow + \downarrow\uparrow$) at the interface between a superconductor and a ferromagnet. These have a short penetration depth into the ferromagnetic region. However, two misoriented ferromagnets breaking spin-rotational symmetry can transform opposite-spin triplets into equal-spin triplets, ($\uparrow\uparrow$) and ($\downarrow\downarrow$) [9]. Due to their equally directed spins along the magnetization direction, these Cooper pairs maintain coherence longer and are instead able to survive for a longer distance inside the ferromagnet. The density of equal-spin triplets in the system depends on the relative orientation of the ferromagnets [8, 9]. This has been demonstrated experimentally (see for instance Refs. [17–21]) by showing a variation of the superconducting critical temperature T_c in a F1/S/F2 or F1/F2/S system when changing the relative magnetization of the F1 and F2 layers. This variation is attributed to the generation of triplet Cooper pairs with increasing misalignment of the magnetizations of the F1 and F2 layer moments. Recent research [22–25] has reported a similar modulation of the critical temperature by changing the orientation of a single homogeneous ferromagnet coupled to a superconductor through a thin heavy normal-metal (HM) film with strong Rashba spin-orbit coupling, which having the property of being odd in both spin and momentum may in itself induce both opposite-spin and equal-spin triplets.

The generation of spin-triplet amplitudes close to the interface between conventional *s*-wave superconductors and non-superconducting materials is of great importance for the physical properties of superconducting hybrid structures. Investigating various superconducting heterostructures is of interest from a fundamental physics point of view, as novel phenomena may occur when artificially combining layers of different superconducting and non-superconducting materials. When it comes to possible applications, one example is the superconducting spin-valve, where a modulation of the superconducting critical temperature upon reorienting the magnetization of a ferromagnet in an S/F1/F2 or F1/S/F2 structure can be used in order to switch superconductivity on and off [1]. A more

thorough understanding of the field of superconducting spintronics is desired as it may lead to the discovery of yet unknown applications.

1.2 SCOPE AND STRUCTURE

In this thesis, we focus on S/HM/F and S/HM thin-film structures, that will mainly be described using the ballistic-limit tight-binding Bogoliubov-de Gennes (BdG) lattice framework. We will first investigate magnetization reorientation driven by the superconducting phase transition in S/HM/F trilayers. This work is motivated by earlier theoretical [22–25] and experimental [25] works showing a T_c-modulation explained by changes in the spin-triplet amplitudes upon reorienting the magnetization. What we consider is a reciprocal effect to the earlier mentioned spin-valve effect. We also consider T_c-modulation using our ballistic-limit theoretical framework, and get results complementing the earlier theoretical works done in the diffusive-limit Usadel framework [22, 25]. In the S/HM bilayer, we consider T_c-modulation upon reorienting the Rashba spin-orbit field, which to our knowledge never before has been investigated. In order to describe the singlet and triplet amplitudes present in the S/HM structure, we introduce an additional theoretical framework where we consider scattering at the interface for a continuum BdG model.

The main theoretical framework used in this thesis, the tight-binding BdG lattice framework, is introduced in Ch. 2. In this chapter, we explain the numerical calculation of the physical quantities of interest, such as the critical temperature, the free energy, singlet and triplet amplitudes, and the superconducting coherence length. We also discuss aspects such as the dimensionality of the model, the choice of parameters and the relevance of the chosen theoretical framework. In Ch. 3 we introduce the additional theoretical framework, the BdG continuum framework. This will, in addition to the theoretical framework presented in Ch. 2, be used in Ch. 5 in order to explain the existence of the various triplet amplitudes present in the system. In this framework, the triplet amplitudes can in the simplest cases be computed analytically, however also in this framework some of our calculations require numerical treatment. The novel results are presented in Chs. 4 and 5. In Ch. 4, we consider magnetization reorientation and T_c-modulation in the S/HM/F system. The T_c-modulation of the S/HM system is considered in Ch. 5. The thesis is concluded by a short summary and outlook in Ch. 6. After the content presented above, we have included the paper presenting the results of Ch. 4.

2

THE LATTICE BOGOLIUBOV-DE GENNES FRAMEWORK

In this chapter, we introduce the tight-binding lattice Bogoliubov-de Gennes (BdG) framework, which will be the main framework used in this thesis for determining the physical properties of the considered systems. We here introduce our Hamiltonian, diagonalize it numerically according to the BdG framework and derive expressions for the physical quantities of interest. We use conventions similar to those in Refs. [26, 27]. The lattice BdG framework considers materials in the ballistic limit of transport, can describe atomically thin layers of a material and fully accounts for the crystal symmetry of the electronic environment. It is therefore well suited for describing thin-film heterostructures.

2.1 DIAGONALIZATION OF THE HAMILTONIAN

In this thesis, we consider heterostructures consisting of thin layers of conventional s-wave superconductors, normal-metals, heavy-metals with Rashba spin-orbit coupling and homogeneous ferromagnets. We first consider systems where the Rashba spin-orbit field is perpendicular to the layer interfaces. In this case, the system can be described by the Hamiltonian [27]

$$\begin{aligned} H = &- t \sum_{\langle \boldsymbol{i},\boldsymbol{j}\rangle,\sigma} c^{\dagger}_{\boldsymbol{i},\sigma} c_{\boldsymbol{j},\sigma} - \sum_{\boldsymbol{i},\sigma} \mu_{\boldsymbol{i}} c^{\dagger}_{\boldsymbol{i},\sigma} c_{\boldsymbol{i},\sigma} - \sum_{\boldsymbol{i}} U_{\boldsymbol{i}} n_{\boldsymbol{i},\uparrow} n_{\boldsymbol{i},\downarrow} \\ &+ \sum_{\boldsymbol{i},\alpha,\beta} c^{\dagger}_{\boldsymbol{i},\alpha} (\boldsymbol{h}_{\boldsymbol{i}} \cdot \boldsymbol{\sigma})_{\alpha,\beta} c_{\boldsymbol{i},\beta} - \frac{i}{2} \sum_{\langle \boldsymbol{i},\boldsymbol{j}\rangle,\alpha,\beta} \lambda_{\boldsymbol{i}} c^{\dagger}_{\boldsymbol{i},\alpha} \hat{n} \cdot (\boldsymbol{\sigma} \times \boldsymbol{d}_{\boldsymbol{i},\boldsymbol{j}})_{\alpha,\beta} c_{\boldsymbol{j},\beta}. \end{aligned} \tag{2.1}$$

The Rashba spin-orbit coupling contribution to the Hamiltonian in the case of a general direction of the spin-orbit field will be considered in the next section. In the above Hamiltonian, t is the hopping integral, $\mu_{\boldsymbol{i}}$ is the chemical potential at lattice site $\boldsymbol{i}$, $U_{\boldsymbol{i}} > 0$ is the attractive on-site interaction that gives rise to superconductivity, $\boldsymbol{h}_{\boldsymbol{i}}$ is the local magnetic exchange field, $\boldsymbol{\sigma}$ is the vector of Pauli matrices, $\lambda_{\boldsymbol{i}}$ is the Rashba spin-orbit coupling magnitude at site $\boldsymbol{i}$, $\hat{n}$ is a unit vector defining the direction of the spin-orbit field, and $\boldsymbol{d}_{\boldsymbol{i},\boldsymbol{j}} \equiv \hat{x}(\delta_{\boldsymbol{i}+\hat{x},\boldsymbol{j}} -$

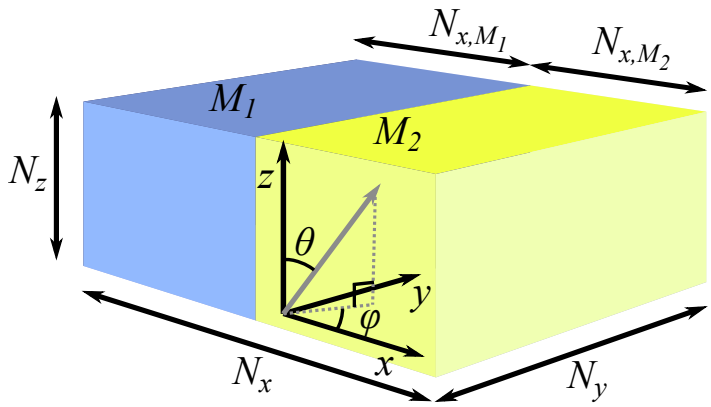

Figure 2.1: We model our system as a 3D $N_x \times N_y \times N_z$ lattice with interface normal along the x axis. The number of lattice sites in the x direction of material M_1 and M_2 are N_{x,M_1} and N_{x,M_2} respectively. A general direction can be described by the polar angle θ and the azimuthal angle ϕ. Any number of layers with interface normal along $\hat{x}$ can be modeled. In this thesis we consider superconducting, normal-metal, heavy-metal and homogeneously ferromagnetic layers.

$\delta_{\boldsymbol{i}-\hat{x},\boldsymbol{j}}) + \hat{y}(\delta_{\boldsymbol{i}+\hat{y},\boldsymbol{j}} - \delta_{\boldsymbol{i}-\hat{y},\boldsymbol{j}}) + \hat{z}(\delta_{\boldsymbol{i}+\hat{z},\boldsymbol{j}} - \delta_{\boldsymbol{i}-\hat{z}.\boldsymbol{j}})$ is the vector from site $\boldsymbol{i}$ to site $\boldsymbol{j}$. $c^{\dagger}_{\boldsymbol{i},\sigma}$ and $c_{\boldsymbol{i},\sigma}$ are the second quantization electron creation and annihilation operators at site $\boldsymbol{i}$ with spin σ, and $n_{\boldsymbol{i},\sigma} \equiv c^{\dagger}_{\boldsymbol{i},\sigma} c_{\boldsymbol{i},\sigma}$ is the number operator. The first two terms in Eq. 2.1 are nonzero in all of the materials that will be considered in this thesis. The third term describes the superconducting on-site attraction, the fourth term describes ferromagnetism, and the last term describes the Rashba spin-orbit coupling in a heavy-metal. These terms are only nonzero in their respective regions.

In the following, we will consider a 3D cubic lattice of size $N_x \times N_y \times N_z$ as shown in Fig. 2.1. The interface normal of the layered system is parallel to the x axis. It follows that $\hat{n} = \hat{x}$, since the spin-orbit field is directed along the interface normal. We assume periodic boundary conditions in the y and z directions, so that all quantities depend on the the x component of the site index only. In the presentation of the results, we will scale all energies to the hopping element t and all lengths to the lattice constant a. For simplicity, we also set the reduced Planck constant $\hbar$ and the Boltzmann constant k_B equal to 1. Therefore, all temperatures are scaled by t/k_B in the presentation of the results.

We now turn to the diagonalization of the Hamiltonian described in Eq. 2.1. The superconducting term (H_U) in Eq. 2.1 is treated by a mean-field approach where

we insert $c_{\boldsymbol{i},\uparrow}c_{\boldsymbol{i},\downarrow} = \left\langle c_{\boldsymbol{i},\uparrow}c_{\boldsymbol{i},\downarrow}\right\rangle + \delta$ and $c^\dagger_{\boldsymbol{i},\uparrow}c^\dagger_{\boldsymbol{i},\downarrow} = \left\langle c^\dagger_{\boldsymbol{i},\uparrow}c^\dagger_{\boldsymbol{i},\downarrow}\right\rangle - \delta^\dagger$ into Eq. 2.1 and neglect terms of second order in the fluctuations δ and $\delta^\dagger$. We get

$$H_U = \sum_{\boldsymbol{i}} \frac{|\Delta_{\boldsymbol{i}}|^2}{U_{\boldsymbol{i}}} + \sum_{\boldsymbol{i}} (\Delta_{\boldsymbol{i}} c^\dagger_{\boldsymbol{i},\uparrow} c^\dagger_{\boldsymbol{i},\downarrow} + \Delta^*_{i_x} c_{\boldsymbol{i},\downarrow} c_{\boldsymbol{i},\uparrow}). \tag{2.2}$$

Above, $\Delta_{\boldsymbol{i}}$ is the superconducting gap at site $\boldsymbol{i}$, and it is given by [27]

$$\Delta_{\boldsymbol{i}} \equiv U_{\boldsymbol{i}} \left\langle c_{\boldsymbol{i},\uparrow} c_{\boldsymbol{i},\downarrow} \right\rangle . \tag{2.3}$$

This is the superconducting order parameter, which we solve for self-consistently. Because of our assumption of periodic boundary conditions along the y and z axes, the Fourier transform [27]

$$c_{\boldsymbol{i},\sigma} = \frac{1}{\sqrt{N_y N_z}} \sum_{k_y,k_z} c_{i_x,k_y,k_z,\sigma} e^{i(k_y i_y + k_z i_z)}. \tag{2.4}$$

can be used to diagonalize the Hamiltonian. The sum is over the allowed k_y and k_z inside the first Brillouin zone, *i.e.* $k_m \in (-\pi, \pi]$ where $m = \{y, z\}$. The k_m values allowed by the periodic boundary conditions are $k_m = \frac{2\pi}{N_m} n$, where n is an integer and N_m is the number of lattice sites in the m-direction. Also note that [26]

$$\begin{aligned} \frac{1}{\sqrt{N_y}} \sum_{i_y} e^{i(k_y - k'_y) i_y} &= \delta_{k_y,k'_y}, \\ \frac{1}{\sqrt{N_z}} \sum_{i_z} e^{i(k_z - k'_z) i_z} &= \delta_{k_z,k'_z}. \end{aligned} \tag{2.5}$$

By using Eqs. 2.4 and 2.5 to rewrite the Hamiltonian in Eq. 2.1, we can show that

$$\begin{aligned} H =& N_y N_z \sum_{i_x} \frac{|\Delta_{i_x}|^2}{U_{i_x}} \\ &+ \sum_{i_x,j_x,k_y,k_z,\sigma} \epsilon_{i_x,j_x,k_y,k_z} c^\dagger_{i_x,k_y,k_z,\sigma} c_{j_x,k_y,k_z,\sigma} \\ &+ \sum_{i_x,k_y k_z} \left[\Delta_{i_x} c^\dagger_{i_x,k_y,k_z,\uparrow} c^\dagger_{i_x,-k_y,-k_z,\downarrow} + \Delta^*_{i_x} c_{i_x,-k_y,-k_z,\downarrow} c_{i_x,k_y,k_z,\uparrow}\right] \\ &+ \sum_{i_x,k_y,k_z,\alpha,\beta} (\boldsymbol{h}_{i_x} \cdot \boldsymbol{\sigma})_{\alpha,\beta} c^\dagger_{i_x,k_y,k_z,\alpha} c_{i_x,k_y,k_z,\beta} \\ &+ \sum_{i_x,k_y,k_z,\alpha,\beta} \lambda_{i_x} \left[(\sigma_y)_{\alpha,\beta} \sin(k_z) - (\sigma_z)_{\alpha,\beta} \sin(k_y)\right] c^\dagger_{i_x,k_y,k_z,\alpha} c_{i_x,k_y,k_z,\beta}, \end{aligned} \tag{2.6}$$

where

$$\epsilon_{i_x,j_x,k_y,k_z} \equiv -2t\left[\cos(k_y)+\cos(k_z)\right]\delta_{i_x,j_x} - t(\delta_{i_x,j_x+1}+\delta_{i_x,j_x-1}) - \mu_{i_x}\delta_{i_x,j_x}. \quad (2.7)$$

We choose a basis

$$B^\dagger_{i_x,k_y,k_z} = [c^\dagger_{i_x,k_y,k_z,\uparrow} \;\; c^\dagger_{i_x,k_y,k_z,\downarrow} \;\; c_{i_x,-k_y,-k_z,\uparrow} \;\; c_{i_x,-k_y,-k_z,\downarrow}] \quad (2.8)$$

and rewrite the Hamiltonian in Eq. 2.6 as

$$H = H_0 + \frac{1}{2}\sum_{i_x,j_x,k_y,k_z} B^\dagger_{i_x,k_y,k_z} H_{i_x,j_x,k_y,k_z} B_{j_x,k_y,k_z}, \quad (2.9)$$

where

$$\begin{aligned} H_{i_x,j_x,k_y,k_z} = \;& \epsilon_{i_x,j_x,k_y,k_z}\hat{\tau}_3\hat{\sigma}_0 \\ & + \delta_{i_x,j_x}\Big[\Delta_{i_x} i\hat{\tau}^+\hat{\sigma}_y - \Delta^*_{i_x} i\hat{\tau}^-\hat{\sigma}_y \\ & + h^x_{i_x}\hat{\tau}_3\hat{\sigma}_x + h^y_{i_x}\hat{\tau}_0\hat{\sigma}_y + h^z_{i_x}\hat{\tau}_3\hat{\sigma}_z \\ & - \lambda_{i_x}\sin(k_y)\hat{\tau}_0\hat{\sigma}_z + \lambda_{i_x}\sin(k_z)\hat{\tau}_3\hat{\sigma}_y\Big], \end{aligned} \quad (2.10)$$

and $\hat{\tau}^\pm = (\hat{\tau}_1 \pm i\hat{\tau}_2)/2$. Above, $\hat{\tau}_i\hat{\sigma}_j \equiv \tau_i \otimes \sigma_j$ is the Kronecker product of the Pauli matrices spanning Nambu and spin space. $h^x_{i_x}$, $h^y_{i_x}$ and $h^z_{i_x}$ are the components of $\boldsymbol{h}_{i_x}$. The constant term is

$$H_0 = N_y N_z \sum_{i_x} \frac{|\Delta_{i_x}|^2}{U_{i_x}} - \sum_{i_x,k_y,k_z}\left\{2t\left[\cos(k_y)+\cos(k_z)\right] + \mu_{i_x}\right\}. \quad (2.11)$$

By defining another basis,

$$W^\dagger_{k_y,k_z} = [B^\dagger_{1,k_y,k_z}, ..., B^\dagger_{i_x,k_y,k_z}, ..., B^\dagger_{N_x,k_y,k_z}], \quad (2.12)$$

Eq. 2.9 can be rewritten as

$$H = H_0 + \frac{1}{2}\sum_{k_y,k_z} W^\dagger_{k_y,k_z} H_{k_y,k_z} W_{k_y,k_z}, \quad (2.13)$$

where

$$H_{k_y,k_z} = \begin{bmatrix} H_{1,1,k_y,k_z} & \cdots & H_{1,N_x,k_y,k_z} \\ \vdots & \ddots & \vdots \\ H_{N_x,1,k_y,k_z} & \cdots & H_{N_x,N_x,k_y,k_z} \end{bmatrix}. \quad (2.14)$$

H_{k_y,k_z} is Hermitian and can be diagonalized numerically with eigenvalues E_{n,k_y,k_z} and eigenvectors Φ_{n,k_y,k_z} given by

$$\begin{aligned}\Phi^{\dagger}_{n,k_y,k_z} &= [\phi^{\dagger}_{1,n,k_y,k_z} \quad \cdots \quad \phi^{\dagger}_{N_x,n,k_y,k_z}],\\ \phi^{\dagger}_{i_x,n,k_y,k_z} &= [u^{*}_{i_x,n,k_y,k_z}\ v^{*}_{i_x,n,k_y,k_z}\ w^{*}_{i_x,n,k_y,k_z}\ x^{*}_{i_x,n,k_y,k_z}].\end{aligned} \tag{2.15}$$

The diagonalization is done numerically and gives a Hamiltonian of the form

$$H = H_0 + \frac{1}{2}\sum_{n,k_y,k_z} E_{n,k_y,k_z}\gamma^{\dagger}_{n,k_y,k_z}\gamma_{n,k_y,k_z}, \tag{2.16}$$

where the new quasiparticle operators are related to the old operators by [26]

$$\begin{aligned}c_{i_x,k_y,k_z,\uparrow} &= \sum_n u_{i_x,n,k_y,k_z}\gamma_{n,k_y,k_z},\\ c_{i_x,k_y,k_z,\downarrow} &= \sum_n v_{i_x,n,k_y,k_z}\gamma_{n,k_y,k_z},\\ c^{\dagger}_{i_x,-k_y,-k_z,\uparrow} &= \sum_n w_{i_x,n,k_y,k_z}\gamma_{n,k_y,k_z},\\ c^{\dagger}_{i_x,-k_y,-k_z,\downarrow} &= \sum_n x_{i_x,n,k_y,k_z}\gamma_{n,k_y,k_z}.\end{aligned} \tag{2.17}$$

To find the eigenvectors and eigenvalues, the initial guess for the order parameter must be improved by iterative treatment. Eq. 2.3 can be rewritten by inserting the operators given in Eq. 2.17 and by using that $\langle\gamma^{\dagger}_{n,k_y,k_z}\gamma_{m,k_y,k_z}\rangle = f\left(E_{n,k_y,k_z}/2\right)\delta_{n,m}$ [27]. We get

$$\Delta_{i_x} = -\frac{U_{i_x}}{N_y N_z}\sum_{n,k_y,k_z} v_{i_x,n,k_y,k_z}w^{*}_{i_x,n,k_y,k_z}\left[1 - f\left(E_{n,k_y,k_z}/2\right)\right]. \tag{2.18}$$

Above, $f(E_{n,k_y,k_z}/2) = 1/[\exp(\beta E_{n,k_y,k_z}/2) + 1]$ is the Fermi-Dirac distribution. $\beta \equiv 1/k_B T$, where k_B is the Boltzmann constant and T is the temperature. Having found E_{n,k_y,k_z} and $\{u, v, w, x\}$, we can compute the physical quantities of interest.

Before we consider Hamiltonians with a general direction of the spin-orbit field, and then turn to the calculation of physical quantities, we will consider a simplified model for our multilayer structures. The method described above demands numerical treatment. To understand the behavior of our materials better, it may be instructive to consider a simpler system that can be treated analytically. We approximate the multilayers considered above as a single layer including all the relevant terms of Eq. 2.1. To justify this assumption the layers in our system must be very thin. We use periodic boundary conditions along all three axes. The

simplest system to consider is a non-superconducting layer containing Rashba spin-orbit coupling and ferromagnetism. By using the Fourier transform

$$c_{\boldsymbol{i},\sigma} = \frac{1}{\sqrt{N_x N_y N_z}} \sum_{\boldsymbol{k}} c_{\boldsymbol{k},\sigma} e^{i\boldsymbol{k}\cdot\boldsymbol{i}} \tag{2.19}$$

and the relation

$$\frac{1}{\sqrt{N_x N_y N_z}} \sum_{\boldsymbol{i}} e^{i(\boldsymbol{k}-\boldsymbol{k}')\cdot\boldsymbol{i}} = \delta_{\boldsymbol{k}\boldsymbol{k}'} \tag{2.20}$$

corresponding to Eqs. 2.4 and 2.5 in our earlier treatment, we rewrite the Hamiltonian given in Eq. 2.1 as

$$H = H_0 + \frac{1}{2} \sum_{\boldsymbol{k}} B_{\boldsymbol{k}}^{\dagger} H_{\boldsymbol{k}} B_{\boldsymbol{k}}. \tag{2.21}$$

The above basis is given by

$$B_{\boldsymbol{k}}^{\dagger} = [c_{\boldsymbol{k},\uparrow}^{\dagger} \quad c_{\boldsymbol{k},\downarrow}^{\dagger} \quad c_{-\boldsymbol{k},\uparrow} \quad c_{-\boldsymbol{k},\downarrow}], \tag{2.22}$$

and the constant term is

$$H_0 = \sum_{\boldsymbol{k}} \epsilon_{\boldsymbol{k}}, \tag{2.23}$$

where

$$\epsilon_{\boldsymbol{k}} \equiv -2t[\cos(k_x) + \cos(k_y) + \cos(k_z)] - \mu. \tag{2.24}$$

The Hamiltonian matrix is a 4×4 block diagonal matrix given by

$$H_{\boldsymbol{k}} = \begin{bmatrix} \epsilon_{\boldsymbol{k}} + h_z - \Lambda_{k_y} & h_x - ih_y - i\Lambda_{k_z} & 0 & 0 \\ h_x + ih_y + i\Lambda_{k_z} & \epsilon_{\boldsymbol{k}} - h_z + \Lambda_{k_y} & 0 & 0 \\ 0 & 0 & -\epsilon_{\boldsymbol{k}} - h_z - \Lambda_{k_y} & -h_x - ih_y + i\Lambda_{k_z} \\ 0 & 0 & -h_x + ih_y - i\Lambda_{k_z} & -\epsilon_{\boldsymbol{k}} + h_z + \Lambda_{k_y} \end{bmatrix}, \tag{2.25}$$

where $\Lambda_{k_y} \equiv \lambda \sin(k_y)$ and $\Lambda_{k_z} \equiv \lambda \sin(k_z)$. The four eigenvalues of the system can be obtained analytically by diagonalizing $H_{\boldsymbol{k}}$. We get

$$\begin{aligned} E_{1,\boldsymbol{k}} &= \epsilon_{\mathbf{k}} + |\boldsymbol{h} + \Lambda_z \hat{y} - \Lambda_y \hat{z}|, \\ E_{2,\boldsymbol{k}} &= \epsilon_{\mathbf{k}} - |\boldsymbol{h} + \Lambda_z \hat{y} - \Lambda_y \hat{z}|, \\ E_{3,\boldsymbol{k}} &= -\epsilon_{\mathbf{k}} + |\boldsymbol{h} - \Lambda_z \hat{y} + \Lambda_y \hat{z}|, \\ E_{4,\boldsymbol{k}} &= -\epsilon_{\mathbf{k}} - |\boldsymbol{h} - \Lambda_z \hat{y} + \Lambda_y \hat{z}|, \end{aligned} \tag{2.26}$$

where $|\boldsymbol{h} \pm \Lambda_z \hat{y} \mp \Lambda_y \hat{z}| = [h^2 + |\Lambda_y|^2 + |\Lambda_z|^2 \mp h\Lambda_y \cos(\theta) \pm h\Lambda_z \sin(\theta)\sin(\phi)]^{1/2}$.

2.2 THE SYMMETRIZED RASHBA SPIN-ORBIT COUPLING OPERATOR

We now want to find the Rashba spin-orbit coupling contribution to the Hamiltonian when the spin-orbit field instead of being oriented along the interface normal can be oriented in any direction. If we have a Rashba spin-orbit field not directed along the interface normal, the Rashba term in Eq. 2.1 is in general non-Hermitian. This term is the second quantized form of [28]

$$\hat{h} = (\hat{n} \times \boldsymbol{\sigma}) \cdot \lambda(x)\hat{\boldsymbol{p}}, \tag{2.27}$$

where $\hat{n} = (\cos(\phi)\sin(\theta), \sin(\phi)\sin(\theta), \cos(\theta))$ is a unit vector directed along the spin-orbit field, $\boldsymbol{\sigma}$ is the vector of Pauli matrices, $\lambda(x)$ is the x dependent Rashba spin-orbit coupling strength and $\hat{\boldsymbol{p}} = (\hat{p}_x, \hat{p}_y, \hat{p}_z) = -i\hbar\nabla$ is the momentum operator. A Hermitian operator satisfies $\hat{h} = \hat{h}^\dagger$. The non-symmetrized spin-orbit coupling operator is not Hermitian, because

$$\hat{h}^\dagger = (\hat{n} \times \boldsymbol{\sigma}) \cdot \hat{\boldsymbol{p}}\lambda(x) = (\hat{n} \times \boldsymbol{\sigma}) \cdot \left\{\lambda(x)\hat{\boldsymbol{p}} + [\hat{\boldsymbol{p}}\lambda(x)]\right\} \neq \hat{h}. \tag{2.28}$$

More generally, the symmetrized version of the Rashba spin-orbit coupling operator can be written

$$\hat{h} = \frac{1}{2}(\hat{n} \times \boldsymbol{\sigma}) \cdot \{\lambda(x), \hat{\boldsymbol{p}}\}. \tag{2.29}$$

This operator is Hermitian because

$$\begin{aligned} \hat{h}^\dagger &= \left\{\frac{1}{2}(\hat{n} \times \boldsymbol{\sigma}) \cdot [\lambda(x)\hat{\boldsymbol{p}} + \hat{\boldsymbol{p}}\lambda(x)]\right\}^\dagger = \frac{1}{2}(\hat{n} \times \boldsymbol{\sigma}) \cdot [\hat{\boldsymbol{p}}\lambda(x) + \lambda(x)\hat{\boldsymbol{p}}] \\ &= \frac{1}{2}(\hat{n} \times \boldsymbol{\sigma}) \cdot \{\lambda(x), \hat{\boldsymbol{p}}\} = \hat{h}. \end{aligned} \tag{2.30}$$

In Eqs. 2.28 and 2.30 we have used that $\hat{\boldsymbol{p}}^\dagger = \hat{\boldsymbol{p}}$ and that $[\lambda(x)]^\dagger = [\lambda(x)]^* = \lambda(x)$. Notice that if $\lambda(x)$ is independent of x and therefore commutes with $\hat{\boldsymbol{p}}$, the anti-commutator in Eq. 2.29 gives $2\lambda\hat{\boldsymbol{p}}$, and we get the same expression as for the non-symmetrized Rashba spin-orbit coupling operator given in Eq. 2.27. We also obtain the non-symmetrized spin-orbit coupling operator by inserting $\hat{n} = \hat{x}$ into Eq. 2.29. By performing the differentiation in Eq. 2.29 according to the product rule, Eq. 2.29 can be written

$$\begin{aligned} \hat{h} =& (\hat{n} \times \boldsymbol{\sigma}) \cdot \{\lambda(x)\hat{p}_x + \frac{1}{2}[\hat{p}_x\lambda(x)]\}\hat{x} \\ &+ \lambda(x)(\hat{n} \times \boldsymbol{\sigma}) \cdot \hat{p}_y\hat{y} \\ &+ \lambda(x)(\hat{n} \times \boldsymbol{\sigma}) \cdot \hat{p}_z\hat{z}. \end{aligned} \tag{2.31}$$

We see that compared to the non-symmetrized operator, the symmetrized version of $\hat{h}$ has an additional term that depends on $\partial_x \lambda(x)$. In order to find the symmetrized second quantized Rashba spin-orbit coupling operator, we need to compute the overlap integral of Eq. 2.31. Disregarding spin for now, the overlap integral of the first of the three terms in Eq. 2.31 is

$$\begin{aligned}
&\left\langle \boldsymbol{i} \middle| (\hat{n} \times \boldsymbol{\sigma}) \cdot \{\lambda(x)\hat{p}_x + \frac{1}{2}[\hat{p}_x \lambda(x)]\}\hat{x} \middle| \boldsymbol{j} \right\rangle \\
&= (\hat{n} \times \boldsymbol{\sigma}) \cdot \hat{x} \int d\boldsymbol{r}\, \phi_{\boldsymbol{i}}^*(\boldsymbol{r})\{\lambda(x)\hat{p}_x + \frac{1}{2}[\hat{p}_x \lambda(x)]\}\phi_{\boldsymbol{j}}^*(\boldsymbol{r}) \\
&= \frac{1}{2}(\hat{n} \times \boldsymbol{\sigma}) \cdot \hat{x}\left[\left\langle \boldsymbol{i} \middle| \lambda(x)\hat{p}_x \middle| \boldsymbol{j} \right\rangle + \left\langle \boldsymbol{j} \middle| \lambda(x)\hat{p}_x \middle| \boldsymbol{i} \right\rangle^*\right].
\end{aligned} \tag{2.32}$$

The result on the third line in the above equation is obtained by partially integrating half of the first term on the second line. By doing this, the second term cancels. The overlap integral we want to calculate is thus

$$\begin{aligned}
\left\langle \boldsymbol{i} \middle| \hat{h} \middle| \boldsymbol{j} \right\rangle = \frac{1}{2}(\hat{n} \times \boldsymbol{\sigma}) \cdot \hat{x}\left[\left\langle \boldsymbol{i} \middle| \lambda(x)\hat{p}_x \middle| \boldsymbol{j} \right\rangle + \left\langle \boldsymbol{j} \middle| \lambda(x)\hat{p}_x \middle| \boldsymbol{i} \right\rangle^*\right] \\
+ (\hat{n} \times \boldsymbol{\sigma}) \cdot \hat{y}\left\langle \boldsymbol{i} \middle| \lambda(x)\hat{p}_y \middle| \boldsymbol{j} \right\rangle \\
+ (\hat{n} \times \boldsymbol{\sigma}) \cdot \hat{z}\left\langle \boldsymbol{i} \middle| \lambda(x)\hat{p}_z \middle| \boldsymbol{j} \right\rangle.
\end{aligned} \tag{2.33}$$

In order to calculate this overlap integral, we need to evaluate the integral

$$\int d\boldsymbol{r}\, \phi_{\boldsymbol{i}}^*(\boldsymbol{r})\lambda(x)\hat{p}_m \phi_{\boldsymbol{j}}(\boldsymbol{r}) = -i \int d\boldsymbol{r}\, \phi_{\boldsymbol{i}}^*(\boldsymbol{r})\lambda(x)\partial_m \phi_{\boldsymbol{j}}(\boldsymbol{r}), \tag{2.34}$$

where $m = \{x, y, z\}$. We discretize the derivative as

$$\partial_m \phi_{\boldsymbol{j}}(\boldsymbol{r}) = \frac{1}{2}[\phi_{\boldsymbol{j}-\hat{\boldsymbol{m}}}(\boldsymbol{r}) - \phi_{\boldsymbol{j}+\hat{\boldsymbol{m}}}(\boldsymbol{r})], \tag{2.35}$$

where $\phi_{\boldsymbol{j}\mp\hat{m}}(\boldsymbol{r}) = \phi(\boldsymbol{r} - \boldsymbol{R}_{\boldsymbol{j}} \pm \hat{m})$ and $\boldsymbol{R}_{\boldsymbol{j}}$ describes the position of lattice site $\boldsymbol{j}$. We justify this approximation by the fact that $\phi_{\boldsymbol{j}}(\boldsymbol{r}) = \phi(\boldsymbol{r} - \boldsymbol{R}_{\boldsymbol{j}})$ and its derivative should only be large very close to $\boldsymbol{r} = \boldsymbol{R}_{\boldsymbol{j}}$ and small otherwise, as long as we assume $\phi_{\boldsymbol{j}}(\boldsymbol{r})$ to be highly localized. The approximation is therefore poor close to $\boldsymbol{r} = \boldsymbol{R}_{\boldsymbol{j}}$ where $\phi_{\boldsymbol{j}}(\boldsymbol{r})$ changes quickly, however when we insert Eq. 2.35 into Eq. 2.34 the contribution from this region will be small due to $\phi_{\boldsymbol{i}}(\boldsymbol{r})$ being negligible this far away from $\boldsymbol{r} = \boldsymbol{R}_{\boldsymbol{i}} \neq \boldsymbol{R}_{\boldsymbol{j}}$. The main contribution to the integral in Eq. 2.34 will instead come from positions close to site $\boldsymbol{i}$. Site $\boldsymbol{i}$ cannot equal site $\boldsymbol{j}$ due to symmetry considerations in Eq. 2.34. Note however that although Eq. 2.35 as required gives a small value and the appropriate sign for the derivative far away from $\boldsymbol{r} = \boldsymbol{R}_{\boldsymbol{j}}$, the maximum of the absolute value of $\partial\phi_{\boldsymbol{j}}(\boldsymbol{r})$ is exactly at $\boldsymbol{r} = \boldsymbol{R}_{\boldsymbol{j}\pm\hat{m}}$. If $\phi_j(\boldsymbol{r})$ is highly localized, we should rather expect the maximum of

the absolute value of $\partial_m \phi_j(\boldsymbol{r})$ to be located close to $\boldsymbol{r} = \boldsymbol{R}_j$. This leads to $\partial\phi_j(\boldsymbol{r})$ being overestimated at $\boldsymbol{r} = \boldsymbol{R}_{j\pm\hat{m}}$, however this should only introduce an extra numerical factor that can be absorbed into λ. By inserting Eq. 2.35, the integral in Eq. 2.34 can be written

$$\int d\boldsymbol{r}\,\phi_i^*(\boldsymbol{r})\lambda(x)\hat{p}_m\phi_j(\boldsymbol{r}) = -\frac{i}{2}\int d\boldsymbol{r}\,\phi_i^*(\boldsymbol{r})\lambda(x)[\phi_{j-\hat{m}}(\boldsymbol{r}) - \phi_{j+\hat{m}}(\boldsymbol{r})]. \quad (2.36)$$

If we assume each ϕ_i to be highly localized, the overlap between the probability distributions of atoms at neighboring lattice sites is small. In this case,

$$\int d\boldsymbol{r}\,\phi_i^*(\boldsymbol{r})\phi_j(\boldsymbol{r}) = \delta_{i,j}. \quad (2.37)$$

In Eq. 2.37 we have assumed that the overlap between the probability distribution corresponding to lattice site $\boldsymbol{i}$ with itself is $\int d\boldsymbol{r}\,\phi_i^*(\boldsymbol{r})\phi_i(\boldsymbol{r}) = 1$, while the overlap with all other probability distributions corresponding to neighboring lattice sites is zero. This means that the magnitude of ϕ_i outside the Wigner-Seitz cell of lattice site $\boldsymbol{i}$ is negligible. It is therefore also reasonable to approximate $\lambda(x)$ to its value inside the Wigner-Seitz cell, provided that λ is constant inside the Wigner-Seitz cell.

For concreteness, we now consider a bilayer consisting of a heavy-metal and another material X, where X can be *e.g.* a superconductor. We assume that $\lambda(x) = \lambda$ is constant inside the heavy-metal, that $\lambda(x) = 0$ inside the other material and that $\lambda(x)$ acts as a step function at the interface. This system is shown in Fig. 2.2. From Eqs. 2.36 and 2.37, we see that as long as both $\boldsymbol{j} + \hat{m}$ and $\boldsymbol{j} - \hat{m}$ are inside the heavy-metal, $\lambda(x) = \lambda$ can be considered to be constant. If we for now only consider this case, applying Eq. 2.37 to Eq. 2.36 gives

$$\int d\boldsymbol{r}\,\phi_i^*(\boldsymbol{r})\lambda(x)\hat{p}_m\phi_j(\boldsymbol{r}) = \frac{i}{2}\lambda(\delta_{\boldsymbol{i},\boldsymbol{j}+\hat{m}} - \delta_{\boldsymbol{i},\boldsymbol{j}-\hat{m}}). \quad (2.38)$$

This holds for all $m = \{y, z\}$. It also holds for all $m = x$ except if $\boldsymbol{j}$ is the lattice site closest to the interface on either side of the interface, *i.e.* as long as $\boldsymbol{j}$ is among the green lattice sites in Fig. 2.2. Since the integral in Eq. 2.38 must equal zero if $\boldsymbol{i} = \boldsymbol{j}$ and also negligible if site $\boldsymbol{i}$ and $\boldsymbol{j}$ are not nearest neighbors, the

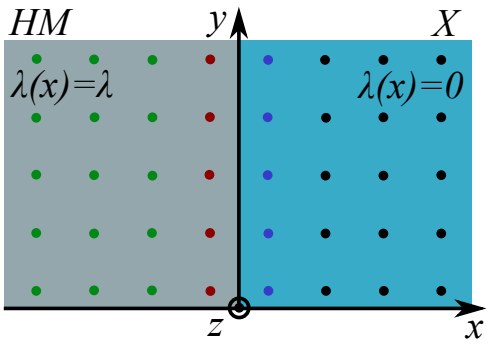

Figure 2.2: We consider a 3D cubic lattice where $\lambda(x) = \lambda$ inside the heavy-metal, and $\lambda(x) = 0$ inside X. If $\boldsymbol{i} = \boldsymbol{j} \pm \hat{y}$ or $\boldsymbol{i} = \boldsymbol{j} \pm \hat{z}$, lattice sites $\boldsymbol{i}$ and $\boldsymbol{j}$ are inside the same material, and we get a bulk contribution to the Hamiltonian if $\boldsymbol{i}$ and $\boldsymbol{j}$ are inside the heavy-metal. For $\boldsymbol{i} = \boldsymbol{j} \pm \hat{x}$, we will consider three cases: *i)* Lattice sites $\boldsymbol{i}$ and $\boldsymbol{j}$ are both inside the heavy-metal and not nearest neighbors to the interface (green lattice sites). *ii)* Lattice site $\boldsymbol{i}$ is inside the heavy-metal and nearest neighbor to the interface (red lattice sites), while $\boldsymbol{j}$ is inside the heavy-metal and not nearest neighbor to the interface (green lattice sites), or vice versa. *iii)* Lattice site $\boldsymbol{i}$ is inside the heavy-metal (red lattice sites) and lattice site $\boldsymbol{j}$ is inside X (blue lattice sites), or vice versa.

result in Eq. 2.38 is reasonable. It is therefore clear that our previous assumption given in Eq. 2.35 indeed gives no qualitative loss. Note also that

$$\begin{aligned}\left(\int d\boldsymbol{r}\,\phi_{\boldsymbol{j}}^{*}(\boldsymbol{r})\lambda(x)\hat{p}_x\phi_{\boldsymbol{i}}(\boldsymbol{r})\right)^{*} &= i\int d\boldsymbol{r}[\partial_x\phi_{\boldsymbol{i}}(\boldsymbol{r})]^{*}\lambda(x)\phi_{\boldsymbol{j}}(\boldsymbol{r}) \\ &= i\int d\boldsymbol{r}[\phi_{\boldsymbol{i}-\hat{x}}^{*}(\boldsymbol{r}) - \phi_{\boldsymbol{i}+\hat{x}}^{*}(\boldsymbol{r})]\lambda(x)\phi_{\boldsymbol{j}}(\boldsymbol{r}) \\ &= \frac{i}{2}\lambda(\delta_{\boldsymbol{i}-\hat{x},\boldsymbol{j}} - \delta_{\boldsymbol{i}+\hat{x},\boldsymbol{j}}) \\ &= \frac{i}{2}\lambda(\delta_{\boldsymbol{i},\boldsymbol{j}+\hat{x}} - \delta_{\boldsymbol{i},\boldsymbol{j}-\hat{x}})\end{aligned} \tag{2.39}$$

gives the same result as in Eq. 2.38 if both of the sites $\boldsymbol{i} \pm \hat{x}$ are inside the heavy-metal region, *i.e.* if $\boldsymbol{i}$ is among the green lattice sites in Fig. 2.2. For the case when site $\boldsymbol{i}$ and $\boldsymbol{j}$ are both inside the heavy-metal, and neither is nearest neighbor to the interface, *i.e.* when both are among the green lattice sites in Fig. 2.2, we therefore get $\frac{1}{2}\left[\langle\boldsymbol{i}|\lambda(x)\hat{p}_x|\boldsymbol{j}\rangle + \langle\boldsymbol{j}|\lambda(x)\hat{p}_x|\boldsymbol{i}\rangle^{*}\right] = \langle\boldsymbol{i}|\lambda(x)\hat{p}_x|\boldsymbol{j}\rangle$. This is reasonable, since we in the beginning of this section stated that for a constant λ we can use the non-symmetrized spin-orbit coupling operator. By inserting Eq. 2.38 into the expression for the overlap integral in Eq. 2.33, we get

$$\begin{aligned}\langle\boldsymbol{i}|\hat{h}|\boldsymbol{j}\rangle = \frac{i}{2}\lambda(\hat{n}\times\boldsymbol{\sigma})\cdot[&\hat{x}(\delta_{\boldsymbol{i},\boldsymbol{j}+\hat{x}} - \delta_{\boldsymbol{i},\boldsymbol{j}-\hat{x}}) \\ &+ \hat{y}(\delta_{\boldsymbol{i},\boldsymbol{j}+\hat{y}} - \delta_{\boldsymbol{i},\boldsymbol{j}-\hat{y}}) \\ &+ \hat{z}(\delta_{\boldsymbol{i},\boldsymbol{j}+\hat{z}} - \delta_{\boldsymbol{i},\boldsymbol{j}-\hat{z}})].\end{aligned} \tag{2.40}$$

By defining the vector from lattice site $\boldsymbol{i}$ to site $\boldsymbol{j}$ as

$$\boldsymbol{d}_{\boldsymbol{i},\boldsymbol{j}} \equiv \hat{x}(\delta_{\boldsymbol{i},\boldsymbol{j}-\hat{x}} - \delta_{\boldsymbol{i},\boldsymbol{j}+\hat{x}}) + \hat{y}(\delta_{\boldsymbol{i},\boldsymbol{j}-\hat{y}} - \delta_{\boldsymbol{i},\boldsymbol{j}+\hat{y}}) + \hat{z}(\delta_{\boldsymbol{i},\boldsymbol{j}-\hat{z}} - \delta_{\boldsymbol{i},\boldsymbol{j}+\hat{z}}), \tag{2.41}$$

we can rewrite Eq. 2.40 as

$$\left\langle \boldsymbol{i}\middle|\hat{h}\middle|\boldsymbol{j}\right\rangle = -\frac{i}{2}\lambda\hat{n}\cdot\left(\boldsymbol{\sigma}\times\boldsymbol{d}_{\boldsymbol{i},\boldsymbol{j}}\right), \tag{2.42}$$

where we have used that $\left(\hat{n}\times\boldsymbol{\sigma}\right)\cdot\boldsymbol{d}_{\boldsymbol{i},\boldsymbol{j}} = \hat{n}\cdot\left(\boldsymbol{\sigma}\times\boldsymbol{d}_{\boldsymbol{i},\boldsymbol{j}}\right)$. We can now write down the second quantized Hamiltonian that applies if both site $\boldsymbol{i}$ and $\boldsymbol{j}$ are inside the heavy-metal and neither is the lattice site closest to the interface,

$$H_\lambda = -\frac{i}{2}\sum_{\langle\boldsymbol{i},\boldsymbol{j}\rangle,\alpha,\beta}\lambda c^\dagger_{\boldsymbol{i},\alpha}\hat{n}\cdot(\boldsymbol{\sigma}\times\boldsymbol{d}_{\boldsymbol{i},\boldsymbol{j}})_{\alpha,\beta}c_{\boldsymbol{j},\beta}. \tag{2.43}$$

Notice that this is exactly the same expression as the non-symmetrized Hamiltonian in Eq. 2.1, although in Eq. 2.43 $\hat{n}$ is allowed to point in any direction. By using the Fourier transform in Eq. 2.4 and the relations in Eq. 2.5, we get

$$\begin{aligned} H_\lambda = \sum_{i_x j_x,k_y,k_z,\alpha,\beta} \lambda\hat{n}\cdot\Big[&\frac{i}{2}(\sigma_z\hat{y}-\sigma_y\hat{z})_{\alpha,\beta}(\delta_{i_x,j_x+1}-\delta_{i_x,j_x-1}) \\ &+(\sigma_x\hat{z}-\sigma_z\hat{x})_{\alpha,\beta}\sin(k_y)\delta_{i_x,j_x} \\ &+(\sigma_y\hat{x}-\sigma_x\hat{y})_{\alpha,\beta}\sin(k_z)\delta_{i_x,j_x}\Big]c^\dagger_{i_x,k_y,k_z,\alpha}c_{j_x,k_y,k_z,\beta}. \end{aligned} \tag{2.44}$$

Notice that as expected, the spin-orbit coupling term in Eq. 2.6 equals Eq. 2.44 if we let $\hat{n} = \hat{x}$. If we proceed by the same method as in Sec. 2.1, we get

$$\begin{aligned} H^\lambda_{i_x,j_x,k_y,k_z} = -\Big[&\sin(k_y)\cos(\phi)\sin(\theta)\hat{\tau}_0\hat{\sigma}_z \\ &-\big(\sin(k_y)\cos(\theta)-\sin(k_z)\sin(\phi)\sin(\theta)\big)\hat{\tau}_0\hat{\sigma}_x \\ &-\ \sin(k_z)\cos(\phi)\sin(\theta)\hat{\tau}_3\hat{\sigma}_y\Big]\lambda\delta_{i_x,j_x} \\ &+\Big[\frac{i}{2}\sin(\phi)\sin(\theta)\hat{\tau}_0\hat{\sigma}_z-\frac{i}{2}\cos(\theta)\hat{\tau}_3\hat{\sigma}_y\Big]\lambda\delta_{i_x,j_x+1} \\ &-\Big[\frac{i}{2}\sin(\phi)\sin(\theta)\hat{\tau}_0\hat{\sigma}_z-\frac{i}{2}\cos(\theta)\hat{\tau}_3\hat{\sigma}_y\Big]\lambda\delta_{i_x,j_x-1}, \end{aligned} \tag{2.45}$$

as a replacement for the the elements of the spin-orbit coupling term in Eq. 2.10 where neither $\boldsymbol{i}$ nor $\boldsymbol{j}$ is the closest lattice site to the interface.

We now consider the $\hat{p}_x$-term in Eq. 2.33 when site $\boldsymbol{i}$ or $\boldsymbol{j}$ is the lattice site closest to the interface, *i.e.* when one is among the green lattice sites and the other among

the red lattice sites in Fig. 2.2. By the use of Eq. 2.35, we can write the integrals in this term as

$$\begin{aligned}\frac{1}{2}\Big[\langle \boldsymbol{i}|\lambda(x)\hat{p}_x|\boldsymbol{j}\rangle + \langle \boldsymbol{j}|\lambda(x)\hat{p}_x|\boldsymbol{i}\rangle^*\Big] = -\frac{i}{4}\Big[&\int d\boldsymbol{r}\,\phi_{\boldsymbol{i}}^*(\boldsymbol{r})\lambda(x)\phi_{\boldsymbol{j}+\hat{x}}(\boldsymbol{r}) \\ - &\int d\boldsymbol{r}\,\phi_{\boldsymbol{i}}^*(\boldsymbol{r})\lambda(x)\phi_{\boldsymbol{j}-\hat{x}}(\boldsymbol{r}) \\ - &\Big(\int d\boldsymbol{r}\,\phi_{\boldsymbol{j}}^*(\boldsymbol{r})\lambda(x)\phi_{\boldsymbol{i}+\hat{x}}(\boldsymbol{r})\Big)^* \\ + &\Big(\int d\boldsymbol{r}\,\phi_{\boldsymbol{j}}^*(\boldsymbol{r})\lambda(x)\phi_{\boldsymbol{i}-\hat{x}}(\boldsymbol{r})\Big)^*\Big].\end{aligned} \tag{2.46}$$

We have to consider two cases: we can either have a HM/X system, as shown in Fig. 2.2, or an X/HM system. First consider a HM/X system, with site $\boldsymbol{j}$ closest to the interface and $\boldsymbol{i} = \boldsymbol{j} - \hat{x}$. The first and fourth term is zero due to $\delta_{\boldsymbol{j}-\hat{x},\boldsymbol{j}+\hat{x}} = 0$ and $\delta_{\boldsymbol{j},\boldsymbol{j}-2\hat{x}} = 0$. The second and third term consider the lattice sites $\boldsymbol{j} - \hat{x}$ and $\boldsymbol{j}$ that are inside the heavy-metal region. We can therefore set $\lambda(x) = \lambda$ in all four terms without adding any extra contribution. We get exactly the same result as in the bulk case, as would be expected when both lattice sites are inside the heavy-metal. If we consider the same system with site $\boldsymbol{i}$ closest to the interface and $\boldsymbol{j} = \boldsymbol{i} - \hat{x}$, the second and third terms are zero due to $\delta_{\boldsymbol{i},\boldsymbol{i}-2\hat{x}} = 0$ and $\delta_{\boldsymbol{i}-\hat{x},\boldsymbol{i}+\hat{x}} = 0$, while the first and fourth terms consider lattice points inside the heavy-metal. As in the previous case, we can set $\lambda(x) = \lambda$ and obtain the same result as for the bulk case. By the same line of reasoning we also get the same result as for the bulk case if we consider the X/HM system with site $\boldsymbol{j}$ closest to the interface and $\boldsymbol{i} = \boldsymbol{j} + \hat{x}$, or with site $\boldsymbol{i}$ closest to the interface and $\boldsymbol{j} = \boldsymbol{i} + \hat{x}$.

It now only remains to consider the case when $\boldsymbol{i}$ and $\boldsymbol{j}$ are the lattice sites closest to the interface on opposite sides of the interface, *i.e.* when one is among the red lattice sites and the other among the blue lattice sites in Fig. 2.2. Consider the case when site $\boldsymbol{j}$ is inside the heavy-metal and site $\boldsymbol{i}$ is inside X. Since the the first two terms in Eq. 2.46 consider the overlap at site $\boldsymbol{i}$, these two terms are zero since $\lambda(x) = 0$ inside X. For the two last terms, $\lambda(x) = \lambda$. We thus only get a contribution from Eq. 2.39, not from Eq. 2.38, and we get exactly half of what we got when both site $\boldsymbol{i}$ and $\boldsymbol{j}$ were inside the heavy-metal. If instead site $\boldsymbol{i}$ is inside the heavy-metal and site $\boldsymbol{j}$ is inside X, the last two terms in Eq. 2.46 are

zero due to $\lambda(x) = 0$, and we similarly get only half of the contribution in the bulk. We get

$$\begin{aligned}\left\langle \boldsymbol{i}\middle|\hat{h}\middle|\boldsymbol{j}\right\rangle = \quad & \frac{i}{2}\lambda(\hat{n}\times\boldsymbol{\sigma})\cdot\left[\frac{1}{2}\hat{x}(\delta_{\boldsymbol{i},\boldsymbol{j}+\hat{x}}-\delta_{\boldsymbol{i},\boldsymbol{j}-\hat{x}})\right.\\ & \left.+\hat{y}(\delta_{\boldsymbol{i},\boldsymbol{j}+\hat{y}}-\delta_{\boldsymbol{i},\boldsymbol{j}-\hat{y}})+\hat{z}(\delta_{\boldsymbol{i},\boldsymbol{j}+\hat{z}}-\delta_{\boldsymbol{i},\boldsymbol{j}-\hat{z}})\right]\\ =& -\frac{i}{2}\lambda(\hat{n}\times\boldsymbol{\sigma})\cdot\left[\frac{1}{2}(\boldsymbol{d}_{\boldsymbol{i},\boldsymbol{j}})_x+(\boldsymbol{d}_{\boldsymbol{i},\boldsymbol{j}})_{||}\right]\\ =& -\frac{i}{2}\lambda\hat{n}\cdot\left[\boldsymbol{\sigma}\times\frac{1}{2}(\boldsymbol{d}_{\boldsymbol{i},\boldsymbol{j}})_x+\boldsymbol{\sigma}\times(\boldsymbol{d}_{\boldsymbol{i},\boldsymbol{j}})_{||}\right],\end{aligned} \tag{2.47}$$

so that the spin-orbit coupling contribution to the Hamiltonian is

$$H_\lambda = -\frac{i}{2}\sum_{\langle \boldsymbol{i},\boldsymbol{j}\rangle,\alpha,\beta}\lambda c^\dagger_{\boldsymbol{i},\alpha}\hat{n}\cdot\left[\boldsymbol{\sigma}\times\frac{1}{2}(\boldsymbol{d}_{\boldsymbol{i},\boldsymbol{j}})_x+\boldsymbol{\sigma}\times(\boldsymbol{d}_{\boldsymbol{i},\boldsymbol{j}})_{||}\right]_{\alpha,\beta}c_{\boldsymbol{j},\beta} \tag{2.48}$$

if lattice site $\boldsymbol{i}$ and $\boldsymbol{j}$ are the lattice sites closest to the interface on opposite sides of the interface. Above, $\boldsymbol{d}_{\boldsymbol{i},\boldsymbol{j}}$ is decomposed into a part perpendicular to the interface $(\boldsymbol{d}_{\boldsymbol{i},\boldsymbol{j}})_x$ and a part parallel to the interface $(\boldsymbol{d}_{\boldsymbol{i},\boldsymbol{j}})_{||}$.

By comparing Eq. 2.48 to Eq. 2.43, we can generalize the bulk expression for the Rashba term of the second quantized Hamiltonian in Eq. 2.45. The symmetrized expression for the Hamiltonian of a hybrid structure with superconductivity and Rashba spin-orbit coupling is

$$\begin{aligned}H_{i_x,j_x,k_y,k_z} =& \epsilon_{i_x,j_x,k_y,k_z}\hat{\tau}_3\hat{\sigma}_0+\left[\Delta_{i_x}i\hat{\tau}^+\hat{\sigma}_y-\Delta^*_{i_x}i\hat{\tau}^-\hat{\sigma}_y\right]\delta_{i_x,j_x}\\ & -\Big[\sin(k_y)\cos(\phi)\sin(\theta)\hat{\tau}_0\hat{\sigma}_z\\ & -\big(\sin(k_y)\cos(\theta)-\sin(k_z)\sin(\phi)\sin(\theta)\big)\hat{\tau}_0\hat{\sigma}_x\\ & -\ \sin(k_z)\cos(\phi)\sin(\theta)\hat{\tau}_3\hat{\sigma}_y\Big]\lambda\delta_{i_x,j_x}\\ & +\left[\frac{i}{4}\sin(\phi)\sin(\theta)\hat{\tau}_0\hat{\sigma}_z-\frac{i}{4}\cos(\theta)\hat{\tau}_3\hat{\sigma}_y\right]\lambda(1+\zeta)\delta_{i_x,j_x+1}\\ & -\left[\frac{i}{4}\sin(\phi)\sin(\theta)\hat{\tau}_0\hat{\sigma}_z-\frac{i}{4}\cos(\theta)\hat{\tau}_3\hat{\sigma}_y\right]\lambda(1+\zeta)\delta_{i_x,j_x-1},\end{aligned} \tag{2.49}$$

where $\zeta = 1$ if site $\boldsymbol{i}$ and $\boldsymbol{j}$ are both inside the heavy-metal and $\zeta = 0$ if site $\boldsymbol{i}$ and $\boldsymbol{j}$ are on opposite sides of the interface. The terms are only nonzero in their respective regions.

2.3 THE FREE ENERGY

The free energy (F) is minimized in the ground state of the system. In Ch. 4, where we consider magnetization reorientation in a S/HM/F heterostructure, we will consider the free energy in order to determine the preferred magnetization direction of the ferromagnetic layer at a given temperature. The free energy is related to the partition function by $Z = e^{-\beta F}$, where $Z \equiv \mathrm{Tr}(e^{-\beta H})$ [29]. By inserting the diagonalized Hamiltonian given in Eq. 2.16, we obtain

$$F = H_0 - \frac{1}{\beta} \sum_{n,k_y,k_z} \ln(1 + e^{-\beta E_{n,k_y,k_z}/2}), \tag{2.50}$$

where $\beta = (k_B T)^{-1}$. Note that if $T \to 0$,

$$F = H_0 + \frac{1}{2} {\sum_{n,k_y,k_z}}' E_{n,k_y,k_z}, \tag{2.51}$$

where $\sum'$ means that the sum is taken over negative eigenenergies only.

Additional magnetic anisotropy terms may be added to the free energy to take the thickness of a thin ferromagnetic film into account more properly. We here take into account perpendicular interfacial anisotropy and shape anisotropy, which are of great importance in thin ferromagnetic films. Materials may also have a magnetocrystalline anisotropy where some magnetization direction is favored due to the bulk crystal structure of the material, but this will not be considered here. Interfacial anisotropy arises due to the electronic structure being different along in-plane directions compared to the out-of-plane direction. We therefore have a difference in the electronic wave function overlap for the in-plane and out-of-plane direction, which favors out-of-plane magnetization. This structural anisotropy only dominates for very thin ferromagnetic layers. Shape anisotropy is caused by the fact that it is energetically favorable to minimize the number of free surface poles. In a thin film, the number of free surface poles is minimized when the magnetization is parallel to the interface, as shown in Fig. 2.3. In this case, the free surface poles only exist on the edge [30]. We model the interfacial and shape anisotropy terms in a simple way and write the additional contribution to the free energy as [31]

$$F_a = -K_{\mathrm{eff}} \cos^2(\theta_p). \tag{2.52}$$

where θ_p is the polar angle relative to the interface normal. When the interface normal is parallel to the x axis, $\theta_p = \arccos(\cos(\phi)\sin(\theta))$, where θ is the polar

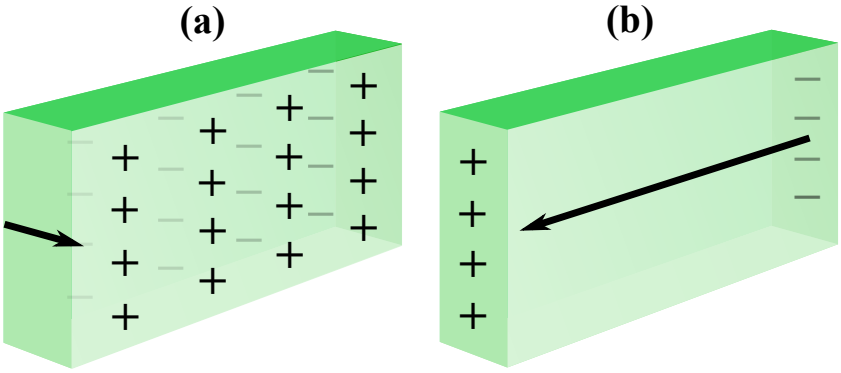

Figure 2.3: (a) If the magnetization (black arrow) is out-of-plane, the number of free surface poles (+ and −) is large. (b) If the magnetization is in-plane, the number of free surface poles is small, since they only exist on the edge. The case shown in (b) is energetically favourable.

angle relative to the z axis and ϕ is the azimuthal angle. K_{eff} is the effective anisotropy constant. We assume a thin ferromagnetic film with one interface to another material and one free surface, and approximate K_{eff} by [31]

$$K_{\text{eff}} = K_v + \frac{K_s + K_i}{t_F}. \tag{2.53}$$

Above, $K_v < 0$ is the bulk anisotropy of the ferromagnet, K_s is the surface anisotropy and $K_i > 0$ is the anisotropy of the interface between the ferromagnet and the other material. K_{eff} may be positive or negative depending on the thickness of the ferromagnetic layer t_F. If $K_{\text{eff}} < 0$, the magnetic anisotropy contribution F_a to the free energy favors IP magnetization and shape anisotropy dominates. For $K_{\text{eff}} > 0$, OOP magnetization is favored and perpendicular anisotropy dominates. To model a non cubic ferromagnet such as Co, we use the average lattice constant, $a = (a_x + a_y + a_z)/3$. By doing this we obtain a rather rough estimate of F_a, but since we in Ch. 4 will be comparing F_a to the superconducting contribution to the free energy, the order of magnitude of the change in F_a is more interesting than the details. The SI unit of K_v is J/m^3, while for K_s and K_i the SI unit is J/m^2. Since we set Boltzmann's constant k_B and the lattice constant a equal to 1, the free energy is effectively given in $[F] = [1/\beta]$=K. Therefore, the anisotropy constants are adapted from SI by K_v(K)= K_v(J/m^3)a^3/k_B and $K_{s,i}$(K)= $K_{s,i}$(J/m^2)a^2/k_B. It follows that in our numerical calculations, the thickness of the ferromagnetic layer is given by the number of lattice points along $\hat{x}$ in the ferromagnetic region, *i.e.* $t_F(1) = t_F(\text{m})/a = N_{x,F}$.

For the simplified model with eigenenergies given by Eq. 2.26, the free energy at $T \to 0$ is given by an expression similar to that in Eq. 2.51,

$$F = H_0 + \frac{1}{2}\sum_{n,\boldsymbol{k}}{}' E_{n,\boldsymbol{k}}, \tag{2.54}$$

where $\sum'$ means that we sum over negative eigenenergies only. To determine F, we simply insert those of the eigenenergies in Eq. 2.26 that are negative into Eq. 2.54.

2.4 THE SUPERCONDUCTING CRITICAL TEMPERATURE

The superconducting critical temperature (T_c) is the temperature at which the superconducting phase transition takes place. In its normal state where $T > T_c$, the superconductor behaves as a normal-metal. For temperatures below T_c, the superconductor shows a superconducting behavior. We find T_c numerically by a binomial search [32] within temperatures below the bulk critical temperature of the superconductor. The critical temperature of the superconducting heterostructure must be within this temperature interval, since the addition of heavy-metal and ferromagnetic layers cannot increase T_c. In each of the n iterations in our binomial search, we test whether the average temperature $T = (T_{c,\max} - T_{c,\min})/2$ in the current temperature interval $[T_{c,\min}, T_{c,\max}]$ is above or below T_c. This is done by choosing an initial guess for Δ_{i_x} at $\Delta_0/1000$ and checking whether the value of $\Delta(T)$ in the middle of the superconducting region increases or decreases from the initial guess after recalculating the gap m times by Eq. 2.18. The gap decreases in the normal state ($T > T_c$) and increases in the superconducting state ($T < T_c$). Δ_0 is the superconducting gap in the middle of the superconductor at $T = 0$. If the current T is below T_c we restrict the temperature range of our search to the temperatures within the previous temperature interval that are above T. Otherwise we restrict our temperature range to the temperatures below T. This is illustrated in Fig. 4.6. After having calculated a new temperature range n times we conclude that the average temperature in this range is the critical temperature. If we assume m to be sufficiently large, this binomial search calculates T_c to an uncertainty of $\pm 2^{-(n+1)} T^{\mathrm{i}}_{c,\max}$, where $T^{\mathrm{i}}_{c,\max}$ is the upper bound on the initial temperature interval. We test whether m is large enough by calculating T_c for increasing values of m. Our choice of m should be the m for which the calculated value of T_c no longer changes when increasing m. For superconducting layers that are much thicker than the coherence length, a low m is sufficient.

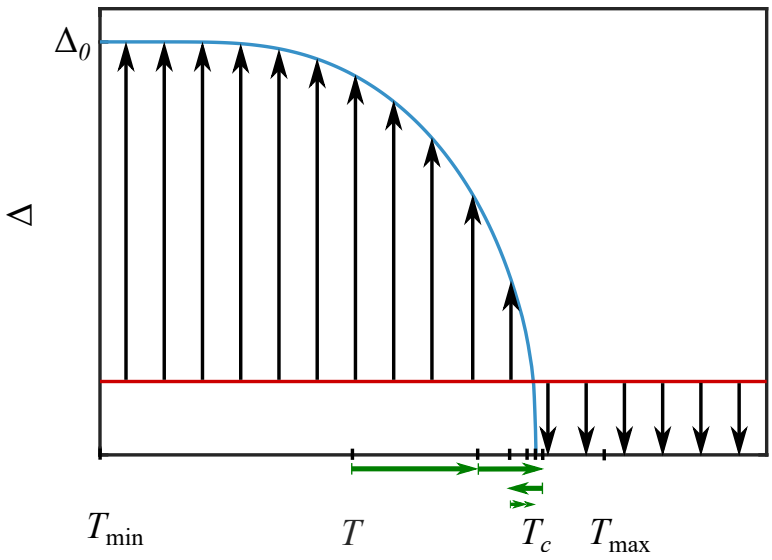

Figure 2.4: The blue curve shows $\Delta(T)$, and the red line is our initial guess for Δ in the middle of the superconducting region. As indicated by the black arrows, recalculating Δ m times results in an increase in Δ if the temperature is below T_c, and a decrease in Δ if the temperature is above T_c. We start our binomial search at $T = (T_{\max} - T_{\min})/2$. At every iteration, we keep the half of the temperature interval that contains T_c, and T is set to the value in the middle of our temperature interval, as indicated by the green arrows. After n iterations, we arrive at T_c.

However, for systems where the length of the superconductor is comparable to its coherence length, bulk superconductivity is not obtained in the middle of the superconducting region, and we must use a large m to get an accurate result.

The number of iterations m can be decreased by improving the initial guess. This was done for the calculations in Ch. 5 in order to make the T_c-calculations manageable. The initial guess can be improved by calculating the superconducting gap as close as possible to the superconducting critical temperature, normalizing it so that the gap is equal to one at the lattice site where the superconducting gap is measured in the T_c-calculation, and multiplying by $\Delta_0/1000$. In this way, the initial guess has approximately the same shape as the superconducting gap for temperatures close to T_c. The gap will therefore increase or decrease over the entire superconducting region.

2.5 THE SINGLET AND TRIPLET AMPLITUDES

The physical mechanism leading to a variation in the superconducting condensation energy when the magnetization direction or the direction of the spin-orbit field is changed is the conversion of singlet Cooper pairs to triplet ones. The singlet to triplet generation can lead to variations in F and T_c, that will be considered in Chs. 4 and 5 for the S/HM/F and S/HM systems. The parity of a Cooper pair is described by spin permutation (S), spatial inversion (P), orbital index permutation (O) and time permutation (T), where SPOT= -1 is required in order to satisfy the Pauli principle, and S^2 =P^2 =O^2 =T^2 = 1 [33]. A singlet Cooper pair ($\uparrow\downarrow - \downarrow\uparrow$) changes sign if the spin indices are interchanged. The triplet Cooper pairs ($\uparrow\downarrow + \downarrow\uparrow$), ($\uparrow\uparrow$) and ($\downarrow\downarrow$) are invariant under interchange of spin indices. Therefore S= -1 for singlets, while S= 1 for triplets. P= $(-1)^l$, where l is the orbital angular momentum quantum number. $l = 0$ for s-wave Cooper pairs, $l = 1$ for p-wave Cooper pairs and $l = 2$ for d-wave Cooper pairs. In this thesis, we will not consider the possibility of orbital index permutation. This implies that T= 1 for s- and d-wave singlets, and p-wave triplets, while T=-1 for p-wave singlets, and s- and d-wave triplets. The S, P, and T parities of the different singlets and triplets are summarized in Table 2.1. A state where T= -1 is called an odd-frequency state, while a state where T= 1 is called an even-frequency state.

	S	P	T	SPT
s-wave singlet	-1	1	1	-1
p-wave singlet	-1	-1	-1	-1
d-wave singlet	-1	1	1	-1
s-wave triplet	1	1	-1	-1
p-wave triplet	1	-1	1	-1
d-wave triplet	1	1	-1	-1

Table 2.1: The above table summarizes the parities of the s-, p-, and d-wave singlets and triplets under spin permutation (S), spatial inversion (P) and time permutation (T). According to the Pauli principle, all of the singlets and triplets must satisfy SPT= -1 if we disregard orbital index permutation.

To reveal the types of triplet Cooper pairs present in our system, we compute the triplet anomalous Green's function amplitudes. In this chapter, we will only

consider s- and p-wave triplets. We will consider s-, p-, and d-wave singlets and triplets in Ch. 3. The on-site odd-frequency s-wave anomalous triplet amplitudes are defined as [27]

$$\begin{aligned} S_{0,\boldsymbol{i}}(\tau) &= \left\langle c_{\boldsymbol{i},\uparrow}(\tau)c_{\boldsymbol{i},\downarrow}(0)\right\rangle + \left\langle c_{\boldsymbol{i},\downarrow}(\tau)c_{\boldsymbol{i},\uparrow}(0)\right\rangle, \\ S_{\sigma,\boldsymbol{i}}(\tau) &= \left\langle c_{\boldsymbol{i},\sigma}(\tau)c_{\boldsymbol{i},\sigma}(0)\right\rangle, \end{aligned} \tag{2.55}$$

where we have defined the time-dependent electron annihilation operator $c_{\boldsymbol{i},\sigma}(\tau) \equiv e^{iH\tau}c_{\boldsymbol{i},\sigma}e^{-iH\tau}$ [34]. Since the s-wave triplet amplitudes defined in the above equation are odd under time permuation, they are only nonzero if $\tau \neq 0$. By differentiating $c_{\boldsymbol{i},\sigma}(\tau)$ with respect to τ we obtain the Heisenberg equation [34],

$$\frac{dc_{\boldsymbol{i},\sigma}(\tau)}{d\tau} = i[H, c_{\boldsymbol{i},\sigma}(\tau)], \tag{2.56}$$

from which we can obtain expressions for $c_{\boldsymbol{i},\uparrow}(\tau)$ and $c_{\boldsymbol{i},\downarrow}(\tau)$ by inserting Eqs. 2.16 and 2.17. Here, τ is the relative time coordinate between the electron operators. τ is scaled by $\hbar/t$ in the following. The even-frequency p-wave anomalous triplet amplitudes are defined [27]

$$\begin{aligned} P^n_{0,\boldsymbol{i}} &= \sum_{\pm} \pm(\left\langle c_{\boldsymbol{i},\uparrow}c_{\boldsymbol{i}\pm\hat{n},\downarrow}\right\rangle + \left\langle c_{\boldsymbol{i},\downarrow}c_{\boldsymbol{i}\pm\hat{n},\uparrow}\right\rangle), \\ P^n_{\sigma,\boldsymbol{i}} &= \sum_{\pm} \pm \left\langle c_{\boldsymbol{i},\sigma}c_{\boldsymbol{i}\pm\hat{n},\sigma}\right\rangle, \end{aligned} \tag{2.57}$$

where $n = \{x, y, z\}$. Since, the p_n-wave triplet amplitude is odd under spatial inversion along $\hat{n}$, $\pm$ is added in order to get nonzero triplet amplitudes when summing over all k_y and k_z. The spins in the above triplet amplitudes are defined with respect to the z axis. We obtain expressions for the triplet amplitudes by inserting the expressions for the electron annihilation operators in Eq. 2.17 into Eqs. 2.55 and 2.57. The s-wave triplet amplitudes are

$$\begin{aligned} S_{0,i_x}(\tau) &= \frac{1}{N_yN_z}\sum_{n,k_y,k_z}[u_{i_x,n,k_y,k_z}x^*_{i_x,n,k_y,k_z} + v_{i_x,n,k_y,k_z}w^*_{i_x,n,k_y,k_z}]e^{-iE_{n,k_y,k_z}\tau/2} \\ &\qquad \cdot [1 - f(E_{n,k_y,k_z}/2)], \\ S_{\uparrow,i_x}(\tau) &= \frac{1}{N_yN_z}\sum_{n,k_y,k_z}u_{i_x,n,k_y,k_z}w^*_{i_x,n,k_y,k_z}e^{-iE_{n,k_y,k_z}\tau/2}[1 - f(E_{n,k_y,k_z}/2)], \\ S_{\downarrow,i_x}(\tau) &= \frac{1}{N_yN_z}\sum_{n,k_y,k_z}v_{i_x,n,k_y,k_z}x^*_{i_x,n,k_y,k_z}e^{-iE_{n,k_y,k_z}\tau/2}[1 - f(E_{n,k_y,k_z}/2)], \end{aligned} \tag{2.58}$$

the p_x-wave triplet amplitudes are

$$\begin{aligned}
P^x_{0,i_x} &= \frac{1}{N_y N_z} \sum_{n,k_y,k_z} [u_{i_x,n,k_y,k_z} x^*_{i_x+1,n,k_y,k_z} - u_{i_x,n,k_y,k_z} x^*_{i_x-1,n,k_y,k_z} \\
&\qquad + v_{i_x,n,k_y,k_z} w^*_{i_x+1,n,k_y,k_z} - v_{i_x,n,k_y,k_z} w^*_{i_x-1,n,k_y,k_z}] \\
&\qquad \cdot [1 - f(E_{n,k_y,k_z}/2)], \\
P^x_{\uparrow,i_x} &= \frac{1}{N_y N_z} \sum_{n,k_y,k_z} [u_{i_x,n,k_y,k_z} w^*_{i_x+1,n,k_y,k_z} - u_{i_x,n,k_y,k_z} w^*_{i_x-1,n,k_y,k_z}] \\
&\qquad \cdot [1 - f(E_{n,k_y,k_z}/2)], \\
P^x_{\downarrow,i_x} &= \frac{1}{N_y N_z} \sum_{n,k_y,k_z} [v_{i_x,n,k_y,k_z} x^*_{i_x+1,n,k_y,k_z} - v_{i_x,n,k_y,k_z} x^*_{i_x-1,n,k_y,k_z}] \\
&\qquad \cdot [1 - f(E_{n,k_y,k_z}/2)],
\end{aligned} \tag{2.59}$$

the p_y-wave triplet amplitudes are

$$\begin{aligned}
P^y_{0,i_x} &= -\frac{2i}{N_y N_z} \sum_{n,k_y,k_z} [u_{i_x,n,k_y,k_z} x^*_{i_x,n,k_y,k_z} + v_{i_x,n,k_y,k_z} w^*_{i_x,n,k_y,k_z}] \\
&\qquad \cdot \sin\left(k_y\right) [1 - f(E_{n,k_y,k_z}/2)], \\
P^y_{\uparrow,i_x} &= -\frac{2i}{N_y N_z} \sum_{n,k_y,k_z} u_{i_x,n,k_y,k_z} w^*_{i_x,n,k_y,k_z} \sin\left(k_y\right) [1 - f(E_{n,k_y,k_z}/2)], \\
P^y_{\downarrow,i_x} &= -\frac{2i}{N_y N_z} \sum_{n,k_y,k_z} v_{i_x,n,k_y,k_z} x^*_{i_x,n,k_y,k_z} \sin\left(k_y\right) [1 - f(E_{n,k_y,k_z}/2)],
\end{aligned} \tag{2.60}$$

and the p_z-wave triplet amplitudes are

$$\begin{aligned}
P^z_{0,i_x} &= -\frac{2i}{N_y N_z} \sum_{n,k_y,k_z} [u_{i_x,n,k_y,k_z} x^*_{i_x,n,k_y,k_z} + v_{i_x,n,k_y,k_z} w^*_{i_x,n,k_y,k_z}] \\
&\qquad \cdot \sin\left(k_z\right) [1 - f(E_{n,k_y,k_z}/2)], \\
P^z_{\uparrow,i_x} &= -\frac{2i}{N_y N_z} \sum_{n,k_y,k_z} u_{i_x,n,k_y,k_z} w^*_{i_x,n,k_y,k_z} \sin\left(k_z\right) [1 - f(E_{n,k_y,k_z}/2)], \\
P^z_{\downarrow,i_x} &= -\frac{2i}{N_y N_z} \sum_{n,k_y,k_z} v_{i_x,n,k_y,k_z} x^*_{i_x,n,k_y,k_z} \sin\left(k_z\right) [1 - f(E_{n,k_y,k_z}/2)].
\end{aligned} \tag{2.61}$$

If we want to compute the triplet amplitudes for a specific direction of the homogeneous ferromagnetic exchange field $\boldsymbol{h}$ such that $(\uparrow\uparrow)_{\boldsymbol{h}}$ and $(\downarrow\downarrow)_{\boldsymbol{h}}$ represent the long-range triplets, the triplet amplitudes must be transformed so that the spins are defined with respect to the vector $\boldsymbol{h}$. The vector $\boldsymbol{h}$ is described by

the polar coordinates (θ, ϕ) with respect to the z axis. We transform the triplet amplitudes by inserting $(c_{\boldsymbol{i},\uparrow})_{\theta,\phi} = \cos(\theta/2)e^{-i\phi/2}(c_{\boldsymbol{i},\uparrow})_z + \sin(\theta/2)e^{i\phi/2}(c_{\boldsymbol{i},\downarrow})_z$ and $(c_{\boldsymbol{i},\downarrow})_{\theta,\phi} = -\sin(\theta/2)e^{-i\phi/2}(c_{\boldsymbol{i},\uparrow})_z + \cos(\theta/2)e^{i\phi/2}(c_{\boldsymbol{i},\downarrow})_z$ [9] into Eqs. 2.55 and 2.57. For the s-wave triplet amplitudes, we get

$$\begin{aligned}
[S_{0,i_x}(\tau)]_{\theta,\phi} &= -\sin(\theta)\{e^{-i\phi}[S_{\uparrow,i_x}(\tau)]_z - e^{i\phi}[S_{\downarrow,i_x}(\tau)]_z\} + \cos(\theta)[S_{0,i_x}(\tau)]_z, \\
[S_{\uparrow,i_x}(\tau)]_{\theta,\phi} &= \cos^2(\theta/2)e^{-i\phi}[S_{\uparrow,i_x}(\tau)]_z + \sin^2(\theta/2)e^{i\phi}[S_{\downarrow,i_x}(\tau)]_z \\
&\quad + \sin(\theta/2)\cos(\theta/2)[S_{0,i_x}(\tau)]_z, \\
[S_{\downarrow,i_x}(\tau)]_{\theta,\phi} &= \sin^2(\theta/2)e^{-i\phi}[S_{\uparrow,i_x}(\tau)]_z + \cos^2(\theta/2)e^{i\phi}[S_{\downarrow,i_x}(\tau)]_z \\
&\quad - \sin(\theta/2)\cos(\theta/2)[S_{0,i_x}(\tau)]_z,
\end{aligned} \tag{2.62}$$

and for the p-wave triplet amplitudes, we get

$$\begin{aligned}
[P^n_{0,i_x}]_{\theta,\phi} &= -\sin(\theta)\{e^{-i\phi}[P^n_{\uparrow,i_x}]_z - e^{i\phi}[P^n_{\downarrow,i_x}]_z\} + \cos(\theta)[P^n_{0,i_x}]_z, \\
[P^n_{\uparrow,i_x}]_{\theta,\phi} &= \cos^2(\theta/2)e^{-i\phi}[P^n_{\uparrow,i_x}]_z + \sin^2(\theta/2)e^{i\phi}[P^n_{\downarrow,i_x}]_z \\
&\quad + \sin(\theta/2)\cos(\theta/2)[P^n_{0,i_x}]_z, \\
[P^n_{\downarrow,i_x}]_{\theta,\phi} &= \sin^2(\theta/2)e^{-i\phi}[P^n_{\uparrow,i_x}]_z + \cos^2(\theta/2)e^{i\phi}[P^n_{\downarrow,i_x}]_z \\
&\quad - \sin(\theta/2)\cos(\theta/2)[P^n_{0,i_x}]_z.
\end{aligned} \tag{2.63}$$

The even-frequency s-wave singlet amplitude is given by

$$S_{s,\boldsymbol{i}} = \left\langle c_{\boldsymbol{i},\uparrow}c_{\boldsymbol{i},\downarrow}\right\rangle - \left\langle c_{\boldsymbol{i},\downarrow}c_{\boldsymbol{i},\uparrow}\right\rangle. \tag{2.64}$$

By inserting the expressions for the annihilation operators given in Eq. 2.17, we find that the s-wave singlet amplitude is proportional to the superconducting gap,

$$S_{s,\boldsymbol{i}} = 2\Delta_{\boldsymbol{i}}/U_{\boldsymbol{i}}. \tag{2.65}$$

By rotating the singlet amplitude similarly to the triplet amplitudes, we find that the singlet amplitude is rotationally invariant with respect to the choice of quantization axis. The quantity

$$\tilde{S}_s = \frac{1}{N_{x,S}}\sum_{i_x}|S_{s,i_x}| \tag{2.66}$$

can therefore be used as a measure of the s-wave singlet amplitude of the system for given directions of the magnetization and spin-orbit field. The sum is taken over the superconducting region only, as we are primarily interested in describing

how the superconducting condensation energy depends on the magnetization direction or the direction of the spin-orbit field. Eq. 2.66 is useful for predicting variations in F and T_c, as the total change in the singlet amplitude indirectly shows the total triplet generation. It is harder to calculate the total triplet amplitude, as it is difficult to determine how the different triplets should be weighted in order to account for the total singlet to triplet generation. Also, the total amplitude of the above calculated s-wave and p-wave triplets may not be a good measure of the total s-wave singlet amplitude as there may be d-wave triplets, and p- and d-wave singlets in the system contributing to the suppression of the s-wave singlet amplitude. To find the total triplet density we would also need some way to account for all choices of τ. It is therefore simpler to examine the singlet to triplet generation by using Eq. 2.66. Note however that Eq. 2.66 is defined at a given temperature. One must therefore be careful when comparing the angular dependence of $\tilde{S}_s$ and T_c, since $\tilde{S}_s$ must be computed for some $T < T_c$.

2.6 THE SUPERCONDUCTING COHERENCE LENGTH

The superconducting coherence length (ξ) of a superconducting hybrid structure is a measure of the distance over which the superconducting gap is affected by the non-superconducting layers, and it is therefore an important length scale when adding ferromagnetic and heavy-metal layers to a superconductor. The effects of the additional layers can be expected to be strongest when ξ is the same length or slightly longer than the thickness of the superconductor. In the ballistic limit the superconducting coherence length is given by [4]

$$\xi = \hbar v_F / \pi \Delta_0. \tag{2.67}$$

The normal state Fermi velocity, v_F, is obtained by the dispersion relation $v_F = \frac{1}{\hbar}\frac{dE_{\boldsymbol{k}}}{d\boldsymbol{k}}\big|_{k=k_F}$ [4]. $E_{\boldsymbol{k}} = -2t[\cos(k_x) + \cos(k_y) + \cos(k_z)] - \mu_N$ is the normal-state eigenenergies obtained from Eq. 2.1 if we use periodic boundary conditions in all three directions. The Fermi momentum k_F corresponds to the Fermi energy E_F, which is the highest occupied energy level at $T = 0$. In our theoretical framework, E_F is located at $E_{\boldsymbol{k}} = 0$. Since our Fermi surface is not spherical, we need to average over all possible v_F. In our algorithm for finding v_F, we choose N_x, N_y and N_z to be sufficiently large (we choose $N_x = N_y = N_z = 100$), so that we have a large number of discrete k_x, k_y and k_z values. In order to find all $\boldsymbol{k}$ located at the Fermi surface, we calculate $E_{\boldsymbol{k}}$ for all combinations of $\{k_x, k_y, k_z\}$ and determine whether $E_{\boldsymbol{k}} \in [\min(E_{\boldsymbol{k}})/100, 0]$, *i.e.* whether $E_{\boldsymbol{k}}$ is

sufficiently close to the Fermi energy. We estimate v_F by averaging over all of the Fermi velocities calculated from the possible Fermi momenta. Δ_0 is the zero temperature superconducting gap of the superconducting heterostructure. Note that Δ_0 is dependent upon the magnetization direction of the ferromagnetic layers and the direction of the Rashba spin-orbit field in the heavy-metal layers. The change in ξ when rotating the magnetization and the spin-orbit field is however typically much smaller than the distance between two lattice points. In our lattice model we round ξ down to the closest integer number of lattice points.

2.7 THE 2D AND 3D LATTICE MODELS

In our calculations, we have used a 3D cubic lattice model with periodic boundary conditions in both the y direction and z direction. It is worth noting that this gives qualitatively different results than if we use a 2D square lattice model with periodic boundary conditions only in the y direction. Since the 2D model does not have periodic boundary conditions in the z direction, we do not get the $\sin(k_z)$-terms in Eqs. 2.10 and 2.49 when considering a 2D square lattice. For the S/HM/F system, this implies that the system is invariant under ϕ-rotations of $\boldsymbol{h}$. Physical quantities such as T_c and F therefore have the same angular dependence in the xz and yz planes, so that the system is not invariant under $\pi/2$-rotations in the yz plane as is expected for a 3D cubic lattice. Similarly, we need to model our S/HM system as a 3D cubic lattice structure in order to have $\pi/2$-rotational invariance of the spin-orbit field in the yz plane. It should therefore be cautioned against simplifying the numerical simulations of a 3D cubic lattice by using a 2D square lattice model when spin-orbit coupling is present due to its $\boldsymbol{k}$-dependence. For $\boldsymbol{k}$-independent interactions, such as a magnetic exchange field, the distinction between 2D and 3D becomes less important. In our calculations we use $N_y = N_z$ so that we get an equal number of k_y and k_z values, thereby obtaining a $\pi/2$-rotational invariance in the yz plane even when N_y and N_z are not much larger than the film thicknesses. It should also be noted that the thickness of the sample parallel to the interfaces is important for the physical results obtained in an experiment. In this thesis, we model thin-film structures in which the width of the sample in the y and z directions is much larger than the thickness of the sample in the x direction.

2.8 THE CHOICE OF PARAMETERS

When modelling heterostructures where thin heavy-metal and ferromagnetic films are added to a superconducting layer, we want to find a set of parameters that results in considerable changes in the physical properties of the system, such as T_c and F. When choosing our system parameters, we must take into account the superconducting coherence length, and the strength and size of the non-superconducting layers compared to the superconducting layer. Our choices of parameters are also restricted to lattice sizes that are not too computationally expensive. Also, we must make sure to choose N_y and N_z large enough to avoid numerical artifacts due to the discreteness of our model.

As mentioned in Sec. 2.6, the superconducting layer is most strongly affected by interface effects when the superconducting coherence length is comparable to the thickness of the superconducting layer. If ξ and $N_{x,S}$ are comparable, bulk superconductivity cannot be obtained in the middle of the superconducting region. Due to its dependence on the superconducting gap and the Fermi velocity, the superconducting coherence length depends on all of the system parameters. Adding a ferromagnetic or heavy-metal layer to a superconductor lowers the superconducting gap and the critical temperature. Adding a heavy-metal layer between the superconductor and a ferromagnetic layer increases Δ and T_c compared to the S/F bilayer, as the heavy-metal partly shields the superconductor from the ferromagnet. The strength and size of an additional layer must be chosen so that it gives as strong an effect as possible without suppressing superconductivity completely or shielding the effect of other non-superconducting layers. In Ref. [25], it is shown that for a diffusive S/HM/F system, the Rashba spin-orbit coupling must neither be too strong nor too weak in order to get a variation in T_c when rotating the magnetization of a diffusive S/HM/F structure from IP to OOP. For such systems the energy penalty that suppresses triplet amplitudes depends on the Rashba spin-orbit coupling parameter λ to the second order. A large λ therefore leads to a strong suppression of triplet amplitudes for all magnetization directions, and T_c is always high. A small λ leads to a negligible triplet suppression, and T_c remains low for all magnetization directions.

In this thesis, we will consider some physical quantities that have a dependence on the magnetization direction or the direction of the spin-orbit field that changes qualitatively if we, by choosing a different set of parameters, change the energy band structure of the system. This is caused by the dependence of the singlet to triplet generation on the eigenenergies. Since the energy band structure depends

on all of the system parameters, all parameters must be taken into consideration if we want to demonstrate a particular behavior of a physical quantity under rotations of the magnetization or spin-orbit field. The importance of the band structure will be further discussed in Chs. 4 and 5.

2.9 THE RELEVANCE OF THE BOGOLIUBOV-DE GENNES FRAMEWORK

Before applying the tight-binding lattice BdG framework to the systems considered in this thesis, we consider its relevance with respect to making predictions for systems that are experimentally realizable. As mentioned, the BdG framework is well suited for describing thin-film heterostructures. We can model atomically thin layers, and capture the crystal symmetry of the sample and its influence on physical quantities. Another advantage is that we can vary the parameters describing our system across a large range. The main weakness of the theoretical framework presented above, is that we are restricted to considering relatively small sample sizes in order to keep the system computationally manageable, especially when considering a 3D lattice.

When considering a thin superconducting layer, the superconducting coherence length must be short in order to be comparable to the thickness of the superconducting layer. ξ is proportional to the inverse of the zero temperature superconducting gap. Considering a thin superconducting layer therefore results in a large value for the superconducting order parameter, and also a large critical temperature. However, if the spatial dimensions of all layers are scaled by the superconducting coherence length, the theoretical framework presented above can still be used to make qualitative and quantitative predictions for experimentally realistic systems. An example that illustrates that the method presented above gives good agreement with experimental results when scaled in this way is Ref. [35], where the authors use the same theoretical formalism that we use in this thesis. The predictions made in Ref. [35] were later found to correspond very well to experimental measurements done in Ref. [36]. We therefore have good reasons to expect that the results obtained in Chs. 4 and 5 should agree well with experimental measurements as long as the system parameters correspond to the same ratio between the layer thickness and the superconducting coherence length, N_x/ξ.

3

BOGOLIUBOV-DE GENNES SCATTERING THEORY

In this chapter, we introduce an additional theoretical framework, where we treat the BdG Hamiltonian for HM/S and F/S systems by continuum scattering theory in order to compute the singlet and triplet even- and odd-frequency retarded anomalous Green's functions of these systems. The original description of this theoretical framework by McMillan is given in Ref. [37]. We will mainly use conventions similar to those in Refs. [38, 39], but Refs. [40–44] are also relevant. These describe a more generalized version of the theoretical framework described by McMillan. The theoretical framework presented in this chapter allows us to obtain analytical expressions for the singlet and triplet amplitudes of the 2D HM/S system with $\hat{n} = \hat{x}$, and thus complements the theoretical framework presented in Ch. 2. We will treat the 2D F/S system with $\boldsymbol{h} = h\hat{z}$ for comparison. We will also treat the case of a 2D HM/S system with $\hat{n} = \hat{z}$, which require numerical treatment. The three systems we consider in this chapter are shown in Fig. 3.1.

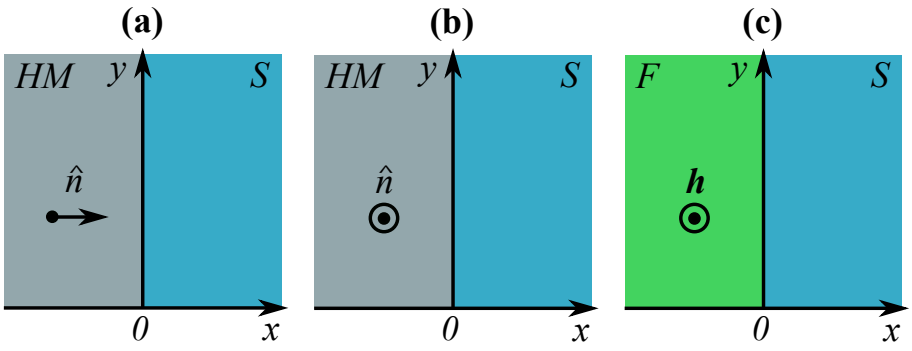

Figure 3.1: Panel (a) shows the 2D HM/S system with $\hat{n} = \hat{x}$, panel (b) shows the HM/S system with $\hat{n} = \hat{z}$, and panel (c) shows the F/S system with $\boldsymbol{h} = h\hat{z}$.

3.1 GREEN'S FUNCTIONS

3.1.1 *The retarded and advanced Green's functions*

In order to compute the singlet and triplet even- and odd-frequency amplitudes present in the superconducting heterostructure, we define the ordinary and anomalous Green's functions $g_{\alpha,\beta}(\boldsymbol{r}_1,\boldsymbol{r}_2;t_1,t_2)$ and $f_{\alpha,\beta}(\boldsymbol{r}_1,\boldsymbol{r}_2;t_1,t_2)$ of the system. These can be written in terms of single-particle field operators $\psi_\sigma(\boldsymbol{r},t)$ as [45, 46]

$$\begin{aligned} g_{\alpha,\beta}(\boldsymbol{r}_1,\boldsymbol{r}_2;t_1,t_2) &= -i\left\langle T\left\{\psi_\alpha(\boldsymbol{r}_1,t_1),\psi_\beta^\dagger(\boldsymbol{r}_2,t_2)\right\}\right\rangle \\ &= -i\theta(t_1-t_2)\left\langle\left\{\psi_\alpha(\boldsymbol{r}_1,t_1),\psi_\beta^\dagger(\boldsymbol{r}_2,t_2)\right\}\right\rangle \\ &\quad + i\theta(t_2-t_1)\left\langle\left\{\psi_\alpha(\boldsymbol{r}_1,t_1),\psi_\beta^\dagger(\boldsymbol{r}_2,t_2)\right\}\right\rangle, \\ f_{\alpha,\beta}(\boldsymbol{r}_1,\boldsymbol{r}_2;t_1,t_2) &= -i\left\langle T\left\{\psi_\alpha(\boldsymbol{r}_1,t_1),\psi_\beta(\boldsymbol{r}_2,t_2)\right\}\right\rangle \\ &= -i\theta(t_1-t_2)\left\langle\left\{\psi_\alpha(\boldsymbol{r}_1,t_1),\psi_\beta(\boldsymbol{r}_2,t_2)\right\}\right\rangle \\ &\quad + i\theta(t_2-t_1)\left\langle\left\{\psi_\alpha(\boldsymbol{r}_1,t_1),\psi_\beta(\boldsymbol{r}_2,t_2)\right\}\right\rangle, \end{aligned} \tag{3.1}$$

where T is the Wick time ordering operator and $\theta(t_1-t_2)$ is the Heaviside step function. Above, $\boldsymbol{r}_1$ and $\boldsymbol{r}_2$ are the positions of the two correlated particles in the 2D system, t_1 and t_2 are the time coordinates of the two correlated particles, and α and β represent spin degrees of freedom. As shown in Fig. 3.2(a), the ordinary Green's function $g_{\alpha,\beta}(\boldsymbol{r}_1,\boldsymbol{r}_2;t_1,t_2)$ can be interpreted as the overlap between creating an electron with spin β at $(\boldsymbol{r}_2,t_2)$ and finding an electron with spin α at position $\boldsymbol{r}_1$ at a later time t_1. As shown in Fig. 3.2(b), the anomalous Green's function $f_{\alpha,\beta}(\boldsymbol{r}_1,\boldsymbol{r}_2;t_1,t_2)$ can be interpreted as the overlap between annihilating an electron with spin β at $(\boldsymbol{r}_2,t_2)$ and finding an electron with spin α at position $\boldsymbol{r}_1$ at a later time t_1. The two electrons described by the anomalous Green's function are the two correlated electrons forming a Cooper pair [47].

The ordinary and anomalous Green's functions can be separated into a retarded and an advanced part. The retarded Green's function is nonzero for $t_1 > t_2$, so that we have a causality between the creation or annihilation of an electron with spin β at $(\boldsymbol{r}_2,t_2)$ and the possible detection of an electron with spin α at $(\boldsymbol{r}_1,t_1)$.

The advanced Green's function is not causal as it is instead nonzero for $t_2 > t_1$. The retarded and advanced Green's functions are given by [45]

$$\begin{aligned}
g^r_{\alpha,\beta}(\boldsymbol{r}_1,\boldsymbol{r}_2;t_1,t_2) &= -i\theta(t_1-t_2)\big\langle\big\{\psi_\alpha(\boldsymbol{r}_1,t_1),\psi^\dagger_\beta(\boldsymbol{r}_2,t_2)\big\}\big\rangle,\\
g^a_{\alpha,\beta}(\boldsymbol{r}_1,\boldsymbol{r}_2;t_1,t_2) &= i\theta(t_2-t_1)\big\langle\big\{\psi_\alpha(\boldsymbol{r}_1,t_1),\psi^\dagger_\beta(\boldsymbol{r}_2,t_2)\big\}\big\rangle,\\
f^r_{\alpha,\beta}(\boldsymbol{r}_1,\boldsymbol{r}_2;t_1,t_2) &= -i\theta(t_1-t_2)\big\langle\big\{\psi_\alpha(\boldsymbol{r}_1,t_1),\psi_\beta(\boldsymbol{r}_2,t_2)\big\}\big\rangle,\\
f^a_{\alpha,\beta}(\boldsymbol{r}_1,\boldsymbol{r}_2;t_1,t_2) &= i\theta(t_2-t_1)\big\langle\big\{\psi_\alpha(\boldsymbol{r}_1,t_1),\psi_\beta(\boldsymbol{r}_2,t_2)\big\}\big\rangle,
\end{aligned} \tag{3.2}$$

such that $g(\boldsymbol{r}_1,\boldsymbol{r}_2;t_1,t_2) = g^r(\boldsymbol{r}_1,\boldsymbol{r}_2;t_1,t_2) + g^a(\boldsymbol{r}_1,\boldsymbol{r}_2;t_1,t_2)$ and $f(\boldsymbol{r}_1,\boldsymbol{r}_2;t_1,t_2) = f^r(\boldsymbol{r}_1,\boldsymbol{r}_2;t_1,t_2) + f^a(\boldsymbol{r}_1,\boldsymbol{r}_2;t_1,t_2)$.

We now construct retarded (advanced) Green's functions in Nambu $\otimes$ spin space in a similar way as is done in Ref. [45]. The ordinary and anomalous retarded (advanced) Green's functions in spin space are given by

$$\begin{aligned}
g^{r(a)}(\boldsymbol{r}_1,\boldsymbol{r}_2;t_1,t_2) &= \begin{pmatrix} g^{r(a)}_{\uparrow,\uparrow}(\boldsymbol{r}_1,\boldsymbol{r}_2;t_1,t_2) & g^{r(a)}_{\uparrow,\downarrow}(\boldsymbol{r}_1,\boldsymbol{r}_2;t_1,t_2) \\ g^{r(a)}_{\downarrow,\uparrow}(\boldsymbol{r}_1,\boldsymbol{r}_2;t_1,t_2) & g^{r(a)}_{\downarrow,\downarrow}(\boldsymbol{r}_1,\boldsymbol{r}_2;t_1,t_2) \end{pmatrix}\\
f^{r(a)}(\boldsymbol{r}_1,\boldsymbol{r}_2;t_1,t_2) &= \begin{pmatrix} f^{r(a)}_{\uparrow,\uparrow}(\boldsymbol{r}_1,\boldsymbol{r}_2;t_1,t_2) & f^{r(a)}_{\uparrow,\downarrow}(\boldsymbol{r}_1,\boldsymbol{r}_2;t_1,t_2) \\ f^{r(a)}_{\downarrow,\uparrow}(\boldsymbol{r}_1,\boldsymbol{r}_2;t_1,t_2) & f^{r(a)}_{\downarrow,\downarrow}(\boldsymbol{r}_1,\boldsymbol{r}_2;t_1,t_2) \end{pmatrix}.
\end{aligned} \tag{3.3}$$

In Nambu $\otimes$ spin space, we can construct the retarded (advanced) Green's function as a 4×4-matrix given by

$$G^{r(a)}(\boldsymbol{r}_1,\boldsymbol{r}_2;t_1,t_2) = \begin{pmatrix} g^{r(a)}(\boldsymbol{r}_1,\boldsymbol{r}_2;t_1,t_2) & f^{r(a)}(\boldsymbol{r}_1,\boldsymbol{r}_2;t_1,t_2) \\ -[f^{r(a)}(\boldsymbol{r}_1,\boldsymbol{r}_2;t_1,t_2)]^* & -[g^{r(a)}(\boldsymbol{r}_1,\boldsymbol{r}_2;t_1,t_2)]^* \end{pmatrix}. \tag{3.4}$$

The elements of the two lower blocks of the above matrix are given by

$$\begin{aligned}
-[g^r_{\alpha,\beta}(\boldsymbol{r}_1,\boldsymbol{r}_2;t_1,t_2)]^* &= -i\theta(t_1-t_2)\big\langle\big\{\psi^\dagger_\alpha(\boldsymbol{r}_1,t_1),\psi_\beta(\boldsymbol{r}_2,t_2)\big\}\big\rangle,\\
-[g^a_{\alpha,\beta}(\boldsymbol{r}_1,\boldsymbol{r}_2;t_1,t_2)]^* &= i\theta(t_2-t_1)\big\langle\big\{\psi^\dagger_\alpha(\boldsymbol{r}_1,t_1),\psi_\beta(\boldsymbol{r}_2,t_2)\big\}\big\rangle,\\
-[f^r_{\alpha,\beta}(\boldsymbol{r}_1,\boldsymbol{r}_2;t_1,t_2)]^* &= -i\theta(t_1-t_2)\big\langle\big\{\psi^\dagger_\alpha(\boldsymbol{r}_1,t_1),\psi^\dagger_\beta(\boldsymbol{r}_2,t_2)\big\}\big\rangle,\\
-[f^a_{\alpha,\beta}(\boldsymbol{r}_1,\boldsymbol{r}_2;t_1,t_2)]^* &= i\theta(t_2-t_1)\big\langle\big\{\psi^\dagger_\alpha(\boldsymbol{r}_1,t_1),\psi^\dagger_\beta(\boldsymbol{r}_2,t_2)\big\}\big\rangle.
\end{aligned} \tag{3.5}$$

The ordinary Green's function formed by the first retarded Green's function and the first anomalous Green's function above can be interpreted as the overlap between annihilating an electron with spin β at $(\boldsymbol{r}_2,t_2)$ and finding a hole with spin α at position $\boldsymbol{r}_1$ at a later time t_1. The ordinary Green's function formed by the second retarded Green's function and the second anomalous Green's function above can be interpreted as the overlap between creating an electron with spin β at $(\boldsymbol{r}_2,t_2)$ and finding a hole with spin α at position $\boldsymbol{r}_1$ at a later time t_1 [47].

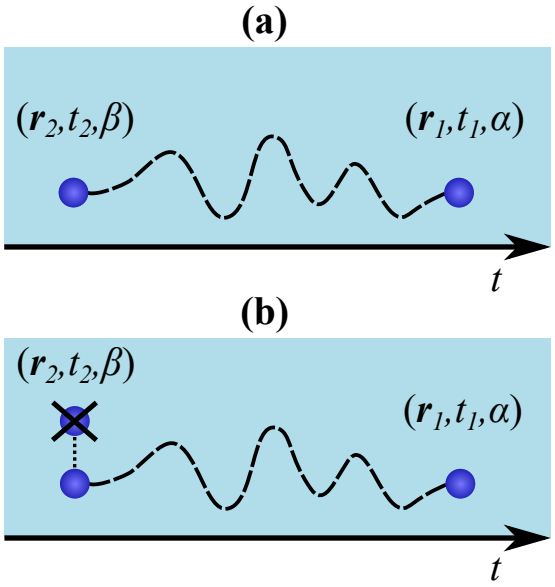

Figure 3.2: (a) The ordinary Green's function, $g_{\alpha,\beta}(\boldsymbol{r}_1,\boldsymbol{r}_2;t_1,t_2)$, can be interpreted as the overlap between creating an electron with spin β at $(\boldsymbol{r}_2,t_2)$, and finding that electron at $(\boldsymbol{r}_1,t_1)$ with a spin α. (b) The anomalous Green's function, $f_{\alpha,\beta}(\boldsymbol{r}_1,\boldsymbol{r}_2;t_1,t_2)$, can be interpreted as the overlap between removing an electron with spin β, which is one of the two electrons in a Cooper pair, from position $\boldsymbol{r}_2$ at time t_2, and finding the remaining electron of the Cooper pair at $(\boldsymbol{r}_1,t_1)$ with spin α. The t axes mark the time evolution if the processes are causal, $t_1 > t_2$.

In 4-vector notation, the retarded and advanced Green's functions in Eq. 3.4 can be written [45]

$$\begin{aligned}[G^r(\boldsymbol{r}_1,\boldsymbol{r}_2;t_1,t_2)]_{ij} &= -i\theta(t_1-t_2)\left\langle\{[\psi(\boldsymbol{r}_1,t_1)]_i,[\psi^\dagger(\boldsymbol{r}_2,t_2)]_j\}\right\rangle,\\ [G^a(\boldsymbol{r}_1,\boldsymbol{r}_2;t_1,t_2)]_{ij} &= i\theta(t_2-t_1)\left\langle\{[\psi(\boldsymbol{r}_1,t_1)]_i,[\psi^\dagger(\boldsymbol{r}_2,t_2)]_j\}\right\rangle,\end{aligned} \tag{3.6}$$

where $\psi(\boldsymbol{r},t) = [\psi_\uparrow(\boldsymbol{r},t)\ \ \psi_\downarrow(\boldsymbol{r},t)\ \ \psi^\dagger_\uparrow(\boldsymbol{r},t)\ \ \psi^\dagger_\downarrow(\boldsymbol{r},t)]^T$.

3.1.2 *The equation of motion of the field operator*

We will now derive an expression for the equation of motion of the field operator, that will be used in order to derive an equation of motion for the retarded Green's function. These equations of motion will be needed when we later on construct an expression for the retarded Green's function in terms of scattering wave functions. We will also derive boundary conditions for the retarded Green's function from the equation of motion. In this section and in Sec. 3.1.3, we will use a similar approach to that in Ref. [45].

Our starting point is the Heisenberg equation of motion for the single-particle field operators [45],

$$i\partial_t \psi_\sigma(\boldsymbol{r},t) = [\psi_\sigma(\boldsymbol{r},t), H]. \tag{3.7}$$

By taking the Hermitian conjugate of the above expression, we obtain the Heisenberg equation of motion for the adjoint field operator,

$$i\partial_t \psi^\dagger_\sigma(\boldsymbol{r},t) = [\psi^\dagger_\sigma(\boldsymbol{r},t), H], \tag{3.8}$$

where we have used that the Hamiltonian is hermitan, *i.e.* $H = H^\dagger$. We now want to find the equation of motion for the field operator $\psi(\boldsymbol{r},t)$ in 4-vector notation. The Hamiltonian can be written in terms of field operators as [27, 45]

$$\begin{aligned} H = &\sum_\sigma \int d\boldsymbol{r}\ \psi^\dagger_\sigma(\boldsymbol{r},t)(-\nabla^2/\eta - \mu)\psi_\sigma(\boldsymbol{r},t) \\ &- \int d\boldsymbol{r} \int d\boldsymbol{r}'\ U(\boldsymbol{r},\boldsymbol{r}')\psi^\dagger_\uparrow(\boldsymbol{r},t)\psi_\uparrow(\boldsymbol{r},t)\psi^\dagger_\downarrow(\boldsymbol{r}',t')\psi_\downarrow(\boldsymbol{r}',t') \\ &+ \sum_{\sigma,\sigma'} \int d\boldsymbol{r}\ \psi^\dagger_\sigma(\boldsymbol{r},t)(\hat{n}\times\boldsymbol{\sigma})_{\sigma,\sigma'}\cdot\lambda\hat{\boldsymbol{p}}\psi_{\sigma'}(\boldsymbol{r},t), \\ &+ \sum_{\sigma,\sigma'} \int d\boldsymbol{r}\ \psi^\dagger_\sigma(\boldsymbol{r},t)(\boldsymbol{h}\cdot\boldsymbol{\sigma})_{\sigma,\sigma'}\psi_{\sigma'}(\boldsymbol{r},t), \end{aligned} \tag{3.9}$$

where $\eta \equiv 2m/\hbar^2$. The terms are only nonzero in their respective regions. We have used the non-symmetrized Rashba spin-orbit coupling operator from Eq. 2.27, as we in our further treatment will find wave functions inside each material by considering the superconductor and the heavy-metal separately, and later introduce the effects of the interface through reflection and transmission amplitudes. When the heavy-metal is considered separately as a bulk material, the symmetrized Hamiltonian reduces to the expression for the non-symmetrized Hamiltonian. For the superconducting term in Eq. 3.9, we use a mean-field approximation [45]

$$\begin{aligned} \psi_\uparrow(\boldsymbol{r},t)\psi_\downarrow(\boldsymbol{r},t) &= \left\langle \psi_\uparrow(\boldsymbol{r},t)\psi_\downarrow(\boldsymbol{r},t)\right\rangle + \delta, \\ \psi^\dagger_\uparrow(\boldsymbol{r},t)\psi^\dagger_\downarrow(\boldsymbol{r},t) &= \left\langle \psi^\dagger_\uparrow(\boldsymbol{r},t)\psi^\dagger_\downarrow(\boldsymbol{r},t)\right\rangle - \delta^\dagger, \end{aligned} \tag{3.10}$$

similar to the mean-field approximation in Sec. 2.1. We also assume that the attractive potential is short ranged and constant within the superconducting material so that $U(\boldsymbol{r},\boldsymbol{r}') = U\delta(\boldsymbol{r}-\boldsymbol{r}')$. The superconducting gap is defined $\Delta \equiv U\left\langle\psi_\uparrow(\boldsymbol{r},t)\psi_\downarrow(\boldsymbol{r},t)\right\rangle$. By inserting Eq. 3.10 into the second term of Eq. 3.9 and neglecting terms of second order in δ and $\delta^\dagger$, we find that the second term in Eq. 3.9 can be written

$$H_U = H_{U,0} + \int d\boldsymbol{r}[\Delta^*(\boldsymbol{r},t)\psi_\downarrow(\boldsymbol{r},t)\psi_\uparrow(\boldsymbol{r},t) + \Delta(\boldsymbol{r},t)\psi^\dagger_\uparrow(\boldsymbol{r},t)\psi^\dagger_\downarrow(\boldsymbol{r},t)], \tag{3.11}$$

where $H_{U,0}$ is a constant term which will not be of importance in our further calculations.

We will now calculate the commutators $[\psi_\sigma(\boldsymbol{r},t),H]$ and $[\psi^\dagger_\sigma(\boldsymbol{r},t),H]$. In doing this, we will use the field operator commutator relation

$$\begin{aligned}[A,BC] &= ABC - BCA \\ &= ABC + BAC - BAC - BCA \\ &= (AB+BA)C - B(AC+CA) \\ &= \{A,B\}C - B\{A,C\},\end{aligned} \tag{3.12}$$

where A, B and C are field operators. We will also use the equal-time anticommutation relations [45]

$$\begin{aligned}\{\psi_\sigma(\boldsymbol{r},t),\psi^\dagger_{\sigma'}(\boldsymbol{r}',t)\} &= \delta_{\sigma,\sigma'}\delta(\boldsymbol{r}-\boldsymbol{r}'), \\ \{\psi_\sigma(\boldsymbol{r},t),\psi_{\sigma'}(\boldsymbol{r}',t)\} &= \{\psi^\dagger_\sigma(\boldsymbol{r},t),\psi^\dagger_{\sigma'}(\boldsymbol{r}',t)\} = 0.\end{aligned} \tag{3.13}$$

We now consider the four terms in Eq. 3.9 separately. We will denote the four terms H_ϵ, H_U, H_λ and H_F, respectively. First, consider the commutator of the field operator with the first term. We get

$$\begin{aligned}[\psi_\sigma(\boldsymbol{r},t),H_\epsilon] &= \sum_\sigma \int d\boldsymbol{r}'\,[\psi_\sigma(\boldsymbol{r},t),\psi^\dagger_{\sigma'}(\boldsymbol{r}',t)(-\nabla^2_{\boldsymbol{r}'}/\eta-\mu)\psi_{\sigma'}(\boldsymbol{r}',t)] \\ &= \sum_{\sigma'} \int d\boldsymbol{r}'\,[\{\psi_\sigma(\boldsymbol{r},t),\psi^\dagger_{\sigma'}(\boldsymbol{r}',t)\}(-\nabla^2_{\boldsymbol{r}'}/\eta-\mu)\psi_{\sigma'}(\boldsymbol{r}',t) \\ &\quad - \psi^\dagger_{\sigma'}(\boldsymbol{r}',t)(-\nabla^2_{\boldsymbol{r}'}/\eta-\mu)\{\psi_\sigma(\boldsymbol{r},t),\psi_{\sigma'}(\boldsymbol{r}',t)\}] \\ &= \sum_{\sigma'} \int d\boldsymbol{r}'\,\delta_{\sigma,\sigma'}\delta(\boldsymbol{r}-\boldsymbol{r}')(-\nabla^2_{\boldsymbol{r}'}/\eta-\mu)\psi_{\sigma'}(\boldsymbol{r}',t) \\ &= (-\nabla^2_{\boldsymbol{r}}/\eta-\mu)\psi_\sigma(\boldsymbol{r},t).\end{aligned} \tag{3.14}$$

The commutator of the adjoint field operator with the first term is

$$\begin{aligned}[\psi^\dagger_\sigma(\boldsymbol{r},t),H_\epsilon] &= \sum_{\sigma'} \int d\boldsymbol{r}'\,[\psi^\dagger_\sigma(\boldsymbol{r},t),\psi^\dagger_{\sigma'}(\boldsymbol{r}',t)(-\nabla^2_{\boldsymbol{r}'}/\eta-\mu)\psi_{\sigma'}(\boldsymbol{r}',t)] \\ &= \sum_{\sigma'} \int d\boldsymbol{r}'\,[\{\psi^\dagger_\sigma(\boldsymbol{r},t),\psi^\dagger_{\sigma'}(\boldsymbol{r}',t)\}(-\nabla^2_{\boldsymbol{r}'}/\eta-\mu)\psi_{\sigma'}(\boldsymbol{r}',t) \\ &\quad - \psi^\dagger_{\sigma'}(\boldsymbol{r}',t)(-\nabla^2_{\boldsymbol{r}'}/\eta-\mu)\{\psi^\dagger_\sigma(\boldsymbol{r},t),\psi_{\sigma'}(\boldsymbol{r}',t)\}] \\ &= -\sum_{\sigma'} \int d\boldsymbol{r}'\,\psi^\dagger_{\sigma'}(\boldsymbol{r}',t)(-\nabla^2_{\boldsymbol{r}'}/\eta-\mu)\delta_{\sigma,\sigma'}\delta(\boldsymbol{r}-\boldsymbol{r}').\end{aligned} \tag{3.15}$$

By partial integration

$$\begin{aligned}\int d\boldsymbol{r}'\,\psi^\dagger_{\sigma'}(\boldsymbol{r}',t)\nabla_{\boldsymbol{r}'}\delta(\boldsymbol{r}-\boldsymbol{r}') &= -\int d\boldsymbol{r}'\,\delta(\boldsymbol{r}-\boldsymbol{r}')\nabla_{\boldsymbol{r}'}\psi^\dagger_{\sigma'}(\boldsymbol{r}',t)\\ \int d\boldsymbol{r}'\,\psi^\dagger_{\sigma'}(\boldsymbol{r}',t)\nabla^2_{\boldsymbol{r}'}\delta(\boldsymbol{r}-\boldsymbol{r}') &= -\int d\boldsymbol{r}'\,[\nabla_{\boldsymbol{r}'}\psi^\dagger_{\sigma'}(\boldsymbol{r}',t)][\nabla_{\boldsymbol{r}'}\delta(\boldsymbol{r}-\boldsymbol{r}')]\\ &= \int d\boldsymbol{r}'\,\delta(\boldsymbol{r}-\boldsymbol{r}')\nabla^2_{\boldsymbol{r}'}\psi^\dagger_{\sigma'}(\boldsymbol{r}',t).\end{aligned} \tag{3.16}$$

We therefore get

$$\begin{aligned}[\psi^\dagger_\sigma(\boldsymbol{r},t),H_\epsilon] &= -\sum_{\sigma'}\int d\boldsymbol{r}'\,\delta_{\sigma,\sigma'}\delta(\boldsymbol{r}-\boldsymbol{r}')(-\nabla^2_{\boldsymbol{r}'}/\eta-\mu)\psi^\dagger_{\sigma'}(\boldsymbol{r}',t)\\ &= (\nabla^2_{\boldsymbol{r}}/\eta+\mu)\psi^\dagger_\sigma(\boldsymbol{r},t).\end{aligned} \tag{3.17}$$

The commutator of the field operator with the second term in Eq. 3.9 is

$$\begin{aligned}[\psi_\sigma(\boldsymbol{r},t),H_U] &= \int d\boldsymbol{r}'\,[\psi_\sigma(\boldsymbol{r},t),\Delta^*(\boldsymbol{r}',t)\psi_\downarrow(\boldsymbol{r}',t)\psi_\uparrow(\boldsymbol{r}',t)\\ &\quad+\Delta(\boldsymbol{r}',t)\psi^\dagger_\uparrow(\boldsymbol{r}',t)\psi^\dagger_\downarrow(\boldsymbol{r}',t)]\\ &= \int d\boldsymbol{r}'\,[\{\psi_\sigma(\boldsymbol{r},t),\psi_\downarrow(\boldsymbol{r}',t)\}\Delta^*(\boldsymbol{r}',t)\psi_\uparrow(\boldsymbol{r}',t)\\ &\quad-\Delta^*(\boldsymbol{r}',t)\psi_\downarrow(\boldsymbol{r}',t)\{\psi_\sigma(\boldsymbol{r},t),\psi_\uparrow(\boldsymbol{r}',t)\}\\ &\quad+\{\psi_\sigma(\boldsymbol{r},t),\psi^\dagger_\uparrow(\boldsymbol{r}',t)\}\Delta(\boldsymbol{r}',t)\psi^\dagger_\downarrow(\boldsymbol{r}',t)\\ &\quad-\Delta(\boldsymbol{r}',t)\psi^\dagger_\uparrow(\boldsymbol{r}',t)\{\psi_\sigma(\boldsymbol{r},t),\psi^\dagger_\downarrow(\boldsymbol{r}',t)\}]\\ &= \int d\boldsymbol{r}'\,[\delta_{\sigma,\uparrow}\delta(\boldsymbol{r}-\boldsymbol{r}')\Delta(\boldsymbol{r}',t)\psi^\dagger_\downarrow(\boldsymbol{r}',t)\\ &\quad-\delta_{\sigma,\downarrow}\delta(\boldsymbol{r}-\boldsymbol{r}')\Delta(\boldsymbol{r}',t)\psi^\dagger_\uparrow(\boldsymbol{r}',t)]\\ &= \delta_{\sigma,\uparrow}\Delta(\boldsymbol{r},t)\psi^\dagger_\downarrow(\boldsymbol{r},t)-\delta_{\sigma,\downarrow}\Delta(\boldsymbol{r},t)\psi^\dagger_\uparrow(\boldsymbol{r},t).\end{aligned} \tag{3.18}$$

The commutator of the adjoint field operator with the second term in Eq. 3.9 is

$$\begin{aligned}[\psi^\dagger_\sigma(\boldsymbol{r},t),H_U] &= \int d\boldsymbol{r}'\,[\psi^\dagger_\sigma(\boldsymbol{r},t),\Delta^*(\boldsymbol{r}',t)\psi_\downarrow(\boldsymbol{r}',t)\psi_\uparrow(\boldsymbol{r}',t)\\ &\quad+\Delta(\boldsymbol{r}',t)\psi^\dagger_\uparrow(\boldsymbol{r}',t)\psi^\dagger_\downarrow(\boldsymbol{r}',t)]\\ &= \int d\boldsymbol{r}'\,[\{\psi^\dagger_\sigma(\boldsymbol{r},t),\psi_\downarrow(\boldsymbol{r}',t)\}\Delta^*(\boldsymbol{r}',t)\psi_\uparrow(\boldsymbol{r}',t)\\ &\quad-\Delta^*(\boldsymbol{r}',t)\psi_\downarrow(\boldsymbol{r}',t)\{\psi^\dagger_\sigma(\boldsymbol{r},t),\psi_\uparrow(\boldsymbol{r}',t)\}\\ &\quad+\{\psi^\dagger_\sigma(\boldsymbol{r},t),\psi^\dagger_\uparrow(\boldsymbol{r}',t)\}\Delta(\boldsymbol{r}',t)\psi^\dagger_\downarrow(\boldsymbol{r}',t)\\ &\quad-\Delta(\boldsymbol{r}',t)\psi^\dagger_\uparrow(\boldsymbol{r}',t)\{\psi^\dagger_\sigma(\boldsymbol{r},t),\psi^\dagger_\downarrow(\boldsymbol{r}',t)\}]\end{aligned}$$

$$
\begin{aligned}
&= \int d\boldsymbol{r}' \, [\delta_{\sigma,\downarrow}\delta(\boldsymbol{r}-\boldsymbol{r}')\Delta^*(\boldsymbol{r}',t)\psi_\uparrow(\boldsymbol{r}',t) \\
&\quad - \delta_{\sigma,\uparrow}\delta(\boldsymbol{r}-\boldsymbol{r}')\Delta^*(\boldsymbol{r}',t)\psi_\downarrow(\boldsymbol{r}',t)] \\
&= \delta_{\sigma,\downarrow}\Delta^*(\boldsymbol{r},t)\psi_\uparrow(\boldsymbol{r},t) - \delta_{\sigma,\uparrow}\Delta^*(\boldsymbol{r},t)\psi_\downarrow(\boldsymbol{r},t).
\end{aligned}
\tag{3.19}
$$

The commutator of the field operator with the third term in Eq. 3.9 is

$$
\begin{aligned}
[\psi_\sigma(\boldsymbol{r},t), H_\lambda] &= \sum_{\sigma',\sigma''} \int d\boldsymbol{r}' \, [\psi_\sigma(\boldsymbol{r},t), \psi^\dagger_{\sigma'}(\boldsymbol{r}',t)(\hat{n}\times\boldsymbol{\sigma})_{\sigma',\sigma''} \cdot \lambda\hat{\boldsymbol{p}}_{\boldsymbol{r}'}\psi_{\sigma''}(\boldsymbol{r}',t)] \\
&= \sum_{\sigma',\sigma''} \int d\boldsymbol{r}' \, [\{\psi_\sigma(\boldsymbol{r},t), \psi^\dagger_{\sigma'}(\boldsymbol{r}',t)\}(\hat{n}\times\boldsymbol{\sigma})_{\sigma',\sigma''} \cdot \lambda\hat{\boldsymbol{p}}_{\boldsymbol{r}'}\psi_{\sigma''}(\boldsymbol{r}',t) \\
&\quad - \psi^\dagger_{\sigma'}(\boldsymbol{r}',t)(\hat{n}\times\boldsymbol{\sigma})_{\sigma',\sigma''} \cdot \lambda\hat{\boldsymbol{p}}_{\boldsymbol{r}'}\{\psi_\sigma(\boldsymbol{r},t), \psi_{\sigma''}(\boldsymbol{r}',t)\}] \\
&= \sum_{\sigma',\sigma''} \int d\boldsymbol{r}' \, \delta_{\sigma,\sigma'}\delta(\boldsymbol{r}-\boldsymbol{r}')(\hat{n}\times\boldsymbol{\sigma})_{\sigma',\sigma''} \cdot \lambda\hat{\boldsymbol{p}}_{\boldsymbol{r}'}\psi_{\sigma''}(\boldsymbol{r}',t) \\
&= \sum_{\sigma''} (\hat{n}\times\boldsymbol{\sigma})_{\sigma,\sigma''} \cdot \lambda\hat{\boldsymbol{p}}_{\boldsymbol{r}}\psi_{\sigma''}(\boldsymbol{r},t).
\end{aligned}
\tag{3.20}
$$

Because $\hat{\boldsymbol{p}} = -i\hbar\nabla$, we need to use Eq. 3.16 in order to find the commutator of the adjoint field operator with the third term in Eq. 3.9. We get

$$
\begin{aligned}
[\psi^\dagger_\sigma(\boldsymbol{r},t), H_\lambda] &= \sum_{\sigma',\sigma''} \int d\boldsymbol{r}' \, [\psi^\dagger_\sigma(\boldsymbol{r},t), \psi^\dagger_{\sigma'}(\boldsymbol{r}',t)(\hat{n}\times\boldsymbol{\sigma})_{\sigma',\sigma''} \cdot \lambda\hat{\boldsymbol{p}}_{\boldsymbol{r}'}\psi_{\sigma''}(\boldsymbol{r}',t)] \\
&= \sum_{\sigma',\sigma''} \int d\boldsymbol{r}' \, [\{\psi^\dagger_\sigma(\boldsymbol{r},t), \psi^\dagger_{\sigma'}(\boldsymbol{r}',t)\}(\hat{n}\times\boldsymbol{\sigma})_{\sigma',\sigma''} \cdot \lambda\hat{\boldsymbol{p}}_{\boldsymbol{r}'}\psi_{\sigma''}(\boldsymbol{r}',t) \\
&\quad - \psi^\dagger_{\sigma'}(\boldsymbol{r}',t)(\hat{n}\times\boldsymbol{\sigma})_{\sigma',\sigma''} \cdot \lambda\hat{\boldsymbol{p}}_{\boldsymbol{r}'}\{\psi^\dagger_\sigma(\boldsymbol{r},t), \psi_{\sigma''}(\boldsymbol{r}',t)\}] \\
&= -\sum_{\sigma',\sigma''} \int d\boldsymbol{r}' \, \psi^\dagger_{\sigma'}(\boldsymbol{r}',t)(\hat{n}\times\boldsymbol{\sigma})_{\sigma',\sigma''} \cdot \lambda\hat{\boldsymbol{p}}_{\boldsymbol{r}'}\delta_{\sigma,\sigma''}\delta(\boldsymbol{r}-\boldsymbol{r}') \\
&= \sum_{\sigma',\sigma''} \int d\boldsymbol{r}' \, \delta_{\sigma,\sigma''}\delta(\boldsymbol{r}-\boldsymbol{r}')(\hat{n}\times\boldsymbol{\sigma})_{\sigma',\sigma''} \cdot \lambda\hat{\boldsymbol{p}}_{\boldsymbol{r}'}\psi^\dagger_{\sigma'}(\boldsymbol{r}',t) \\
&= \sum_{\sigma'} (\hat{n}\times\boldsymbol{\sigma})_{\sigma',\sigma} \cdot \lambda\hat{\boldsymbol{p}}_{\boldsymbol{r}}\psi^\dagger_{\sigma'}(\boldsymbol{r},t).
\end{aligned}
\tag{3.21}
$$

The commutator of the field operator with the fourth term in Eq. 3.9 is

$$
[\psi_\sigma(\boldsymbol{r},t), H_F] = \sum_{\sigma',\sigma''} \int d\boldsymbol{r}' \, [\psi_\sigma(\boldsymbol{r},t), \psi^\dagger_{\sigma'}(\boldsymbol{r}',t)(\boldsymbol{h}\cdot\boldsymbol{\sigma})_{\sigma',\sigma''}\psi_{\sigma''}(\boldsymbol{r}',t)]
$$

$$
\begin{aligned}
&= \sum_{\sigma',\sigma''} \int d\boldsymbol{r}' \, [\{\psi_\sigma(\boldsymbol{r},t), \psi^\dagger_{\sigma'}(\boldsymbol{r}',t)\}(\boldsymbol{h}\cdot\boldsymbol{\sigma})_{\sigma',\sigma''}\psi_{\sigma''}(\boldsymbol{r}',t) \\
&\quad - \psi^\dagger_{\sigma'}(\boldsymbol{r}',t)(\boldsymbol{h}\cdot\boldsymbol{\sigma})_{\sigma',\sigma''}\{\psi_\sigma(\boldsymbol{r},t), \psi_{\sigma''}(\boldsymbol{r}',t)\}] \\
&= \sum_{\sigma',\sigma''} \int d\boldsymbol{r}' \, \delta_{\sigma,\sigma'}\delta(\boldsymbol{r}-\boldsymbol{r}')(\boldsymbol{h}\cdot\boldsymbol{\sigma})_{\sigma',\sigma''}\psi_{\sigma''}(\boldsymbol{r}',t) \\
&= \sum_{\sigma''} (\boldsymbol{h}\cdot\boldsymbol{\sigma})_{\sigma,\sigma''}\psi_{\sigma''}(\boldsymbol{r},t).
\end{aligned}
\tag{3.22}
$$

Finally, the commutator of the adjoint field operator with the fourth term in Eq. 3.9 is

$$
\begin{aligned}
[\psi^\dagger_\sigma(\boldsymbol{r},t), H_F] &= \sum_{\sigma',\sigma''} \int d\boldsymbol{r}' \, [\psi^\dagger_\sigma(\boldsymbol{r},t), \psi^\dagger_{\sigma'}(\boldsymbol{r}',t)(\boldsymbol{h}\cdot\boldsymbol{\sigma})_{\sigma',\sigma''}\psi_{\sigma''}(\boldsymbol{r}',t)] \\
&= \sum_{\sigma',\sigma''} \int d\boldsymbol{r}' \, [\{\psi^\dagger_\sigma(\boldsymbol{r},t), \psi^\dagger_{\sigma'}(\boldsymbol{r}',t)\}(\boldsymbol{h}\cdot\boldsymbol{\sigma})_{\sigma',\sigma''}\psi_{\sigma''}(\boldsymbol{r}',t) \\
&\quad - \psi^\dagger_{\sigma'}(\boldsymbol{r}',t)(\boldsymbol{h}\cdot\boldsymbol{\sigma})_{\sigma',\sigma''}\{\psi^\dagger_\sigma(\boldsymbol{r},t), \psi_{\sigma''}(\boldsymbol{r}',t)\}] \\
&= -\sum_{\sigma',\sigma''} \int d\boldsymbol{r}' \, \delta_{\sigma,\sigma''}\delta(\boldsymbol{r}-\boldsymbol{r}')(\boldsymbol{h}\cdot\boldsymbol{\sigma})_{\sigma',\sigma''}\psi^\dagger_{\sigma'}(\boldsymbol{r}',t) \\
&= -\sum_{\sigma'} (\boldsymbol{h}\cdot\boldsymbol{\sigma})_{\sigma',\sigma}\psi^\dagger_{\sigma'}(\boldsymbol{r},t).
\end{aligned}
\tag{3.23}
$$

Inserting Eqs. 3.14 and 3.17 - 3.23 into Eqs. 3.7 and 3.8 and writing the resulting equation in 4-vector notation, we get

$$
\begin{aligned}
i\partial_t\psi(\boldsymbol{r},t) &= H(\boldsymbol{r})\psi(\boldsymbol{r},t), \\
-i\partial_t\psi^\dagger(\boldsymbol{r},t) &= \psi^\dagger(\boldsymbol{r},t)H^\dagger(\boldsymbol{r}),
\end{aligned}
\tag{3.24}
$$

where

$$
\begin{aligned}
H(\boldsymbol{r}) =& (-\nabla^2/\eta - \mu)\hat{\tau}_3\hat{\sigma}_0 + \Delta i\hat{\tau}^+\hat{\sigma}_y - \Delta^* i\hat{\tau}^-\hat{\sigma}_y \\
&+ i\lambda(n_x\partial_y - n_y\partial_x)\hat{\tau}_0\hat{\sigma}_z + i\lambda n_z\partial_x\hat{\tau}_3\hat{\sigma}_y - i\lambda n_z\partial_y\hat{\tau}_0\hat{\sigma}_x \\
&+ h_x\hat{\tau}_3\hat{\sigma}_x + h_y\hat{\tau}_0\hat{\sigma}_y + h_z\hat{\tau}_3\hat{\sigma}_z.
\end{aligned}
\tag{3.25}
$$

n_x, n_y and n_z are the components of $\hat{n}$. h_x, h_y and h_z are the components of $\boldsymbol{h}$. Eq. 3.24 is the equation of motion for the 4-vector field operator.

Note that in our 4-vector notation, † means transposing the matrix or vector, and complex conjugating all of its elements. We do not take the hermitian conjugate of operators contained within the matrix, but rather the complex conjugate. Therefore, the operators contained within the elements of $H(\boldsymbol{r})$ are not invariant under

the † operator, and $H^\dagger(-i\partial_x, -i\partial_y) = H(i\partial_x, i\partial_y)$. This means that we must be particularly careful when taking the hermitian conjugate of a Hamiltonian matrix that has been subjected to a spatial Fourier transform, or where we have already applied the Hamiltonian to a wave vector, letting $-i\partial_x \to k_x$ and $-i\partial_y \to k_y$. In this case, $H^\dagger(k_x, k_y) = H(-k_x, -k_y)$.

3.1.3 *The equation of motion of the retarded Green's function*

We next want to find the equation of motion of the retarded Green's function $G^r(\boldsymbol{r}_1, \boldsymbol{r}_2; t_1, t_2)$. By writing the retarded Green's function in 4-vector notation using Eq. 3.6, we find that

$$\begin{aligned}[i\partial_{t_1} G^r(\boldsymbol{r}_1, \boldsymbol{r}_2; t_1, t_2)]_{i,j} =& \partial_{t_1}\theta(t_1 - t_2)\left\langle\{[\psi(\boldsymbol{r}_1, t_1)]_i, [\psi^\dagger(\boldsymbol{r}_2, t_2)]_j\}\right\rangle \\ =& \delta(t_1 - t_2)\left\langle\{[\psi(\boldsymbol{r}_1, t_1)]_i, [\psi^\dagger(\boldsymbol{r}_2, t_2)]_j\}\right\rangle \\ &+ \theta(t_1 - t_2)\left\langle\{[\partial_{t_1}\psi(\boldsymbol{r}_1, t_1)]_i, [\psi^\dagger(\boldsymbol{r}_2, t_2)]_j\}\right\rangle\end{aligned} \tag{3.26}$$

and that

$$\begin{aligned}[i\partial_{t_2} G^r(\boldsymbol{r}_1, \boldsymbol{r}_2; t_1, t_2)]_{i,j} =& \partial_{t_2}\theta(t_1 - t_2)\left\langle\{[\psi(\boldsymbol{r}_1, t_1)]_i, [\psi^\dagger(\boldsymbol{r}_2, t_2)]_j\}\right\rangle \\ =& -\delta(t_1 - t_2)\left\langle\{[\psi(\boldsymbol{r}_1, t_1)]_i, [\psi^\dagger(\boldsymbol{r}_2, t_2)]_j\}\right\rangle \\ &+ \theta(t_1 - t_2)\left\langle\{[\psi(\boldsymbol{r}_1, t_1)]_i, [\partial_{t_2}\psi^\dagger(\boldsymbol{r}_2, t_2)]_j\}\right\rangle.\end{aligned} \tag{3.27}$$

By applying the equal-time field operator anticommutation relations in Eq. 3.13, we find that the first term in Eqs. 3.26 and 3.27 is given by

$$\pm\delta(t_1 - t_2)\left\langle\{[\psi(\boldsymbol{r}_1, t_1)]_i, [\psi^\dagger(\boldsymbol{r}_2, t_2)]_j\}\right\rangle = \pm\delta(t_1 - t_2)\delta(\boldsymbol{r}_1 - \boldsymbol{r}_2)(\hat{\tau}_0\hat{\sigma}_0)_{i,j}, \tag{3.28}$$

respectively. By applying the equation of motion of the 4-vector field operator given in Eq. 3.24 to the second term in Eqs. 3.26 and 3.27, we get

$$\begin{aligned}&\theta(t_1 - t_2)\left\langle\{[\partial_{t_1}\psi(\boldsymbol{r}_1, t_1)]_i, [\psi^\dagger(\boldsymbol{r}_2, t_2)]_j\}\right\rangle \\ &= -i\theta(t_1 - t_2)\left\langle\{[H(\boldsymbol{r}_1)\psi(\boldsymbol{r}_1, t_1)]_i, [\psi^\dagger(\boldsymbol{r}_2, t_2)]_j\}\right\rangle \\ &= -i\theta(t_1 - t_2)\sum_k \left\langle\{[H(\boldsymbol{r}_1)]_{i,k}[\psi(\boldsymbol{r}_1, t_1)]_k, [\psi^\dagger(\boldsymbol{r}_2, t_2)]_j\}\right\rangle \\ &= \sum_k [H(\boldsymbol{r}_1)]_{i,k}[-i\theta(t_1 - t_2)\left\langle\{[\psi(\boldsymbol{r}_1, t_1)]_k, [\psi^\dagger(\boldsymbol{r}_2, t_2)]_j\}\right\rangle] \\ &= \sum_k [H(\boldsymbol{r}_1)]_{i,k}[G^r(\boldsymbol{r}_1, \boldsymbol{r}_2; t_1, t_2)]_{k,j} \\ &= [H(\boldsymbol{r}_1)G^r(\boldsymbol{r}_1, \boldsymbol{r}_2; t_1, t_2)]_{i,j}\end{aligned} \tag{3.29}$$

and

$$\begin{aligned}
&\theta(t_1-t_2)\left\langle\{[\psi(\boldsymbol{r}_1,t_1)]_i,[\partial_{t_2}\psi^\dagger(\boldsymbol{r}_2,t_2)]_j\}\right\rangle \\
&= i\theta(t_1-t_2)\left\langle\{[\psi(\boldsymbol{r}_1,t_1)]_i,[\psi^\dagger(\boldsymbol{r}_2,t_2)H^\dagger(\boldsymbol{r}_2)]_j\}\right\rangle \\
&= i\theta(t_1-t_2)\sum_k\left\langle\{[\psi(\boldsymbol{r}_1,t_1)]_i,[\psi^\dagger(\boldsymbol{r}_2,t_2)]_k[H^\dagger(\boldsymbol{r}_2)]_{k,j}\}\right\rangle \\
&= -\sum_k[-i\theta(t_1-t_2)\left\langle\{[\psi(\boldsymbol{r}_1,t_1)]_i,[\psi^\dagger(\boldsymbol{r}_2,t_2)]_k\}\right\rangle][H^\dagger(\boldsymbol{r}_2)]_{k,j} \\
&= -\sum_k[G^r(\boldsymbol{r}_1,\boldsymbol{r}_2;t_1,t_2)]_{i,k}[H^\dagger(\boldsymbol{r}_2)]_{k,j} \\
&= -[G^r(\boldsymbol{r}_1,\boldsymbol{r}_2;t_1,t_2)H^\dagger(\boldsymbol{r}_2)]_{i,j}.
\end{aligned} \tag{3.30}$$

The resulting equations of motion of the retarded Green's function are

$$\begin{aligned}
[i\partial_{t_1}-H(\boldsymbol{r}_1)]G^r(\boldsymbol{r}_1,\boldsymbol{r}_2;t_1,t_2) &= \delta(t_1-t_2)\delta(\boldsymbol{r}_1-\boldsymbol{r}_2)\hat{\tau}_0\hat{\sigma}_0, \\
G^r(\boldsymbol{r}_1,\boldsymbol{r}_2;t_1,t_2)[-i\partial_{t_2}-H^\dagger(\boldsymbol{r}_2)] &= \delta(t_1-t_2)\delta(\boldsymbol{r}_1-\boldsymbol{r}_2)\hat{\tau}_0\hat{\sigma}_0,
\end{aligned} \tag{3.31}$$

where $[i\partial_{t_1}-H(\boldsymbol{r}_1)]$ acts to the right and $[-i\partial_{t_2}-H^\dagger(\boldsymbol{r}_2)]$ acts to the left.

We now introduce the average time coordinate $T\equiv(t_1+t_2)/2$ and the relative time coordinate $t\equiv t_1-t_2$. The Fourier transform in the relative time coordinate is [45]

$$G^r(\boldsymbol{r}_1,\boldsymbol{r}_2;T,\omega)=\int_{-\infty}^{\infty}dt\,e^{i\omega t}G^r(\boldsymbol{r}_1,\boldsymbol{r}_2;T,t). \tag{3.32}$$

The derivatives ∂_{t_1} and ∂_{t_2} in the equations of motion for the retarded Green's function in Eq. 3.31 can, according to the chain rule, be written

$$\begin{aligned}
\frac{\partial}{\partial t_1} &= \frac{\partial t}{\partial t_1}\frac{\partial}{\partial t}+\frac{\partial T}{\partial t_1}\frac{\partial}{\partial T}=\frac{\partial}{\partial t}+\frac{1}{2}\frac{\partial}{\partial T}, \\
\frac{\partial}{\partial t_2} &= \frac{\partial t}{\partial t_2}\frac{\partial}{\partial t}+\frac{\partial T}{\partial t_2}\frac{\partial}{\partial T}=-\frac{\partial}{\partial t}+\frac{1}{2}\frac{\partial}{\partial T}.
\end{aligned} \tag{3.33}$$

In this thesis, we will only consider systems where the retarded Green's function is independent of T. Therefore, $\partial_{t_1}G^r(\boldsymbol{r}_1,\boldsymbol{r}_2;T,t)=\partial_tG^r(\boldsymbol{r}_1,\boldsymbol{r}_2;T,t)$ and $\partial_{t_2}G^r(\boldsymbol{r}_1,\boldsymbol{r}_2;T,t)=-\partial_tG^r(\boldsymbol{r}_1,\boldsymbol{r}_2;T,t)$. For brevity of notation, we will omit T in the following. Using partial integration, we find that

$$\begin{aligned}
\int_{-\infty}^{\infty}dt\,e^{i\omega t}[\partial_tG^r(\boldsymbol{r}_1,\boldsymbol{r}_2;t)] &= -i\omega\int_{-\infty}^{\infty}dt\,e^{i\omega t}G^r(\boldsymbol{r}_1,\boldsymbol{r}_2;t) \\
&= -i\omega G^r(\boldsymbol{r}_1,\boldsymbol{r}_2;\omega).
\end{aligned} \tag{3.34}$$

If we apply the Fourier transform given in Eq. 3.32 to the equation of motion given in Eq. 3.31 and also use Eq. 3.34, the equations of motion of the retarded Green's function can be written

$$\begin{aligned}[\omega - H(\boldsymbol{r}_1)]G^r(\boldsymbol{r}_1, \boldsymbol{r}_2; \omega) &= \delta(\boldsymbol{r}_1 - \boldsymbol{r}_2)\hat{\tau}_0\hat{\sigma}_0, \\ G^r(\boldsymbol{r}_1, \boldsymbol{r}_2; \omega)[\omega - H^\dagger(\boldsymbol{r}_2)] &= \delta(\boldsymbol{r}_1 - \boldsymbol{r}_2)\hat{\tau}_0\hat{\sigma}_0.\end{aligned} \tag{3.35}$$

The former of these two equations of motion describes propagation from $\boldsymbol{r}_2$ affecting the field at $\boldsymbol{r}_1$. In order to find a physical interpretation of the latter equation of motion, we write it on a similar form as the former,

$$[\omega - H(\boldsymbol{r}_2)][G^r(\boldsymbol{r}_1, \boldsymbol{r}_2; \omega)]^\dagger = \delta(\boldsymbol{r}_1 - \boldsymbol{r}_2)\hat{\tau}_0\hat{\sigma}_0. \tag{3.36}$$

From Eq. 3.2, we can easily see that $g^a_{\alpha,\beta}(\boldsymbol{r}_1, \boldsymbol{r}_2; t_1, t_2) = [g^r_{\beta,\alpha}(\boldsymbol{r}_2, \boldsymbol{r}_1; t_2, t_1)]^*$, and that $f^a_{\alpha,\beta}(\boldsymbol{r}_1, \boldsymbol{r}_2; t_1, t_2) = -f^r_{\beta,\alpha}(\boldsymbol{r}_2, \boldsymbol{r}_1; t_2, t_1)$. By rewriting the elements of the Green's functions to the relative time coordinate and applying the Fourier transform in relative time given by Eq. 3.32, we find that $g^a_{\alpha,\beta}(\boldsymbol{r}_1, \boldsymbol{r}_2; \omega) = [g^r_{\beta,\alpha}(\boldsymbol{r}_2, \boldsymbol{r}_1; \omega)]^*$, and that $f^a_{\alpha,\beta}(\boldsymbol{r}_1, \boldsymbol{r}_2; \omega) = -f^r_{\beta,\alpha}(\boldsymbol{r}_2, \boldsymbol{r}_1; \omega)$. It follows that $G^a(\boldsymbol{r}_1, \boldsymbol{r}_2; \omega) = [G^r(\boldsymbol{r}_2, \boldsymbol{r}_1; \omega)]^\dagger$, and that Eq. 3.36 can be written

$$[\omega - H(\boldsymbol{r}_2)]G^a(\boldsymbol{r}_2, \boldsymbol{r}_1; \omega) = \delta(\boldsymbol{r}_1 - \boldsymbol{r}_2)\hat{\tau}_0\hat{\sigma}_0. \tag{3.37}$$

This equation of motion describes a propagation from $\boldsymbol{r}_1$ affecting the field at $\boldsymbol{r}_2$.

We now introduce the center of mass coordinate $Y \equiv (y_1 + y_2)/2$ and the relative coordinate $y \equiv y_1 - y_2$ along the y axis. The Fourier transform along the relative y coordinate is [45]

$$G^r(x_1, x_2, Y, p_y; \omega) = \int_{-\infty}^{\infty} dy\, e^{-ip_y y} G^r(x_1, x_2, Y, y; \omega). \tag{3.38}$$

$H(\boldsymbol{r}_1)$ is dependent upon ∂_{y_1} and $\partial^2_{y_1}$, and $H(\boldsymbol{r}_2)$ is dependent upon ∂_{y_2} and $\partial^2_{y_2}$. The partial derivatives ∂_{y_1} and ∂_{y_2} can be written

$$\begin{aligned}\frac{\partial}{\partial y_1} &= \frac{\partial y}{\partial y_1}\frac{\partial}{\partial y} + \frac{\partial Y}{\partial y_1}\frac{\partial}{\partial Y} = \frac{\partial}{\partial y} + \frac{1}{2}\frac{\partial}{\partial Y}, \\ \frac{\partial}{\partial y_2} &= \frac{\partial y}{\partial y_2}\frac{\partial}{\partial y} + \frac{\partial Y}{\partial y_2}\frac{\partial}{\partial Y} = -\frac{\partial}{\partial y} + \frac{1}{2}\frac{\partial}{\partial Y}.\end{aligned} \tag{3.39}$$

So far, we have not done any assumptions with regard to the position of the interface between the superconductor and the non-superconducting material. We now choose to consider a bilayer with the interface normal along the x axis and assume translational invariance in the y direction. The retarded Green's function must

then be independent of Y, so that $\partial_{y_1} G^r(x_1, x_2, y, Y; \omega) = \partial_y G^r(x_1, x_2, y, Y; \omega)$ and $\partial_{y_2} G^r(x_1, x_2, y, Y; \omega) = -\partial_y G^r(x_1, x_2, y, Y; \omega)$. For brevity of notation, we will omit Y in the following. By partial integration, we find that

$$\begin{aligned}
&\int_{-\infty}^{\infty} dy\, e^{-ip_y y}[\partial_y G^r(x_1, x_2, y; \omega)] \\
&= ip_y \int_{-\infty}^{\infty} dy\, e^{-ip_y y} G^r(x_1, x_2, y; \omega) \\
&= ip_y G^r(x_1, x_2, p_y; \omega)
\end{aligned} \tag{3.40}$$

and that

$$\begin{aligned}
&\int_{-\infty}^{\infty} dy\, e^{-ip_y y}[\partial_y^2 G^r(x_1, x_2, y; \omega)] \\
&= ip_y \int_{-\infty}^{\infty} dy\, e^{-ip_y y}[\partial_y G^r(x_1, x_2, y; \omega)] \\
&= -p_y^2 \int_{-\infty}^{\infty} dy\, e^{-ip_y y} G^r(x_1, x_2, y; \omega) \\
&= -p_y^2 G^r(x_1, x_2, p_y; \omega).
\end{aligned} \tag{3.41}$$

By applying the Fourier transform in the relative y coordinate given in Eq. 3.38 to the equation of motion given in Eq. 3.35 and also using Eqs. 3.40 and 3.41, we can write the equations of motion of the retarded Green's function as

$$\begin{aligned}
[\omega - H_{p_y}(x_1)] G^r(x_1, x_2, p_y; \omega) &= \delta(x_1 - x_2)\hat{\tau}_0\hat{\sigma}_0, \\
G^r(x_1, x_2, p_y; \omega)[\omega - H_{-p_y}(x_2)] &= \delta(x_1 - x_2)\hat{\tau}_0\hat{\sigma}_0,
\end{aligned} \tag{3.42}$$

where

$$\begin{aligned}
H_{p_y}(x_1) = (-\partial_{x_1}^2/\eta + p_y^2/\eta - \mu)\hat{\tau}_3\hat{\sigma}_0 + \Delta i\hat{\tau}^+\hat{\sigma}_y - \Delta^* i\hat{\tau}^-\hat{\sigma}_y \\
+ i\lambda(in_x p_y - n_y\partial_x)\hat{\tau}_0\hat{\sigma}_z + i\lambda n_z\partial_x\hat{\tau}_3\hat{\sigma}_y + \lambda n_z p_y\hat{\tau}_0\hat{\sigma}_x \\
+ h_x\hat{\tau}_3\hat{\sigma}_x + h_y\hat{\tau}_0\hat{\sigma}_y + h_z\hat{\tau}_3\hat{\sigma}_z.
\end{aligned} \tag{3.43}$$

3.1.4 *The scattering retarded Green's function*

We now want to write the retarded Green's function in terms of scattering wave functions. We first follow a similar approach to that in Refs. [29, 46] in order to justify that the retarded Green's function can be written in terms of wave functions. To avoid confusing notation, we will use the capital Ψ for wave functions, while the lowercase ψ is reserved for field operators. The wave function $\Psi(\boldsymbol{r}, t)$ is a

column 4-vector in Nambu ⊗ spin space, where the first element correspond to spin-up electrons, the second element correspond to spin-down electrons, the third element correspond to spin-up holes, and the fourth element correspond to spin-down holes. Since the Green's function describes a propagation from one state at $(\boldsymbol{r}_2, t_2)$ to another state at $(\boldsymbol{r}_1, t_1)$, $\Psi(\boldsymbol{r}_1, t_1)$ can be expressed [29]

$$\Psi(\boldsymbol{r}_1, t_1) = \int d\boldsymbol{r}_2 \, G(\boldsymbol{r}_1, \boldsymbol{r}_2; t_1, t_2)\Psi(\boldsymbol{r}_2, t_2), \tag{3.44}$$

where we integrate over all of space. By using the bra-ket notation and the completeness relation $\int d\boldsymbol{r}_2 \, |\boldsymbol{r}_2\rangle\langle \boldsymbol{r}_2| = 1$, this wave function can also be written

$$\begin{aligned}
\Psi(\boldsymbol{r}_1, t_1) &= \left\langle \boldsymbol{r}_1 \middle| \Psi(t_1) \right\rangle \\
&= \left\langle \boldsymbol{r}_1 \middle| e^{-iH(\boldsymbol{r}_1)(t_1 - t_2)} \Psi(t_2) \right\rangle \\
&= \int d\boldsymbol{r}_2 \left\langle \boldsymbol{r}_1 \middle| e^{-iH(\boldsymbol{r}_1)(t_1 - t_2)} \middle| \boldsymbol{r}_2 \right\rangle \left\langle \boldsymbol{r}_2 \middle| \Psi(t_2) \right\rangle \\
&= \int d\boldsymbol{r}_2 \left\langle \boldsymbol{r}_1 \middle| e^{-iH(\boldsymbol{r}_1)(t_1 - t_2)} \middle| \boldsymbol{r}_2 \right\rangle \Psi(\boldsymbol{r}_2, t_2),
\end{aligned} \tag{3.45}$$

where $e^{-iH(\boldsymbol{r}_1)(t_1 - t_2)}$ is the time evolution operator. By comparing the above equation to Eq. 3.44, we find that the Green's function can be written

$$\begin{aligned}
G(\boldsymbol{r}_1, \boldsymbol{r}_2; t_1, t_2) &= \left\langle \boldsymbol{r}_1 \middle| e^{-iH(\boldsymbol{r}_1)(t_1 - t_2)} \middle| \boldsymbol{r}_2 \right\rangle \\
&= \sum_l \left\langle \boldsymbol{r}_1 \middle| l \right\rangle \left\langle l \middle| e^{-iH(\boldsymbol{r}_1)(t_1 - t_2)} \middle| \boldsymbol{r}_2 \right\rangle \\
&= \sum_l \left\langle \boldsymbol{r}_1 \middle| l \right\rangle \left\langle l \middle| \boldsymbol{r}_2 \right\rangle e^{-iE_l(t_1 - t_2)} \\
&= \sum_l \Psi_l(\boldsymbol{r}_1, t_1)\Psi_l^\dagger(\boldsymbol{r}_2, t_2),
\end{aligned} \tag{3.46}$$

where $\Psi_l(\boldsymbol{r}_1, t_1) = \Psi_l(\boldsymbol{r}_1)e^{-iE_l t_1}$ and $\Psi_l(\boldsymbol{r}_2, t_2) = \Psi_l(\boldsymbol{r}_2)e^{-iE_l t_2}$. Above, we have used the completeness relation $\sum_l |l\rangle\langle l| = 1$ to introduce the sum over energy eigenstates. By defining $\tilde{\Psi}_l^T(\boldsymbol{r}_2, t_2) \equiv \Psi_l^\dagger(\boldsymbol{r}_2, t_2)$, this can be rewritten as

$$G(\boldsymbol{r}_1, \boldsymbol{r}_2; t_1, t_2) = \sum_l \Psi_l(\boldsymbol{r}_1, t_1)\tilde{\Psi}_l^T(\boldsymbol{r}_2, t_2), \tag{3.47}$$

where $\tilde{\Psi}_l(\boldsymbol{r}_2, t_2) = \tilde{\Psi}_l(\boldsymbol{r}_2)e^{iE_l t_2}$. Note that although $\tilde{\Psi}_l(\boldsymbol{r}_2, t_2) = \Psi_l^*(\boldsymbol{r}_2, t_2)$, according to the above definition of $\tilde{\Psi}_l^T(\boldsymbol{r}_2, t_2)$, the wave functions that we will derive in Sec. 3.2 need not in general be each others complex conjugates, as this is only one of the possible solutions. We only require the wave functions to satisfy

their effective time-dependent and time-independent Schrödinger equations, that we derive below.

Since the retarded Green's function describes causal processes, it is given by

$$G^r(\boldsymbol{r}_1, \boldsymbol{r}_2; t_1, t_2) = \sum_l \Psi_l(\boldsymbol{r}_1, t_1)\tilde{\Psi}_l^T(\boldsymbol{r}_2, t_2)\theta(t_1 - t_2). \tag{3.48}$$

In this thesis, we will consider scattering processes at a fixed energy E. We can therefore write the Green's function as

$$G^r(\boldsymbol{r}_1, \boldsymbol{r}_2; t_1, t_2) = \Psi(\boldsymbol{r}_1, t_1)\tilde{\Psi}^T(\boldsymbol{r}_2, t_2)\theta(t_1 - t_2), \tag{3.49}$$

where $\Psi(\boldsymbol{r}_1, t_1) = \Psi(\boldsymbol{r}_1)e^{-iEt_1}$ and $\tilde{\Psi}(\boldsymbol{r}_2, t_2) = \tilde{\Psi}(\boldsymbol{r}_2)e^{iEt_2}$. $\Psi(\boldsymbol{r}_1, t_1)$ and $\tilde{\Psi}(\boldsymbol{r}_2, t_2)$ can be written as a sum over the wave functions $\Psi_n(\boldsymbol{r}_1, t_1)$ and $\tilde{\Psi}_m(\boldsymbol{r}_2, t_2)$ describing the different scattering processes,

$$\begin{aligned} \Psi(\boldsymbol{r}_1, t_1) &= \sum_n e_n \Psi_n(\boldsymbol{r}_1, t_1), \\ \tilde{\Psi}(\boldsymbol{r}_2, t_2) &= \sum_m f_m \tilde{\Psi}_m(\boldsymbol{r}_2, t_2). \end{aligned} \tag{3.50}$$

e_n and f_m are yet unknown coefficients. The wave functions $\Psi_n(\boldsymbol{r}_1, t_1)$ and $\tilde{\Psi}_m(\boldsymbol{r}_2, t_2)$ can be written as a sum over wave functions describing individual particles present in the system,

$$\begin{aligned} \Psi_n(\boldsymbol{r}_1, t_1) &= \sum_r g_{n,r} \Psi_{n,r}(\boldsymbol{r}_1, t_1), \\ \tilde{\Psi}_m(\boldsymbol{r}_2, t_2) &= \sum_s h_{m,s} \tilde{\Psi}_{m,s}(\boldsymbol{r}_2, t_2). \end{aligned} \tag{3.51}$$

The coefficients $g_{n,r}$ and $h_{m,s}$ are equal to one for the incoming particle. For reflected particles, $g_{n,r}$ and $h_{m,s}$ are reflection amplitudes. For transmitted particles, $g_{n,r}$ and $h_{m,s}$ are are transmission amplitudes.

In order for the retarded Green's function given in Eq. 3.49 to satisfy the equations of motion given in Eq. 3.31, the wave functions of the individual particles and quasi-particles must satisfy

$$\begin{aligned} [i\partial_{t_1} - H(\boldsymbol{r}_1)]\Psi_{n,r}(\boldsymbol{r}_1, t_1) &= 0, \\ \tilde{\Psi}_{m,s}^T(\boldsymbol{r}_2, t_2)[-i\partial_{t_2} - H^\dagger(\boldsymbol{r}_2)] &= 0. \end{aligned} \tag{3.52}$$

The operator in the first equation operates to the right, and the operator in the second equation operates to the left. If we use that $[H^\dagger(\boldsymbol{r}_2)]^T = H^*(\boldsymbol{r}_2)$, these equations may be rewritten as

$$\begin{aligned} i\partial_{t_1}\Psi_{n,r}(\boldsymbol{r}_1, t_1) &= H(\boldsymbol{r}_1)\Psi_{n,r}(\boldsymbol{r}_1, t_1), \\ -i\partial_{t_2}\tilde{\Psi}_{m,s}(\boldsymbol{r}_2, t_2) &= H^*(\boldsymbol{r}_2)\tilde{\Psi}_{m,s}(\boldsymbol{r}_2, t_2). \end{aligned} \tag{3.53}$$

The above equations are the effective time-dependent Schrödinger equations describing the wave functions. The Green's function given in Eq. 3.49 must also satisfy the equations of motion given in Eq. 3.35. This implies that the wave functions of the individual particles and quasi-particles must satisfy

$$\begin{aligned}[\omega - H(\boldsymbol{r}_1)]\Psi_{n,r}(\boldsymbol{r}_1, t_1) &= 0, \\ \tilde{\Psi}^T_{m,s}(\boldsymbol{r}_2, t_2)[\omega - H^\dagger(\boldsymbol{r}_2)] &= 0.\end{aligned} \tag{3.54}$$

The above equations can be rewritten as

$$\begin{aligned}H(\boldsymbol{r}_1)\Psi_{n,r}(\boldsymbol{r}_1, t_1) &= \omega\Psi_{n,r}(\boldsymbol{r}_1, t_1) \\ H^*(\boldsymbol{r}_2)\tilde{\Psi}_{m,s}(\boldsymbol{r}_2, t_2) &= \omega\tilde{\Psi}_{m,s}(\boldsymbol{r}_2, t_2).\end{aligned} \tag{3.55}$$

These are the effective time-independent Shrödinger equations describing the wave functions, and ω is the eigenenergy. We now assume that $\Psi_{n,r}(\boldsymbol{r}_1, t_1)$ and $\tilde{\Psi}_{m,s}(\boldsymbol{r}_2, t_2)$ are separable, so that they can be written

$$\begin{aligned}\Psi_{n,r}(\boldsymbol{r}_1, t_1) &= R_{n,r}(\boldsymbol{r}_1)T_{n,r}(t_1), \\ \tilde{\Psi}_{m,s}(\boldsymbol{r}_2, t_2) &= \tilde{R}_{m,s}(\boldsymbol{r}_2)\tilde{T}_{m,s}(t_2).\end{aligned} \tag{3.56}$$

We first consider the time dependent part. By combining Eqs. 3.53 and 3.55 and inserting the above expressions for $\Psi_{n,r}(\boldsymbol{r}_1, t_1)$ and $\tilde{\Psi}_{m,s}(\boldsymbol{r}_2, t_2)$, we find that

$$\begin{aligned}i\partial_{t_1}T_{n,r}(t_1) &= \omega T_{n,r}(t_1), \\ -i\partial_{t_2}\tilde{T}_{m,s}(t_2) &= \omega\tilde{T}_{m,s}(t_2).\end{aligned} \tag{3.57}$$

The solution to the above differential equations is

$$\begin{aligned}T_{n,r}(t_1) &= C_{n,r}e^{-i\omega t_1}, \\ \tilde{T}_{m,s}(t_2) &= \tilde{C}_{m,s}e^{i\omega t_2}.\end{aligned} \tag{3.58}$$

By comparison to the time dependence found earlier, we find that $\omega = E$. We refer to the energy as E in the following, to distinguish between this parameter and the ω introduced by Fourier transforming the Green's function with respect to the relative time coordinate later on.

We determine the spatial parts of the wave functions from Eq. 3.55 using a similar approach to that in Ref. [44]. We assume the wave functions to be plane waves, so that $\Psi_{n,r}(\boldsymbol{r}_1, t_1) \propto e^{ik_x x_1 + ik_y y_1}$ and $\tilde{\Psi}_{m,s}(\boldsymbol{r}_2, t_2) \propto e^{ik_x x_2 + ik_y y_2}$. Since $(-i\partial_{x_1})e^{ik_x x_1} = k_x e^{ik_x x_1}$ and $(-i\partial_{y_1})e^{ik_y y_1} = k_y e^{ik_y y_1}$, we can replace all $(-i\partial_{x_1})$ and $(-i\partial_{y_1})$ in $H(\boldsymbol{r}_1)$ by k_x and k_y. Since $(-i\partial_{x_2})^* e^{ik_x x_2} = -k_x e^{ik_x x_2}$ and $(-i\partial_{y_2})^* e^{ik_y y_2} = -k_y e^{ik_y y_2}$, we can replace all $(-i\partial_{x_2})$ and $(-i\partial_{y_2})$ in $H^*(\boldsymbol{r}_2)$ with

$-k_x$ and $-k_y$. Expressions for the wave functions are therefore found by solving [38, 39]

$$\begin{aligned} H(\boldsymbol{k})\Psi_{n,r}(\boldsymbol{r}_1,t_1) &= E\Psi_{n,r}(\boldsymbol{r}_1,t_1) \\ H^*(-\boldsymbol{k})\tilde{\Psi}_{m,s}(\boldsymbol{r}_2,t_2) &= E\tilde{\Psi}_{m,s}(\boldsymbol{r}_2,t_2), \end{aligned} \tag{3.59}$$

where

$$\begin{aligned} H(\boldsymbol{k}) =&(k^2/\eta-\mu)\hat{\tau}_3\hat{\sigma}_0+\Delta i\hat{\tau}^+\hat{\sigma}_y-\Delta^* i\hat{\tau}^-\hat{\sigma}_y \\ &-\lambda(n_xk_y-n_yk_x)\hat{\tau}_0\hat{\sigma}_z-\lambda n_zk_x\hat{\tau}_3\hat{\sigma}_y+\lambda n_zk_y\hat{\tau}_0\hat{\sigma}_x \\ &+h_x\hat{\tau}_3\hat{\sigma}_x+h_y\hat{\tau}_0\hat{\sigma}_y+h_z\hat{\tau}_3\hat{\sigma}_z, \end{aligned} \tag{3.60}$$

$\Psi_{n,r}(\boldsymbol{r}_1,t_1)\propto\Phi_{n,r}e^{ik_xx_1+ik_yy_1-iEt_1}$, and $\tilde{\Psi}_{m,s}(\boldsymbol{r}_2,t_2)\propto\Phi_{n,r}e^{ik_xx_2+ik_yy_2+iEt_2}$. $\Phi_{n,r(m,s)}$ is a 4×1 vector in Nambu $\otimes$ spin space. The value of k_x for each $\Psi_{n,r}(\boldsymbol{r}_1,t_1)$ and $\tilde{\Psi}_{m,s}(\boldsymbol{r}_2,t_2)$ is determined by solving Eq. 3.59 for the material of interest. Due to the translational invariance in the y direction, k_y is the same for all particles and quasi-particles present in the system. k_y can take any value. We will return to finding explicit expressions for the wave functions $\Psi_n(\boldsymbol{r}_1,t_1)$ and $\tilde{\Psi}_m(\boldsymbol{r}_2,t_2)$ describing the possible scattering processes in the HM/S structures with $\hat{n}=\{\hat{x},\hat{z}\}$ and the F/S structure with $\boldsymbol{h}=h\hat{z}$ in Sec. 3.2.

We now need to find which types of particles or quasi-particles may exist in each region of our bilayer structures. We let the interface be positioned at $x=0$. The material is non-superconducting for $x<0$ and superconducting for $x>0$, as earlier described in Fig. 3.1. A N/S junction without spin-orbit coupling has no spin-splitting of the energy bands, and there are therefore only four different incoming particles/quasi-particles: A right-moving electron, a right-moving hole, a left-moving electron-like quasi-particle and a left-moving hole-like quasi-particle. In HM/S and F/S junctions the particles exist in spin-split energy bands, that depending on the direction of the spin-orbit field and magnetization may or may not have spin-mixing. We therefore have eight different incoming particle/quasi-particle wave functions: Two different electron wave functions (spin up and spin down electrons in the case of no spin-mixing of the energy bands), two different hole wave functions (spin up and spin down holes in the case of no spin-mixing of the energy bands), two different electron-like quasi-particle wave functions and two different hole-like quasi-particle wave functions. For the four scattering processes where the incoming (quasi-)particle is incoming from the left, we let $\{1,2,3,4\}$ be the possible n and m indices. For the four scattering processes where the incoming quasi-particle is incoming from the right, we let $\{5,6,7,8\}$ be the possible n and m indices.

In order to construct the retarded Green's function, we must find which of the eight possible n and m indices are contributing to $\Psi(\boldsymbol{r}_1, t_1)$ and $\tilde{\Psi}(\boldsymbol{r}_2, t_2)$ in Eq. 3.49. Of the two equations of motion of the retarded Green's function given by Eq. 3.35, the first describes propagation from $\boldsymbol{r}_2$ affecting the field at $\boldsymbol{r}_1$. The second is equivalent to Eq. 3.37 and describes propagation from $\boldsymbol{r}_1$ affecting the field at $\boldsymbol{r}_2$ [44]. Since $\Psi(\boldsymbol{r}_1, t_1)$ is derived from the first of the two equations of motion, and $\tilde{\Psi}(\boldsymbol{r}_2, t_2)$ is derived from the second of the two equations of motion, $\tilde{\Psi}(\boldsymbol{r}_2, t_2)$ must be interpreted as having the opposite direction of propagation compared to $\Psi(\boldsymbol{r}_1, t_1)$ [40]. The Green's function describes the propagation from $\boldsymbol{r}_2$ to $\boldsymbol{r}_1$. This is satisfied if $\Psi(\boldsymbol{r}_1, t_1)$ describes propagation from $\boldsymbol{r}_2$ to $\boldsymbol{r_1}$, while $\tilde{\Psi}(\boldsymbol{r}_2, t_2)$ describes propagation from $\boldsymbol{r}_1$ to $\boldsymbol{r}_2$.

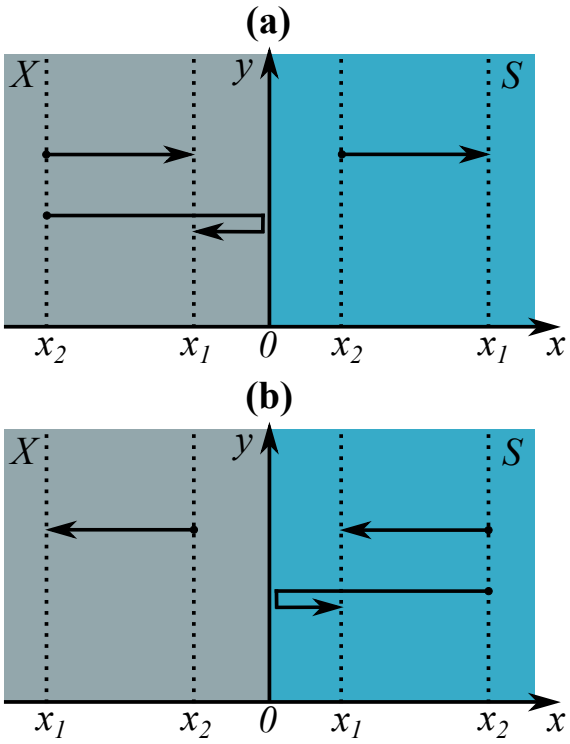

Figure 3.3: Panel (a) shows the possible ways for a (quasi-)particle to propagate from x_2 to $x_1 > x_2$ inside X and S, if the incoming particle comes from the left. X is a non-superconducting material such as a heavy-metal or ferromagnet. Panel (b) shows the possible ways for a (quasi-)particle to propagate from x_2 to $x_1 < x_2$ inside X and S, if the incoming particle comes from the right. Note that each arrow may represent the propagation of several different types of (quasi-)particles, and that a (quasi-)particle can be reflected as a different (quasi-)particle.

We now have to consider the two cases shown in Fig. 3.3. If $x_1 > x_2$, the retarded Green's function describes an overall propagation from the left to the right. From Fig. 3.3(a), we see that in the non-superconducting region, this means

that $\Psi(\boldsymbol{r}_1, t_1)$ needs to describe all scattering processes where the incoming particle comes from the left. This corresponds to the indices $n = \{1, 2, 3, 4\}$. In the superconducting region we can imagine the particle to either represent the transmission of quasi-particles due to particles incoming from the left (as shown in Fig. 3.3(a)), or the reflection of quasi-particles due to quasi-particles incoming from the right. However, consider the case when x_1 is on the superconducting side, and x_2 is close to the interface. If moving x_2 infinitesimally to the left means that x_2 crosses the interface and moves into the non-superconducting region, then the propagating (quasi-)particles can no longer originate from quasi-particles incoming from the right. Including indices corresponding to scattering processes caused by quasi-particles incoming from the right would therefore cause an incontinuity of the Green's function. If, on the other hand, x_1 is inside the non-superconducting region and x_2 moves from the non-superconducting region to the superconducting region, this does not disqualify particles from the left side as the source. Therefore, $\Psi(\boldsymbol{r}_1, t_1)$ must only include scattering processes where the incoming particle comes from the left. For $x_1 > x_2$, the indices giving a contribution to $\Psi(\boldsymbol{r}_1, t_1)$ are therefore $n = \{1, 2, 3, 4\}$ both in the non-superconducting and superconducting region.

If $x_1 < x_2$, the retarded Green's function describes an overall propagation from the right to the left. From Fig. 3.3(b), we see that in the superconducting region, this means that $\Psi(\boldsymbol{r}_1, t_1)$ needs to describe all scattering processes where the incoming particle comes from the right. This corresponds to the indices $n = \{5, 6, 7, 8\}$. In the non-superconducting region we can imagine the particle to either represent the transmission of particles due to quasi-particles incoming from the right (as shown in Fig. 3.3(b)), or the reflection of particles due to particles incoming from the left. However, by the same argument as above, only scattering processes caused by quasi-particles incoming from the right are allowed. For $x_1 < x_2$, the indices giving a contribution to $\Psi(\boldsymbol{r}_1, t_1)$ are therefore $n = \{5, 6, 7, 8\}$ both in the non-superconducting and superconducting region.

In order for the retarded Green's function to describe propagation from $\boldsymbol{r}_2$ to $\boldsymbol{r}_1$, $\tilde{\Psi}(\boldsymbol{r}_2, t_2)$ must describe propagation from $\boldsymbol{r}_1$ to $\boldsymbol{r}_2$. For $x_1 > x_2$, we have the same situation as for $\Psi(\boldsymbol{r}_1, t_1)$ when $x_1 < x_2$, and for $x_1 < x_2$, we have the same situation as for $\Psi(\boldsymbol{r}_1, t_1)$ when $x_1 > x_2$. For $x_1 > x_2$, the indices giving a contribution to $\tilde{\Psi}(\boldsymbol{r}_2, t_2)$ are therefore $m = \{5, 6, 7, 8\}$, while for $x_1 < x_2$, the indices giving a contribution to $\tilde{\Psi}_m(\boldsymbol{r}_2, t_2)$ are $m = \{1, 2, 3, 4\}$.

Using that $n = \{1,2,3,4\}$ and $m = \{5,6,7,8\}$ for $x_1 > x_2$, and that $n = \{5,6,7,8\}$ and $m = \{1,2,3,4\}$ for $x_1 < x_2$, the retarded Green's function given in Eq. 3.49 can be written [39]

$$
\begin{aligned}
&[G^r(\boldsymbol{r}_1,\boldsymbol{r}_2;t_1,t_2)]_{x_1>x_2} = \\
&\quad \Psi_1(\boldsymbol{r}_1,t_1)[\alpha_{11}\tilde{\Psi}_5^T(\boldsymbol{r}_2,t_2)+\alpha_{12}\tilde{\Psi}_6^T(\boldsymbol{r}_2,t_2)+\alpha_{13}\tilde{\Psi}_7^T(\boldsymbol{r}_2,t_2)+\alpha_{14}\tilde{\Psi}_8^T(\boldsymbol{r}_2,t_2)] \\
&+ \Psi_2(\boldsymbol{r}_1,t_1)[\alpha_{21}\tilde{\Psi}_5^T(\boldsymbol{r}_2,t_2)+\alpha_{22}\tilde{\Psi}_6^T(\boldsymbol{r}_2,t_2)+\alpha_{23}\tilde{\Psi}_7^T(\boldsymbol{r}_2,t_2)+\alpha_{24}\tilde{\Psi}_8^T(\boldsymbol{r}_2,t_2)] \\
&+ \Psi_3(\boldsymbol{r}_1,t_1)[\alpha_{31}\tilde{\Psi}_5^T(\boldsymbol{r}_2,t_2)+\alpha_{32}\tilde{\Psi}_6^T(\boldsymbol{r}_2,t_2)+\alpha_{33}\tilde{\Psi}_7^T(\boldsymbol{r}_2,t_2)+\alpha_{34}\tilde{\Psi}_8^T(\boldsymbol{r}_2,t_2)] \\
&+ \Psi_4(\boldsymbol{r}_1,t_1)[\alpha_{41}\tilde{\Psi}_5^T(\boldsymbol{r}_2,t_2)+\alpha_{42}\tilde{\Psi}_6^T(\boldsymbol{r}_2,t_2)+\alpha_{43}\tilde{\Psi}_7^T(\boldsymbol{r}_2,t_2)+\alpha_{44}\tilde{\Psi}_8^T(\boldsymbol{r}_2,t_2)], \\
&[G^r(\boldsymbol{r}_1,\boldsymbol{r}_2;t_1,t_2)]_{x_1<x_2} = \\
&\quad \Psi_5(\boldsymbol{r}_1,t_1)[\beta_{11}\tilde{\Psi}_1^T(\boldsymbol{r}_2,t_2)+\beta_{12}\tilde{\Psi}_2^T(\boldsymbol{r}_2,t_2)+\beta_{13}\tilde{\Psi}_3^T(\boldsymbol{r}_2,t_2)+\beta_{14}\tilde{\Psi}_4^T(\boldsymbol{r}_2,t_2)] \\
&+ \Psi_6(\boldsymbol{r}_1,t_1)[\beta_{21}\tilde{\Psi}_1^T(\boldsymbol{r}_2,t_2)+\beta_{22}\tilde{\Psi}_2^T(\boldsymbol{r}_2,t_2)+\beta_{23}\tilde{\Psi}_3^T(\boldsymbol{r}_2,t_2)+\beta_{24}\tilde{\Psi}_4^T(\boldsymbol{r}_2,t_2)] \\
&+ \Psi_7(\boldsymbol{r}_1,t_1)[\beta_{31}\tilde{\Psi}_1^T(\boldsymbol{r}_2,t_2)+\beta_{32}\tilde{\Psi}_2^T(\boldsymbol{r}_2,t_2)+\beta_{33}\tilde{\Psi}_3^T(\boldsymbol{r}_2,t_2)+\beta_{34}\tilde{\Psi}_4^T(\boldsymbol{r}_2,t_2)] \\
&+ \Psi_8(\boldsymbol{r}_1,t_1)[\beta_{41}\tilde{\Psi}_1^T(\boldsymbol{r}_2,t_2)+\beta_{42}\tilde{\Psi}_2^T(\boldsymbol{r}_2,t_2)+\beta_{43}\tilde{\Psi}_3^T(\boldsymbol{r}_2,t_2)+\beta_{44}\tilde{\Psi}_4^T(\boldsymbol{r}_2,t_2)].
\end{aligned}
\tag{3.61}
$$

The new coefficients α_{ij} and β_{kl} are found by solving the boundary conditions of the retarded Green's function at $x_1 = x_2$, which we will derive in the following section.

3.1.5 *The boundary conditions of the retarded Green's function*

We will now derive the boundary conditions of the retarded Green's function at $x_1 = x_2$ from the equation of motion given in Eq. 3.42. We first integrate Eq. 3.42 twice along x_1 and consider the value of this double integral from $x_1 = x_2 - \delta$ to $x_1 = x_2 + \delta$ in the limit $\delta \to 0$. For terms proportional to $\partial_{x_1}^2 G^r(x_1, x_2, p_y; \omega)$, we get

$$
\begin{aligned}
&\lim_{\delta\to 0}\int_{x_2-\delta}^{x_2+\delta} dx_1 \int_0^{x_1} dx_1'\, \partial_{x_1'}^2 G^r(x_1', x_2, p_y; \omega) \\
&= \lim_{\delta\to 0}\int_{x_2-\delta}^{x_2+\delta} dx_1\, \partial_{x_1} G^r(x_1, x_2, p_y; \omega) \\
&= \lim_{\delta\to 0}[G^r(x_1, x_2, p_y; \omega)]_{x_2-\delta}^{x_2+\delta} \\
&= [G^r(x_1 > x_2, p_y; \omega)]_{x_1=x_2} - [G^r(x_1 < x_2, p_y; \omega)]_{x_1=x_2}
\end{aligned}
\tag{3.62}
$$

by partial integration. For terms proportional to $\partial_{x_1} G^r(x_1, x_2, p_y; \omega)$, we get

$$\begin{aligned}&\lim_{\delta\to 0}\int_{x_2-\delta}^{x_2+\delta} dx_1 \int_0^{x_1} dx_1'\, \partial_{x_1'} G^r(x_1', x_2, p_y; \omega)\\ &= \lim_{\delta\to 0}\int_{x_2-\delta}^{x_2+\delta} dx_1\, G^r(x_1, x_2, p_y; \omega).\end{aligned} \tag{3.63}$$

For terms proportional to $G^r(x_1, x_2, p_y; \omega)$ we get

$$\lim_{\delta\to 0}\int_{x_2-\delta}^{x_2+\delta} dx_1 \int_0^{x_1} dx_1'\, G^r(x_1', x_2, p_y; \omega). \tag{3.64}$$

For the right-hand side of Eq. 3.42, we get

$$\begin{aligned}&\lim_{\delta\to 0}\int_{x_2-\delta}^{x_2+\delta} dx_1 \int_0^{x_1} dx_1'\, \delta(x_1' - x_2)\hat{\tau}_0\hat{\sigma}_0\\ &= \lim_{\delta\to 0}\int_{x_2-\delta}^{x_2+\delta} dx_1\, \hat{\tau}_0\hat{\sigma}_0 = \lim_{\delta\to 0}[x_1]_{x_2-\delta}^{x_2+\delta}\hat{\tau}_0\hat{\sigma}_0 = 0.\end{aligned} \tag{3.65}$$

Therefore, the terms on the left-hand side must sum to zero. This is satisfied if the retarded Green's function is continuous at $x_1 = x_2$, *i.e.* if Eq 3.62 is equal to zero. If the retarded Green's function is continuous at $x_1 = x_2$, it follows that the integral and double integral of the retarded Green's function over $x_1 = x_2$ must also be continuous, *i.e.* Eqs. 3.63 and 3.64 are also zero. Is it possible for the retarded Green's function to be discontinuous at $x_1 = x_2$? If so, $\partial_{x_1} G^r(x_1, x_2, p_y; \omega) \propto \delta(x_1 - x_2)$ and $\partial_{x_1}^2 G^r(x_1, x_2, p_y; \omega) \propto \delta(x_1 - x_2)/x_1$. Since we have no such terms on the right-hand side of Eq. 3.42, the retarded Green's function cannot be discontinuous at $x_1 = x_2$. The first boundary condition is therefore the continuity of the retarded Green's function at $x_1 = x_2$ [39],

$$[G^r(x_1 > x_2, p_y; \omega)]_{x_1=x_2} = [G^r(x_1 < x_2, p_y; \omega)]_{x_1=x_2}. \tag{3.66}$$

To obtain the second boundary condition, we integrate Eq. 3.42 from $x_1 = x_2 - \delta$ to $x_1 = x_2 + \delta$ in the limit $\delta \to 0$ and use the continuity of the Green's function at $x_1 = x_2$. For terms proportional to $\partial_{x_1}^2 G^r(x_1, x_2, p_y; \omega)$ we get

$$\begin{aligned}&\lim_{\delta\to 0}\int_{x_2-\delta}^{x_2+\delta} dx_1\, \partial_{x_1}^2 G^r(x_1, x_2, p_y; \omega)\\ &= \lim_{\delta\to 0}[\partial_{x_1} G^r(x_1, x_2, p_y; \omega)]_{x_2-\delta}^{x_2+\delta}\\ &= [\partial_{x_1} G^r(x_1 > x_2, p_y; \omega)]_{x_1=x_2} - [\partial_{x_1} G^r(x_1 < x_2, p_y; \omega)]_{x_1=x_2}.\end{aligned} \tag{3.67}$$

For terms proportional to $\partial_{x_1} G^r(x_1, x_2, p_y; \omega)$ we get

$$\begin{aligned}
&\lim_{\delta\to 0}\int_{x_2-\delta}^{x_2+\delta} dx_1\, \partial_{x_1} G^r(x_1, x_2, p_y; \omega) \\
&= \lim_{\delta\to 0}[G^r(x_1, x_2, p_y; \omega)]_{x_2-\delta}^{x_2+\delta} \\
&= [G^r(x_1 > x_2, p_y; \omega)]_{x_1=x_2} - [G^r(x_1 < x_2, p_y; \omega)]_{x_1=x_2} = 0
\end{aligned} \tag{3.68}$$

by using the continuity of the retarded Green's function. For terms proportional to $G^r(x_1, x_2, p_y; \omega)$ we get

$$\lim_{\delta\to 0}\int_{x_2-\delta}^{x_2+\delta} dx_1\, G^r(x_1, x_2, p_y; \omega), \tag{3.69}$$

which must also be equal to zero when the retarded Green's function is continuous. After the integration, the only nonzero terms on the left-hand side of Eq. 3.42 are

$$\{[\partial_{x_1} G^r(x_1 > x_2, p_y; \omega)]_{x_1=x_2} - [\partial_{x_1} G^r(x_1 < x_2, p_y; \omega)]_{x_1=x_2}\}\hat{\tau}_3\hat{\sigma}_0/\eta. \tag{3.70}$$

For the right-hand side of Eq. 3.42, we get

$$\lim_{\delta\to 0}\int_{x_2-\delta}^{x_2+\delta} dx_1\, \delta(x_1 - x_2)\hat{\tau}_0\hat{\sigma}_0 = \hat{\tau}_0\hat{\sigma}_0. \tag{3.71}$$

By equating Eqs. 3.70 and 3.71 and multiplying both sides of the resulting equation by $\hat{\tau}_0\hat{\sigma}_3\eta$, we get [39]

$$[\partial_{x_1} G^r(x_1 > x_2, p_y; \omega)]_{x_1=x_2} - [\partial_{x_1} G^r(x_1 < x_2, p_y; \omega)]_{x_1=x_2} = \eta\hat{\tau}_3\hat{\sigma}_0. \tag{3.72}$$

This is the second boundary condition of the retarded Green's function.

3.1.6 *The even- and odd-frequency retarded Green's functions*

We now turn to deriving the even- and odd-frequency singlet and triplet retarded anomalous Green's functions from the elements of the retarded Green's function given in Eq. 3.61. The singlet and triplet retarded (advanced) anomalous Green's functions can be constructed from the elements of $f^r(\boldsymbol{r}_1, \boldsymbol{r}_2; t_1, t_2)$ and $f^a(\boldsymbol{r}_1, \boldsymbol{r}_2; t_1, t_2)$ given in Eq. 3.3. We define [38, 39]

$$\begin{aligned}
f_0^{r(a)}(\boldsymbol{r}_1, \boldsymbol{r}_2; t_1, t_2) &\equiv [f_{\uparrow,\downarrow}^{r(a)}(\boldsymbol{r}_1, \boldsymbol{r}_2; t_1, t_2) - f_{\downarrow,\uparrow}^{r(a)}(\boldsymbol{r}_1, \boldsymbol{r}_2; t_1, t_2)]/2 \\
f_1^{r(a)}(\boldsymbol{r}_1, \boldsymbol{r}_2; t_1, t_2) &\equiv f_{\uparrow,\uparrow}^{r(a)}(\boldsymbol{r}_1, \boldsymbol{r}_2; t_1, t_2) \\
f_2^{r(a)}(\boldsymbol{r}_1, \boldsymbol{r}_2; t_1, t_2) &\equiv f_{\downarrow,\downarrow}^{r(a)}(\boldsymbol{r}_1, \boldsymbol{r}_2; t_1, t_2), \\
f_3^{r(a)}(\boldsymbol{r}_1, \boldsymbol{r}_2; t_1, t_2) &\equiv [f_{\uparrow,\downarrow}^{r(a)}(\boldsymbol{r}_1, \boldsymbol{r}_2; t_1, t_2) + f_{\downarrow,\uparrow}^{r(a)}(\boldsymbol{r}_1, \boldsymbol{r}_2; t_1, t_2)]/2.
\end{aligned} \tag{3.73}$$

Above, $f_0^{r(a)}(\boldsymbol{r}_1, \boldsymbol{r}_2; t_1, t_2)$ is the singlet retarded (advanced) anomalous Green's function, $f_1^{r(a)}(\boldsymbol{r}_1, \boldsymbol{r}_2; t_1, t_2)$ and $f_2^{r(a)}(\boldsymbol{r}_1, \boldsymbol{r}_2; t_1, t_2)$ are the equal-spin triplet retarded (advanced) anomalous Green's functions, while $f_3^{r(a)}(\boldsymbol{r}_1, \boldsymbol{r}_2; t_1, t_2)$ is the opposite-spin triplet retarded (advanced) anomalous Green's function. We are interested in decomposing the above singlet and triplet retarded Green's functions into even- and odd-frequency contributions. In order to do this, we consider an anomalous Green's function $f_{\alpha,\beta}(\boldsymbol{r}_1, \boldsymbol{r}_2; t_1, t_2)$, and follow a similar approach as in Ref. [33]. The Green's function needs to satisfy the Pauli principle, *i.e.* two identical half-integer spin fermions cannot simultaneously be in the same quantum state. Therefore, the Green's function must be odd under interchange of the particles at equal times [33],

$$f_{\alpha,\beta}(\boldsymbol{r}_1, \boldsymbol{r}_2; t_1, t_1) = -f_{\beta,\alpha}(\boldsymbol{r}_2, \boldsymbol{r}_1; t_1, t_1). \tag{3.74}$$

In the following, we will write the above Green's function in the center of mass coordinate $\boldsymbol{R} \equiv (\boldsymbol{r}_1 + \boldsymbol{r}_2)/2$, the relative spatial coordinate $\boldsymbol{r} \equiv \boldsymbol{r}_1 - \boldsymbol{r}_2$, the average time coordinate $T \equiv (t_1 + t_2)/2$, and the relative time coordinate $t \equiv t_1 - t_2$. We will use the Fourier transforms [33] in the relative spatial coordinate,

$$f_{\alpha,\beta}(\boldsymbol{R}, \boldsymbol{p}; T, t) = \int d\boldsymbol{r}\; e^{-i\boldsymbol{p}\cdot\boldsymbol{r}} f_{\alpha,\beta}(\boldsymbol{R}, \boldsymbol{r}; T, t), \tag{3.75}$$

and in the relative time coordinate,

$$f_{\alpha,\beta}(\boldsymbol{R}, \boldsymbol{p}; T, \omega) = \int_{-\infty}^{\infty} dt\; e^{i\omega t} f_{\alpha,\beta}(\boldsymbol{R}, \boldsymbol{p}; T, t). \tag{3.76}$$

The above spatial integral goes over all of space. By applying the spatial Fourier transform in Eq. 3.75 to the definition of the Pauli principle in Eq. 3.74, we get

$$\begin{aligned} f_{\alpha,\beta}(\boldsymbol{R}, \boldsymbol{p}; T, 0) &= -\int d\boldsymbol{r}\; e^{-i\boldsymbol{p}\cdot\boldsymbol{r}} f_{\beta,\alpha}(\boldsymbol{R}, -\boldsymbol{r}; T, 0) \\ &= -\int d(-\boldsymbol{r})\; e^{-i(-\boldsymbol{p})\cdot(-\boldsymbol{r})} f_{\beta,\alpha}(\boldsymbol{R}, -\boldsymbol{r}; T, 0) \\ &= -f_{\beta,\alpha}(\boldsymbol{R}, -\boldsymbol{p}; T, 0). \end{aligned} \tag{3.77}$$

If we integrate $f_{\alpha,\beta}(\boldsymbol{R}, \boldsymbol{p}; T, \omega)$ over all ω, apply the Fourier transform of the relative time given in Eq. 3.76, and apply the reformulated definition of the Pauli principle given in Eq. 3.77, we get

$$\int_{-\infty}^{\infty} d\omega\; f_{\alpha,\beta}(\boldsymbol{R}, \boldsymbol{p}; T, \omega) = \int_{-\infty}^{\infty} d\omega \int_{-\infty}^{\infty} dt\; e^{i\omega t} f_{\alpha,\beta}(\boldsymbol{R}, \boldsymbol{p}; T, t)$$

$$
\begin{aligned}
&= \int_{-\infty}^{\infty} dt\ \delta(t) f_{\alpha,\beta}(\boldsymbol{R}, \boldsymbol{p}; T, t) \\
&= f_{\alpha,\beta}(\boldsymbol{R}, \boldsymbol{p}; T, 0) \\
&= -f_{\beta,\alpha}(\boldsymbol{R}, -\boldsymbol{p}; T, 0) \\
&= -\int_{-\infty}^{\infty} dt\ \delta(t) f_{\beta,\alpha}(\boldsymbol{R}, -\boldsymbol{p}; T, t) \\
&= -\int_{-\infty}^{\infty} d\omega \int_{-\infty}^{\infty} dt\ e^{i\omega t} f_{\beta,\alpha}(\boldsymbol{R}, -\boldsymbol{p}; T, t) \\
&= -\int_{-\infty}^{\infty} d\omega\ f_{\beta,\alpha}(\boldsymbol{R}, -\boldsymbol{p}; T, \omega).
\end{aligned}
\tag{3.78}
$$

The above equation is a reformulated definition of the Pauli principle. There are two ways to satisfy the above equation,

$$f_{\alpha,\beta}(\boldsymbol{R}, \boldsymbol{p}; T, \omega) = -f_{\beta,\alpha}(\boldsymbol{R}, -\boldsymbol{p}; T, \omega) \tag{3.79}$$

or

$$f_{\alpha,\beta}(\boldsymbol{R}, \boldsymbol{p}; T, \omega) = -f_{\beta,\alpha}(\boldsymbol{R}, -\boldsymbol{p}; T, -\omega). \tag{3.80}$$

The latter allows for a Green's function that is odd under inversion of ω. Odd-frequency Green's functions are odd under interchange of time coordinates [33],

$$f^{O}_{\alpha,\beta}(\boldsymbol{r}_1, \boldsymbol{r}_2; t_1, t_2) = -f^{O}_{\alpha,\beta}(\boldsymbol{r}_1, \boldsymbol{r}_2; t_2, t_1). \tag{3.81}$$

If we apply the Fourier transforms in space and time given in Eqs. 3.75 and 3.76, we find that Eq. 3.81 can be written

$$f^{O}_{\alpha,\beta}(\boldsymbol{R}, \boldsymbol{p}; T, \omega) = -f^{O}_{\alpha,\beta}(\boldsymbol{R}, \boldsymbol{p}; T, -\omega). \tag{3.82}$$

The above equation is odd under inversion of ω, and Eq. 3.80 therefore allows for odd-frequency pairing. Even-frequency Green's functions are even under interchange of the time coordinates [33],

$$f^{E}_{\alpha,\beta}(\boldsymbol{r}_1, \boldsymbol{r}_2; t_1, t_2) = f^{E}_{\alpha,\beta}(\boldsymbol{r}_1, \boldsymbol{r}_2; t_2, t_1). \tag{3.83}$$

If we apply the Fourier transforms in space and time given in Eqs. 3.75 and 3.76, we find that Eq. 3.83 can be written

$$f^{E}_{\alpha,\beta}(\boldsymbol{R}, \boldsymbol{p}; T, \omega) = f^{E}_{\alpha,\beta}(\boldsymbol{R}, \boldsymbol{p}; T, -\omega). \tag{3.84}$$

The above equation is even under inversion of ω. Therefore, both Eq. 3.79 and Eq. 3.80 allow for even-frequency pairing, since the sign change in the former equation must be caused by the sign change of other parameters than ω, and since the sign change in the latter equation may be caused by the sign change of other parameters than ω.

Next, we want to decompose the Green's function into a retarded and an advanced contribution. Let the anomalous retarded and advanced Green's functions be defined as in Eq. 3.2. We can easily see that

$$f^a_{\alpha,\beta}(\boldsymbol{r}_1, \boldsymbol{r}_2; t_1, t_2) = -f^r_{\beta,\alpha}(\boldsymbol{r}_2, \boldsymbol{r}_1; t_2, t_1). \tag{3.85}$$

By rewriting Eq. 3.85 to relative coordinates in space and time and applying the Fourier transforms in Eqs. 3.75 and 3.76, we can instead write

$$f^a_{\alpha,\beta}(\boldsymbol{R}, \boldsymbol{p}; T, \omega) = -f^r_{\beta,\alpha}(\boldsymbol{R}, -\boldsymbol{p}; T, -\omega). \tag{3.86}$$

We write the singlet and triplet retarded anomalous Green's functions given in Eq. 3.73 in the coordinates $\boldsymbol{R}$, $\boldsymbol{r}$, T and t, and apply the Fourier transforms in Eqs. 3.75 and 3.76. By inserting Eq. 3.86, we find that

$$\begin{aligned} f^a_0(\boldsymbol{R}, \boldsymbol{p}; T, \omega) &= f^r_0(\boldsymbol{R}, -\boldsymbol{p}; T, -\omega), \\ f^a_i(\boldsymbol{R}, \boldsymbol{p}; T, \omega) &= -f^r_i(\boldsymbol{R}, -\boldsymbol{p}; T, -\omega), \end{aligned} \tag{3.87}$$

where $i = \{1, 2, 3\}$. The reason for the difference in sign for singlets and triplets in the above equation is that singlet Green's functions are odd under interchange of spins, while triplet Green's functions are even under interchange of spins.

We now decompose the retarded Green's functions into even- and odd-frequency contributions,

$$\begin{aligned} f^r_0(\boldsymbol{R}, \boldsymbol{p}; T, \omega) &= f^{r,E}_0(\boldsymbol{R}, \boldsymbol{p}; T, \omega) + f^{r,O}_0(\boldsymbol{R}, \boldsymbol{p}; T, \omega), \\ f^r_i(\boldsymbol{R}, \boldsymbol{p}; T, \omega) &= f^{r,E}_i(\boldsymbol{R}, \boldsymbol{p}; T, \omega) + f^{r,O}_i(\boldsymbol{R}, \boldsymbol{p}; T, \omega). \end{aligned} \tag{3.88}$$

By using Eq. 3.86, we also find that

$$\begin{aligned} f^a_0(\boldsymbol{R}, \boldsymbol{p}; T, -\omega) &= f^r_0(\boldsymbol{R}, -\boldsymbol{p}; T, \omega) \\ &= f^{r,E}_0(\boldsymbol{R}, -\boldsymbol{p}; T, \omega) + f^{r,O}_0(\boldsymbol{R}, -\boldsymbol{p}; T, \omega), \\ f^a_i(\boldsymbol{R}, \boldsymbol{p}; T, -\omega) &= -f^r_i(\boldsymbol{R}, -\boldsymbol{p}; T, \omega) \\ &= -f^{r,E}_i(\boldsymbol{R}, -\boldsymbol{p}; T, \omega) - f^{r,O}_i(\boldsymbol{R}, -\boldsymbol{p}; T, \omega). \end{aligned} \tag{3.89}$$

If we rewrite Eqs. 3.79 and 3.80 in terms of the singlet and triplet Green's functions, we get

$$\begin{aligned} f^r_0(\boldsymbol{R}, \boldsymbol{p}; T, \omega) &= f^r_0(\boldsymbol{R}, -\boldsymbol{p}; T, \pm\omega), \\ f^r_i(\boldsymbol{R}, \boldsymbol{p}; T, \omega) &= -f^r_i(\boldsymbol{R}, -\boldsymbol{p}; T, \pm\omega). \end{aligned} \tag{3.90}$$

In the above equation, ω must have a negative sign and $f^r_{0(i)}$ must be odd under inversion of ω for the retarded Green's function to be an odd-frequency Green's function. Eq. 3.90 can therefore be written

$$\begin{aligned} f_0^{r,E}(\boldsymbol{R},\boldsymbol{p};T,\omega) &= f_0^{r,E}(\boldsymbol{R},-\boldsymbol{p};T,\omega),\\ f_0^{r,O}(\boldsymbol{R},\boldsymbol{p};T,\omega) &= -f_0^{r,O}(\boldsymbol{R},-\boldsymbol{p};T,\omega),\\ f_i^{r,E}(\boldsymbol{R},\boldsymbol{p};T,\omega) &= -f_i^{r,E}(\boldsymbol{R},-\boldsymbol{p};T,\omega),\\ f_i^{r,O}(\boldsymbol{R},\boldsymbol{p};T,\omega) &= f_i^{r,O}(\boldsymbol{R},-\boldsymbol{p};T,\omega). \end{aligned} \tag{3.91}$$

By inserting the above equation into Eq. 3.89, we find that

$$\begin{aligned} f_0^{a}(\boldsymbol{R},\boldsymbol{p};T,-\omega) &= f_0^{r,E}(\boldsymbol{R},\boldsymbol{p};T,\omega) - f_0^{r,O}(\boldsymbol{R},\boldsymbol{p};T,\omega),\\ f_i^{a}(\boldsymbol{R},\boldsymbol{p};T,-\omega) &= f_i^{r,E}(\boldsymbol{R},\boldsymbol{p};T,\omega) - f_i^{r,O}(\boldsymbol{R},\boldsymbol{p};T,\omega). \end{aligned} \tag{3.92}$$

By solving Eqs. 3.88 and 3.92 for $f_0^{r,E(O)}(\boldsymbol{R},\boldsymbol{p};T,\omega)$ and $f_i^{r,E(O)}(\boldsymbol{R},\boldsymbol{p};T,\omega)$, we find that the expressions for the even- and odd-frequency singlet and triplet retarded anomalous Green's functions are

$$\begin{aligned} f_0^{r,E(O)}(\boldsymbol{R},\boldsymbol{p};T,\omega) &= [f_0^{r}(\boldsymbol{R},\boldsymbol{p};T,\omega) \pm f_0^{a}(\boldsymbol{R},\boldsymbol{p};T,-\omega)]/2,\\ f_i^{r,E(O)}(\boldsymbol{R},\boldsymbol{p};T,\omega) &= [f_i^{r}(\boldsymbol{R},\boldsymbol{p};T,\omega) \pm f_i^{a}(\boldsymbol{R},\boldsymbol{p};T,-\omega)]/2. \end{aligned} \tag{3.93}$$

By the use of Eq. 3.87, we can rewrite the above equation as

$$\begin{aligned} f_0^{r,E(O)}(\boldsymbol{R},\boldsymbol{p};T,\omega) &= [f_0^{r}(\boldsymbol{R},\boldsymbol{p};T,\omega) \pm f_0^{r}(\boldsymbol{R},-\boldsymbol{p};T,\omega)]/2,\\ f_i^{r,E(O)}(\boldsymbol{R},\boldsymbol{p};T,\omega) &= [f_i^{r}(\boldsymbol{R},\boldsymbol{p};T,\omega) \mp f_i^{r}(\boldsymbol{R},-\boldsymbol{p};T,\omega)]/2. \end{aligned} \tag{3.94}$$

If we do the inverse Fourier transform of the spatial Fourier transform in Eq. 3.75,

$$f_{\alpha,\beta}(\boldsymbol{R},\boldsymbol{r};T,\omega) = \frac{1}{(2\pi)^2}\int d\boldsymbol{p}\; e^{i\boldsymbol{r}\cdot\boldsymbol{p}} f_{\alpha,\beta}(\boldsymbol{R},\boldsymbol{p};T,\omega), \tag{3.95}$$

and use the coordinates $\boldsymbol{r}_1$ and $\boldsymbol{r}_2$ instead of the center of mass and relative coordinate, we get

$$\begin{aligned} f_0^{r,E(O)}(\boldsymbol{r}_1,\boldsymbol{r}_2;T,\omega) &= [f_0^{r}(\boldsymbol{r}_1,\boldsymbol{r}_2;T,\omega) \pm f_0^{r}(\boldsymbol{r}_2,\boldsymbol{r}_1;T,\omega)]/2,\\ f_i^{r,E(O)}(\boldsymbol{r}_1,\boldsymbol{r}_2;T,\omega) &= [f_i^{r}(\boldsymbol{r}_1,\boldsymbol{r}_2;T,\omega) \mp f_i^{r}(\boldsymbol{r}_2,\boldsymbol{r}_1;T,\omega)]/2. \end{aligned} \tag{3.96}$$

Since we are considering a system that is translationally invariant in the y direction, we now use center of mass and relative coordinates in the y direction as we did in Sec. 3.1.3 and apply the Fourier transform in y given in Eq. 3.38. As in Sec. 3.1.3, we omit T and the center of mass coordinate Y, since the retarded

Green's functions is independent of these variables. The resulting expressions for the even- and odd-frequency singlet and triplet anomalous retarded Green's functions are [38, 39]

$$\begin{aligned} f_0^{r,E(O)}(x_1, x_2, p_y; \omega) &= [f_0^r(x_1, x_2, p_y; \omega) \pm f_0^r(x_2, x_1, -p_y; \omega)]/2, \\ f_i^{r,E(O)}(x_1, x_2, p_y; \omega) &= [f_i^r(x_1, x_2, p_y; \omega) \mp f_i^r(x_2, x_1, -p_y; \omega)]/2, \end{aligned} \tag{3.97}$$

where

$$\begin{aligned} f_0^r(x_1, x_2, p_y; \omega) &= [f_{\uparrow,\downarrow}^r(x_1, x_2, p_y; \omega) - f_{\downarrow,\uparrow}^r(x_1, x_2, p_y; \omega)]/2, \\ f_1^r(x_1, x_2, p_y; \omega) &= f_{\uparrow,\uparrow}^r(x_1, x_2, p_y; \omega), \\ f_2^r(x_1, x_2, p_y; \omega) &= f_{\downarrow,\downarrow}^r(x_1, x_2, p_y; \omega), \\ f_3^r(x_1, x_2, p_y; \omega) &= [f_{\uparrow,\downarrow}^r(x_1, x_2, p_y; \omega) + f_{\downarrow,\uparrow}^r(x_1, x_2, p_y; \omega)]/2. \end{aligned} \tag{3.98}$$

3.2 THE SCATTERING WAVE FUNCTIONS

In this section, we find expressions for the scattering wave functions needed to construct the retarded Green's function given in Eq. 3.61. Our approach will be to first consider each material in the bilayer separately, and solve Eq. 3.59 using the appropriate terms of the Hamiltonian given in Eq. 3.60. Recall that $\Psi_{n,r}(\boldsymbol{r}_1, t_1) \propto \Phi_{n,r} e^{ik_x^{n,r} x_1 + ik_y y_1 - iEt_1}$ and $\tilde{\Psi}_{m,s}(\boldsymbol{r}_2, t_2) \propto \Phi_{m,s} e^{ik_x^{m,s} x_2 + ik_y y_2 + iEt_2}$. Solving Eq. 3.59 yields expressions for the allowed $\Phi_{n,r(m,s)}$, E, and $k_x^{n,r(m,s)}$. k_y can take any value. From the expressions for the scattering wave functions $\Psi_{n,r}(\boldsymbol{r}_1, t_1)$ and $\tilde{\Psi}_{m,s}(\boldsymbol{r}_2, t_2)$ of the individual particles and quasi-particles, we construct the wave functions of each possible scattering process using Eq. 3.51. Thereafter, we compute the reflection and transmission coefficients of the particles and quasi-particles scattering at the interface between the superconductor and the non-superconducting material, thereby obtaining the wave functions describing the scattering processes. We follow a similar approach as in Refs. [16, 48].

Before turning to the computation of the scattering wave functions, we will discuss the possible scattering processes. As mentioned earlier, we will consider systems with the interface at $x = 0$, a superconducting material at $x > 0$ and a non-superconducting material at $x < 0$. First, consider non-superconducting materials without spin-mixing. For particles incoming from the left, we can have Andreev reflections of spin-up electrons into spin-down holes (see Fig. 3.4) or vice versa, or spin-down electrons into spin-up holes and vice versa. We can also have normal reflections of electrons and holes. For non-superconducting materials

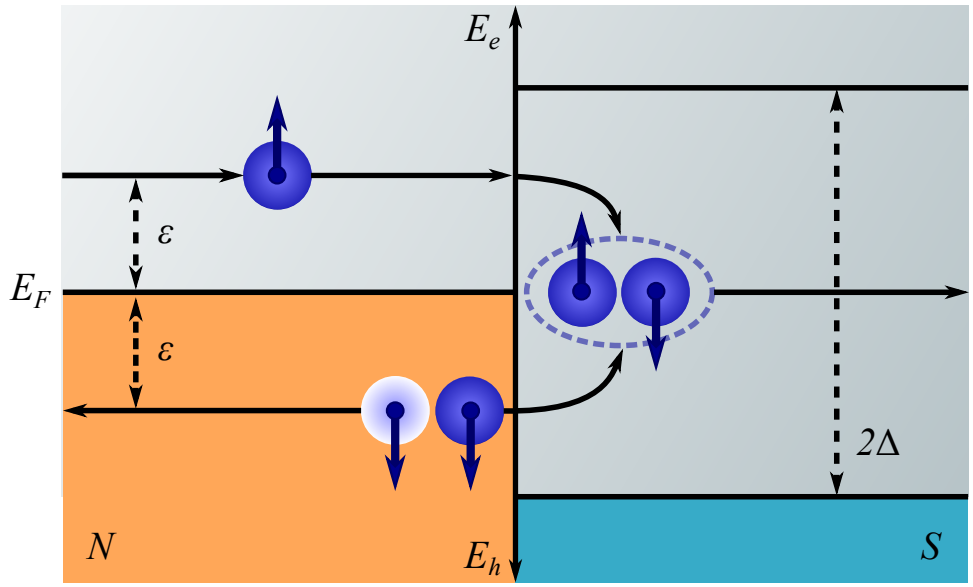

Figure 3.4: Due to the superconducting gap, a spin-up electron (dark blue) at energy $E_F + \epsilon$, where $\epsilon < \Delta$, cannot be directly transmitted from the normal-metal into the superconducting region. Instead, a spin-zero Cooper pair is transmitted at the Fermi energy. For this to happen, the spin-up electron must couple to a spin-down electron at energy $E_F - \epsilon$. The spin-down electron leaves behind a spin-down hole (white) with energy $E_F + \epsilon$ and the opposite momentum of the incoming spin-up electron. In the figure, the axes of the electron energy E_e and the hole energy E_h are oppositely directed.

with spin-dependent interactions, such as spin-orbit coupling or inhomogeneous magnetic textures, Andreev reflection is not restricted to holes with opposite spin of the incoming electrons and electrons with the opposite spin of the incoming holes. We can therefore have Andreev reflections from any spin-mixed electron wave function to any spin-mixed hole wave function. The normal reflections are also not restricted to particles of the same spin, and we can therefore have normal reflections between any of the spin-mixed electron wave functions, and between any of the spin-mixed hole wave functions. For quasi-particles incoming from the right, we can have Andreev reflections of spin-up quasi-electrons into spin-down quasi-holes and vice versa or of spin-down quasi-electrons into spin-up quasi-holes and vice versa. We can also have normal reflections of the quasi-particles. Andreev reflections lead to the propagation of a different particle or quasi-particle into the material at the opposite side of the interface. Direct transmission of the particles and quasi-particles is prohibited by the superconducting gap, that exists only on one side of the interface.

3.2.1 *The superconducting scattering wave functions*

We first consider the scattering wave function inside the superconductor. We assume $\Phi_{n,r(m,s)} = [u^* \ v^* \ w^* \ x^*]^\dagger$. The first of the two equations given in Eq. 3.59 gives the set of equations

$$\begin{aligned} Eu &= (q^2/\eta - \mu)u + \Delta x, \\ Ev &= (q^2/\eta - \mu)v - \Delta w, \\ Ew &= (-q^2/\eta + \mu)w - \Delta^* v, \\ Ex &= (-q^2/\eta + \mu)x + \Delta^* u. \end{aligned} \tag{3.99}$$

By eliminating u and x from the first and fourth equation, or equivalently by elimininating v and w from the second and third equation, we find that the allowed k_x values are

$$\pm' q_x^{\pm} = \pm' \left\{ -k_y^2 + \eta \left[\mu \pm \sqrt{E^2 - |\Delta|^2} \right] \right\}^{1/2}. \tag{3.100}$$

Above, we have named the allowed k_x values in the superconducting region $\pm' q_x^{\pm}$, where $q_x^{\pm}$ is defined to be positive, and the sign is given by $\pm'$. Due to translational invariance in the y direction, k_y is the same inside the superconductor and the non-superconducting material, and we do not rename this parameter. k_y can take positive and negative values. The eigenenergy is given by $E = \pm\sqrt{(k^2/\eta - \mu)^2 + |\Delta|^2}$. In our treatment, we will assume $E < |\Delta|$, so that $q_x^{\pm}$ is a complex number.

For $\Delta = 0$, we find that q_x^+ is the k_x value of a free electron, while q_x^- is the the k_x value of a free hole. Particles characterized by q_x^+ are therefore electron-like quasiparticles, while particles characterized by q_x^- are hole-like quasiparticles. At $\Delta = 0$, the eigenenergy is $E = \pm(k^2/\eta - \mu)$ for a free electron and a free hole respectively. The group velocity perpendicular to the interface is, $v_g = \frac{1}{\hbar}\frac{\partial E}{\partial k_x} = \pm\frac{\hbar k_x}{m}$. A wavefunction $\propto e^{ik_x^{\pm}x} = e^{\pm imv_g x/\hbar}$ with a positive group velocity is therefore right-moving for an electron and left-moving for a hole. Generalizing this to the case of electron-like and hole-like quasiparticles, we find that a right-moving quasi-electron has a wave function $\propto e^{iq_x^+ x}$, while a right-moving quasi-hole has a wave function $\propto e^{-iq_x^- x}$.

Since the first and fourth equation, and the second and third equation in Eq. 3.99 can be solved as two separate sets of equations, we expect solutions on the form $\Phi = [u^* \ 0 \ 0 \ x^*]^\dagger$ and $\Phi = [0 \ v^* \ w^* \ 0]^\dagger$. By inserting the normalization

condition $|u|^2 + |x|^2 = 1$ and the allowed k_x values given in Eq. 3.100 into the first and fourth equation, we find that

$$\begin{aligned} |u|^2 &= \frac{1}{2}\left[1 \pm \sqrt{E^2 - |\Delta|^2}/E\right], \\ |x|^2 &= \frac{1}{2}\left[1 \mp \sqrt{E^2 - |\Delta|^2}/E\right]. \end{aligned} \tag{3.101}$$

We define

$$\begin{aligned} u_0^2 &\equiv \frac{1}{2}\left[1 + \sqrt{E^2 - |\Delta|^2}/E\right], \\ v_0^2 &\equiv \frac{1}{2}\left[1 - \sqrt{E^2 - |\Delta|^2}/E\right]. \end{aligned} \tag{3.102}$$

We can therefore either have $|u|^2 = u_0^2$ and $|x|^2 = v_0^2$, or $|u|^2 = v_0^2$ and $|x|^2 = u_0^2$. It can easily be seen that the second and third equation in Eq. 3.99 can be obtained from the first and fourth equation by $u \longrightarrow v$, $x \longrightarrow -w$ or by $u \longrightarrow -v$, $x \longrightarrow w$. We thus choose the set of eigenvectors

$$\Phi_{n,r(m,s)} = \left\{ \begin{pmatrix} u_0 \\ 0 \\ 0 \\ v_0 \end{pmatrix}, \begin{pmatrix} 0 \\ -u_0 \\ v_0 \\ 0 \end{pmatrix}, \begin{pmatrix} 0 \\ -v_0 \\ u_0 \\ 0 \end{pmatrix}, \begin{pmatrix} v_0 \\ 0 \\ 0 \\ u_0 \end{pmatrix} \right\}. \tag{3.103}$$

The first two eigenvectors in Eq. 3.103 correspond to $\pm q_x^+$, while the last two eigenvectors corresponds to $\pm q_x^-$.

We plot the energy bands of the superconductor, $E = \pm\sqrt{(k^2/\eta - \mu)^2 + |\Delta|^2}$, in Fig. 3.5 in order to identify the allowed scattering processes. The scattering wave functions on the superconducting side of the interface is

$$\begin{aligned} \Psi_n(\boldsymbol{r}, t) = \Psi^R_{\text{in},n}(\boldsymbol{r}, t) &+ c_{n,1}[u_0 \;\; 0 \;\; 0 \;\; v_0]^T e^{iq_x^+ x + ik_y y - iEt} \\ &+ c_{n,2}[0 \;\; -u_0 \;\; v_0 \;\; 0]^T e^{iq_x^+ x + ik_y y - iEt} \\ &+ d_{n,1}[0 \;\; -v_0 \;\; u_0 \;\; 0]^T e^{-iq_x^- x + ik_y y - iEt} \\ &+ d_{n,2}[v_0 \;\; 0 \;\; 0 \;\; u_0]^T e^{-iq_x^- x + ik_y y - iEt}, \;\; x > 0, \end{aligned} \tag{3.104}$$

where the quasi-particles incoming from the right are described by the wave functions

$$\begin{aligned} \Psi^R_{\text{in},5}(\boldsymbol{r}, t) &= [u_0 \;\; 0 \;\; 0 \;\; v_0]^T e^{-iq_x^+ x + ik_y y - iEt} \\ \Psi^R_{\text{in},6}(\boldsymbol{r}, t) &= [0 \;\; -u_0 \;\; v_0 \;\; 0]^T e^{-iq_x^+ x + ik_y y - iEt}, \\ \Psi^R_{\text{in},7}(\boldsymbol{r}, t) &= [0 \;\; -v_0 \;\; u_0 \;\; 0]^T e^{iq_x^- x + ik_y y - iEt}, \\ \Psi^R_{\text{in},8}(\boldsymbol{r}, t) &= [v_0 \;\; 0 \;\; 0 \;\; u_0]^T e^{iq_x^- x + ik_y y - iEt}. \end{aligned} \tag{3.105}$$

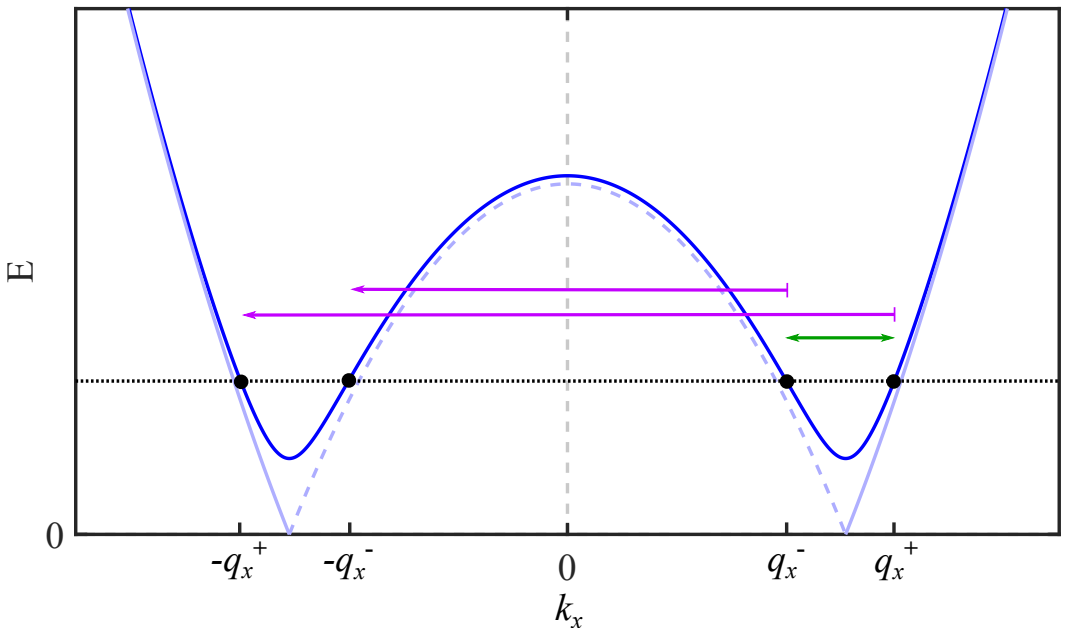

Figure 3.5: The superconducting order parameter Δ opens a gap in the energy spectrum leading to a quasi-particle energy band (dark blue). Quasi-particles residing in the part of the energy band that has a similar shape as the electron energy band at $\Delta = 0$ (light blue solid line) are called electron-like quasi-particles. The quasi-particles residing in the part of the energy band that has a similar shape as the hole energy band at $\Delta = 0$ (light blue dashed line) are called hole-like quasi-particles. The green arrow shows the possible Andreev reflections, while the purple arrows show the possible normal reflections for quasi-electrons and quasi-holes at the energy marked by the black dotted line.

$i = \{1, 2, 3, 4, 5, 6, 7, 8\}$ and $\Psi^R_{\text{in},1}(\boldsymbol{r}, t) = \Psi^R_{\text{in},2}(\boldsymbol{r}, t) = \Psi^R_{\text{in},3}(\boldsymbol{r}, t) = \Psi^R_{\text{in},4}(\boldsymbol{r}, t) = 0$. We reserve the indices $\{1, 2, 3, 4\}$ for scattering processes with particles or quasi-particles scattering at the interface from the left.

We also need to find the wave functions of the conjugated process, $H^*(-\boldsymbol{k})\tilde{\Psi} = E\tilde{\Psi}$. From Eq. 3.60, we see that the only change in the Hamiltonian is $\Delta \to \Delta^*$. Since u_0, v_0, $q_x^\pm$ and E only depend on the superconducting gap through $|\Delta|^2$, we get exactly the same wave function as before,

$$\begin{aligned}\tilde{\Psi}_m(\boldsymbol{r}, t) = \tilde{\Psi}^R_{\text{in},m}(\boldsymbol{r}, t) &+ \tilde{c}_{m,1}[u_0 \;\; 0 \;\; 0 \;\; v_0]^T e^{iq_x^+ x + ik_y y + iEt} \\ &+ \tilde{c}_{m,2}[0 \;\; -u_0 \;\; v_0 \;\; 0]^T e^{iq_x^+ x + ik_y y + iEt} \\ &+ \tilde{d}_{m,1}[0 \;\; -v_0 \;\; u_0 \;\; 0]^T e^{-iq_x^- x + ik_y y + iEt} \\ &+ \tilde{d}_{m,2}[v_0 \;\; 0 \;\; 0 \;\; u_0]^T e^{-iq_x^- x + ik_y y + iEt}, \quad x > 0,\end{aligned} \tag{3.106}$$

where the incoming quasiparticles are

$$\begin{aligned}
\tilde{\Psi}^R_{\text{in},5}(\boldsymbol{r},t) &= [u_0 \;\; 0 \;\; 0 \;\; v_0]^T e^{-iq_x^+ x + ik_y y + iEt}, \\
\tilde{\Psi}^R_{\text{in},6}(\boldsymbol{r},t) &= [0 \;\; -u_0 \;\; v_0 \;\; 0]^T e^{-iq_x^+ x + ik_y y + iEt}, \\
\tilde{\Psi}^R_{\text{in},7}(\boldsymbol{r},t) &= [0 \;\; -v_0 \;\; u_0 \;\; 0]^T e^{iq_x^- x + ik_y y + iEt}, \\
\tilde{\Psi}^R_{\text{in},8}(\boldsymbol{r},t) &= [v_0 \;\; 0 \;\; 0 \;\; u_0]^T e^{iq_x^- x + ik_y y + iEt},
\end{aligned} \tag{3.107}$$

and $\tilde{\Psi}^R_{\text{in},1}(\boldsymbol{r},t) = \tilde{\Psi}^R_{\text{in},2}(\boldsymbol{r},t) = \tilde{\Psi}^R_{\text{in},3}(\boldsymbol{r},t) = \tilde{\Psi}^R_{\text{in},4}(\boldsymbol{r},t) = 0$.

3.2.2 *The heavy-metal scattering wave functions for $\hat{n} = \hat{x}$*

We now consider a 2D heavy-metal with a Rashba spin-orbit field along the x axis. From Eq. 3.60, we find that the Hamiltonian matrix is

$$H(\boldsymbol{k}) = \begin{pmatrix}
\frac{k^2}{\eta} - \mu - \lambda k_y & 0 & 0 & 0 \\
0 & \frac{k^2}{\eta} - \mu + \lambda k_y & 0 & 0 \\
0 & 0 & -\frac{k^2}{\eta} + \mu - \lambda k_y & 0 \\
0 & 0 & 0 & -\frac{k^2}{\eta} + \mu + \lambda k_y
\end{pmatrix}. \tag{3.108}$$

We thus have a diagonal Hamiltonian without spin-mixing of the energy bands. The eigenenergies are $E = \pm(k^2/\eta - \mu) \mp' \lambda k_y$, where $\pm$ correspond to electrons and holes respectively, while $\mp'$ correspond to spin up and spin down respectively. The eigenvectors are on the form

$$\Phi_{n,r(m,s)} = \left\{ \begin{pmatrix} 1 \\ 0 \\ 0 \\ 0 \end{pmatrix}, \begin{pmatrix} 0 \\ 1 \\ 0 \\ 0 \end{pmatrix}, \begin{pmatrix} 0 \\ 0 \\ 1 \\ 0 \end{pmatrix}, \begin{pmatrix} 0 \\ 0 \\ 0 \\ 1 \end{pmatrix} \right\}, \tag{3.109}$$

corresponding to spin-up electrons, spin-down electrons, spin-up holes and spin-down holes, respectively. The allowed k_x values corresponding to these eigenvectors are $\pm'' k_x^{e(h),\uparrow(\downarrow)} = \pm''\{-k_y^2 + \eta[\mu \pm (E \pm' \lambda k_y)]\}^{1/2}$. $k_x^{e(h),\uparrow(\downarrow)}$ are per definition positive, and $\pm''$ correspond to positive and negative k_x.

In Fig. 3.6 we have plotted the energy bands and indicated the allowed scattering processes. We rename the k_x values $k_{e1} = k_x^{e,\uparrow}$, $k_{e2} = k_x^{e,\downarrow}$, $k_{h1} = k_x^{h,\downarrow}$ and

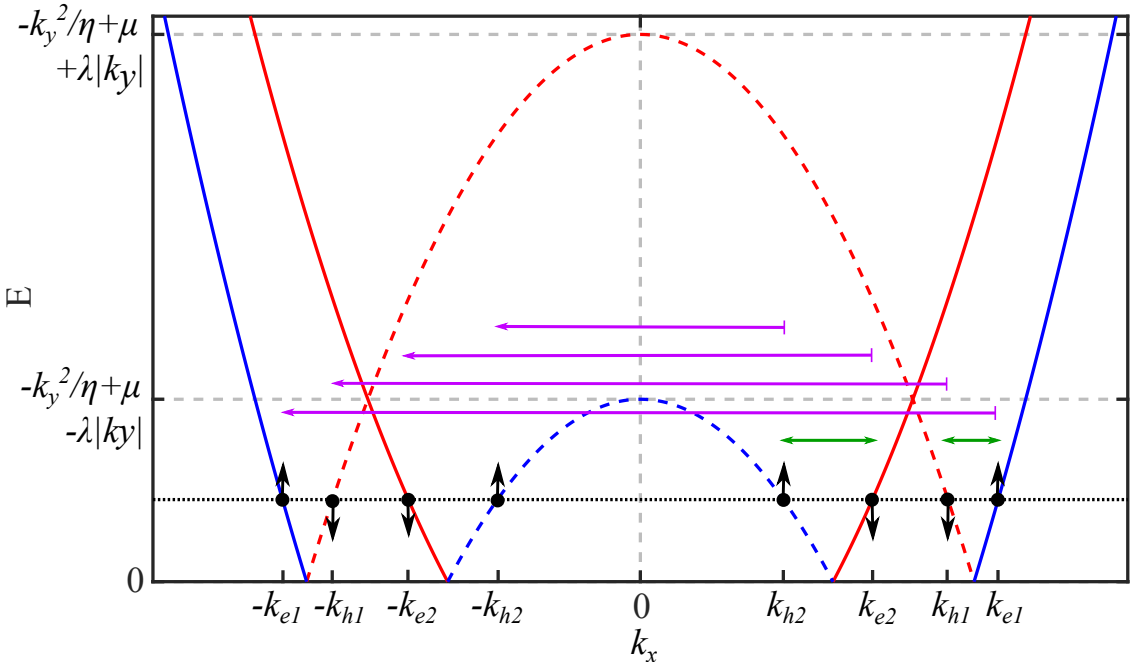

Figure 3.6: For a 2D heavy-metal with $\hat{n} = \hat{x}$, the energy bands are spin split by the Rashba spin-orbit coupling into a band for spin up electrons (blue solid line), spin down electrons (red solid line), spin up holes (blue dashed line) and spin down holes (red dashed line). The green arrows show the possible Andreev reflections, while the purple arrows show the possible normal reflections for electrons and holes at the energy marked by the black dotted line. We name the k_x values of the spin up electron, spin down hole, spin down electron and spin up hole k_{e1}, k_{h1}, k_{e2} and k_{h2}, respectively.

$k_{h2} = k_x^{h,\uparrow}$. The wave functions describing the allowed scattering processes are

$$\begin{aligned}\Psi_n(\boldsymbol{r},t) = \Psi^L_{\text{in},n}(\boldsymbol{r},t) &+ a_{n,1}[1\ \ 0\ \ 0\ \ 0]^T e^{-ik_{e1}x+ik_y y-iEt} \\ &+ a_{n,2}[0\ \ 1\ \ 0\ \ 0]^T e^{-ik_{e2}x+ik_y y-iEt} \\ &+ b_{n,1}[0\ \ 0\ \ 1\ \ 0]^T e^{ik_{h2}x+ik_y y-iEt} \\ &+ b_{n,2}[0\ \ 0\ \ 0\ \ 1]^T e^{ik_{h1}x+ik_y y-iEt},\ \ x<0,\end{aligned} \tag{3.110}$$

where the incoming spin-up electrons, spin-down electrons, spin-up holes and spin-down holes are described by

$$\begin{aligned}\Psi^L_{\text{in},1}(\boldsymbol{r},t) &= [1\ \ 0\ \ 0\ \ 0]^T e^{ik_{e1}x+ik_y y-iEt}, \\ \Psi^L_{\text{in},2}(\boldsymbol{r},t) &= [0\ \ 1\ \ 0\ \ 0]^T e^{ik_{e2}x+ik_y y-iEt}, \\ \Psi^L_{\text{in},3}(\boldsymbol{r},t) &= [0\ \ 0\ \ 1\ \ 0]^T e^{-ik_{h2}x+ik_y y-iEt}, \\ \Psi^L_{\text{in},4}(\boldsymbol{r},t) &= [0\ \ 0\ \ 0\ \ 1]^T e^{-ik_{h1}x+ik_y y-iEt},\end{aligned} \tag{3.111}$$

respectively. $\Psi^L_{\text{in},5}(\boldsymbol{r},t) = \Psi^L_{\text{in},6}(\boldsymbol{r},t) = \Psi^L_{\text{in},7}(\boldsymbol{r},t) = \Psi^L_{\text{in},8}(\boldsymbol{r},t) = 0$. The indices $\{5,6,7,8\}$ are reserved for particles incoming from the right.

If we consider the Hamiltonian of the conjugated process $H^*(-\boldsymbol{k})$ we see that the only change in the Hamiltonian in Eq. 3.108 is $\lambda \to -\lambda$. This corresponds to $k_{e1} \leftrightarrow k_{e2}$ and $k_{h1} \leftrightarrow k_{h2}$, or equivalently $[1\,0\,0\,0]^\dagger \leftrightarrow [0\,1\,0\,0]^\dagger$ and $[0\,0\,1\,0]^\dagger \leftrightarrow [0\,0\,0\,1]^\dagger$. The resulting scattering wave functions are

$$\begin{aligned}\tilde{\Psi}_m(\boldsymbol{r},t) = \Psi^L_{\text{in},m}(\boldsymbol{r},t) &+ \tilde{a}_{m,1}[0\ \ 1\ \ 0\ \ 0]^T e^{-ik_{e1}x+ik_y y+iEt} \\ &+ \tilde{a}_{m,2}[1\ \ 0\ \ 0\ \ 0]^T e^{-ik_{e2}x+ik_y y+iEt} \\ &+ \tilde{b}_{m,1}[0\ \ 0\ \ 0\ \ 1]^T e^{ik_{h2}x+ik_y y+iEt} \\ &+ \tilde{b}_{m,2}[0\ \ 0\ \ 1\ \ 0]^T e^{ik_{h1}x+ik_y y+iEt},\ \ x<0,\end{aligned} \tag{3.112}$$

where

$$\begin{aligned}\tilde{\Psi}^L_{\text{in},1}(\boldsymbol{r},t) &= [0\ \ 1\ \ 0\ \ 0]^T e^{ik_{e1}x+ik_y y+iEt}, \\ \tilde{\Psi}^L_{\text{in},2}(\boldsymbol{r},t) &= [1\ \ 0\ \ 0\ \ 0]^T e^{ik_{e2}x+ik_y y+iEt}, \\ \tilde{\Psi}^L_{\text{in},3}(\boldsymbol{r},t) &= [0\ \ 0\ \ 0\ \ 1]^T e^{-ik_{h2}x+ik_y y+iEt}, \\ \tilde{\Psi}^L_{\text{in},4}(\boldsymbol{r},t) &= [0\ \ 0\ \ 1\ \ 0]^T e^{-ik_{h1}x+ik_y y+iEt},\end{aligned} \tag{3.113}$$

and $\tilde{\Psi}^L_{\text{in},5}(\boldsymbol{r},t) = \tilde{\Psi}^L_{\text{in},6}(\boldsymbol{r},t) = \tilde{\Psi}^L_{\text{in},7}(\boldsymbol{r},t) = \tilde{\Psi}^L_{\text{in},8}(\boldsymbol{r},t) = 0$.

3.2.3 *The heavy-metal scattering wave functions for $\hat{n} = \hat{z}$*

For a 2D heavy-metal with a Rashba spin-orbit field along the z axis, the Hamiltonian matrix is

$$H(\boldsymbol{k}) = \begin{pmatrix} \frac{k^2}{\eta} - \mu & \lambda(k_y + ik_x) & 0 & 0 \\ \lambda(k_y - ik_x) & \frac{k^2}{\eta} - \mu & 0 & 0 \\ 0 & 0 & -\frac{k^2}{\eta} + \mu & \lambda(k_y - ik_x) \\ 0 & 0 & \lambda(k_y + ik_x) & -\frac{k^2}{\eta} + \mu \end{pmatrix} \tag{3.114}$$

according to Eq. 3.60. If we write $\boldsymbol{k}$ in polar coordinates, such that $k_x = k\cos(\phi)$ and $k_y = k\sin(\phi)$, we can write $\lambda(k_y \pm ik_x) = \pm i\lambda k e^{\mp i\phi}$. The above Hamiltonian is block diagonal, and we can solve the two blocks separately. By setting the determinant of each block equal to zero, we find expressions for the eigenenergies and allowed k-values. The allowed k values are $k^{e(h),+(-)} = [(\lambda\eta/2)^2 + \eta(\mu \pm E)]^{1/2} \pm \pm' \lambda\eta/2$, where $\pm$ correspond to electrons and holes respectively and $\pm'$ correspond to the two different spin-mixed states that we denote $+$ and $-$ respectively. The allowed k_x values are given by $\pm'' k_x^{e(h),+(-)} = \pm'' k^{e(h),+(-)}\cos(\phi)$. We define $k_x^{e(h),+(-)}$ to be positive by setting $\phi \in [-\pi/2, \pi/2]$. $\pm''$ correspond

to positive and negative momenta in the x direction. The eigenenergies are $E = \pm(k^2/\eta - \mu) \mp' \lambda k$. We can write the eigenvectors of the form

$$\Phi_{n,r(m,s)} = \left\{ \begin{pmatrix} 1 \\ ie^{i\phi} \\ 0 \\ 0 \end{pmatrix}, \begin{pmatrix} -1 \\ ie^{i\phi} \\ 0 \\ 0 \end{pmatrix}, \begin{pmatrix} 0 \\ 0 \\ 1 \\ ie^{-i\phi} \end{pmatrix}, \begin{pmatrix} 0 \\ 0 \\ -1 \\ ie^{-i\phi} \end{pmatrix} \right\}. \tag{3.115}$$

By solving the first equation in Eq. 3.59, we find that the first eigenvector corresponds to $k_x^{e,+}$, the second eigenvector correspond to $k_x^{e,-}$, the third eigenvector corresponds to $k_x^{h,-}$, and the forth eigenvector corresponds to $k_x^{h,+}$.

In Fig. 3.7 we have plotted the energy bands and indicated the allowed scattering processes. We rename the k_x values $k_{e1} = k_x^{e,+}$, $k_{e2} = k_x^{e,-}$, $k_{h1} = k_x^{h,-}$ and $k_{h2} = k_x^{h,+}$. The scattering wave functions on the heavy-metal side of the interface describing the allowed scattering processes are

$$\begin{aligned} \Psi_n(\boldsymbol{r},t) = \Psi^L_{\text{in},n}(\boldsymbol{r},t) &+ a_{n,1}[1 \;\; ie^{i\phi} \;\; 0 \;\; 0]^T e^{-ik_{e1}x+ik_y y-iEt} \\ &+ a_{n,2}[-1 \;\; ie^{i\phi} \;\; 0 \;\; 0]^T e^{-ik_{e2}x+ik_y y-iEt} \\ &+ b_{n,1}[0 \;\; 0 \;\; 1 \;\; ie^{-i\phi}]^T e^{ik_{h1}x+ik_y y-iEt} \\ &+ b_{n,2}[0 \;\; 0 \;\; -1 \;\; ie^{-i\phi}]^T e^{ik_{h2}x+ik_y y-iEt}, \;\; x<0, \end{aligned} \tag{3.116}$$

where

$$\begin{aligned} \Psi^L_{\text{in},1}(\boldsymbol{r},t) &= [1 \;\; ie^{i\phi} \;\; 0 \;\; 0]^T e^{ik_{e1}x+ik_y y-iEt}, \\ \Psi^L_{\text{in},2}(\boldsymbol{r},t) &= [-1 \;\; ie^{i\phi} \;\; 0 \;\; 0]^T e^{ik_{e2}x+ik_y y-iEt}, \\ \Psi^L_{\text{in},3}(\boldsymbol{r},t) &= [0 \;\; 0 \;\; 1 \;\; ie^{-i\phi}]^T e^{-ik_{h1}x+ik_y y-iEt}, \\ \Psi^L_{\text{in},4}(\boldsymbol{r},t) &= [0 \;\; 0 \;\; -1 \;\; ie^{-i\phi}]^T e^{-ik_{h2}x+ik_y y-iEt} \end{aligned} \tag{3.117}$$

are the four quasi-particle states scattering at the interface from the left. $\Psi^L_{\text{in},5}(\boldsymbol{r},t) = \Psi^L_{\text{in},6}(\boldsymbol{r},t) = \Psi^L_{\text{in},7}(\boldsymbol{r},t) = \Psi^L_{\text{in},8}(\boldsymbol{r},t) = 0$. Again, the indices $\{5,6,7,8\}$ are reserved for quasi-particles scattering at the interface from the right.

We now consider the second equation in Eq. 3.59, where the Hamiltonian is given by $H^*(-\boldsymbol{k})$. If we let $\boldsymbol{k} \to -\boldsymbol{k}$, then $\phi \to \phi + \pi$ and $e^{\pm i\phi} \to -e^{\pm i\phi}$. When we also apply the complex conjugate, we see that the only change in the Hamiltonian in Eq. 3.114 is $\phi \to -\phi$. The scattering wave functions of the conjugated process are therefore

$$\begin{aligned} \tilde{\Psi}_m(\boldsymbol{r},t) = \tilde{\Psi}^L_{\text{in},m}(\boldsymbol{r},t) &+ \tilde{a}_{m,1}[1 \;\; ie^{-i\phi} \;\; 0 \;\; 0]^T e^{-ik_{e1}x+ik_y y+iEt} \\ &+ \tilde{a}_{m,2}[-1 \;\; ie^{-i\phi} \;\; 0 \;\; 0]^T e^{-ik_{e2}x+ik_y y+iEt} \\ &+ \tilde{b}_{m,1}[0 \;\; 0 \;\; 1 \;\; ie^{i\phi}]^T e^{ik_{h1}x+ik_y y+iEt} \\ &+ \tilde{b}_{m,2}[0 \;\; 0 \;\; -1 \;\; ie^{i\phi}]^T e^{ik_{h2}x+ik_y y+iEt}, \;\; x<0, \end{aligned} \tag{3.118}$$

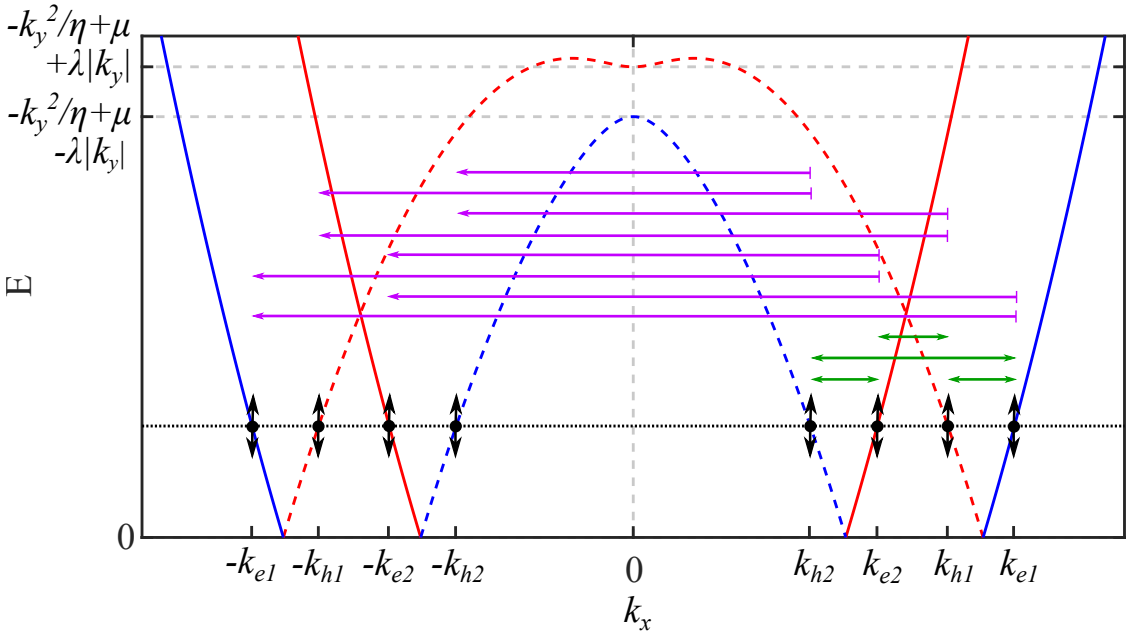

Figure 3.7: For a 2D heavy-metal with $\hat{n} = \hat{z}$, we have four spin degenerate energy bands. Two are electron bands (solid lines) and two are hole bands (dashed lines). The blue and red energy bands correspond to $\pm$ in $k^{e(h),+(-)}$ respectively. The green arrows show the possible Andreev reflections, while the purple arrows show the possible normal reflections for electrons and holes at the energy marked by the black dotted line. We name the k_x values of the + electron band, − hole band, − electron band and + hole band k_{e1}, k_{h1}, k_{e2} and k_{h2} respectively. This plot shows the energy bands for a specific choice of k_y, however the allowed reflections will be the same regardless of the choice of k_y.

where

$$\begin{aligned}
\tilde{\Psi}^L_{\text{in},1}(\boldsymbol{r},t) &= [1 \;\; ie^{-i\phi} \;\; 0 \;\; 0]^T e^{ik_{e1}x+ik_y y+iEt},\\
\tilde{\Psi}^L_{\text{in},2}(\boldsymbol{r},t) &= [-1 \;\; ie^{-i\phi} \;\; 0 \;\; 0]^T e^{ik_{e2}x+ik_y y+iEt},\\
\tilde{\Psi}^L_{\text{in},3}(\boldsymbol{r},t) &= [0 \;\; 0 \;\; 1 \;\; ie^{i\phi}]^T e^{-ik_{h1}x+ik_y y+iEt},\\
\tilde{\Psi}^L_{\text{in},4}(\boldsymbol{r},t) &= [0 \;\; 0 \;\; -1 \;\; ie^{i\phi}]^T e^{-ik_{h2}x+ik_y y+iEt},
\end{aligned} \tag{3.119}$$

and $\tilde{\Psi}^L_{\text{in},5}(\boldsymbol{r},t) = \tilde{\Psi}^L_{\text{in},6}(\boldsymbol{r},t) = \tilde{\Psi}^L_{\text{in},7}(\boldsymbol{r},t) = \tilde{\Psi}^L_{\text{in},8}(\boldsymbol{r},t) = 0$.

3.2.4 *The ferromagnetic scattering wave functions*

The Hamiltonian of a 2D ferromagnet with $\boldsymbol{h} = h\hat{z}$ is very similar to the Hamiltonian of the 2D heavy-metal with $\hat{n} = \hat{x}$. We therefore consider the 2D F/S

junction with magnetization along $\hat{z}$ for comparison. The Hamiltonian matrix of a 2D ferromagnet with $\boldsymbol{h} = h\hat{z}$ is

$$H(\boldsymbol{k}) = \begin{pmatrix} \frac{k^2}{\eta} - \mu + h & 0 & 0 & 0 \\ 0 & \frac{k^2}{\eta} - \mu - h & 0 & 0 \\ 0 & 0 & -\frac{k^2}{\eta} + \mu - h & 0 \\ 0 & 0 & 0 & -\frac{k^2}{\eta} + \mu + h \end{pmatrix}. \tag{3.120}$$

The eigenenergies are therefore $E = \pm(k^2/\eta - \mu \pm' h)$, where $\pm$ refers to electrons and holes respectively and $\pm'$ refers to spin up and spin down respectively. The allowed k_x values are $\pm'' k_x^{e(h),\uparrow(\downarrow)} = \pm''[-k_y^2 + \eta(\mu \pm (E \pm' \mp h))]^{1/2}$, which means that we can obtain the allowed k_x values of the ferromagnetic case from the allowed k_x values of the heavy-metal by letting $\lambda k_y \to \mp h$. The signs $\pm''$ refers to positive and negative k_x values.

We plot the energy bands and indicate the allowed reflection processes in Fig. 3.8. We rename the k_x values $k_{e1} = k_x^{e,\downarrow}$, $k_{e2} = k_x^{e,\uparrow}$, $k_{h1} = k_x^{h,\downarrow}$ and $k_{h2} = k_x^{h,\uparrow}$. Compared to the 2D heavy-metal, the spin of the electron energy bands are interchanged, so that $k_{e1} \leftrightarrow k_{e2}$. We thus obtain the scattering wave functions by interchanging k_{e1} and k_{e2} for the scattering wave functions of the 2D HM given in Eqs. 3.110 and 3.122. We get

$$\begin{aligned} \Psi_n(\boldsymbol{r},t) = \Psi^L_{\text{in},n}(\boldsymbol{r},t) &+ a_{n,1}[1\ 0\ 0\ 0]^T e^{-ik_{e2}x + ik_y y - iEt} \\ &+ a_{n,2}[0\ 1\ 0\ 0]^T e^{-ik_{e1}x + ik_y y - iEt} \\ &+ b_{n,1}[0\ 0\ 1\ 0]^T e^{ik_{h2}x + ik_y y - iEt} \\ &+ b_{n,2}[0\ 0\ 0\ 1]^T e^{ik_{h1}x + ik_y y - iEt}, \quad x < 0, \end{aligned} \tag{3.121}$$

where

$$\begin{aligned} \Psi^L_{\text{in},1}(\boldsymbol{r},t) &= [1\ 0\ 0\ 0]^T e^{ik_{e2}x + ik_y y - iEt}, \\ \Psi^L_{\text{in},2}(\boldsymbol{r},t) &= [0\ 1\ 0\ 0]^T e^{ik_{e1}x + ik_y y - iEt}, \\ \Psi^L_{\text{in},3}(\boldsymbol{r},t) &= [0\ 0\ 1\ 0]^T e^{-ik_{h2}x + ik_y y - iEt}, \\ \Psi^L_{\text{in},4}(\boldsymbol{r},t) &= [0\ 0\ 0\ 1]^T e^{-ik_{h1}x + ik_y y - iEt}, \end{aligned} \tag{3.122}$$

and $\Psi^L_{\text{in},5}(\boldsymbol{r},t) = \Psi^L_{\text{in},6}(\boldsymbol{r},t) = \Psi^L_{\text{in},7}(\boldsymbol{r},t) = \Psi^L_{\text{in},8}(\boldsymbol{r},t) = 0$. Again, the indices $\{5,6,7,8\}$ are reserved for quasi-particles scattering at the interface from the right.

The conjugated wave functions are obtained from solving the second equation given in Eq. 3.59. For the ferromagnetic case $H^*(-\boldsymbol{k}) = H(\boldsymbol{k})$. In contrast to

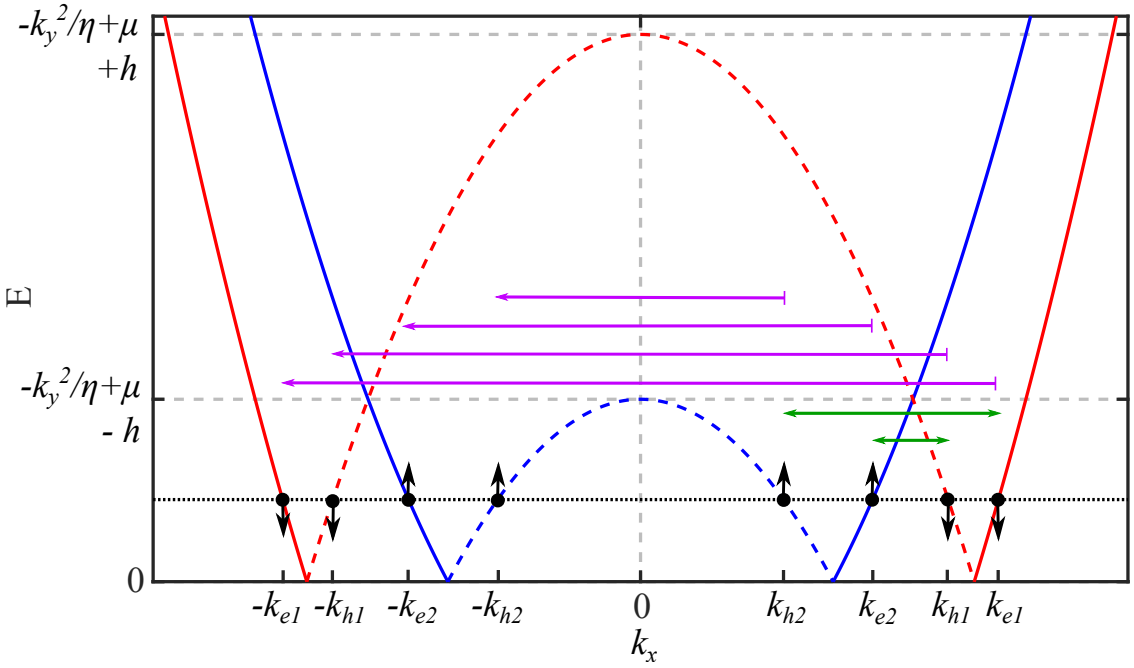

Figure 3.8: For a 2D ferromagnet with $\boldsymbol{h} = h\hat{z}$, the energy bands are spin split into bands for spin up electrons (blue solid line), spin down electrons (red solid line), spin up holes (blue dashed line) and spin down holes (red dashed line). The green arrows show the possible Andreev reflections, while the purple arrows show the possible normal reflections for electrons and holes at the energy marked by the black dotted line. We name the k_x values of the spin down electron, spin down hole, spin up electron and spin up hole k_{e1}, k_{h1}, k_{e2} and k_{h2}, respectively.

the case of the 2D heavy-metal with $\hat{n} = \hat{x}$, the spatial part of the scattering wave functions of the conjugated process do not differ from the scattering wave functions $\Psi_n(\boldsymbol{r}, t)$. Therefore,

$$\begin{aligned}\tilde{\Psi}_m(\boldsymbol{r}, t) = \tilde{\Psi}^L_{\text{in},m}(\boldsymbol{r}, t) &+ \tilde{a}_{m,1}[1\ \ 0\ \ 0\ \ 0]^T e^{-ik_{e2}x+ik_y y+iEt} \\ &+ \tilde{a}_{m,2}[0\ \ 1\ \ 0\ \ 0]^T e^{-ik_{e1}x+ik_y y+iEt} \\ &+ \tilde{b}_{m,1}[0\ \ 0\ \ 1\ \ 0]^T e^{ik_{h2}x+ik_y y+iEt} \\ &+ \tilde{b}_{m,2}[0\ \ 0\ \ 0\ \ 1]^T e^{ik_{h1}x+ik_y y+iEt}, \quad x < 0,\end{aligned} \tag{3.123}$$

where

$$\begin{aligned}\tilde{\Psi}^L_{\text{in},1}(\boldsymbol{r}, t) &= [1\ \ 0\ \ 0\ \ 0]^T e^{ik_{e2}x+ik_y y+iEt}, \\ \tilde{\Psi}^L_{\text{in},2}(\boldsymbol{r}, t) &= [0\ \ 1\ \ 0\ \ 0]^T e^{ik_{e1}x+ik_y y+iEt}, \\ \tilde{\Psi}^L_{\text{in},3}(\boldsymbol{r}, t) &= [0\ \ 0\ \ 1\ \ 0]^T e^{-ik_{h2}x+ik_y y+iEt}, \\ \tilde{\Psi}^L_{\text{in},4}(\boldsymbol{r}, t) &= [0\ \ 0\ \ 0\ \ 1]^T e^{-ik_{h1}x+ik_y y+iEt},\end{aligned} \tag{3.124}$$

and $\tilde{\Psi}^L_{\text{in},5}(\boldsymbol{r}, t) = \tilde{\Psi}^L_{\text{in},6}(\boldsymbol{r}, t) = \tilde{\Psi}^L_{\text{in},7}(\boldsymbol{r}, t) = \tilde{\Psi}^L_{\text{in},8}(\boldsymbol{r}, t) = 0$.

3.2.5 *The reflection and transmission coefficients*

In order to find expressions for the reflection and transmission coefficients, we must consider the boundary conditions of $\Psi_n(\boldsymbol{r},t)$ and $\tilde{\Psi}_m(\boldsymbol{r},t)$ at $x=0$. For $\Psi_n(\boldsymbol{r},t)$, the boundary conditions are [48]

$$\begin{aligned}[\Psi_n(\boldsymbol{r},t)]_{x=0^+} &= [\Psi_n(\boldsymbol{r},t)]_{x=0^-},\\ [\hat{v}\Psi_n(\boldsymbol{r},t)]_{x=0^+} &= [\hat{v}\Psi_n(\boldsymbol{r},t)]_{x=0^-}.\end{aligned} \tag{3.125}$$

$\hat{v} \equiv \partial H(k_x \rightarrow -i\partial_x, k_y)/\partial(-i\partial_x)$ is the velocity operator. $\tilde{\Psi}_m(\boldsymbol{r},t)$ satisfies a similar set of boundary conditions with $\hat{v} \equiv \partial H^*(-k_x \rightarrow i\partial_x, -k_y)/\partial(-i\partial_x)$. The first boundary condition simply states that the wave function must be continuous at the interface.

We now want to justify the second boundary condition. The Hamiltonian given in Eq. 3.60 can in general be written $H(k_x) = H_0 + H_1 k_x^2 + H_2 k_x$, where H_0, H_1, and H_2 are k_x independent 4×4 matrices. First, we let $k_x \rightarrow (-i\partial_x)$ and $\lambda\partial_x \rightarrow \{\lambda\theta(-x), \partial_x\}/2$ in the Hamiltonian. The anti-commutation $\{\lambda\theta(-x), \partial_x\}/2$ comes from the symmetrization of the Hamiltonian of a material with a finite component of the Rashba spin-orbit field parallel to the interface. The Hamiltonian becomes $H(x) = H_0 + H_1\partial_x^2 + H_2\{\theta(-x), \partial_x\}/2$. We then integrate the time-independent Schrödinger equation $H(x)\Psi_n(\boldsymbol{r},t) = E\Psi_n(\boldsymbol{r},t)$ from $x=0^-$ to $x=0^+$. For the terms proportional to $\Psi_n(\boldsymbol{r},t)$, we find that

$$\int_{0^-}^{0^+} dx\, [H_0 - E]\Psi_n(\boldsymbol{r},t) = 0, \tag{3.126}$$

due to the continuity of the wave function. For the second term in the Hamiltonian, we find that

$$\int_{0^-}^{0^+} dx\, H_1\partial_x^2\Psi_n(\boldsymbol{r},t) = H_1\{[\partial_x\Psi_n(\boldsymbol{r},t)]_{0^+} - [\partial_x\Psi_n(\boldsymbol{r},t)]_{0^-}\} \tag{3.127}$$

by partial integration. For the third term in the Hamiltonian, we find that

$$\begin{aligned}\int_{0^-}^{0^+} dx\, \frac{H_2}{2}\{\theta(-x), \partial_x\}\Psi_n(\boldsymbol{r},t) &= \frac{H_2}{2}\int_{0^-}^{0^+} dx\, [\theta(-x)\partial_x + \partial_x\theta(-x)]\Psi_n(\boldsymbol{r},t)\\ &= \frac{H_2}{2}\int_{0^-}^{0^+} dx\, [2\theta(-x)\partial_x - \delta(x)]\Psi_n(\boldsymbol{r},t)\end{aligned}$$

$$
\begin{aligned}
&= H_2\{[\theta(-x)\Psi_n(\boldsymbol{r},t)]_{0^+} - [\theta(-x)\Psi_n(\boldsymbol{r},t)]_{0^-}\} \\
&\quad + \frac{H_2}{2}\int_{0^-}^{0^+} dx\, \delta(x)\Psi_n(\boldsymbol{r},t) \\
&= H_2\{-[\Psi_n(\boldsymbol{r},t)]_{x=0^-} + \frac{1}{2}[\Psi_n(\boldsymbol{r},t)]_{x=0}\} \\
&= -\frac{H_2}{2}[\Psi_n(\boldsymbol{r},t)]_{x=0^-}
\end{aligned}
\tag{3.128}
$$

by partial integration. After integration from $x = 0^-$ to $x = 0^+$, the time-independent Schrödinger equation becomes

$$
H_1[\partial_x\Psi_n(\boldsymbol{r},t)]_{0^+} = H_1[\partial_x\Psi_n(\boldsymbol{r},t)]_{0^-} + \frac{H_2}{2}[\Psi_n(\boldsymbol{r},t)]_{x=0^-}. \tag{3.129}
$$

We now want to show that the above expression for the second boundary condition is equivalent to the second boundary condition in Eq. 3.125. If so, we have justified the second boundary condition. In order to show this, we apply the second boundary condition in Eq. 3.125 to $\Psi_n(\boldsymbol{r},t)$. The Hamiltonian in the velocity operator can be written $H(x) = H_0 + H_1\partial_x^2 + H_2\partial_x$. Note that we, in the definition of the velocity operator, do not let $\partial_x \to \{\theta(-x), \partial_x\}/2$. The velocity operator is then

$$
\hat{v} = i\frac{\partial}{\partial(\partial_x)}[H_0 + H_1\partial_x^2 + H_2\partial_x] = 2H_1\partial_x + H_2. \tag{3.130}
$$

H_2 is equal to zero in the superconducting region. The second boundary condition can therefore be written

$$
2iH_1[\partial_x\Psi_n(\boldsymbol{r},t)]_{0^+} = 2i\{H_1[\partial_x\Psi_n(\boldsymbol{r},t)]_{0^-} + \frac{H_2}{2}[\Psi_n(\boldsymbol{r},t)]_{x=0^-}\}. \tag{3.131}
$$

This is equivalent to Eq. 3.129. From this, we see that the symmetrization of the Rashba term enters the continuum BdG framework through the second boundary condition in Eq. 3.125.

To further justify the second boundary condition, we will also derive an expression for the probability current density along the x axis. The probability current density $\boldsymbol{j}$ can be found from the continuity equation [49, 50]

$$
\frac{\partial\rho}{\partial t} + \nabla\cdot\boldsymbol{j} = 0. \tag{3.132}
$$

For one-dimensional wave functions not defined as 4-vectors in Nambu ⊗ spin space, $\rho \equiv \psi^*(\boldsymbol{r},t)\psi(\boldsymbol{r},t)$. In Nambu ⊗ spin space, we define $\rho \equiv \psi^\dagger(\boldsymbol{r},t)\psi(\boldsymbol{r},t)$. As in the end of Sec. 3.1.2 and in Secs. 3.1.3 and 3.1.4, † is interpreted as a matrix transpose that do not affect operators contained within the matrix elements, and a complex conjugation of the matrix elements. By using the product rule and the time-dependent Schrödinger equation given by the first equation in Eq. 3.53, we find that

$$\begin{aligned}\frac{\partial\rho}{\partial t} &= [\partial t\Psi^\dagger(\boldsymbol{r},t)]\Psi(\boldsymbol{r},t) + \Psi^\dagger(\boldsymbol{r},t)[\partial t\Psi(\boldsymbol{r},t)] \\ &= i\{[\Psi^\dagger(\boldsymbol{r},t)H^\dagger(\boldsymbol{r})]\Psi(\boldsymbol{r},t) - \Psi^\dagger(\boldsymbol{r},t)[H(\boldsymbol{r})\Psi(\boldsymbol{r},t)]\}.\end{aligned} \tag{3.133}$$

Above, the Hamiltonian in the first term acts to the left. If we let $k_x \rightarrow -i\partial_x$ and $k_y \rightarrow -i\partial_y$ in the Hamiltonian given in Eq. 3.60, the Hamiltonian can be written

$$H(\boldsymbol{r}) = (\nabla^2/\eta - \mu)\hat{\tau}_3\hat{\sigma}_0 - i\lambda(\hat{n}\times\tilde{\boldsymbol{\sigma}})\cdot\nabla + h_x\hat{\tau}_3\hat{\sigma}_x + h_y\hat{\tau}_0\hat{\sigma}_y + h_z\hat{\tau}_3\hat{\sigma}_z, \tag{3.134}$$

where

$$\tilde{\boldsymbol{\sigma}} \equiv \begin{pmatrix}\boldsymbol{\sigma} & 0\\ 0 & \boldsymbol{\sigma}^*\end{pmatrix}. \tag{3.135}$$

Since † is a matrix transpose and a complex conjugation of the matrix elements, $H^\dagger(-i\nabla) = H(i\nabla)$. The only change in the Hamiltonian under hermitian conjugation is a sign change in the spin-orbit coupling term. It is easily seen that Eq. 3.133 is zero for terms in the above Hamiltonian that contains no spatial derivatives. For the kinetic term, we get

$$\begin{aligned}&i\{[\nabla^2\Psi^\dagger(\boldsymbol{r},t)]\hat{\tau}_3\hat{\sigma}_0\Psi(\boldsymbol{r},t) - \Psi^\dagger(\boldsymbol{r},t)\hat{\tau}_3\hat{\sigma}_0\nabla^2\Psi(\boldsymbol{r},t)\}/\eta \\ &= \nabla\cdot\{[i\nabla\Psi^\dagger(\boldsymbol{r},t)]\hat{\tau}_3\hat{\sigma}_0\Psi(\boldsymbol{r},t) - \Psi^\dagger(\boldsymbol{r},t)\hat{\tau}_3\hat{\sigma}_0 i\nabla\Psi(\boldsymbol{r},t)\}/\eta \\ &= \nabla\cdot\{-[\Psi^\dagger(\boldsymbol{r},t)\hat{\tau}_3\hat{\sigma}_0 i\nabla\Psi(\boldsymbol{r},t)]^\dagger - \Psi^\dagger(\boldsymbol{r},t)\hat{\tau}_3\hat{\sigma}_0 i\nabla\Psi(\boldsymbol{r},t)\}/\eta \\ &= \nabla\cdot\mathrm{Re}\{\Psi^\dagger(\boldsymbol{r},t)[-2i\nabla\hat{\tau}_3\hat{\sigma}_0/\eta]\Psi(\boldsymbol{r},t)\}.\end{aligned} \tag{3.136}$$

Above, we have used that $[f_1^\dagger f_2]^\dagger + f_1^\dagger f_2 = 2\mathrm{Re}\{f_1^\dagger f_2\}$ if the two complex vectors f_1 and f_2 satisfy $f_1^T f_2 = f_2^T f_1$. The contribution to Eq. 3.133 from the spin-orbit coupling term in the Hamiltonian is

$$\begin{aligned}&i\{i\lambda[\nabla\Psi^\dagger(\boldsymbol{r},t)]\cdot(\hat{n}\times\tilde{\boldsymbol{\sigma}})\Psi(\boldsymbol{r},t) + \Psi^\dagger(\boldsymbol{r},t)(\hat{n}\times\tilde{\boldsymbol{\sigma}})\cdot i\lambda\nabla\Psi(\boldsymbol{r},t)\} \\ &= -\nabla\cdot\Psi^\dagger(\boldsymbol{r},t)\lambda(\hat{n}\times\tilde{\boldsymbol{\sigma}})\Psi(\boldsymbol{r},t) \\ &= -\nabla\cdot\{[\Psi^\dagger(\boldsymbol{r},t)\lambda(\hat{n}\times\tilde{\boldsymbol{\sigma}})\Psi(\boldsymbol{r},t)]^\dagger + \Psi^\dagger(\boldsymbol{r},t)\lambda(\hat{n}\times\tilde{\boldsymbol{\sigma}})\Psi(\boldsymbol{r},t)\}/2 \\ &= \nabla\cdot\mathrm{Re}\{\Psi^\dagger(\boldsymbol{r},t)[-\lambda(\hat{n}\times\tilde{\boldsymbol{\sigma}})]\Psi(\boldsymbol{r},t)\}.\end{aligned} \tag{3.137}$$

By combining the kinetic term and the spin-orbit coupling term, we find from Eq. 3.133 that

$$\boldsymbol{j} = \mathrm{Re}\{\Psi^\dagger(\boldsymbol{r},t)[2i\nabla\hat{\tau}_3\hat{\sigma}_0/\eta + \lambda(\hat{n}\times\tilde{\boldsymbol{\sigma}})]\Psi(\boldsymbol{r},t)\}. \tag{3.138}$$

The probability current density along the x-axis is

$$\begin{aligned} j_x &= \mathrm{Re}\{\Psi^\dagger(\boldsymbol{r},t)[2i\partial_x\hat{\tau}_3\hat{\sigma}_0/\eta + \lambda(\hat{n}\times\tilde{\boldsymbol{\sigma}})\cdot\hat{x}]\Psi(\boldsymbol{r},t)\} \\ &= \mathrm{Re}\{\Psi^\dagger(\boldsymbol{r},t)\hat{v}\Psi(\boldsymbol{r},t)\}. \end{aligned} \tag{3.139}$$

To have conservation of the probability current density at $x = 0$, $\hat{v}\Psi(\boldsymbol{r},t)$ must be continuous at the interface, in accordance with the second boundary condition. This also motivates naming $\hat{v}$ the velocity operator, since $\hat{v}\Psi(\boldsymbol{r},t)$ determines the current.

If the spin-orbit coupling part of the Hamiltonian is independent of k_x, H_2 is equal to zero in Eq. 3.129. The second boundary condition in Eq. 3.125 then simplifies to

$$[\partial_x\Psi_n(\boldsymbol{r},t)]_{x=0^+} = [\partial_x\Psi_n(\boldsymbol{r},t)]_{x=0^-}. \tag{3.140}$$

This is the case for the HM/S system with $\hat{n} = \hat{x}$ and for the F/S system with $\boldsymbol{h} = h\hat{z}$. The second boundary condition simplifies in the same way for $\tilde{\Psi}_m(\boldsymbol{r},t)$.

Expressions for the reflection and transmission coefficients can in some simple cases be found analytically by solving the boundary conditions in Eq. 3.125 using software such as Maple. This will be done for the 2D HM/S system with $\hat{n} = \hat{x}$ and for the 2D F/S system with $\boldsymbol{h} = h\hat{z}$ in the following sections. For the 2D HM/S system with $\hat{n} = \hat{z}$, the expressions for the reflection and transmission coefficients are more lengthy, and it is also more difficult to solve the boundary conditions of the Green's function in Eqs. 3.66 and 3.72 analytically due to the spin-mixing of the energy bands. For this system, we will therefore solve the boundary conditions in Eqs. 3.66, 3.72 and 3.125 numerically.

3.3 THE SINGLET AND TRIPLET RETARDED GREEN'S FUNCTIONS

We will now calculate the even- and odd-frequency singlet and triplet retarded anomalous Green's functions on both sides of the interface for a 2D HM/S system with $\hat{n} = \hat{x}$, a 2D HM/S system with $\hat{n} = \hat{z}$, and a 2D F/S system with $\boldsymbol{h} = h\hat{z}$. In order to evaluate which of the s-, p- and d-wave singlet and triplet amplitudes are

nonzero, we will consider the symmetry of the singlet and triplet amplitudes under inversion of x and p_y. We will use the wave functions presented in Secs. 3.2.1-3.2.4 relevant to each system. The reflection and transmission coefficients of the wave functions will be calculated by the method outlined in Sec. 3.2.5. The retarded Green's function will be constructed according to Eq. 3.61, and the even- and odd-frequency singlet and triplet retarded anomalous Green's functions will be calculated using Eqs. 3.97, 3.98, 3.3 and 3.4.

3.3.1 *The heavy-metal/superconductor system with $\hat{n} = \hat{x}$*

Consider the case of a 2D HM/S system with the spin-orbit field along the x axis. Using the method outlined above, we find that on the heavy-metal side of the interface, where $x_1, x_2 < 0$, the anomalous elements of the retarded Green's function are

$$\begin{aligned}
f^r_{\uparrow,\downarrow}(x_1, x_2, y_1, y_2; t_1, t_2) =& \frac{\eta}{i}\frac{u_0 v_0 (q_x^+ + q_x^-)}{D_1}\theta(t_1 - t_2) \\
&\cdot e^{-k_{e1}x_1 + ik_{h1}x_2} e^{ik_y(y_1 - y_2) - iE(t_1 - t_2)}, \\
f^r_{\downarrow,\uparrow}(x_1, x_2, y_1, y_2; t_1, t_2) =& -\frac{\eta}{i}\frac{u_0 v_0 (q_x^+ + q_x^-)}{D_2}\theta(t_1 - t_2) \\
&\cdot e^{-k_{e2}x_1 + ik_{h2}x_2} e^{ik_y(y_1 - y_2) - iE(t_1 - t_2)}, \\
f^r_{\uparrow,\uparrow}(x_1, x_2, y_1, y_2; t_1, t_2) =& 0, \\
f^r_{\downarrow,\downarrow}(x_1, x_2, y_1, y_2; t_1, t_2) =& 0,
\end{aligned} \tag{3.141}$$

where

$$D_{1(2)} \equiv u_0^2(k_{e1(2)} + q_x^+)(k_{h1(2)} + q_x^-) + v_0^2(k_{h1(2)} - q_x^+)(-k_{e1(2)} + q_x^-). \tag{3.142}$$

There are no equal-spin triplet amplitudes inside the heavy-metal. We rewrite the above expression to the relative y coordinate $y \equiv y_1 - y_2$ and the relative time coordinate $t \equiv t_1 - t_2$. In the relative time coordinate,

$$f_{\alpha,\beta}(x_1, x_2, y; t) \propto \theta(t) e^{-iEt}. \tag{3.143}$$

If we insert the integral representation [46] of the Heaviside step function given in Eq. 0.4, we get

$$\begin{aligned}
f_{\alpha,\beta}(x_1, x_2, y; t) &\propto -\frac{1}{2\pi i}\int_{-\infty}^{\infty} d\tilde{\omega}\, \frac{1}{\tilde{\omega} + i\delta^+} e^{-i(\tilde{\omega} + E)t} \\
&= -\frac{1}{2\pi i}\int_{-\infty}^{\infty} d\omega\, \frac{1}{\omega - E + i\delta^+} e^{-i\omega t},
\end{aligned} \tag{3.144}$$

where $\delta^+ \to 0^+$. Using that the inverse Fourier transform in relative time is

$$f_{\alpha,\beta}(x_1, x_2, y; t) = \frac{1}{2\pi}\int_{-\infty}^{\infty} d\omega\, f_{\alpha,\beta}(x_1, x_2, y; \omega)e^{-i\omega t}, \tag{3.145}$$

we find that Eq. 3.143 corresponds to

$$f_{\alpha,\beta}(x_1, x_2, y; \omega) \propto \frac{i}{\omega - E + i\delta^+}. \tag{3.146}$$

We use the above relation and apply the Fourier transforms in y given in Eq. 3.38. From Eq. 3.98, we find that the singlet and opposite-spin triplet retarded anomalous Green's functions in the heavy-metal region are given by

$$\begin{aligned} f_0^r(x_1, x_2, p_y; \omega) =& \frac{\eta}{2} u_0 v_0 (q_x^+ + q_x^-)\delta(p_y - k_y)\frac{1}{\omega - E + i\delta^+} \\ &\cdot \left[\frac{1}{D_1}e^{-ik_{e1}x_1 + ik_{h1}x_2} + \frac{1}{D_2}e^{-ik_{e2}x_1 + ik_{h2}x_2}\right], \\ f_3^r(x_1, x_2, p_y; \omega) =& \frac{\eta}{2} u_0 v_0 (q_x^+ + q_x^-)\delta(p_y - k_y)\frac{1}{\omega - E + i\delta^+} \\ &\cdot \left[\frac{1}{D_1}e^{-ik_{e1}x_1 + ik_{h1}x_2} - \frac{1}{D_2}e^{-ik_{e2}x_1 + ik_{h2}x_2}\right]. \end{aligned} \tag{3.147}$$

By inserting the above expression into Eq. 3.97, we find that the nonzero even- and odd-frequency singlet and triplet retarded anomalous Green's functions inside the heavy-metal region are

$$\begin{aligned} f_0^{r,E(O)}(x_1, x_2, p_y; \omega) =& \frac{\eta}{4} u_0 v_0 (q_x^+ + q_x^-)\frac{1}{\omega - E + i\delta^+} \\ &\cdot \left[\left(\frac{1}{D_1}e^{-ik_{e1}x_1 + ik_{h1}x_2} + \frac{1}{D_2}e^{-ik_{e2}x_1 + ik_{h2}x_2}\right)\delta(p_y - k_y)\right. \\ &\left. \pm \left(\frac{1}{D_1}e^{-ik_{e1}x_2 + ik_{h1}x_1} + \frac{1}{D_2}e^{-ik_{e2}x_2 + ik_{h2}x_1}\right)\delta(-p_y - k_y)\right], \\ f_3^{r,E(O)}(x_1, x_2, p_y; \omega) =& \frac{\eta}{4} u_0 v_0 (q_x^+ + q_x^-)\frac{1}{\omega - E + i\delta^+} \\ &\cdot \left[\left(\frac{1}{D_1}e^{-ik_{e1}x_1 + ik_{h1}x_2} - \frac{1}{D_2}e^{-ik_{e2}x_1 + ik_{h2}x_2}\right)\delta(p_y - k_y)\right. \\ &\left. \mp \left(\frac{1}{D_1}e^{-ik_{e1}x_2 + ik_{h1}x_1} - \frac{1}{D_2}e^{-ik_{e2}x_2 + ik_{h2}x_1}\right)\delta(-p_y - k_y)\right]. \end{aligned} \tag{3.148}$$

The only variables in Eq. 3.148 that are not invariant under $k_y \to -k_y$ are

$$\begin{aligned} k_x^{e,\uparrow(\downarrow)} &= \{-k_y^2 + \eta[\mu + (E \pm \lambda k_y)]\}^{1/2} \to \{-k_y^2 + \eta[\mu + (E \mp \lambda k_y)]\}^{1/2}, \\ k_x^{h,\uparrow(\downarrow)} &= \{-k_y^2 + \eta[\mu - (E \pm \lambda k_y)]\}^{1/2} \to \{-k_y^2 + \eta[\mu - (E \mp \lambda k_y)]\}^{1/2}. \end{aligned} \tag{3.149}$$

The effect of changing the sign of k_y is therefore to interchange the k_x values of spin up and spin down particles. Therefore, if $k_y \to -k_y$, then $k_{e1} \leftrightarrow k_{e2}$, $k_{h1} \leftrightarrow k_{h2}$, and $D_1 \leftrightarrow D_2$. We can therefore rewrite Eq. 3.148 as

$$\begin{aligned} f_0^{r,E(O)}(x_1,x_2,p_y;\omega) =& \frac{\eta}{4}u_0v_0(q_x^+ + q_x^-)\delta(p_y-k_y)\frac{1}{\omega - E + i\delta^+} \\ & \cdot\left[\left(\frac{1}{D_1}e^{-ik_{e1}x_1+ik_{h1}x_2} + \frac{1}{D_2}e^{-ik_{e2}x_1+ik_{h2}x_2}\right)\right. \\ & \left.\pm\left(\frac{1}{D_2}e^{-ik_{e2}x_2+ik_{h2}x_1} + \frac{1}{D_1}e^{-ik_{e1}x_2+ik_{h1}x_1}\right)\right], \\ f_3^{r,E(O)}(x_1,x_2,p_y;\omega) =& \frac{\eta}{4}u_0v_0(q_x^+ + q_x^-)\delta(p_y-k_y)\frac{1}{\omega - E + i\delta^+} \\ & \cdot\left[\left(\frac{1}{D_1}e^{-ik_{e1}x_1+ik_{h1}x_2} - \frac{1}{D_2}e^{-ik_{e2}x_1+ik_{h2}x_2}\right)\right. \\ & \left.\mp\left(\frac{1}{D_2}e^{-ik_{e2}x_2+ik_{h2}x_1} - \frac{1}{D_1}e^{-ik_{e1}x_2+ik_{h1}x_1}\right)\right]. \end{aligned} \tag{3.150}$$

If we rewrite this to a center of mass coordinate $X \equiv (x_1 + x_2)/2$ and a relative coordinate $x \equiv x_1 - x_2$, we get

$$\begin{aligned} f_0^{r,E(O)}(X,x,p_y;\omega) =& \frac{\eta}{4}u_0v_0(q_x^+ + q_x^-)\delta(p_y-k_y)\frac{1}{\omega - E + i\delta^+} \\ & \cdot\left[\frac{1}{D_1}e^{-i(k_{e1}-k_{h1})X}\left(e^{-i(k_{e1}+k_{h1})x/2} \pm e^{i(k_{e1}+k_{h1})x/2}\right)\right. \\ & \left.+\frac{1}{D_2}e^{-i(k_{e2}-k_{h2})X}\left(e^{-i(k_{e2}+k_{h2})x/2} \pm e^{i(k_{e2}+k_{h2})x/2}\right)\right], \\ f_3^{r,E(O)}(X,x,p_y;\omega) =& \frac{\eta}{4}u_0v_0(q_x^+ + q_x^-)\delta(p_y-k_y)\frac{1}{\omega - E + i\delta^+} \\ & \cdot\left[\frac{1}{D_1}e^{-i(k_{e1}-k_{h1})X}\left(e^{-i(k_{e1}+k_{h1})x/2} \pm e^{i(k_{e1}+k_{h1})x/2}\right)\right. \\ & \left.-\frac{1}{D_2}e^{-i(k_{e2}-k_{h2})X}\left(e^{-i(k_{e2}+k_{h2})x/2} \pm e^{i(k_{e2}+k_{h2})x/2}\right)\right]. \end{aligned} \tag{3.151}$$

The nonzero singlet and triplet odd- and even-frequency retarded anomalous Green's functions in the heavy-metal region can therefore be written

$$
\begin{aligned}
f_0^{r,E}(X,x,p_y;\omega) =& \frac{\eta}{2}u_0v_0(q_x^+ + q_x^-)\delta(p_y-k_y)\frac{1}{\omega - E + i\delta^+} \\
&\cdot\left[\frac{1}{D_1}e^{-i(k_{e1}-k_{h1})X}\cos((k_{e1}+k_{h1})x/2)\right. \\
&\left.+\frac{1}{D_2}e^{-i(k_{e2}-k_{h2})X}\cos((k_{e2}+k_{h2})x/2)\right], \\
f_0^{r,O}(X,x,p_y;\omega) =& \frac{\eta}{2i}u_0v_0(q_x^+ + q_x^-)\delta(p_y-k_y)\frac{1}{\omega - E + i\delta^+} \\
&\cdot\left[\frac{1}{D_1}e^{-i(k_{e1}-k_{h1})X}\sin((k_{e1}+k_{h1})x/2)\right. \\
&\left.+\frac{1}{D_2}e^{-i(k_{e2}-k_{h2})X}\sin((k_{e2}+k_{h2})x/2)\right], \\
f_3^{r,E}(X,x,p_y;\omega) =& \frac{\eta}{2}u_0v_0(q_x^+ + q_x^-)\delta(p_y-k_y)\frac{1}{\omega - E + i\delta^+} \\
&\cdot\left[\frac{1}{D_1}e^{-i(k_{e1}-k_{h1})X}\cos((k_{e1}+k_{h1})x/2)\right. \\
&\left.-\frac{1}{D_2}e^{-i(k_{e2}-k_{h2})X}\cos((k_{e2}+k_{h2})x/2)\right], \\
f_3^{r,O}(X,x,p_y;\omega) =& \frac{\eta}{2i}u_0v_0(q_x^+ + q_x^-)\delta(p_y-k_y)\frac{1}{\omega - E + i\delta^+} \\
&\cdot\left[\frac{1}{D_1}e^{-i(k_{e1}-k_{h1})X}\sin((k_{e1}+k_{h1})x/2)\right. \\
&\left.-\frac{1}{D_2}e^{-i(k_{e2}-k_{h2})X}\sin((k_{e2}+k_{h2})x/2)\right].
\end{aligned}
\tag{3.152}
$$

On the superconducting side of the interface, where $x_1, x_2 > 0$, we find that the anomalous elements of the retarded Green's function are

$$
\begin{aligned}
f^r_{\uparrow,\downarrow}(x_1,x_2,y_1,y_2;t_1,t_2) =& -\frac{\eta}{i}\frac{u_0v_0}{u_0^2-v_0^2}\theta(t_1-t_2)e^{ik_y(y_1-y_2)}e^{-iE(t_1-t_2)} \\
&\cdot\left\{\frac{1}{D_1}\left(k_{e1}+k_{h1}\right)\left(u_0^2e^{iq_x^+x_1-iq_x^-x_2}+v_0^2e^{iq_x^+x_2-iq_x^-x_1}\right)\right. \\
&-\frac{1}{2}\left[\left(\frac{1}{q_x^+}e^{iq_x^+(x_1-x_2)}+\frac{1}{q_x^-}e^{-iq_x^-(x_1-x_2)}\right)\theta(x_1-x_2)\right. \\
&\left.+\left(\frac{1}{q_x^+}e^{-iq_x^+(x_1-x_2)}+\frac{1}{q_x^-}e^{iq_x^-(x_1-x_2)}\right)\theta(x_2-x_1)\right] \\
&\left.-\frac{E_1}{2D_1}\frac{1}{q_x^+}e^{iq_x^+(x_1+x_2)}-\frac{F_1}{2D_1}\frac{1}{q_x^-}e^{-iq_x^-(x_1+x_2)}\right\},
\end{aligned}
$$

$$
\begin{aligned}
f^r_{\downarrow,\uparrow}(x_1,x_2,y_1,y_2;t_1,t_2) =& \frac{\eta}{i}\frac{u_0v_0}{u_0^2-v_0^2}\theta(t_1-t_2)e^{ik_y(y_1-y_2)}e^{-iE(t_1-t_2)} \\
&\cdot\Bigg\{\frac{1}{D_2}\left(k_{e2}+k_{h2}\right)\left(u_0^2e^{iq_x^+x_1-iq_x^-x_2}+v_0^2e^{iq_x^+x_2-iq_x^-x_1}\right) \\
&-\frac{1}{2}\Bigg[\left(\frac{1}{q_x^+}e^{iq_x^+(x_1-x_2)}+\frac{1}{q_x^-}e^{-iq_x^-(x_1-x_2)}\right)\theta(x_1-x_2) \\
&+\left(\frac{1}{q_x^+}e^{-iq_x^+(x_1-x_2)}+\frac{1}{q_x^-}e^{iq_x^-(x_1-x_2)}\right)\theta(x_2-x_1)\Bigg] \\
&-\frac{E_2}{2D_2}\frac{1}{q_x^+}e^{iq_x^+(x_1+x_2)}-\frac{F_2}{2D_2}\frac{1}{q_x^-}e^{-iq_x^-(x_1+x_2)}\Bigg\}, \\
f^r_{\uparrow,\uparrow}(x_1,x_2,y_1,y_2;t_1,t_2) =& 0, \\
f^r_{\downarrow,\downarrow}(x_1,x_2,y_1,y_2;t_1,t_2) =& 0.
\end{aligned}
\tag{3.153}
$$

$D_{1(2)}$ are defined in the same way as inside the heavy-metal, while

$$
\begin{aligned}
E_{1(2)} &\equiv u_0^2(-k_{e1(2)}+q_x^+)(\ \ k_{h1(2)}+q_x^-)+v_0^2(-k_{h1(2)}-q_x^+)(-k_{e1(2)}+q_x^-), \\
F_{1(2)} &\equiv u_0^2(\ \ k_{e1(2)}+q_x^+)(-k_{h1(2)}+q_x^-)+v_0^2(\ \ k_{h1(2)}-q_x^+)(\ \ k_{e1(2)}+q_x^-).
\end{aligned}
\tag{3.154}
$$

From the above equation, we see that there are no equal-spin triplet amplitudes inside the superconductor. There are thus no equal-spin triplets in the system. We rewrite the above expression to the relative coordinates y and t, and apply the Fourier transform in y given in Eq. 3.38. The dependence of the retarded Green's functions upon ω takes the same form as for the heavy-metal region. From Eq. 3.98, we find that the singlet and opposite-spin triplet retarded anomalous Green's functions inside the superconducting region are given by

$$
\begin{aligned}
f^r_0(x_1,x_2,p_y;\omega) =& -\frac{\eta}{2}\frac{u_0v_0}{u_0^2-v_0^2}\delta(p_y-k_y)\frac{1}{\omega-E+i\delta^+} \\
&\cdot\left\{\left[\frac{1}{D_1}(k_{e1}+k_{h1})+\frac{1}{D_2}(k_{e2}+k_{h2})\right]\right. \\
&\cdot\left(u_0^2e^{iq_x^+x_1-iq_x^-x_2}+v_0^2e^{iq_x^+x_2-iq_x^-x_1}\right) \\
&-\left(\frac{1}{q_x^+}e^{iq_x^+|x_1-x_2|}+\frac{1}{q_x^-}e^{-iq_x^-|x_1-x_2|}\right) \\
&\left.-\frac{1}{2}\left(\frac{E_1}{D_1}+\frac{E_2}{D_2}\right)\frac{1}{q_x^+}e^{iq_x^+(x_1+x_2)}-\frac{1}{2}\left(\frac{F_1}{D_1}+\frac{F_2}{D_2}\right)\frac{1}{q_x^-}e^{-iq_x^-(x_1+x_2)}\right\},
\end{aligned}
$$

$$
\begin{aligned}
f_3^r(x_1,x_2,p_y;\omega) = &-\frac{\eta}{2}\frac{u_0v_0}{u_0^2-v_0^2}\delta(p_y-k_y)\frac{1}{\omega-E+i\delta^+}\\
&\cdot\left\{\left[\frac{1}{D_1}(k_{e1}+k_{h1})-\frac{1}{D_2}(k_{e2}+k_{h2})\right]\right.\\
&\cdot\left(u_0^2e^{iq_x^+x_1-iq_x^-x_2}+v_0^2e^{+iq_x^+x_2-iq_x^-x_1}\right)\\
&\left.-\frac{1}{2}\left(\frac{E_1}{D_1}-\frac{E_2}{D_2}\right)\frac{1}{q_x^+}e^{iq_x^+(x_1+x_2)}-\frac{1}{2}\left(\frac{F_1}{D_1}-\frac{F_2}{D_2}\right)\frac{1}{q_x^-}e^{-iq_x^-(x_1+x_2)}\right\}.
\end{aligned}
\tag{3.155}
$$

Just as for the heavy-metal region, we insert this into Eq. 3.97 and use that when $k_y \to -k_y$, then $k_{e1} \leftrightarrow k_{e2}$, $k_{h1} \leftrightarrow k_{h2}$, $D_1 \leftrightarrow D_2$, $E_1 \leftrightarrow E_2$, and $F_1 \leftrightarrow F_2$. We get

$$
\begin{aligned}
f_0^{r,E(O)}(x_1,x_2,p_y;\omega) = &-\frac{\eta}{4}\frac{u_0v_0}{u_0^2-v_0^2}\delta(p_y-k_y)\frac{1}{\omega-E+i\delta^+}\\
&\cdot\left\{\left[\frac{1}{D_1}(k_{e1}+k_{h1})+\frac{1}{D_2}(k_{e2}+k_{h2})\right]\right.\\
&\cdot\left[u_0^2\left(e^{iq_x^+x_1-iq_x^-x_2}\pm e^{iq_x^+x_2-iq_x^-x_1}\right)\right.\\
&\left.+v_0^2\left(e^{iq_x^+x_2-iq_x^-x_1}\pm e^{iq_x^+x_1-iq_x^-x_2}\right)\right]\\
&-\frac{1}{2}(1\pm1)\left[2\left(\frac{1}{q_x^+}e^{iq_x^+|x_1-x_2|}+\frac{1}{q_x^-}e^{-iq_x^-|x_1-x_2|}\right)\right.\\
&\left.\left.+\left(\frac{E_1}{D_1}+\frac{E_2}{D_2}\right)\frac{1}{q_x^+}e^{iq_x^+(x_1+x_2)}+\left(\frac{F_1}{D_1}+\frac{F_2}{D_2}\right)\frac{1}{q_x^-}e^{-iq_x^-(x_1+x_2)}\right]\right\},\\
f_3^{r,E(O)}(x_1,x_2,p_y;\omega) = &-\frac{\eta}{4}\frac{u_0v_0}{u_0^2-v_0^2}\delta(p_y-k_y)\frac{1}{\omega-E+i\delta^+}\\
&\cdot\left\{\left[\frac{1}{D_1}(k_{e1}+k_{h1})-\frac{1}{D_2}(k_{e2}+k_{h2})\right]\right.\\
&\cdot\left[u_0^2\left(e^{iq_x^+x_1-iq_x^-x_2}\pm e^{iq_x^+x_2-iq_x^-x_1}\right)\right.\\
&\left.+v_0^2\left(e^{iq_x^+x_2-iq_x^-x_1}\pm e^{iq_x^+x_1-iq_x^-x_2}\right)\right]-\frac{1}{2}(1\pm1)\\
&\left.\cdot\left[\left(\frac{E_1}{D_1}-\frac{E_2}{D_2}\right)\frac{1}{q_x^+}e^{iq_x^+(x_1+x_2)}+\left(\frac{F_1}{D_1}-\frac{F_2}{D_2}\right)\frac{1}{q_x^-}e^{-iq_x^-(x_1+x_2)}\right]\right\}.
\end{aligned}
\tag{3.156}
$$

In the center of mass and relative x coordinates, the above expressions can be written

$$
\begin{aligned}
f_0^{r,E(O)}(X,x,p_y;\omega) = &-\frac{\eta}{4}\frac{u_0v_0}{u_0^2-v_0^2}\delta(p_y-k_y)\frac{1}{\omega-E+i\delta^+}\\
&\cdot\left\{\left[\frac{1}{D_1}(k_{e1}+k_{h1})+\frac{1}{D_2}(k_{e2}+k_{h2})\right]e^{i(q_x^+-q_x^-)X}\right.\\
&\cdot\left[u_0^2\left(e^{i(q_x^++q_x^-)x/2}\pm e^{-i(q_x^++q_x^-)x/2}\right)\right.\\
&\left.+v_0^2\left(e^{-i(q_x^++q_x^-)x/2}\pm e^{i(q_x^++q_x^-)x/2}\right)\right]\\
&-\frac{1}{2}(1\pm1)\left[2\left(\frac{1}{q_x^+}e^{iq_x^+|x|}+\frac{1}{q_x^-}e^{-iq_x^-|x|}\right)\right.\\
&\left.\left.+\left(\frac{E_1}{D_1}+\frac{E_2}{D_2}\right)\frac{1}{q_x^+}e^{2iq_x^+X}+\left(\frac{F_1}{D_1}+\frac{F_2}{D_2}\right)\frac{1}{q_x^-}e^{-2iq_x^-X}\right]\right\},\\
f_3^{r,E(O)}(X,x,p_y;\omega) = &-\frac{\eta}{4}\frac{u_0v_0}{u_0^2-v_0^2}\delta(p_y-k_y)\frac{1}{\omega-E+i\delta^+}\\
&\cdot\left\{\left[\frac{1}{D_1}(k_{e1}+k_{h1})-\frac{1}{D_2}(k_{e2}+k_{h2})\right]e^{i(q_x^+-q_x^-)X}\right.\\
&\cdot\left[u_0^2\left(e^{i(q_x^++q_x^-)x/2}\pm e^{-i(q_x^++q_x^-)x/2}\right)\right.\\
&\left.+v_0^2\left(e^{-i(q_x^++q_x^-)x/2}\pm e^{i(q_x^++q_x^-)x/2}\right)\right]-\frac{1}{2}(1\pm1)\\
&\left.\cdot\left[\left(\frac{E_1}{D_1}-\frac{E_2}{D_2}\right)\frac{1}{q_x^+}e^{2iq_x^+X}+\left(\frac{F_1}{D_1}-\frac{F_2}{D_2}\right)\frac{1}{q_x^-}e^{-2iq_x^-X}\right]\right\}.
\end{aligned}
\tag{3.157}
$$

The nonzero singlet and triplet retarded anomalous Green's functions in the superconducting region are thus

$$
\begin{aligned}
f_0^{r,E}(X,x,p_y;\omega) = &-\frac{\eta}{2}\frac{u_0v_0}{u_0^2-v_0^2}\delta(p_y-k_y)\frac{1}{\omega-E+i\delta^+}\\
&\cdot\left\{\left[\frac{1}{D_1}(k_{e1}+k_{h1})+\frac{1}{D_2}(k_{e2}+k_{h2})\right]\right.\\
&\cdot e^{i(q_x^+-q_x^-)X}\cos((q_x^++q_x^-)x/2)\\
&-\left(\frac{1}{q_x^+}e^{iq_x^+|x|}+\frac{1}{q_x^-}e^{-iq_x^-|x|}\right)\\
&\left.-\frac{1}{2}\left(\frac{E_1}{D_1}+\frac{E_2}{D_2}\right)\frac{1}{q_x^+}e^{2iq_x^+X}-\frac{1}{2}\left(\frac{F_1}{D_1}+\frac{F_2}{D_2}\right)\frac{1}{q_x^-}e^{-2iq_x^-X}\right\},
\end{aligned}
$$

$$
\begin{aligned}
f_0^{r,O}(X,x,p_y;\omega) =& \frac{\eta}{2i}\frac{u_0v_0}{u_0^2-v_0^2}\delta(p_y-k_y)\frac{1}{\omega-E+i\delta^+} \\
&\cdot\left\{\left[\frac{1}{D_1}(k_{e1}+k_{h1})+\frac{1}{D_2}(k_{e2}+k_{h2})\right]\right. \\
&\left.\cdot\, e^{i(q_x^+-q_x^-)X}(u_0^2-v_0^2)\sin((q_x^++q_x^-)x/2)\right\}, \\
f_3^{r,E}(X,x,p_y;\omega) =& -\frac{\eta}{2}\frac{u_0v_0}{u_0^2-v_0^2}\delta(p_y-k_y)\frac{1}{\omega-E+i\delta^+} \\
&\cdot\left\{\left[\frac{1}{D_1}(k_{e1}+k_{h1})-\frac{1}{D_2}(k_{e2}+k_{h2})\right]\right. \\
&\cdot\, e^{i(q_x^+-q_x^-)X}\cos((q_x^++q_x^-)x/2) \\
&\left.-\frac{1}{2}\left(\frac{E_1}{D_1}-\frac{E_2}{D_2}\right)\frac{1}{q_x^+}e^{2iq_x^+X}-\frac{1}{2}\left(\frac{F_1}{D_1}-\frac{F_2}{D_2}\right)\frac{1}{q_x^-}e^{-2iq_x^-X}\right\}, \\
f_3^{r,O}(X,x,p_y;\omega) =& \frac{\eta}{2i}\frac{u_0v_0}{u_0^2-v_0^2}\delta(p_y-k_y)\frac{1}{\omega-E+i\delta^+} \\
&\cdot\left\{\left[\frac{1}{D_1}(k_{e1}+k_{h1})-\frac{1}{D_2}(k_{e2}+k_{h2})\right]\right. \\
&\left.\cdot\, e^{i(q_x^+-q_x^-)X}(u_0^2-v_0^2)\sin((q_x^++q_x^-)x/2)\right\}.
\end{aligned}
\tag{3.158}
$$

It can easily be checked that the Green's functions given in Eqs. 3.152 and 3.158 satisfy the Pauli principle by examining their parity under spatial inversion $(x,p_y)\rightarrow(-x,-p_y)$. By examining spatial inversion (P), exchange of spin (S) and time permutation (T), we find that SPT$=-1$ as required by the Pauli principle, see Table 3.1.

The generation of triplets, and p- and d-wave singlets, from the s-wave singlet Cooper pairs intrinsic to the superconducting material leads to a decrease in the superconducting condensation energy. Determining the spatial symmetries of the even- and odd-frequency singlet and triplet retarded anomalous Green's functions is therefore useful for explaining the behavior of quantities such as the superconducting gap and the critical temperature. To determine whether the singlet and triplet even- and odd-frequency retarded anomalous Green's functions are s-wave, p-wave or d-wave Green's functions, we investigate spatial inversion in the x and y direction separately. P_x is inversion of the relative x coordinate, $x\rightarrow -x$. P_y is inversion of the momentum along the y axis, $p_y\rightarrow -p_y$. The s,

	S	P	T	SPT
f_0^E	-1	1	1	-1
f_0^O	-1	-1	-1	-1
f_3^E	1	-1	1	-1
f_3^O	1	1	-1	-1

Table 3.1: The total SPT parity must be negative for all of the Green's functions in order to obey the Pauli principle. The singlet Green's functions $f_0^{E(O)}$ are odd under spin exchange (S), while the triplet Green's functions $f_0^{E(O)}$ are even under spin exchange. The even-frequency Green's functions $f_{0(3)}^E$ are even under time permutation (T), while the odd-frequency Green's functions $f_{0(3)}^O$ are odd under time permutation. This implies that f_0^E and f_3^O must be even under spatial inversion (P), while f_0^O and f_3^E must be odd under spatial inversion. This can be easily checked by letting $(x, p_y) \to (-x, -p_y)$ in Eqs. 3.152 and 3.158.

p and d orbitals in a 2D system are shown in Fig. 3.9. For $\mathrm{P} = 1$, we may have $\mathrm{P}_x = \mathrm{P}_y = 1$, which describes an s- or a $d_{x^2-y^2}$-wave amplitude, or $\mathrm{P}_x = \mathrm{P}_y = -1$, which describes a d_{xy}-wave amplitude. For $\mathrm{P} = -1$, we may have $\mathrm{P}_x = 1$ and $\mathrm{P}_y = -1$, which describes a p_y-wave amplitude, or $\mathrm{P}_x = -1$ and $\mathrm{P}_y = 1$, which describes a p_x-wave amplitude.

Note that considering P, P_x, and P_y is not sufficient for determining whether a Green's function has an s-wave or a $d_{x^2-y^2}$-wave symmetry. We can show that s-wave singlets and triplets are present by integrating over all spatial coordinates. As can be seen from Fig. 3.9, $d_{x^2-y^2}$-wave amplitudes will then disappear, while s-wave amplitudes yield a nonzero result. A simple way of integrating over all spatial coordinates is to do a Fourier transform along x,

$$f_{0(3)}^{r,E(O)}(X, p_x, p_y; \omega) = \int_{\infty}^{\infty} dx\, f_{0(3)}^{r,E(O)}(X, x, p_y; \omega) e^{-ip_x x}, \tag{3.159}$$

and then setting $p_x = p_y = 0$. This is equivalent to integrating over all spatial coordinates, because

$$f_{0(3)}^{r,E(O)}(X, p_x, p_y; \omega) = \int_{-\infty}^{\infty} dx \int_{-\infty}^{\infty} dy\, f_{0(3)}^{r,E(O)}(X, x, y; \omega) e^{-ip_x x - ip_y y} \tag{3.160}$$

implies that

$$f_{0(3)}^{r,E(O)}(X, p_x = 0, p_y = 0; \omega) = \int_{-\infty}^{\infty} dx \int_{-\infty}^{\infty} dy\, f_{0(3)}^{r,E(O)}(X, x, y; \omega). \tag{3.161}$$

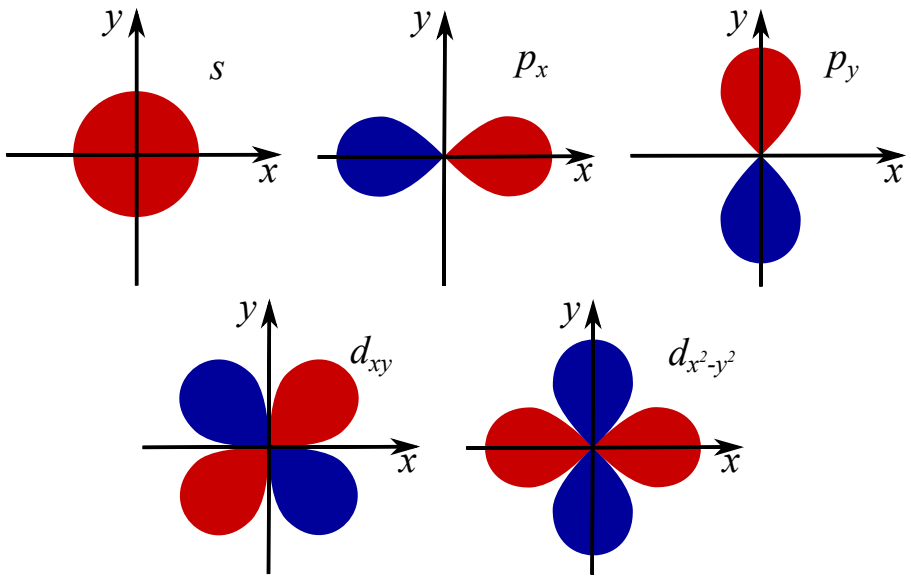

Figure 3.9: The spatial symmetries of the s, p_x, p_y, d_{xy}, and $d_{x^2-y^2}$ orbitals in a 2D system is sketched above. An orbital is odd under spatial inversion if the spatial coordinate moves to a region with a different color under the spatial inversion. If the spatial coordinate moves to a region that has the same color, the orbital is even under spatial inversion.

If $f_{0(3)}^{r,E(O)}(X, p_x = 0, p_y = 0; \omega)$ is nonzero, there may be $d_{x^2-y^2}$-wave singlets (triplets) in the system in addition to the s-wave singlets (triplets). Although it is hard to prove their presence, we can in some cases instead show that $d_{x^2-y^2}$-wave amplitudes are not present. If k_y only enters the singlet (triplet) retarded anomalous Green's function through $\delta(p_y - k_y)$, it cannot change sign when changing p_y, regardless of our choice of p_x. $f_{0(3)}^{r,E(O)}(X, x, p_y; \omega)$ must therefore be an s-wave, and not a $d_{x^2-y^2}$-wave amplitude. This makes sense physically, since we for a system with translational invariance in the y-direction, where the allowed k_x values are independent of k_y, should have no symmetry breaking in the y direction that may cause a creation of $d_{x^2-y^2}$-wave correlations. If $f_{0(3)}^{r,E(O)}(X, x, p_y; \omega)$ is independent of x, p_x only enters $f_{0(3)}^{r,E(O)}(X, p_x, p_y; \omega)$ through $\delta(p_x)$, and there can be no change in the sign of the singlet (triplet) amplitude when changing p_x. This means that we also in this case cannot have $d_{x^2-y^2}$-wave singlets (triplets).

The symmetries under P_x, P_y and P for the Green's functions in Eqs. 3.152 and 3.158 are given in Table 3.2. We see from the table that f_0^E can be an s-wave

	P_x	P_y	P
f_0^E	1	1	1
f_0^O	−1	1	−1
f_3^E	1	−1	−1
f_3^O	−1	−1	1

Table 3.2: The above table shows the parities of the HM/S system with spin-orbit field along the x axis under $x \to -x$ (P_x) and $p_y \to -p_y$ (P_y) for the nonzero singlet and triplet even- and odd-frequency retarded anomalous Green's functions given by Eqs. 3.152 and 3.158. Spatial inversion (P) must be 1 for f_0^E and f_3^O and −1 for f_0^O and f_3^E as shown in Table 3.1.

or a $d_{x^2-y^2}$-wave amplitude. By applying the Fourier transform along x given in Eq. 3.159, we find that

$$\begin{aligned} f_0^{r,E}(X, p_x, p_y; \omega) =& \frac{\eta}{2} u_0 v_0 (q_x^+ + q_x^-) \delta(p_y - k_y) \frac{1}{\omega - E + i\delta^+} \\ & \cdot \Bigg\{ \frac{1}{2D_1} e^{-i(k_{e1} - k_{h1})X} \\ & \cdot [\delta(p_x - (k_{e1} + k_{h1})/2) + \delta(p_x + (k_{e1} + k_{h1})/2)] \\ & + \frac{1}{2D_2} e^{-i(k_{e2} - k_{h2})X} \\ & \cdot [\delta(p_x - ((k_{e2} + k_{h2})/2) + \delta(p_x + ((k_{e2} + k_{h2})/2)] \Bigg\}, \end{aligned} \tag{3.162}$$

inside the heavy-metal region. For $p_x = p_y = 0$, we get

$$\begin{aligned} f_0^{r,E}(X, p_x, p_y; \omega) =& \eta u_0 v_0 (q_x^+ + q_x^-) \delta(k_y) \frac{1}{\omega - E + i\delta^+} \\ & \cdot \frac{1}{D_1} e^{-2ik_{e1}X} \delta(k_{e1} + k_{h1}) \neq 0, \end{aligned} \tag{3.163}$$

because $k_y = 0$ implies that $k_{e1} = k_{e2}$, $k_{h1} = k_{h2}$, and $D_1 = D_2$. There must be s-wave singlets present in the heavy-metal region. The even-frequency singlet retarded anomalous Green's function in the superconducting region contains terms independent of x. As discussed above, this means that there must also be s-wave singlets present in the superconducting region. f_0^E thus represents conventional singlet s-wave superconducting correlations, but may in addition represent $d_{x^2-y^2}$-wave singlets, due to the k_y dependence of the allowed k_y values. We can see from Table 3.2 that f_0^O must be a p_x-wave amplitude, f_3^E must be a

p_y-wave amplitude, and that f_3^O must be a d_{xy}-wave amplitude. The five other retarded anomalous Green's functions that satisfy the Pauli principle, *i.e.* the d_{xy}-wave even-frequency singlet, the p_y-wave odd-frequency singlet, the p_x-wave even-frequency opposite-spin triplet, the $d_{x^2-y^2}$-wave odd-frequency opposite-spin triplet, and the s-wave odd-frequency opposite-spin triplet, are not present. All equal-spin triplet amplitudes are also zero.

3.3.2 *The heavy-metal/superconductor system with $\hat{n} = \hat{z}$*

Consider the case of a 2D HM/S system with the spin-orbit field directed along the z axis. In this case, solving the boundary conditions of the wave functions given in Eq. 3.125 yields more complicated expressions for the reflection and transmission coefficients than in the the $\hat{n} = \hat{x}$ case. Also, solving the boundary conditions of the retarded Green's function given in Eqs. 3.66 and 3.72 cannot be done analytically due to the spin-mixing of the energy bands. We therefore solve the boundary conditions of the wave functions and of the retarded Green's function numerically. Using the obtained expressions for the reflection and transmission coefficients and for the coefficients α_i and β_i in Eq. 3.61, we calculate the even- and odd-frequency singlet and triplet retarded anomalous Green's functions. In order to determine which of the even- and odd-frequency singlets and triplets are even (odd) under $x_1 \leftrightarrow x_2$, we subtract (add) the retarded anomalous Green's functions with x_1 and x_2 interchanged. If the result is zero, then the retarded anomalous Green's function under consideration is even (odd) in P_x. To determine whether the retarded anomalous Green's function is even (odd) in P_y, we subtract (add) the retarded anomalous Green's functions with opposite signs of p_y. The retarded anomalous Green's function under consideration is even (odd) in P_x if the result is zero. Note that some of the retarded anomalous Green's functions may be neither even nor odd in P_x and P_y. In this case we have a mixing of terms with different spatial symmetries. We also check that the retarded anomalous Green's functions show the correct behavior under spatial inversion by subtracting (adding) the retarded anomalous Green's functions with $x_1 \leftrightarrow x_2$ and $p_y \rightarrow -p_y$. If the result is zero, the retarded anomalous Green's function is even (odd) in P.

We consider some different sets of parameters and find that all of the chosen parameter sets give the spatial parities described in Table 3.3. From the table, we see that we have the same singlet and opposite-spin triplet amplitudes as

	P_x	P_y	P
f_0^E	1	1	1
f_0^O	−1	1	−1
f_3^E	1	−1	−1
f_3^O	−1	−1	1
f_1^E	-	-	−1
f_1^O	-	-	1
f_2^E	-	-	−1
f_2^O	-	-	1

Table 3.3: The above table shows the parities of the HM/S system with spin-orbit field along the z axis under $x_1 \leftrightarrow -x_2$ (P_x) and $p_y \rightarrow -p_y$ (P_y) for the singlet and triplet even- and odd-frequency retarded anomalous Green's functions present in the system. In addition to the parities shown in Table 3.2, we have nonzero equal-spin triplet amplitudes with mixing (-) of the possible symmetries in P_x and P_y.

in the $\hat{n} = \hat{x}$ case. In addition, we have nonzero equal-spin triplet amplitudes. Since these are neither even nor odd in P_x and P_y, we must have a mix of triplet amplitudes with different symmetries under P_x and P_y. f_1^E and f_2^E must therefore be a mix of p_x- and p_y-wave even-frequency triplets. f_1^O and f_2^O may either be a mix of and s- and d_{xy}-wave triplets, a mix of $d_{x^2-y^2}$- and d_{xy}-wave triplets, or a mix of s-, $d_{x^2-y^2}$-, and d_{xy}-wave triplets.

3.3.3 *The ferromagnet/superconductor system*

By the same method as for the HM/S system with $\hat{n} = \hat{x}$, we will now find the singlet and triplet even- and odd-frequency retarded anomalous Green's functions of the F/S system with magnetization along the z axis. We find that on the ferromagnetic side of the interface, where $x_1, x_2 < 0$, the anomalous elements of the retarded Green's function are

$$\begin{aligned}
f^r_{\uparrow,\downarrow}(x_1, x_2, y_1, y_2; t_1, t_2) =& \frac{\eta}{i}\frac{u_0 v_0 (q_x^+ + q_x^-)}{C_{21}}\theta(t_1 - t_2) \\
&\cdot e^{-ik_{e2}x_1 + ik_{h1}x_2} e^{ik_y(y_1 - y_2)} e^{-iE(t_1 - t_2)}, \\
f^r_{\downarrow,\uparrow}(x_1, x_2, y_1, y_2; t_1, t_2) =& -\frac{\eta}{i}\frac{u_0 v_0 (q_x^+ + q_x^-)}{C_{12}}\theta(t_1 - t_2) \\
&\cdot e^{-ik_{e1}x_1 + ik_{h2}x_2} e^{ik_y(y_1 - y_2)} e^{-iE(t_1 - t_2)}, \\
f^r_{\uparrow,\uparrow}(x_1, x_2, y_1, y_2; t_1, t_2) =& 0, \\
f^r_{\downarrow,\downarrow}(x_1, x_2, y_1, y_2; t_1, t_2) =& 0,
\end{aligned} \tag{3.164}$$

where

$$C_{12(21)} \equiv u_0^2 (k_{e1(2)} + q_x^+)(k_{h2(1)} + q_x^-) + v_0^2 (k_{h2(1)} - q_x^+)(-k_{e1(2)} + q_x^-). \tag{3.165}$$

From the above equation, we see that there are no equal-spin triplet amplitudes in the ferromagnetic region. We rewrite the above expression to the relative coordinates y and t, and apply the Fourier transform in y given in Eq. 3.38. The dependence of the retarded Green's functions upon ω takes the same form as for the HM/S system with $\hat{n} = \hat{x}$. From Eq. 3.98, we find that the singlet and opposite-spin triplet retarded anomalous Green's functions in the ferromagnetic region are given by

$$\begin{aligned}
f^r_0(x_1, x_2, y_1, y_2; t_1, t_2) =& \frac{\eta}{2} u_0 v_0 (q_x^+ + q_x^-)\delta(p_y - k_y)\frac{1}{\omega - E + i\delta^+} \\
&\cdot \left[\frac{1}{C_{21}} e^{-ik_{e2}x_1 + ik_{h1}x_2} + \frac{1}{C_{12}} e^{-ik_{e1}x_1 + ik_{h2}x_2}\right], \\
f^r_3(x_1, x_2, y_1, y_2; t_1, t_2) =& \frac{\eta}{2} u_0 v_0 (q_x^+ + q_x^-)\delta(p_y - k_y)\frac{1}{\omega - E + i\delta^+} \\
&\cdot \left[\frac{1}{C_{21}} e^{-ik_{e2}x_1 + ik_{h1}x_2} - \frac{1}{C_{12}} e^{-ik_{e1}x_1 + ik_{h2}x_2}\right].
\end{aligned} \tag{3.166}$$

Notice that in contrast to the HM/S system, none of the parameters are dependent upon k_y. By inserting the above expression into Eq. 3.97 and using that all parameters are invariant under $k_y \to -k_y$, we find that the nonzero even- and

odd-frequency singlet and triplet retarded anomalous Green's functions in the ferromagnetic region are

$$\begin{aligned} f_0^{r,E(O)}(x_1,x_2,p_y;\omega) =& \frac{\eta}{4}u_0v_0(q_x^+ + q_x^-)\delta(p_y-k_y)\frac{1}{\omega - E + i\delta^+} \\ & \cdot\left[\left(\frac{1}{C_{21}}e^{-ik_{e2}x_1+ik_{h1}x_2} + \frac{1}{C_{12}}e^{-ik_{e1}x_1+ik_{h2}x_2}\right)\right. \\ & \left.\pm\left(\frac{1}{C_{21}}e^{-ik_{e2}x_2+ik_{h1}x_1} + \frac{1}{C_{12}}e^{-ik_{e1}x_2+ik_{h2}x_1}\right)\right], \\ f_3^{r,E(O)}(x_1,x_2,p_y;\omega) =& \frac{\eta}{4}u_0v_0(q_x^+ + q_x^-)\delta(p_y-k_y)\frac{1}{\omega - E + i\delta^+} \\ & \cdot\left[\left(\frac{1}{C_{21}}e^{-ik_{e2}x_1+ik_{h1}x_2} - \frac{1}{C_{12}}e^{-ik_{e1}x_1+ik_{h2}x_2}\right)\right. \\ & \left.\mp\left(\frac{1}{C_{21}}e^{-ik_{e2}x_2+ik_{h1}x_1} - \frac{1}{C_{12}}e^{-ik_{e1}x_2+ik_{h2}x_1}\right)\right]. \end{aligned} \tag{3.167}$$

By rewriting the above expression to the center of mass coordinate $X \equiv (x_1 + x_2)/2$ and the relative coordinate $x \equiv x_1 - x_2$, we find that

$$\begin{aligned} f_0^{r,E(O)}(X,x,p_y;\omega) =& \frac{\eta}{4}u_0v_0(q_x^+ + q_x^-)\delta(p_y-k_y)\frac{1}{\omega - E + i\delta^+} \\ & \cdot\left[\frac{1}{C_{21}}e^{-i(k_{e2}-k_{h1})X}\left(e^{-i(k_{e2}+k_{h1})x/2} \pm e^{i(k_{e2}+k_{h1})x/2}\right)\right. \\ & \left.+\frac{1}{C_{12}}e^{-i(k_{e1}-k_{h2})X}\left(e^{-i(k_{e1}+k_{h2})x/2} \pm e^{i(k_{e1}+k_{h2})x/2}\right)\right], \\ f_3^{r,E(O)}(X,x,p_y;\omega) =& \frac{\eta}{4}u_0v_0(q_x^+ + q_x^-)\delta(p_y-k_y)\frac{1}{\omega - E + i\delta^+} \\ & \cdot\left[\frac{1}{C_{21}}e^{-i(k_{e2}-k_{h1})X}\left(e^{-i(k_{e2}+k_{h1})x/2} \mp e^{i(k_{e2}+k_{h1})x/2}\right)\right. \\ & \left.-\frac{1}{C_{12}}e^{-i(k_{e1}-k_{h2})X}\left(e^{-i(k_{e1}+k_{h2})x/2} \mp e^{i(k_{e1}+k_{h2})x/2}\right)\right], \end{aligned} \tag{3.168}$$

The nonzero singlet and triplet even- and odd-frequency retarded anomalous Green's functions inside the ferromagnet are

$$\begin{aligned} f_0^{r,E}(X,x,p_y;\omega) =& \frac{\eta}{2}u_0v_0(q_x^+ + q_x^-)\delta(p_y-k_y)\frac{1}{\omega - E + i\delta^+} \\ & \cdot\left[\frac{1}{C_{21}}e^{-i(k_{e2}-k_{h1})X}\cos((k_{e2}+k_{h1})x/2)\right. \\ & \left.+\frac{1}{C_{12}}e^{-i(k_{e1}-k_{h2})X}\cos((k_{e1}+k_{h2})x/2)\right], \end{aligned}$$

$$
\begin{aligned}
f_0^{r,O}(X,x,p_y;\omega) =& \frac{\eta}{2i}u_0v_0(q_x^+ + q_x^-)\delta(p_y-k_y)\frac{1}{\omega - E + i\delta^+} \\
&\cdot\left[\frac{1}{C_{21}}e^{-i(k_{e2}-k_{h1})X}\sin((k_{e2}+k_{h1})x/2)\right. \\
&\left.+\frac{1}{C_{12}}e^{-i(k_{e1}-k_{h2})X}\sin((k_{e1}+k_{h2})x/2)\right], \\
f_3^{r,E}(X,x,p_y;\omega) =& \frac{\eta}{2i}u_0v_0(q_x^+ + q_x^-)\delta(p_y-k_y)\frac{1}{\omega - E + i\delta^+} \\
&\cdot\left[\frac{1}{C_{21}}e^{-i(k_{e2}-k_{h1})X}\sin((k_{e2}+k_{h1})x/2)\right. \\
&\left.-\frac{1}{C_{12}}e^{-i(k_{e1}-k_{h2})X}\sin((k_{e1}+k_{h2})x/2)\right], \\
f_3^{r,O}(X,x,p_y;\omega) =& \frac{\eta}{2}u_0v_0(q_x^+ + q_x^-)\delta(p_y-k_y)\frac{1}{\omega - E + i\delta^+} \\
&\cdot\left[\frac{1}{C_{21}}e^{-i(k_{e2}-k_{h1})X}\cos((k_{e2}+k_{h1})x/2)\right. \\
&\left.-\frac{1}{C_{12}}e^{-i(k_{e1}-k_{h2})X}\cos((k_{e1}+k_{h2})x/2)\right].
\end{aligned}
\tag{3.169}
$$

On the superconducting side of the interface, where $x_1, x_2 > 0$, we find that the anomalous elements of the retarded Green's function are

$$
\begin{aligned}
f_{\uparrow,\downarrow}^r(x_1,x_2,y_1y_2;t_1,t_2) =& -\frac{\eta}{i}\frac{u_0v_0}{u_0^2-v_0^2}\theta(t_1-t_2)e^{ik_y(y_1-y_2)}e^{-iE(t_1-t_2)} \\
&\cdot\left\{\frac{1}{C_{21}}\left(k_{e2}+k_{h1}\right)\left(u_0^2e^{iq_x^+x_1-iq_x^-x_2}+v_0^2e^{iq_x^+x_2-iq_x^-x_1}\right)\right. \\
&-\frac{1}{2}\left[\left(\frac{1}{q_x^+}e^{iq_x^+(x_1-x_2)}+\frac{1}{q_x^-}e^{-iq_x^-(x_1-x_2)}\right)\theta(x_1-x_2)\right. \\
&\left.+\left(\frac{1}{q_x^+}e^{-iq_x^+(x_1-x_2)}+\frac{1}{q_x^-}e^{iq_x^-(x_1-x_2)}\right)\theta(x_2-x_1)\right] \\
&\left.+\frac{A_{21}}{2C_{21}}\frac{1}{q_x^+}e^{iq_x^+(x_1+x_2)}+\frac{B_{21}}{2C_{21}}\frac{1}{q_x^-}e^{-iq_x^-(x_1-x_2)}\right\},
\end{aligned}
$$

$$
\begin{aligned}
f^r_{\downarrow,\uparrow}(x_1,x_2,y_1y_2;t_1,t_2) =& \frac{\eta}{i}\frac{u_0v_0}{u_0^2-v_0^2}\theta(t_1-t_2)e^{ik_y(y_1-y_2)}e^{-iE(t_1-t_2)} \\
&\cdot\Bigg\{\frac{1}{C_{12}}\big(k_{e1}+k_{h2}\big)\big(u_0^2e^{iq_x^+x_1-iq_x^-x_2}+v_0^2e^{iq_x^+x_2-iq_x^-x_1}\big) \\
&-\frac{1}{2}\Bigg[\left(\frac{1}{q_x^+}e^{iq_x^+(x_1-x_2)}+\frac{1}{q_x^-}e^{-iq_x^-(x_1-x_2)}\right)\theta(x_1-x_2) \\
&+\left(\frac{1}{q_x^+}e^{-iq_x^+(x_1-x_2)}+\frac{1}{q_x^-}e^{iq_x^-(x_1-x_2)}\right)\theta(x_2-x_1)\Bigg] \\
&+\frac{A_{12}}{2C_{12}}\frac{1}{q_x^+}e^{iq_x^+(x_1+x_2)}+\frac{B_{12}}{2C_{12}}\frac{1}{q_x^-}e^{-iq_x^-(x_1-x_2)}\Bigg\}, \\
f^r_{\uparrow,\uparrow}(x_1,x_2,y_1,y_2;t_1,t_2) =& 0, \\
f^r_{\downarrow,\downarrow}(x_1,x_2,y_1,y_2;t_1,t_2) =& 0.
\end{aligned}
\tag{3.170}
$$

$C_{12(21)}$ are defined in the same way as inside the ferromagnet, while

$$
\begin{aligned}
A_{12(21)} &\equiv u_0^2(k_{e1(2)}-q_x^+)(k_{h2(1)}+q_x^-)+v_0^2(k_{h2(1)}+q_x^+)(-k_{e1(2)}+q_x^-) \\
B_{12(21)} &\equiv u_0^2(k_{e1(2)}+q_x^+)(k_{h2(1)}-q_x^-)+v_0^2(k_{h2(1)}-q_x^+)(-k_{e1(2)}-q_x^-).
\end{aligned}
\tag{3.171}
$$

From the above equation, we see that there are no equal-spin triplets amplitudes inside the superconductor. There are therefore no equal-spin triplets in the F/S system. We rewrite the above expression to the relative coordinates y and t, and apply the Fourier transform in y given in Eq. 3.38. The dependence of the retarded Green's functions upon ω takes the same form as for the HM/S system with $\hat{n}=\hat{x}$. From Eq. 3.98, we find that the singlet and opposite-spin triplet retarded anomalous Green's functions inside the superconducting region are given by

$$
\begin{aligned}
f^r_0(x_1,x_2,p_y;\omega) =& -\frac{\eta}{2}\frac{u_0v_0}{u_0^2-v_0^2}\delta(p_y-k_y)\frac{1}{\omega-E+i\delta^+} \\
&\cdot\Bigg\{\left[\frac{1}{C_{21}}(k_{e2}+k_{h1})+\frac{1}{C_{12}}(k_{e1}+k_{h2})\right] \\
&\cdot\big(u_0^2e^{iq_x^+x_1-iq_x^-x_2}+v_0^2e^{iq_x^+x_2-iq_x^-x_1}\big) \\
&-\left(\frac{1}{q_x^+}e^{iq_x^+|x_1-x_2|}+\frac{1}{q_x^-}e^{-iq_x^-|x_1-x_2|}\right) \\
&+\frac{1}{2}\left(\frac{A_{21}}{C_{21}}+\frac{A_{12}}{C_{12}}\right)\frac{1}{q_x^+}e^{iq_x^+(x_1+x_2)} \\
&+\frac{1}{2}\left(\frac{B_{21}}{C_{21}}+\frac{B_{12}}{C_{12}}\right)\frac{1}{q_x^-}e^{-iq_x^-(x_1+x_2)}\Bigg\},
\end{aligned}
$$

$$
\begin{aligned}
f_3^r(x_1,x_2,p_y;\omega) = &-\frac{\eta}{2}\frac{u_0v_0}{u_0^2-v_0^2}\delta(p_y-k_y)\frac{1}{\omega-E+i\delta^+}\\
&\cdot\left\{\left[\frac{1}{C_{21}}(k_{e2}+k_{h1})-\frac{1}{C_{12}}(k_{e1}+k_{h2})\right]\right.\\
&\cdot\left(u_0^2e^{iq_x^+x_1-iq_x^-x_2}+v_0^2e^{iq_x^+x_2-iq_x^-x_1}\right)\\
&+\frac{1}{2}\left(\frac{A_{21}}{C_{21}}-\frac{A_{12}}{C_{12}}\right)\frac{1}{q_x^+}e^{iq_x^+(x_1+x_2)}\\
&\left.+\frac{1}{2}\left(\frac{B_{21}}{C_{21}}-\frac{B_{12}}{C_{12}}\right)\frac{1}{q_x^-}e^{-iq_x^-(x_1+x_2)}\right\}.
\end{aligned}
\tag{3.172}
$$

Just as for the ferromagnetic region, we insert this into Eq. 3.97 and use that all parameters are invariant under $k_y \to -k_y$. We get

$$
\begin{aligned}
f_0^{r,E(O)}(x_1,x_2,p_y;\omega) = &-\frac{\eta}{4}\frac{u_0v_0}{u_0^2-v_0^2}\delta(p_y-k_y)\frac{1}{\omega-E+i\delta^+}\\
&\cdot\left\{\left[\frac{1}{C_{21}}(k_{e2}+k_{h1})+\frac{1}{C_{12}}(k_{e1}+k_{h2})\right]\right.\\
&\cdot\left[u_0^2\left(e^{iq_x^+x_1-iq_x^-x_2}\pm e^{iq_x^+x_2-iq_x^-x_1}\right)\right.\\
&\left.+v_0^2\left(e^{iq_x^+x_2-iq_x^-x_1}\pm e^{iq_x^+x_1-iq_x^-x_2}\right)\right]\\
&+\frac{1}{2}(1\pm1)\left[-2\left(\frac{1}{q_x^+}e^{iq_x^+|x_1-x_2|}+\frac{1}{q_x^-}e^{-iq_x^-|x_1-x_2|}\right)\right.\\
&+\left(\frac{A_{21}}{C_{21}}+\frac{A_{12}}{C_{12}}\right)\frac{1}{q_x^+}e^{iq_x^+(x_1+x_2)}\\
&\left.\left.+\left(\frac{B_{21}}{C_{21}}+\frac{B_{12}}{C_{12}}\right)\frac{1}{q_x^-}e^{-iq_x^-(x_1+x_2)}\right]\right\},
\end{aligned}
\tag{3.173}
$$

$$
\begin{aligned}
f_3^{r,E(O)}(x_1,x_2,p_y;\omega) = &-\frac{\eta}{4}\frac{u_0v_0}{u_0^2-v_0^2}\delta(p_y-k_y)\frac{1}{\omega-E+i\delta^+}\\
&\cdot\left\{\left[\frac{1}{C_{21}}(k_{e2}+k_{h1})-\frac{1}{C_{12}}(k_{e1}+k_{h2})\right]\right.\\
&\cdot\left[u_0^2\left(e^{iq_x^+x_1-iq_x^-x_2}\mp e^{iq_x^+x_2-iq_x^-x_1}\right)\right.\\
&\left.+v_0^2\left(e^{iq_x^+x_2-iq_x^-x_1}\mp e^{iq_x^+x_1-iq_x^-x_2}\right)\right]+\frac{1}{2}(1\mp1)\\
&\cdot\left[\left(\frac{A_{21}}{C_{21}}-\frac{A_{12}}{C_{12}}\right)\frac{1}{q_x^+}e^{iq_x^+(x_1+x_2)}\right.\\
&\left.\left.+\left(\frac{B_{21}}{C_{21}}-\frac{B_{12}}{C_{12}}\right)\frac{1}{q_x^-}e^{-iq_x^-(x_1+x_2)}\right]\right\}.
\end{aligned}
$$

In the center of mass and relative x coordinates, the above expressions can be written

$$
\begin{aligned}
f_0^{r,E(O)}(X,x,p_y;\omega) = &-\frac{\eta}{4}\frac{u_0v_0}{u_0^2-v_0^2}\delta(p_y-k_y)\frac{1}{\omega-E+i\delta^+}\\
&\cdot\left\{\left[\frac{1}{C_{21}}(k_{e2}+k_{h1})+\frac{1}{C_{12}}(k_{e1}+k_{h2})\right]e^{i(q_x^+-q_x^-)X}\right.\\
&\cdot\left[u_0^2\left(e^{i(q_x^++q_x^-)x/2}\pm e^{-i(q_x^++q_x^-)x/2}\right)\right.\\
&\left.+v_0^2\left(e^{-i(q_x^++q_x^-)x/2}\pm e^{i(q_x^++q_x^-)x/2}\right)\right]\\
&+\frac{1}{2}(1\pm 1)\left[-2\left(\frac{1}{q_x^+}e^{iq_x^+|x|}+\frac{1}{q_x^-}e^{-iq_x^-|x|}\right)\right.\\
&+\left(\frac{A_{21}}{C_{21}}+\frac{A_{12}}{C_{12}}\right)\frac{1}{q_x^+}e^{2iq_x^+X}\\
&\left.\left.+\left(\frac{B_{21}}{C_{21}}+\frac{B_{12}}{C_{12}}\right)\frac{1}{q_x^-}e^{-2iq_x^-X}\right]\right\},
\end{aligned}
\tag{3.174}
$$

$$
\begin{aligned}
f_3^{r,E(O)}(X,x,p_y;\omega) = &-\frac{\eta}{4}\frac{u_0v_0}{u_0^2-v_0^2}\delta(p_y-k_y)\frac{1}{\omega-E+i\delta^+}\\
&\cdot\left\{\left[\frac{1}{C_{21}}(k_{e2}+k_{h1})-\frac{1}{C_{12}}(k_{e1}+k_{h2})\right]e^{i(q_x^+-q_x^-)X}\right.\\
&\cdot\left[u_0^2\left(e^{i(q_x^++q_x^-)x/2}\mp e^{-i(q_x^++q_x^-)x/2}\right)\right.\\
&\left.+v_0^2\left(e^{-i(q_x^++q_x^-)x/2}\mp e^{i(q_x^++q_x^-)x/2}\right)\right]+\frac{1}{2}(1\mp 1)\\
&\cdot\left[\left(\frac{A_{21}}{C_{21}}-\frac{A_{12}}{C_{12}}\right)\frac{1}{q_x^+}e^{2iq_x^+X}\right.\\
&\left.\left.+\left(\frac{B_{21}}{C_{21}}-\frac{B_{12}}{C_{12}}\right)\frac{1}{q_x^-}e^{-2iq_x^-X}\right]\right\}.
\end{aligned}
$$

The nonzero singlet and triplet retarded anomalous Green's functions inside the superconducting region are

$$
\begin{aligned}
f_0^{r,E}(X,x,p_y;\omega) = &-\frac{\eta}{2}\frac{u_0v_0}{u_0^2-v_0^2}\delta(p_y-k_y)\frac{1}{\omega-E+i\delta^+}\\
&\cdot\left\{\left[\frac{1}{C_{21}}(k_{e2}+k_{h1})+\frac{1}{C_{12}}(k_{e1}+k_{h2})\right]\right.\\
&\cdot e^{i(q_x^+-q_x^-)X}\cos((q_x^++q_x^-)x/2)\\
&-\left(\frac{1}{q_x^+}e^{iq_x^+|x|}+\frac{1}{q_x^-}e^{-iq_x^-|x|}\right)\\
&+\frac{1}{2}\left(\frac{A_{21}}{C_{21}}+\frac{A_{12}}{C_{12}}\right)\frac{1}{q_x^+}e^{2iq_x^+X}\\
&\left.+\frac{1}{2}\left(\frac{B_{21}}{C_{21}}+\frac{B_{12}}{C_{12}}\right)\frac{1}{q_x^-}e^{-2iq_x^-X}\right\},\\
f_0^{r,O}(X,x,p_y;\omega) = &\frac{\eta}{2i}\frac{u_0v_0}{u_0^2-v_0^2}\delta(p_y-k_y)\frac{1}{\omega-E+i\delta^+}\\
&\cdot\left\{\left[\frac{1}{C_{21}}(k_{e2}+k_{h1})+\frac{1}{C_{12}}(k_{e1}+k_{h2})\right]\right.\\
&\left.\cdot e^{i(q_x^+-q_x^-)X}(u_0^2-v_0^2)\sin((q_x^++q_x^-)x/2)\right\},\qquad (3.175)\\
f_3^{r,E}(X,x,p_y;\omega) = &\frac{\eta}{2i}\frac{u_0v_0}{u_0^2-v_0^2}\delta(p_y-k_y)\frac{1}{\omega-E+i\delta^+}\\
&\cdot\left\{\left[\frac{1}{C_{21}}(k_{e2}+k_{h1})-\frac{1}{C_{12}}(k_{e1}+k_{h2})\right]\right.\\
&\left.\cdot e^{i(q_x^+-q_x^-)X}(u_0^2-v_0^2)\sin((q_x^++q_x^-)x/2)\right\}\\
f_3^{r,O}(X,x,p_y;\omega) = &-\frac{\eta}{2}\frac{u_0v_0}{u_0^2-v_0^2}\delta(p_y-k_y)\frac{1}{\omega-E+i\delta^+}\\
&\cdot\left\{\left[\frac{1}{C_{21}}(k_{e2}+k_{h1})-\frac{1}{C_{12}}(k_{e1}+k_{h2})\right]\right.\\
&\cdot e^{i(q_x^+-q_x^-)X}\cos((q_x^++q_x^-)x/2)\\
&+\frac{1}{2}\left(\frac{A_{21}}{C_{21}}-\frac{A_{12}}{C_{12}}\right)\frac{1}{q_x^+}e^{2iq_x^+X}\\
&\left.+\frac{1}{2}\left(\frac{B_{21}}{C_{21}}-\frac{B_{12}}{C_{12}}\right)\frac{1}{q_x^-}e^{-2iq_x^-X}\right\}.
\end{aligned}
$$

Table 3.4 shows the symmetries of Eqs. 3.169 and 3.175 under spatial inversion, inversion of only x and inversion of only p_y. By comparison with Table 3.1,

	P_x	P_y	P
f_0^E	1	1	1
f_0^O	−1	1	−1
f_3^E	−1	1	−1
f_3^O	1	1	1

Table 3.4: The above table shows the parities P_x and P_y for the nonzero singlet and triplet retarded anomalous Green's functions. For spatial inversion (P), we must have P= 1 for f_0^E and f_3^O and P= −1 for f_0^O and f_3^E according to the Pauli principle (see Table 3.1).

we see that the above Green's functions satisfy the Pauli principle. The Green's functions in Eqs. 3.169 and 3.175 are even under inversion of p_y. This means that the p_y- wave and d_{xy}-wave amplitudes must be zero. We also know that the Green's functions in Eqs. 3.169 and 3.175 only depend upon k_y through $\delta(p_y - k_y)$. As discussed in Sec. 3.3.1, this means that the $d_{x^2-y^2}$-wave amplitude must be zero. We can only have s-wave and p_x-wave amplitudes in the system. The nonzero singlet and triplet retarded anomalous Green's functions are therefore the s-wave even-frequency singlet, the p_x-wave odd-frequency singlet, the p_x-wave even-frequency opposite-spin triplet and the s-wave odd-frequency opposite-spin triplet. Although the Hamiltonian matrices are quite similar, the 2D HM/S system with $\hat{n} = \hat{x}$ and the 2D F/S system with $\boldsymbol{h} = h\hat{z}$ do not allow for generation of the same types of triplets. The crucial difference between these two systems is that the k_x values are k_y dependent for the HM/S system, while for the F/S system the retarded anomalous Green's function only depends on k_y through $\delta(p_y - k_y)$.

We have now established which of the superconducting correlations are present in each of our three systems. This will allow us to understand the physical reason for the dependence of the superconducting critical temperature upon the symmetry breaking in each of these three systems. This will be further discussed in Ch. 5.

4

MAGNETIZATION REORIENTATION

4.1 INTRODUCTION AND MOTIVATION

Recent theoretical [22–25] and experimental [25] work has demonstrated how the superconducting critical temperature can be modified by rotating the magnetization of a single homogeneous ferromagnet proximity-coupled to a superconducting layer. This occurs when the superconductor and the ferromagnet are separated by a thin heavy normal-metal that provides an enhanced interfacial Rashba spin-orbit interaction. Measurements [25] performed on a Nb/Pt/Co/Pt system showed a suppression of the critical temperature for an in-plane magnetization, that was attributed to a reduced superconducting gap due to triplet generation. A reduced gap also implies an increase in the free energy since part of the superconducting condensation energy is lost. We may therefore suspect the superconducting contribution to the free energy to favor an out-of-plane magnetization direction.

Motivated by this, we explore the possibility of a magnetization reorientation driven by the superconducting phase transition. We discover that by lowering the temperature, in addition to reorientation of the favored magnetization direction from IP to OOP, a $\pi/4$ IP rotation for thicker ferromagnetic layers is possible. This opens the possibility for temperature-induced switching of the magnetization both between the IP and OOP orientation and switching within a plane parallel to the interface. Furthermore, computation of the critical temperature of the structure in the ballistic limit shows a dependence on the IP orientation of the magnetization, in contrast to what is previously found for the diffusive limit. This finding is relevant with respect to thin-film heterostructures since these are likely to be in the ballistic regime of transport rather than in the diffusive regime.

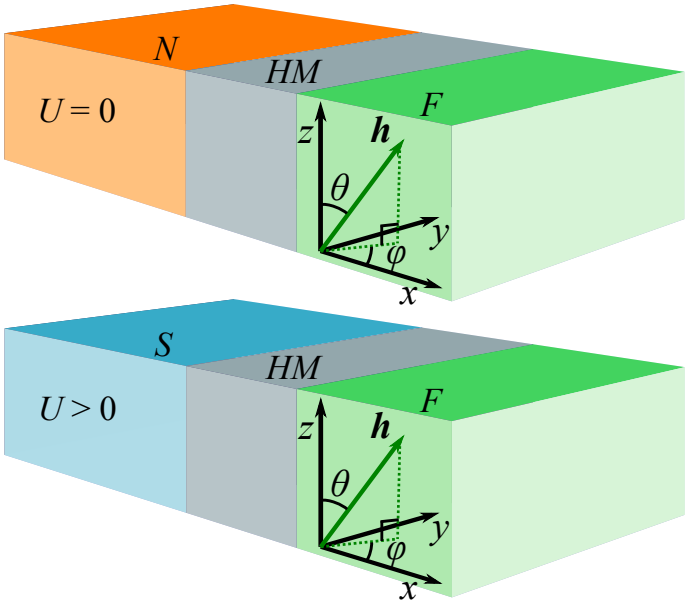

Figure 4.1: Suggested experimental setup for demonstrating a magnetization reorientation due to a change in temperature. We have a stack of a normal-metal layer ($T > T_c$, $U = 0$) or a superconducting layer ($T < T_c$, $U > 0$), a heavy-metal layer and a ferromagnetic layer. We model our system as a 3D cubic lattice with interface normal along the x direction. The exchange field $\boldsymbol{h}$ is described by the polar and azimuthal angles with respect to the z axis, (θ, ϕ). Note that the above model is not to scale.

4.2 MODEL

We consider a 3D cubic lattice of size $N_x \times N_y \times N_z$ as shown in Fig. 4.1. The lattice consists of three layers: a superconducting layer, a thin heavy-metal layer with Rashba spin-orbit coupling and a thin ferromagnetic layer. For enabling experimental observation of the effects considered in this chapter, the system should have as good an interface quality as possible to maximize the proximity effect, and heavy-metal interlayers should be used to boost the spin-orbit coupling strength. For concrete material choices, we suggest a Nb superconductor with Pt interlayers, which should give a strong proximity effect and strong spin-orbit coupling (see for instance Ref. [51]). In addition, the ferromagnet should be soft and have as weak an anisotropy as possible. We suggest using a 7% Mo-doped permalloy, which has a very low switching energy [52]. We describe the trilayer system shown in Fig. 4.1 by the Hamiltonian in Eqs. 2.1 and 2.6 and follow the theoretical framework described in Sec. 2.1. The magnetic exchange field of the ferromagnet is expressed by $\boldsymbol{h} = h(\cos(\phi)\sin(\theta), \sin(\phi)\sin(\theta), \cos(\theta))$, where θ is the polar angle with respect to the z axis and ϕ is the azimuthal angle. Note that as described in Sec. 2.1, the interface normals are parallel to the x axis and

we assume periodic boundary conditions in the y and z directions. Recall that as stated in Sec. 2.1, we scale all energies to the hopping element, t, and all lengths to the lattice constant, a, and we also set the reduced Planck constant $\hbar$ and the Boltzmann constant k_B equal to 1. Therefore, all temperatures are scaled by t/k_B in the presentation of the results.

4.3 RESULTS AND DISCUSSION

4.3.1 *The non-superconducting contribution to the free energy*

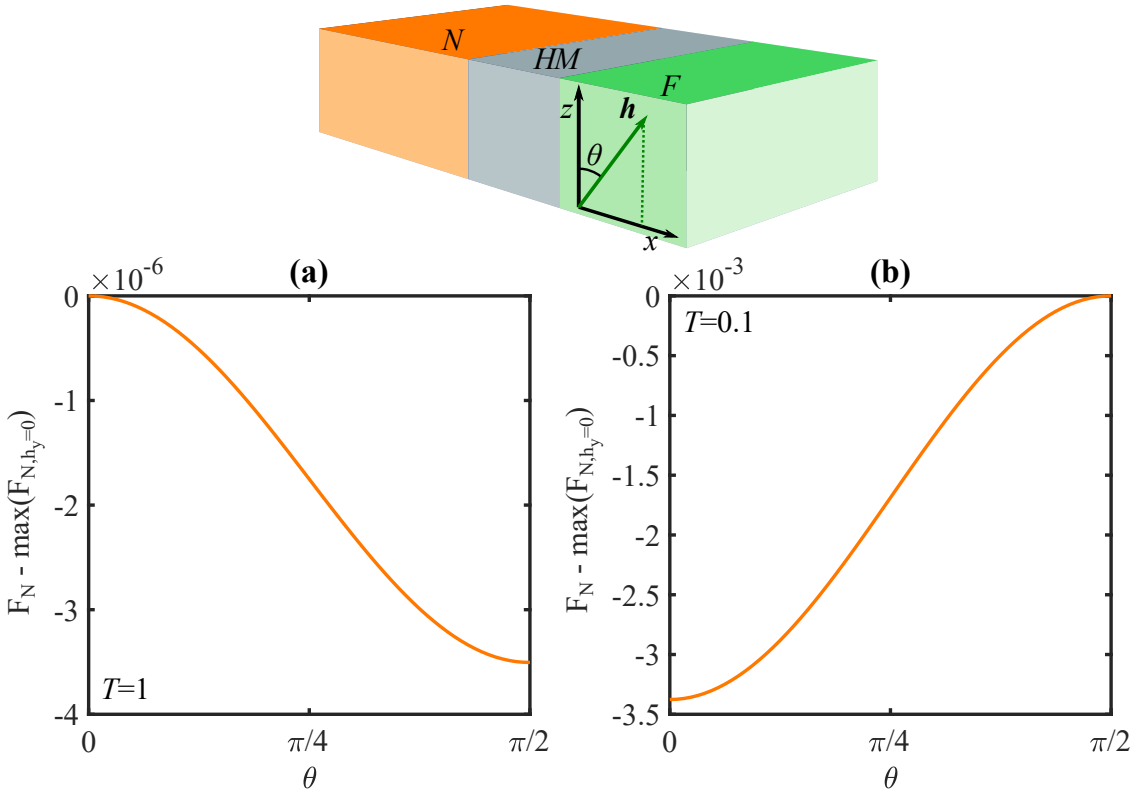

Figure 4.2: Panels (a) and (b) show $F_N(\theta) - \max(F_{N,h_y=0})$ in the xz plane for $T = 1$ and $T = 0.1$. The parameters used are specified in the main text. In (a) OOP magnetization is favored. In (b) IP magnetization is favored.

We first look at a system as shown in Fig. 4.1, where we have a normal-metal rather than a superconductor, *i.e.* $U = 0$. This is important in order to later distinguish the influence of the superconducting phase on the preferred magnetization orientation compared to the normal-state phase. We diagonalize the Hamiltonian described in Eqs. 2.1 and 2.10 numerically using the parameters $N_{x,N} = 9$,

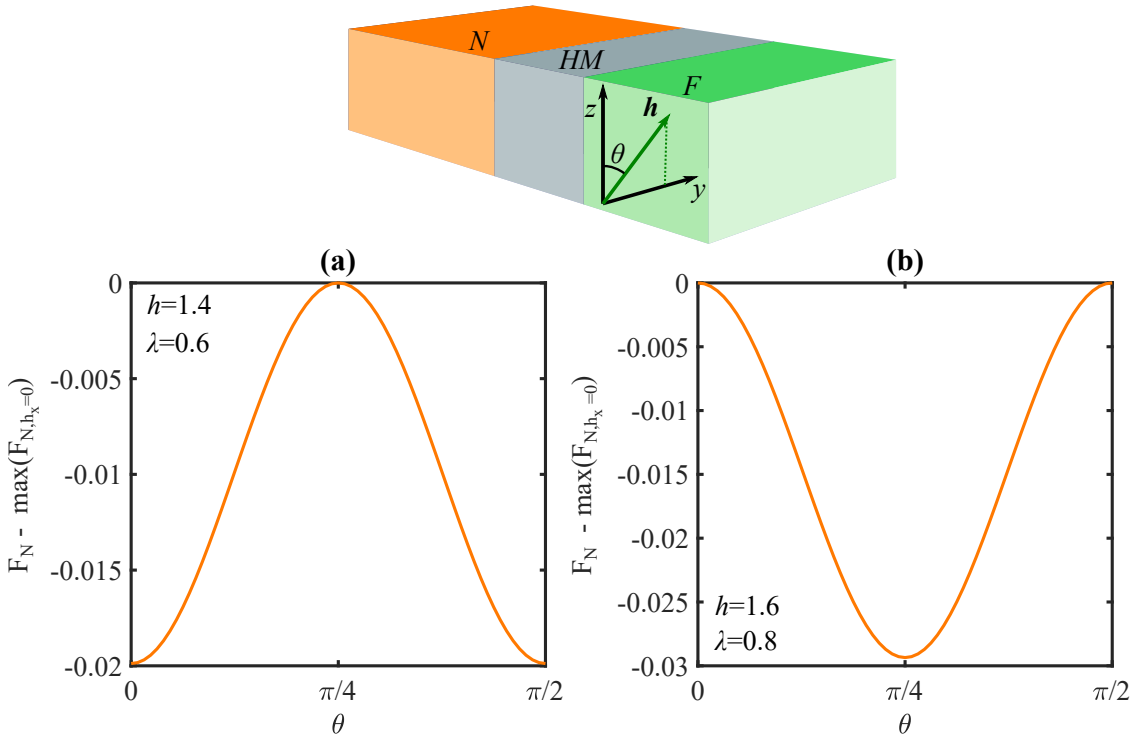

Figure 4.3: Panels (a) and (b) show $F_N(\theta) - \max(F_{N,h_x=0})$ in the yz plane for $h = 1.4$, $\lambda = 0.6$ and for $h = 1.6$, $\lambda = 0.8$. The other parameters used are given in the main text. $T = 0.01$. We see a $\pi/4$-rotation of the minimum from (a) to (b).

$N_{x,HM} = N_{x,F} = 3$, $N_y = N_z = 50$, $\mu_N = 1.8$, $\mu_{HM} = 1.7$, $\mu_F = 1.6$, $h = 1.4$ and $\lambda = 0.6$. We then plot the free energy for the N/HM/F-trilayer, $F_N(\theta)$, to find the preferred direction of $\mathbf{h}$ for a given T. In all free-energy plots we subtract the maximal free energy within the plane of rotation we are considering, *i.e.* $\max(F_{N,h_y=0})$ when considering the xz plane and $\max(F_{N,h_x=0})$ when considering the yz plane. We do this to make it easier to compare the change in free energy for different parameter choices. Figure 4.2 shows $F_N(\theta)$ in the xz plane for $T = 1$ and $T = 0.1$. We see that the preferred magnetization direction may change as the temperature is increased. The preferred direction may also change when changing h, λ or the layer thicknesses. The angular dependence of F is the same for the xy and xz planes. Figure 4.3 shows $F_N(\theta)$ in the yz plane at $T = 0.01$ for different choices of h and λ. We see that the preferred direction of $\boldsymbol{h}$ is rotated by $\pi/4$ when changing the parameters from $h = 1.4$, $\lambda = 0.6$ to $h = 1.6$, $\lambda = 0.8$. A similar rotation may also happen when changing T or the layer thicknesses. Note that the free energy is invariant under a $\pi/2$-rotation in the yz plane. This is reasonable, because a $\pi/2$-rotation of the cubic system around the interface normal should leave the system invariant independently of the magnetization direction. For sufficiently high temperatures, F_N becomes constant. We underline

that the effective magnetization anisotropy that arises here is distinct from the anisotropy terms described in Eqs. 2.52 and 2.53, the latter not being included in the analysis yet. We will shortly come back to the physical origin of the magnetic anisotropy in the present case. It is evident that the preferred direction of **h** is highly dependent on the choice of parameters. To make a superconducting switch we must therefore make sure that the non-superconducting contribution to the free energy favors a different magnetization direction than the superconducting contribution so that the superconducting and non-superconducting contributions compete. We must also check whether a change in the preferred magnetization direction is actually caused by the superconducting contribution to F and not by the non-superconducting contribution.

To understand the angular dependence of the free energy better, we consider the HM/F bilayer by using the simplified model described in the last part of Sec. 2.1. By approximating the HM/F bilayer as one single ferromagnetic layer with Rashba spin-orbit coupling and with periodic boundary conditions along all three axes, we obtain the eigenenergies expressed in Eq. 2.26. If we assume T to be small, we may calculate F_N according to Eq. 2.54. We see that F_N is directly proportional to the sum over negative eigenenergies. By rewriting the eigenenergies for the xy plane ($\theta = \pi/2$) using the polar angle with respect to the y axis, $\theta' = \pi/2 - \phi$, we find that the eigenenergies are on exactly the same form as for the xz plane ($\phi = 0$). The free energy for the xy and xz plane is therefore exactly the same, as expected. By substituting $\theta \longrightarrow \theta + \pi/2$ in Eq. 2.26 we can also show that the eigenenergies and thus the free energy is invariant under any $\pi/2$-rotation in the yz plane. It is also worth noting that for $\lambda = 0$ the angular dependence in Eq. 2.26 vanishes. For a ferromagnetic layer without additional symmetry breaking caused by spin-orbit coupling, the free energy is constant. Since the sum is taken over negative eigenenergies only when computing the free energy, the value of F_N depends on which of the four eigenenergies are negative. Each of the four eigenenergies in Eq. 2.26 have two competing terms. There are several cases:

1. $\epsilon_{\mathbf{k}} < 0$ and the absolute value of the second term is smaller than $|\epsilon_{\mathbf{k}}|$: $E_{1,k}$ and $E_{2,k}$ contribute. The second terms therefore cancel and there is no angular dependence.

2. $\epsilon_{\mathbf{k}} > 0$ and the absolute value of the second term is smaller than $|\epsilon_{\mathbf{k}}|$: $E_{3,k}$ and $E_{4,k}$ contribute. The second terms therefore cancel and there is no angular dependence.

3. The absolute value of the second term is larger than $|\epsilon_{\mathbf{k}}|$:
   $E_{2,\boldsymbol{k}}$ and $E_{4,\boldsymbol{k}}$ contribute. The first terms cancel and the remaining terms have angular dependence.

4. $\epsilon_{\mathbf{k}} < 0$, the absolute value of the second terms in $E_{1,\boldsymbol{k}}$ and $E_{2,\boldsymbol{k}}$ are larger than $|\epsilon_{\mathbf{k}}|$ and the absolute value of the second terms in $E_{3,\boldsymbol{k}}$ and $E_{4,\boldsymbol{k}}$ are smaller than $|\epsilon_{\mathbf{k}}|$:
   Only $E_{2,\boldsymbol{k}}$ contributes. $E_{2,\boldsymbol{k}}$ has an angular dependence.

5. $\epsilon_{\mathbf{k}} > 0$, the absolute value of the second terms in $E_{1,\boldsymbol{k}}$ and $E_{2,\boldsymbol{k}}$ are smaller than $|\epsilon_{\mathbf{k}}|$ and the absolute value of the second terms in $E_{3,\boldsymbol{k}}$ and $E_{4,\boldsymbol{k}}$ are larger than $|\epsilon_{\mathbf{k}}|$:
   Only $E_{4,\boldsymbol{k}}$ contributes. $E_{4,\boldsymbol{k}}$ has an angular dependence.

In case 3 the free energy is $F_N = H_0 + \frac{1}{2}\sum_{\mathbf{k}}(E_{2,\boldsymbol{k}} + E_{4,\boldsymbol{k}})$ and F_N is minimized if $\pm[h\Lambda_y \cos(\theta) + ih\Lambda_z \sin(\theta)\sin(\phi)]$ is zero. If we consider the xz plane, the azimuthal angle ϕ is zero. The free energy in the xz plane is therefore minimized when $\cos(\theta) = 0$, *i.e.* when the magnetization is oriented along the x axis. In case 4 and 5 the free energy depends on only one of the eigenenergies. The free energy is therefore minimized when the contributing eigenenergy is minimized. We see from Eq. 2.26 that the (θ, ϕ) at which F_N is minimized depends on the values of h and λ. The five cases above consider the eigenenergies for a specific choice of $\mathbf{k}$. To obtain the free energy we must sum over all values of $\mathbf{k}$. Since the same case may not hold for all $\mathbf{k}$, the angular dependence of F_N may be even more complicated than considered above. We may therefore conclude that the free energy is highly dependent on h and λ even in this simple approximation. In our numeric calculations of the free energy, we must also take into account finite temperature and separate layers leading to the non-periodic boundary conditions in the x direction. It is therefore reasonable that the angular dependence of F_N changes upon changing h, λ, T and the layer thicknesses. Motivated by this, we may suspect the energy band structure to be responsible for the angular dependence of F_N also in our numerical calculations.

Before turning to the superconducting case, we return to our numerical results for the non-superconducting case and examine the energy band structure of the system in order to explain the change in free energy of the N/HM/F trilayer. If we consider small temperatures so that F_N can be approximated by Eq. 2.51, the free energy is determined by the sum over negative eigenenergies. If eigenenergies are shifted from above to below zero when some parameter is changed or if the eigenenergies below zero shift closer or farther away from zero, $F_N(\theta)$ will

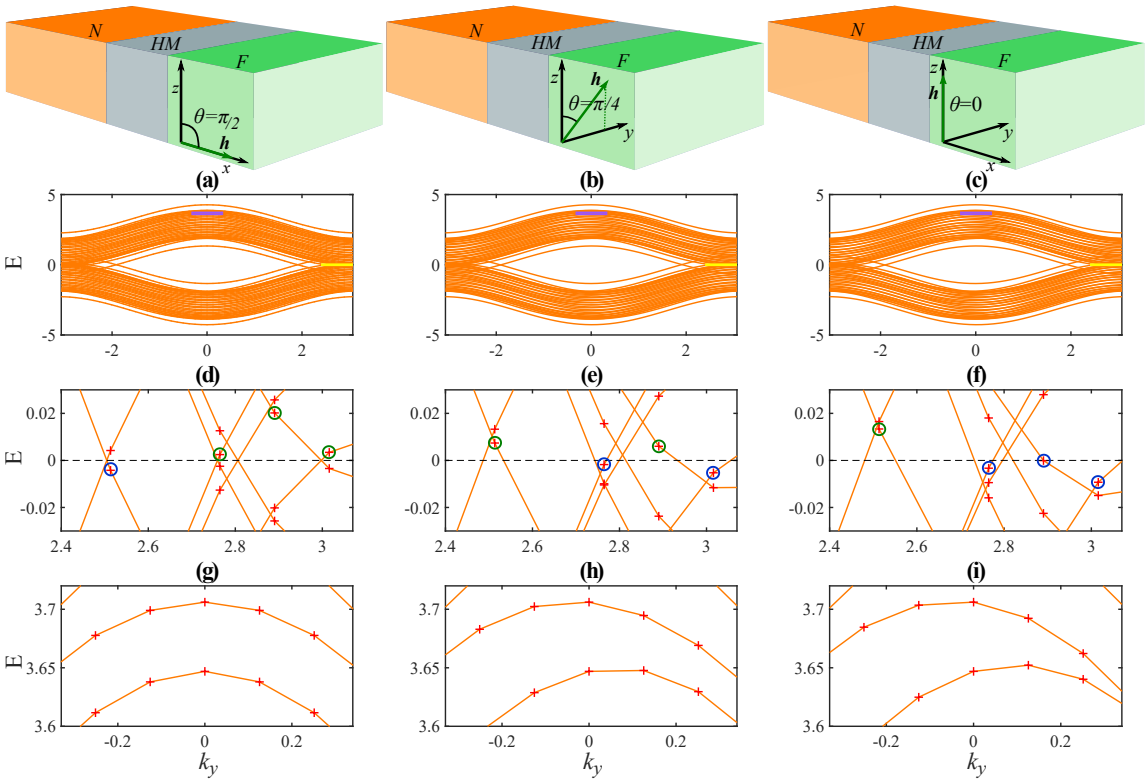

Figure 4.4: Panels (a)-(i) show the energy band structure, $E_{n,k_y,k_z=0}(k_y)$, of the N/HM/S system. The parameters used are given in the main text. In (a), (d), and (g) we have OOP magnetization corresponding to the maximum of F_N for low T. In (b), (e), and (h) we have IP magnetization with $\theta = \pi/4$ corresponding to the maximum IP value of F_N for low T. In (c), (f), and (i) we have IP magnetization with $\theta = 0$ corresponding to the minimum of F_N for low T. Panels (d)-(f) show the band structure in the region marked in yellow in panels (a)-(c). The crosses mark the discrete eigenenergies. The encircled eigenenergies are shifted from above zero energy (green circle) to below zero energy (blue circle) or vice versa when rotating $\boldsymbol{h}$. At $T = 0$ only eigenenergies below zero energy contribute to F_N. Panels (g)-(i) show the band structure in the region marked in purple in panels (a)-(c). Also for these higher energy bands that contribute to F at finite temperatures, there is a shift in the energy bands when rotating $\boldsymbol{h}$.

change. When increasing the temperature from zero, the smallest of the positive eigenenergies will give a contribution to the free energy. The band structure close to zero energy (relative the chemical potential) should therefore be of great importance to the free energy at low temperatures. In Fig. 4.4 we have plotted the energy bands, $E_{n,k_y,k_z=0}(k_y)$, for three different magnetization directions. We consider the out-of-plane case $(\theta, \phi) = (\pi/2, 0)$ and two in-plane cases $(\theta, \phi) = (\pi/4, \pi/2)$ and $(0, 0)$, respectively. We have used the same parameters as in Fig. 4.2. In Fig. 4.4, panels (a)-(c) show the overall band structure of the three magnetization directions. Panels (d)-(f) corresponds to the region marked in

yellow in panels (a)-(c) and show some of the eigenenergies close to zero energy. We see a variation in band structure between the different directions of $\boldsymbol{h}$. As a result some eigenenergies are shifted from above to below zero energy and vice versa. For $T \to 0$ it is therefore likely that the differences in band structure cause the variation in F_N for different magnetization directions. Note that this effective anisotropy is not caused by the discreteness of k_y and k_z. In the limit where we have continuous energy bands, $N_y, N_z \to \infty$, the shifting of the energy bands should cause the same effect since finite sections of the continuous energy bands are shifted from above to below zero energy and vice versa. Panels (g)-(i) correspond to the purple region in panels (a)-(c) and show higher energy bands that only contribute to the free energy at finite temperatures. We see that the band structure has an angular dependence also at finite temperatures. It is therefore reasonable that F_N has an angular dependence also for low, finite temperatures. For temperatures that are sufficiently high to make all energy eigenvalues partially occupied, $F_N(\theta)$ becomes gradually more independently of the magnetization direction. Since $F_N(\theta)$ becomes constant for high temperatures, this indicates that the relative shift between the energy bands is such that it leaves the sum over all eigenenergies constant.

4.3.2 *The superconducting contribution to the free energy*

We now look at a system as shown in Fig. 4.1, where we have a superconductor, *i.e.* $U > 0$. The basic question we seek to address is, is it possible to trigger a reorientation of the preferred magnetization direction in the system via a superconducting phase transition, *i.e.* by adjusting the temperature from above to below T_c? We diagonalize the Hamiltonian described in Eqs. 2.1 and 2.10 numerically using the parameters $N_{x,S} = 9$, $N_{x,HM} = N_{x,F} = 3$, $N_y = N_z = 50$, $\mu_S = 1.8$, $\mu_{HM} = 1.7$, $\mu_F = 1.6$, $U = 1.9$, $h = 1.4$ and $\lambda = 0.6$. For this parameter set the superconducting coherence length is $\xi = 5$. We expect that our results can be generalized to systems with thicker layers as long as the relative thicknesses of the layers compared to the coherence length stay constant, as explained previously in Sec. 2.9.

We first look at the effects on Δ and T_c by adding the heavy-metal and ferromagnetic layer to the superconducting layer. $\Delta(T)$ is plotted in Fig. 4.5 for the S, S/F and S/HM/F systems. Δ and T_c decrease when adding a ferromagnetic layer to the superconducting layer. Adding a heavy-metal layer between the superconduc-

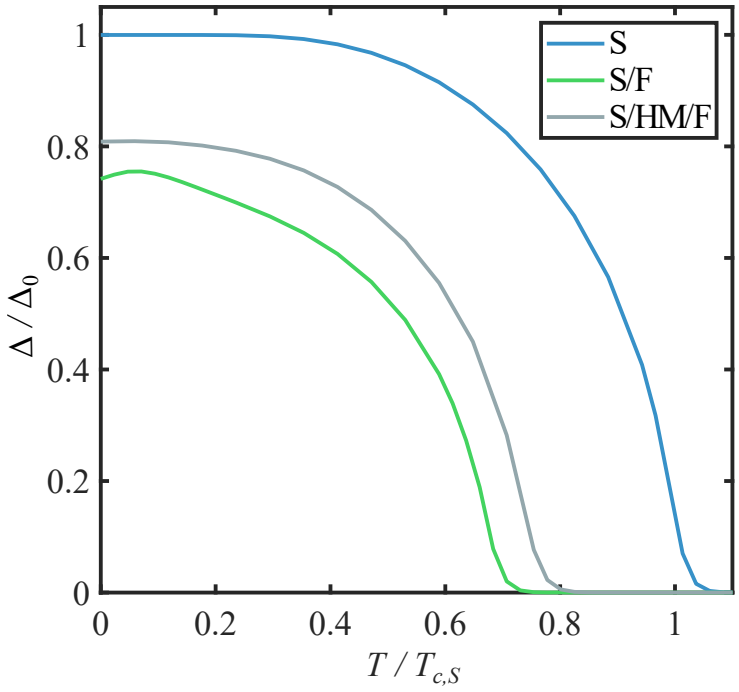

Figure 4.5: The three curves show the superconducting gap as a function of temperature for a S, S/F and S/HM/F system. The parameters are given in the main text, and $\boldsymbol{h} = h\hat{z}$. $T_{c,S}$ is the critical temperature of the superconducting layer computed with $n = 20$ and $m = 200$. Note that the smoothness of the curves at T_c and the decrease in the superconducting gap when decreasing T for the S/F system are numerical artifacts.

tor and the ferromagnet partly shields the superconductor from the effect of the ferromagnet, leading to an effective increase in Δ and T_c. We see that our set of parameters leads to a strong suppression of Δ and T_c, where the HM layer has a visible effect without entirely suppressing the effect of the ferromagnetic layer. Note that the curves in Fig. 4.5 should be at their steepest at T_c. The smoothness of the curves when $\Delta/\Delta_0 \to 0$ is a numerical artifact caused by the fact that it takes more iterations to calculate Δ accurately the closer we get to the critical temperature. Note also that there should be no decrease in the S/F curve when decreasing T at low temperatures. This is a numerical artifact caused by a too low number of k_y and k_z values. A low number of k_y and k_z values is especially problematic for eigenenergies within the superconducting gap, since most energy bands crossing the gap are very steep and cannot be well described by a low number of discrete eigenenergies. For the purely superconducting system there are no eigenstates within the gap, and for the S/HM/F system there are less energy bands crossing the gap than for the S/F system. We therefore only get numerical artifacts for the S/F system. Despite these numerical artifacts, Fig. 4.5 can give us a rough picture of the effects of the additional layers on Δ and T_c.

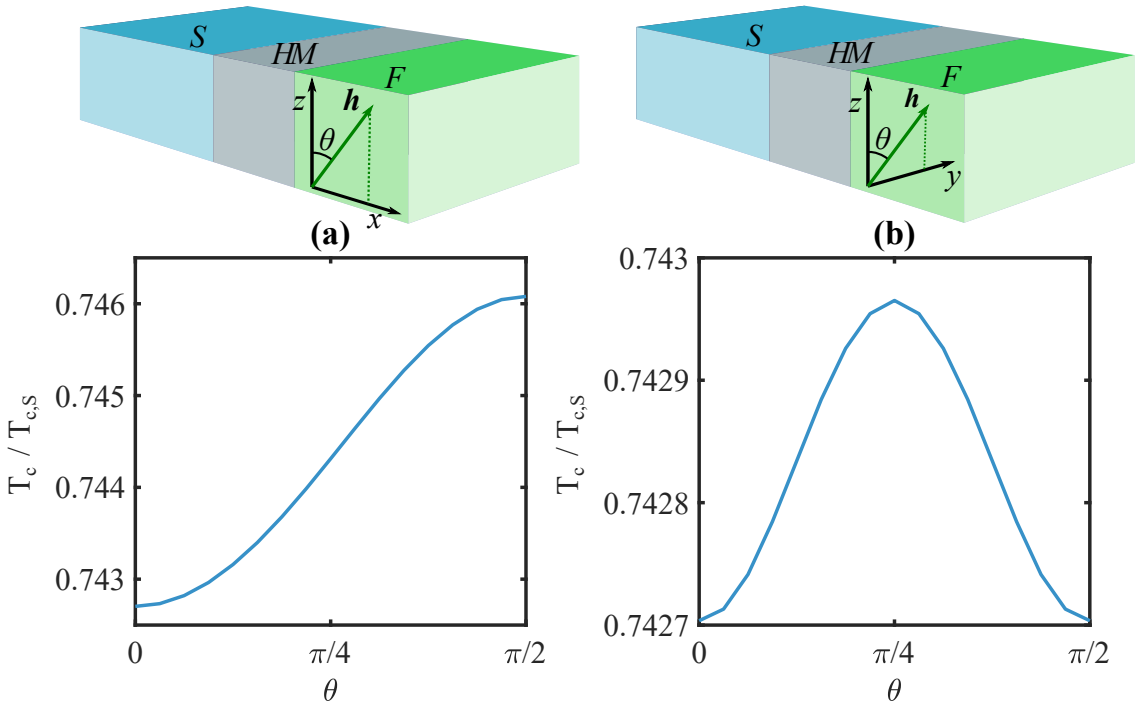

Figure 4.6: Panel (a) shows $T_c/T_{c,S}$ when rotating the magnetization from IP to OOP. Panel (b) shows $T_c/T_{c,S}$ for an IP rotation. The parameters used are specified in the main text.

We now consider the dependence of the superconducting critical temperature on the magnetization direction. Since we have chosen a size of the superconductor larger than the coherence length, the magnitude of the change in critical temperature is rather small. $T_c(\theta)/T_{c,S}$ is plotted in Fig. 4.6. $T_{c,S}$ is the critical temperature of the superconducting layer without the heavy-metal layer and the ferromagnetic layer. In (a) we see a suppression of T_c for IP magnetization as found by experiments [25] on a similar system. Panel (b) shows an additional IP variation in T_c where T_c is suppressed along the cubic axes. In our system, where the thickness of the superconductor is less than twice the coherence length, we do not obtain a substantial bulk region with a constant gap. When calculating T_c, we measure the change in the gap in the middle of the superconducting region when recalculating the gap m times. This means that for superconducting layers that are not much longer than the coherence length, our method for calculating T_c is not entirely accurate unless m is chosen to be very large. This is shown in figure 4.7, where we see that until m is chosen large enough, the calculated value of T_c decreases when increasing m. We set $m = 150$, since the curve has stabilized at this point. The change in T_c when increasing m by 10 is then $10^{-4}T_{c,S}$, which is a small change compared to the total change in T_c when rotating $\boldsymbol{h}$. We have checked that we get a qualitatively similar behavior of T_c to that in Fig. 4.6 for

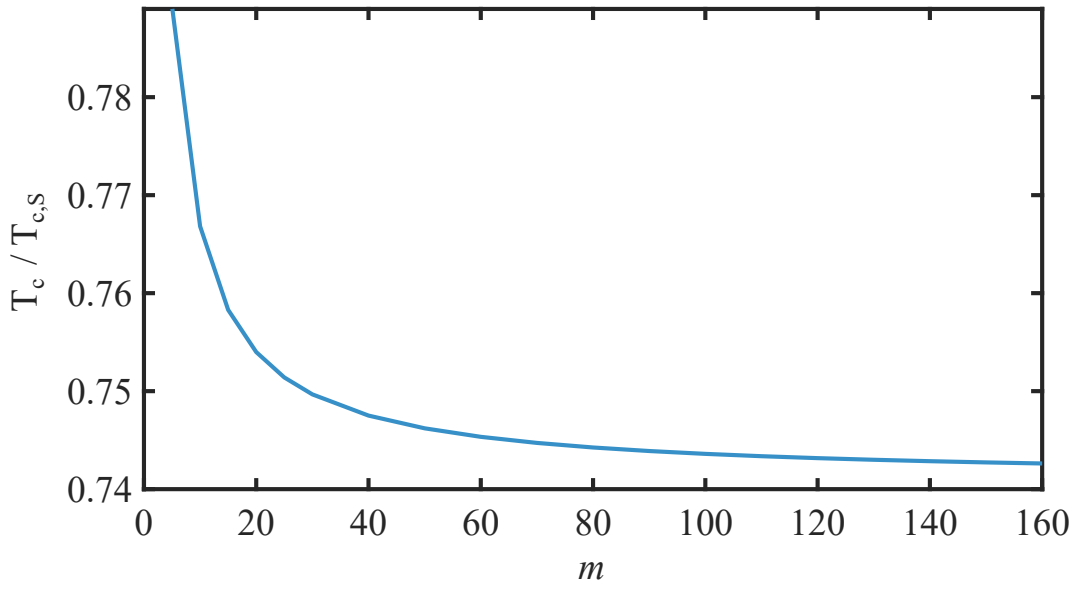

Figure 4.7: The curve shows the calculated value of T_c for different choices of m. To obtain an accurate value for T_c, m must be chosen as large as possible and at least around $m = 150$ where the curve has stabilized. $T_{c,S}$ is calculated with $m = 200$. The parameters are given in the main text. $\boldsymbol{h}$ is directed along the z axis

thicker superconducting layers. $T_{c,S}$ was calculated with $m = 200$. The number of times we divided our temperature interval is $n = 20$, making m the parameter that restricts the accuracy of our T_c calculation.

The reason why we chose a superconductor of only 9 lattice points is that a long superconducting layer requires a low U to obtain a coherence length that is comparable to the thickness of the superconducting layer. This results in a very low critical temperature. At very low temperatures only the eigenenergies below zero contribute to the free energy as shown in Eq. 2.51. If we have few k_y and k_z values the shifting of eigenenergies from above to below zero energy will have a great impact on the free energy. This is especially a problem when computing the non-superconducting contribution to the free energy, where we have no gap and many eigenenergies are close to $E = 0$. We therefore do not get a smooth curve when plotting $F_N(\theta)$. To avoid this problem we must either choose a short superconductor such that we can look at higher temperatures, or let N_y and N_z be very large. The latter option makes the free energy and critical temperature calculations computationally expensive, which is why we chose the former. Note that we would expect a stronger variation in T_c if we made our superconductor comparable to the coherence length rather than almost two times larger. Figure 4.8 shows the dependence of T_c on the thickness of the superconducting layer for our choice of parameters. We see that when increasing $N_{x,S}$ the critical

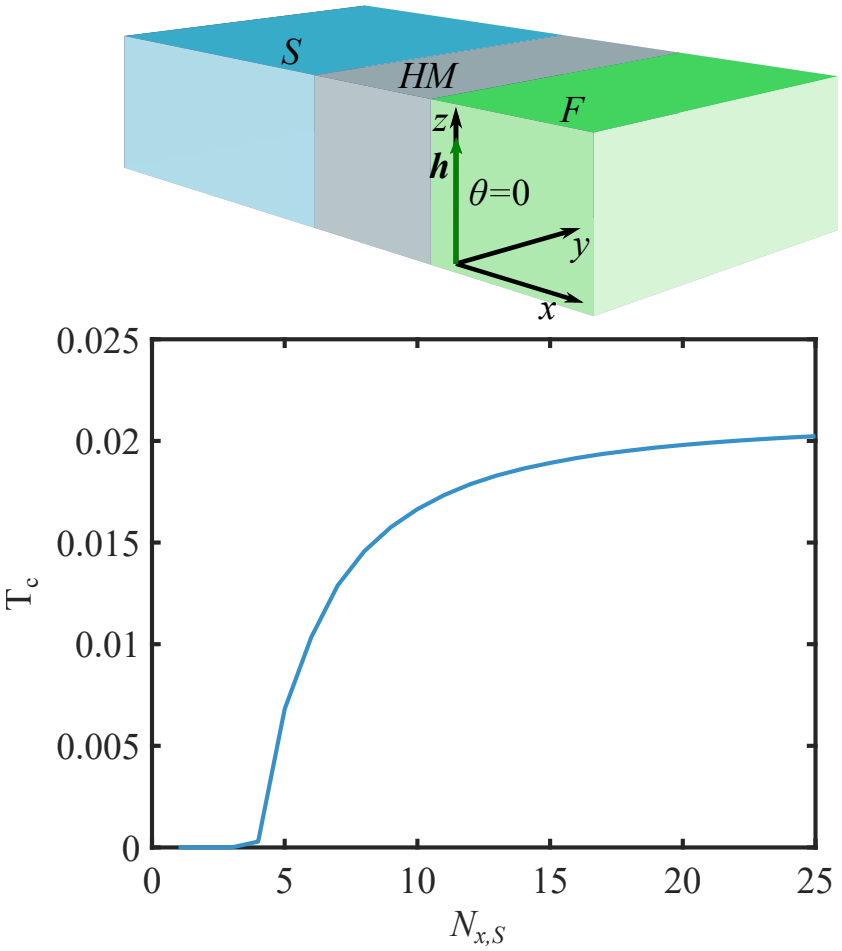

Figure 4.8: The critical temperature of the S/HM/F system decreases when decreasing the thickness of the superconducting layer. Below a certain $N_{x,S}$, superconductivity vanishes completely. For large $N_{x,S}$ the critical temperature approaches the critical temperature of a superconducting layer not coupled to the HM/F bilayer. The parameters are given in the main text. $\boldsymbol{h}$ is directed along the z axis.

temperature approaches the critical temperature of a single superconducting layer, because the HM/F layers becomes negligible. When decreasing $N_{x,S}$ the critical temperature decreases. For $N_{x,S} = 4$ the critical temperature is very small, and for thinner superconducting layers $T_c = 0$, implying that the system is no longer superconducting. Notice that the superconducting layer thickness used to obtain our results, $N_{x,S} = 9$, is within the region where T_c has decreased visibly from the critical temperature of a single superconducting layer, but where superconductivity is still not entirely suppressed. Note that since the coherence length depends on the size of the superconducting region, ξ is not necessarily equal to 5 lattice points for all choices of $N_{x,S}$.

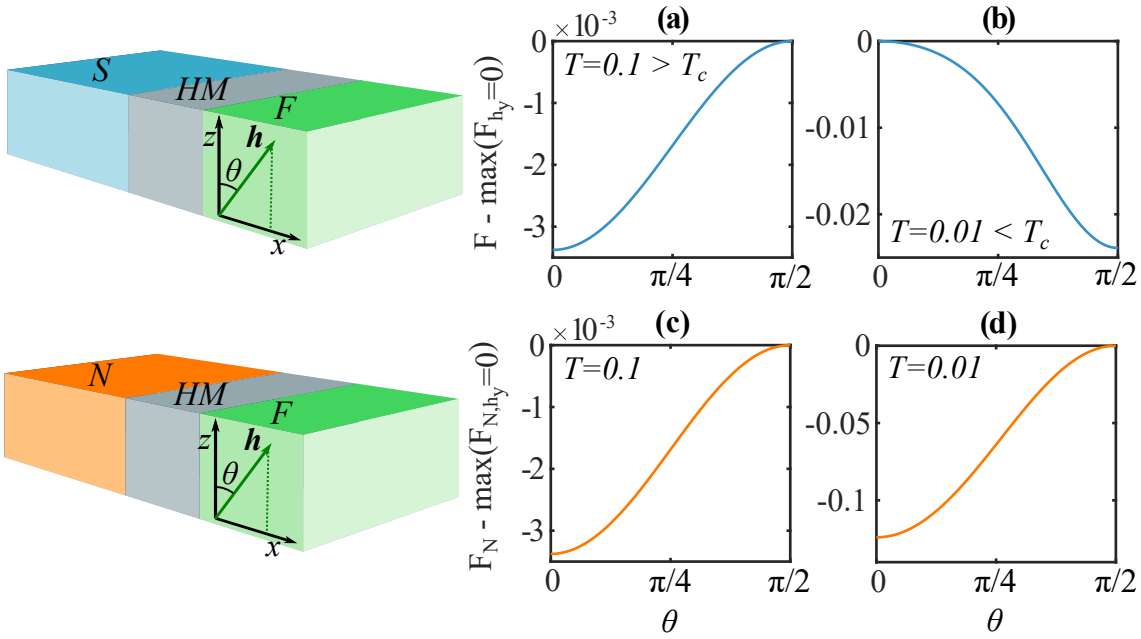

Figure 4.9: Panels (a) and (b) show $F(\theta) - \max(F_{h_y=0})$ in the xz plane for $T = 0.1 > T_c = 0.017$ and $T = 0.01 < T_c$ respectively. Panels (c) and (d) show the normal state contribution to the free energy at the same temperatures. The parameters used are specified in the main text. From (a) and (b) we see that by decreasing the temperature below T_c the preferred magnetization direction of the ferromagnet changes from IP to OOP. Since the normal state contribution shown in (c) and (d) favors IP magnetization, the change in the preferred magnetization direction must be due to superconductivity.

From the angular dependence of T_c we may expect a superconducting contribution to the free energy in which F is increased for the IP orientation, especially along the cubic axes. Figure 4.9 shows the free energy in the xz plane for $T = 0.1 > T_c$, $T = 0.01 < T_c$ and $T = 0.005 < T_c$. As expected, we see a change in the preferred magnetization direction due to the fact that the superconducting contribution to F favors OOP magnetization while the non superconducting contribution to F favors IP magnetization. Figure 4.10 shows the free energy in the yz plane for the same temperatures. For sufficiently low T the superconducting contribution to the free energy starts to dominate, and we have an IP $\pi/4$ rotation of the minimum of the free energy. Notice however that the IP variation in the free energy is weaker than the IP-OOP variation. Therefore OOP magnetization is favored as the ground-state of the system despite the fact that the free energy also varies when the magnetization is rotated IP. For both the xz and yz planes the change in preferred magnetization direction will generally occur at lower temperatures than T_c, meaning that the superconducting contribution does not necessarily start to dominate exactly at the critical temperature. When increasing T, the preferred magnetization direction at some point changes from IP to OOP without any

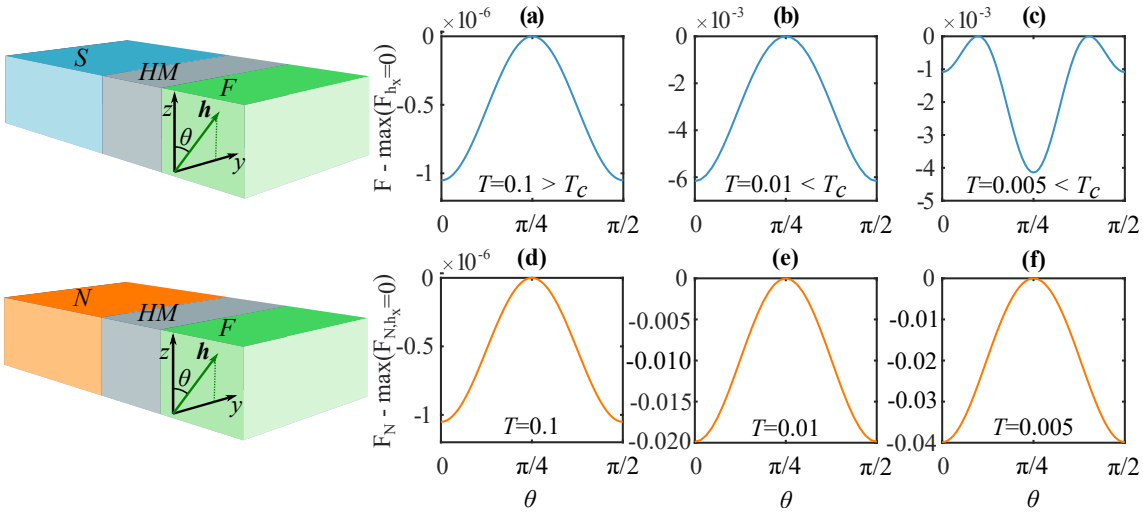

Figure 4.10: Panels (a), (b) and (c) show $F(\theta) - \max(F_{h_x=0})$ in the yz plane for $T = 0.1 > T_c = 0.017$, $T = 0.01 < T_c$ and $T = 0.005 < T_c$ respectively. Panels (d), (e) and (f) show the normal state contribution to the free energy at the same temperatures. The parameters used are specified in the main text. From (a), (b) and (c) we see that the IP minimum of the free energy rotates by $\pi/4$ at some temperature between 0.01 and 0.005, which are both below T_c. Since the normal state contribution shown in (d), (e) and (f) favors magnetization along the crystal axes at all of these three temperatures, the change in the preferred magnetization direction must be due to superconductivity.

involvement of superconductivity. This is exemplified by the behavior of $F_N(\theta)$ in Fig. 4.2 which was plotted for a temperature $T > T_c$. The superconducting switch must therefore be operated over a limited temperature range around the temperature at which the change in the preferred magnetization direction occurs. However, we will later discuss how the superconducting contribution to the free energy, causing an effective magnetic anistropy, can be experimentally detected even in the cases in which the superconducting contribution is not sufficiently strong to change the preferred magnetization orientation.

The angular dependence of T_c and of the superconducting contribution to F can be explained by the generation of triplet Cooper pairs. At an S/F interface, the spin splitting of the energy bands of the ferromagnet causes transformation of singlet Cooper pairs into opposite-spin triplets. The Rashba spin-orbit coupling terms in the Hamiltonian in Eq. 2.10 are proportional to $\sin(k_y)$ and $\sin(k_z)$. Therefore, electrons experience different energies if the sign of (k_y, k_z) is changed. This symmetry-breaking causes triplet generation at the S/HM interface, and enables equal-spin triplet generation, depending on the relative orientation of the magnetization and the spin-orbit field. In Fig. 4.12 we have plotted the triplet amplitudes corresponding to OOP magnetization and the IP magnetization

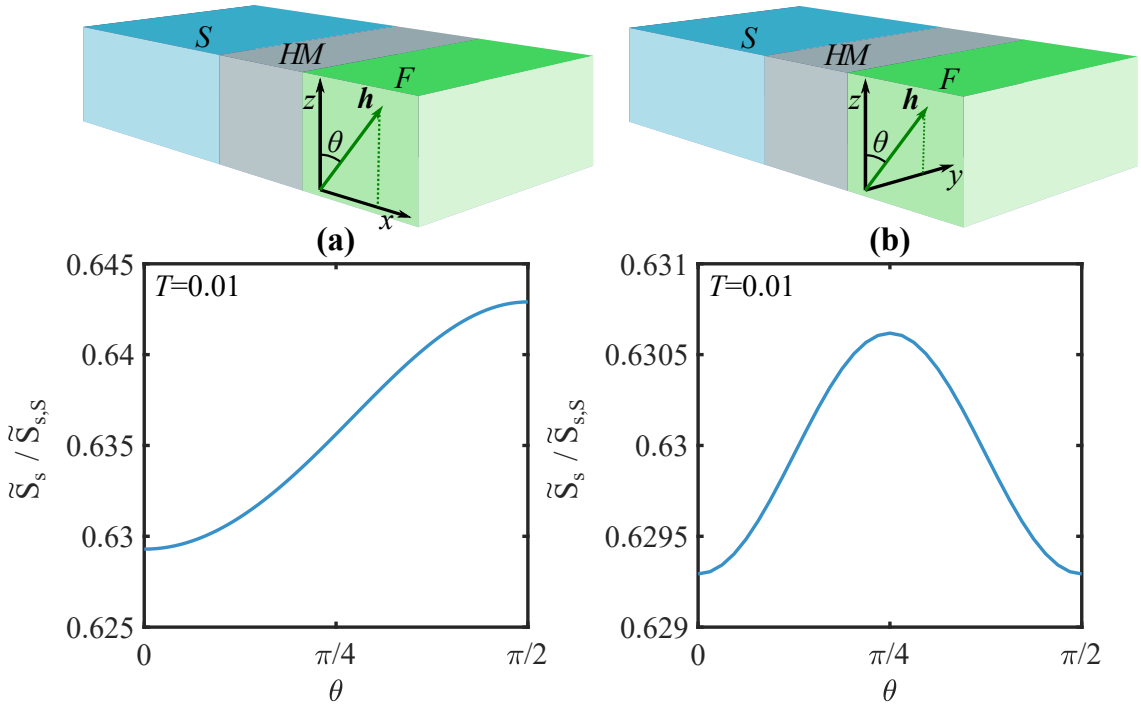

Figure 4.11: Panels (a) and (b) show the singlet amplitude $\tilde{S}_s/\tilde{S}_{s,S}$ in the xz and yz planes. The parameters are given in the main text. $T = 0.01 < T_c = 0.017$.

directions $(\theta, \phi) = (\pi/2, \pi/4)$ and $(0, 0)$, respectively. The relative time used in the computation of the s-wave odd-ω triplet amplitudes is $\tau = 5$. We see that there is a generation of short-range and long-range triplet amplitudes depending on the magnetization direction. The generation of triplet amplitudes lowers the singlet amplitude in the superconductor, since singlet Cooper pairs are converted into triplet Cooper pairs. In Fig. 4.11 we have plotted $\tilde{S}_s/\tilde{S}_{s,S}$, where $\tilde{S}_s$ is defined in Eq. 2.55. $\tilde{S}_{s,S}$ is the singlet amplitude in the superconducting layer without the heavy-metal layer and the ferromagnetic layer. We see that the singlet amplitude is suppressed for IP magnetization, especially along the cubic axes. Since the singlet amplitude is proportional to the superconducting order parameter, a suppression of the singlet amplitude should lead to a decrease in T_c and an increase in F. This is exactly what we have seen from Figs. 4.6, 4.9 and 4.10. We may therefore explain the variation in T_c and F by the generation of triplet amplitudes depending on the relative orientations of the spin-orbit field and the magnetization.

The diffusive limit calculations in Ref. [25] found an IP suppression of T_c as in our calculations. However, in the diffusive limit T_c was found to be invariant under IP rotations of the magnetization. In Ref. [25] the HM/F layer is modeled as a single layer with the exchange field and the spin-orbit coupling as homogeneous background fields, which similarly to what occurs in the ballistic limit results

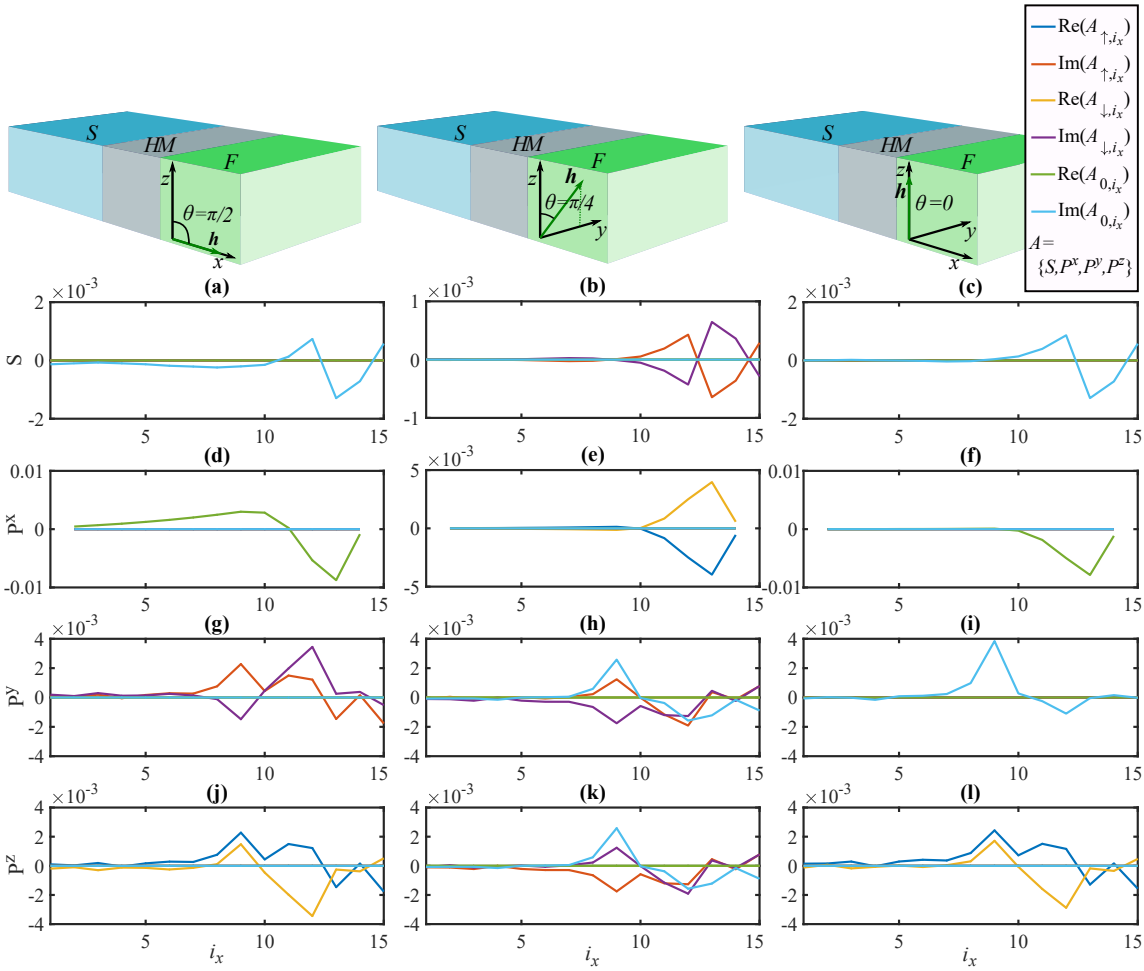

Figure 4.12: Panels (a)-(l) show the triplet amplitudes generated in the S/HM/F system at $T = 0.01 < T_c = 0.017$. The parameters are given in the main text. Panels (a)-(c) show the s-wave triplet amplitudes, panels (d)-(f) show the p_x-wave triplet amplitudes, panels (g)-(i) show the p_y-wave triplet amplitudes and panels (j)-(l) show the p_z-wave triplet amplitudes. The first column corresponds to OOP magnetization, the second column corresponds to IP magnetization with $\theta = \pi/4$ and the third column corresponds to IP magnetization with $\theta = 0$. Note that all amplitudes that are not visible in the plots are either zero or close to zero.

in a generation of both short-range and long-range triplets close to the interface. The IP suppression of T_c compared to T_c at OOP magnetization is both for the ballistic and the diffusive limit a result of differences in the triplet generation when the exchange field is parallel and perpendicular to the interface between the superconductor and the HM/F layer. The change in T_c under IP rotations of the magnetization reported in this thesis is a result of differences in the triplet generation at different IP magnetization directions due to the crystal structure of the lattice in the HM region. This is the reason why these variations are not found in the diffusive limit calculations in Ref. [25], which does not model the S/HM/F

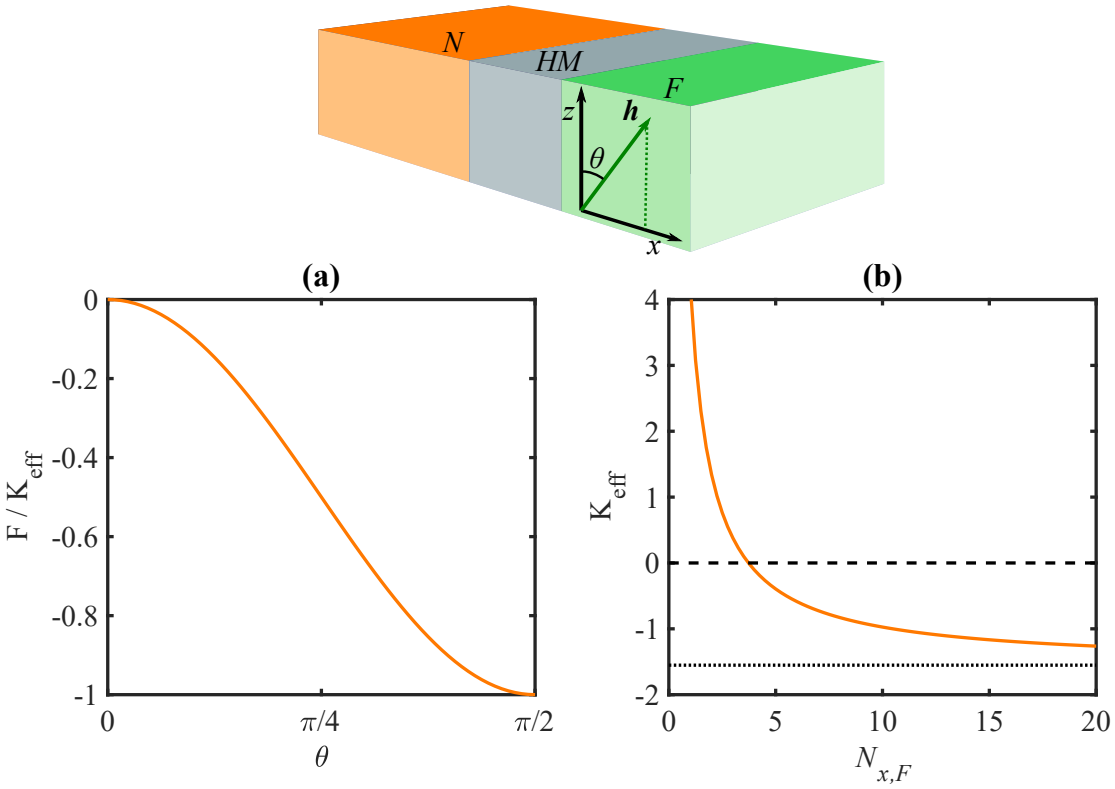

Figure 4.13: Panel (a) shows the perpendicular/shape anisotropy contribution to F. Panel (b) shows the effective anisotropy constant, K_{eff}, as a function of the ferromagnet thickness.

system by a lattice model. For very thin films, like the ones considered experimentally in Ref. [25], we expect the sample to approach the ballistic limit such that a variation in T_c for IP rotations of the magnetization should be observable.

4.3.3 *The shape anisotropy contribution to the free energy*

Until now, we have disregarded the intrinsic magnetic anisotropy of the thin ferromagnetic film, which does not depend on the coupling to itinerant electrons c and $c^\dagger$ in our model. For concreteness, we will now consider the case of a Pt heavy-metal layer and a Co(111) ferromagnetic layer. In this case, the anisotropy constants are [31] $K_v = -0.77$ MJ/m^3, $K_i = 1.15$ mJ/m^2 and $K_s = -0.28$ mJ/m^2. The lattice constants of Co are [53] $a_x = a_y = 251$pm and $a_z = 407$pm. The anisotropy contribution to the free energy is plotted in Fig. 4.13(a) for this choice of parameters. The effective anisotropy constant defined in Eq. 2.53 is plotted in Fig. 4.13(b) as a function of $N_{x,F}$. By solving $K_{\text{eff}} = 0$, we find that the anisotropy

contribution to the free energy favors an OOP magnetization for $N_{x,F} \leq 3$ and an IP magnetization for $N_{x,F} \geq 4$. Since we may generalize our results to any system size as long as the layer thickness relative to ξ stays constant, we may consider a system with any $N_{x,F}$. By making the ferromagnetic layer thick enough to give a contribution to $F(\theta)$ favoring an IP magnetization, but thin enough that K_{eff} is small, it is in principle possible to get an IP-OOP superconducting switch despite the fact that the non-superconducting contribution to F has gained an extra term. We may also make the ferromagnetic layer so thick that the non-superconducting contribution to the free energy enforces IP magnetization. Since the shape anisotropy contribution to the free energy is invariant under rotations in the yz plane, we may get a $\pi/4$ rotation in the magnetization as shown in Fig. 4.10. This means that an IP superconducting switch in the magnetization direction is in principle possible, even if the preferred magnetization direction is OOP when disregarding shape anisotropy. The possibility of changing the preferred direction in the yz plane is interesting as the magnetic field of the ferromagnet in such a case is not perpendicular to the superconducting layer. We therefore disregard demagnetising currents close to the interface in the superconducting region as well as vortex formation inside the superconductor [54]. For magnetization with an OOP component, demagnetization effects may be of greater importance.

It is worth noting that even if the ferromagnetic layer is so thick that the non-superconducting contribution dominates, it may still be possible to measure the superconducting contribution to the free energy. The superconducting contribution to the free energy in an F1/S/F2 system can be measured [55] by applying an external magnetic field and measuring the critical field needed to flip the magnetization from an antiparallel to a parallel alignment. It should be possible to do similar measurements on the S/HM/F-system. For instance, one could apply an external field to flip the magnetization of the ferromagnet between the IP and the OOP direction. The superconducting contribution favors OOP magnetization and would therefore reduce the critical field needed to flip the magnetization from IP to OOP orientation. Such a reduction of the critical field would thus be an evidence of a superconductivity-induced anisotropy term for the ferromagnet.

4.4 CONCLUDING REMARKS

The work presented in this chapter predicts a possible reorientation of the magnetization direction of a thin-film ferromagnet upon lowering the temperature below

the superconducting critical temperature T_c when the ferromagnet is separated from a superconductor by a thin heavy-metal film. Especially for a thin ferromagnetic film with weak shape anisotropy, the superconducting phase transition should induce an in-plane to out-of-plane rotation of the magnetization. We have also found that if the shape anisotropy is strong enough to enforce an in-plane magnetization direction, a $\pi/4$ in-plane rotation of the magnetization can occur upon lowering the temperature below T_c. In addition, we have considered the dependence of T_c on the magnetization direction. Here, we find that our lattice-model calculations predict an additional in-plane variation in T_c compared to previous diffusive-limit calculations, which only show an in-plane suppression of T_c independently of the in-plane magnetization orientation. Both the T_c suppression and the magnetization reorientation can be explained by the generation of short-range and long-range triplet Cooper pairs close to the interfaces depending on the relative orientations of the exchange field of the ferromagnet and the spin-orbit field of the heavy-metal. The results presented in this chapter should be reproducible experimentally for systems with the same ratio between the layer thickness and the superconducting coherence length.

5

T_c MODULATION IN S/HM BILAYERS

5.1 INTRODUCTION AND MOTIVATION

Experiments have previously demonstrated how the critical temperature of F1/S/F2 and F1/F2/S systems can be modulated by changing the relative orientation of the magnetization of the two homogeneous ferromagnets [17–21]. Diffusive limit calculations [22–25], and the ballistic limit calculations presented in the previous chapter, have also shown that a similar modulation of the critical temperature can be expected when rotating the magnetization of a single homogeneous ferromagnet in a S/HM/F or S/HM/F/HM heterostructure. For such a system, it has been shown experimentally that the critical temperature is suppressed for an in-plane magnetization compared to the out-of-plane magnetization [25]. Compared to the S/F structure, the thin HM films boosts the Rashba spin-orbit coupling that breaks the invariance under magnetization reorientations. The Rashba spin-orbit coupling leads to a symmetry breaking that allows for a variation in the triplet generation when rotating the magnetization of the S/HM/F system. In fact, while ferromagnetism only leads to a spin-splitting of the energy bands of spin-up and spin-down electrons [8], Rashba spin-orbit coupling is in addition odd under inversion of the momentum component perpendicular to the spin-orbit field. We may therefore suspect that while a S/F structure is invariant under rotations of the magnetization, a S/HM structure is not invariant under rotations of the Rashba spin-orbit field.

Motivated by this, we explore the possibility of a modulation of the superconducting critical temperature under reorientations of the Rashba spin-orbit field in a bilayer consisting of a superconductor and a heavy normal-metal, without the presence of ferromagnetism. We discover a suppression of the critical temperature for in-plane spin-orbit fields, and also a variation in the suppression of the critical temperature depending on the orientation of the in-plane component of the spin-orbit field. We further find that the difference in critical temperature for IP and OOP spin-orbit fields can at least partly be accounted for by the absence

of s-wave odd-frequency triplets for OOP spin-orbit fields. Since s-wave triplet amplitudes are robust with respect to impurity scattering, we expect our prediction of an IP suppression of the critical temperature to be observable in diffusive systems, as well as in the ballistic systems covered by our theoretical framework.

5.2 MODEL

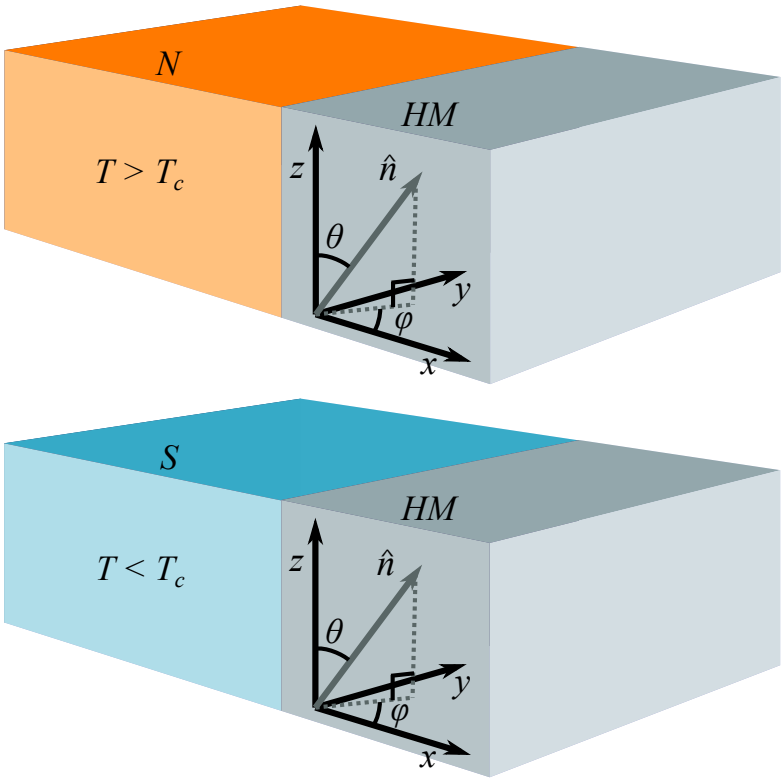

Figure 5.1: In order to demonstrate a T_c suppression depending on the direction of the spin-orbit field, we consider a system consisting of a superconducting layer and a heavy-metal layer with Rashba spin-orbit coupling. The direction of the spin-orbit field $\hat{n}$ is described by the polar and azimuthal angles (θ, ϕ) with respect to the z axis. We model our system as a 3D cubic lattice with interface normal along the x direction. The figure is not to scale.

For our main calculations, we consider a 3D cubic lattice of size $N_x \times N_y \times N_z$ as shown in Fig. 5.1. The lattice consists of two layers: a superconducting layer and a heavy-metal layer with Rashba spin-orbit coupling. The spin-orbit field is directed along $\hat{n} = \hat{x}\cos(\phi)\sin(\theta) + \hat{y}\sin(\phi)\sin(\theta) + \hat{z}\cos(\theta)$, where θ is the polar angle with respect to the z axis and ϕ is the azimuthal angle. Since $\hat{n}$ can have a component parallel to the interface, we symmetrize the spin-orbit

coupling term of the Hamiltonian as described in Sec. 2.2. For the remaining terms we follow the theoretical framework presented in Sec. 2.1. The system is thus described by the Hamiltonian given in Eq. 2.49, where the terms are only nonzero in their respective regions. Recall that we choose our interface normal to be directed along the x axis, and that we use periodic boundary conditions in the y and z direction. As before, we scale all energies to the hopping element t and all lengths to the lattice constant a, and we set the reduced Planck constant $\hbar$ and the Boltzmann constant k_B equal to 1, as in the previous sections. All temperatures are therefore scaled by t/k_B in the presentation of the results.

In this chapter, we will also consider a 2D square lattice HM/S system by following the theoretical framework presented in Ch. 3. We consider the simpler 2D system in order to explain the changes in triplet generation when $\hat{n}$ is reoriented from an IP ($\hat{n} = \hat{z}$) to an OOP ($\hat{n} = \hat{x}$) direction. In the $\hat{n} = \hat{x}$ case, the nonzero singlet and triplet retarded anomalous Green's functions are given by the analytical expressions in Eqs. 3.152 and 3.158. In the $\hat{n} = \hat{z}$ case, the singlet and triplet retarded anomalous Green's functions must be calculated numerically. In order to compare the results obtained from the theoretical frameworks described in Chs. 2 and 3, we also consider a 2D square lattice of size $N_x \times N_y$ using the same approach as in Ch. 2. In order to treat a 2D system by the theoretical framework presented in Ch. 2, we consider a system with one atomic layer in the z direction and apply periodic boundary conditions only in the y direction. For comparison, we also consider a 2D F/S system with magnetization along the z direction.

5.3 RESULTS AND DISCUSSION

We diagonalize the Hamiltonian given in Eq. 2.49 numerically for the S/HM system shown in Fig. 5.1. We first consider the superconducting critical temperature using the parameters $N_{x,S} = 7$, $N_{x,HM} = 3$, $N_y = N_z = 85$, $\mu_S = 1.9$, $\mu_{HM} = 1.7$, $U = 2.1$ and $\lambda = 0.8$. This choice of parameters gives a superconducting coherence length of $\xi = 4$. We compute the critical temperature by the improved method described in Sec. 2.4. $T_c/T_{c,S}$ is plotted in Fig. 5.2. $T_{c,S}$ is the critical temperature of the superconducting layer without proximity to a heavy-metal layer. In Fig. 5.2(a) we see a suppression of the critical temperature for an IP spin-orbit field compared to an OOP spin-orbit field. Figure 5.2(b) shows that there is also an IP variation in T_c, which for this choice of parameters gives the strongest in-plane suppression of T_c for spin-orbit fields oriented at a $\pi/4$ angle

with respect to the z axis. In computing the critical temperature, we have used $n = 20$ and $m = 35$. $T_c(m)$ is plotted in Fig. 5.3, and we see that at $m = 35$ the change in T_c by increasing m is small. By increasing m by 10, the change in T_c is proportional to $1/100$ of the change in T_c under IP rotations. $T_{c,S}$ was calculated with $n = 20$ and $m = 100$. If we consider another set of parameters, $N_{x,S} = 5$,

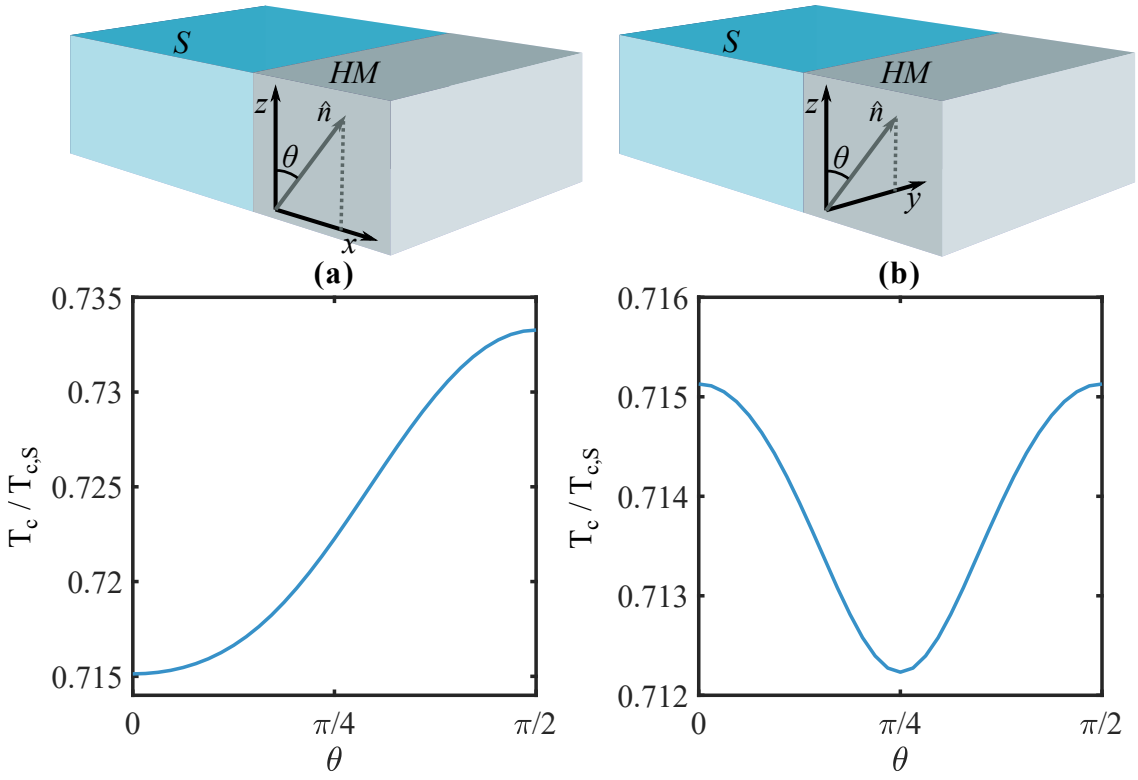

Figure 5.2: Panels (a) and (b) show $T_c/T_{c,S}$ for rotations of $\hat{n}$ in the xz and yz planes respectively. The parameters are specified in the main text. Notice that for the given choice of parameters we have an IP suppression of the critical temperature at $\theta = \pi/4$.

$N_{x,HM} = 2$, $N_y = N_z = 100$, $\mu_S = 1.9$, $\mu_{HM} = 1.7$, $U = 1.9$ and $\lambda = 0.2$ giving a coherence length of $\xi = 7$, we instead find the IP suppression to be strongest along the y axis and z axis. For this choice of parameters $T_c/T_{c,S}$ is plotted in Fig. 5.4. Notice that compared to what we find from Fig 5.2(a) and (b), the IP variation in Fig. 5.4(b) is much smaller compared to the IP to OOP variation in Fig. 5.4(a). Also, although the ratio between the coherence length and the superconductor thickness is much larger for the second set of parameters, the T_c modulation is weaker since the spin-orbit coupling is weaker. We have used $n = 25$ and $m = 40$, which gives a change in T_c proportional to $1/1000$ of the IP change in T_c when increasing m by 10. $T_{c,S}$ was calculated with $n = 25$ and $m = 100$. We have found that the critical temperature is always suppressed for IP spin-orbit fields compared to an OOP spin-orbit field, as shown in Figs. 5.2(a) and 5.4(a). For IP rotations, T_c may be suppressed either for spin-orbit fields

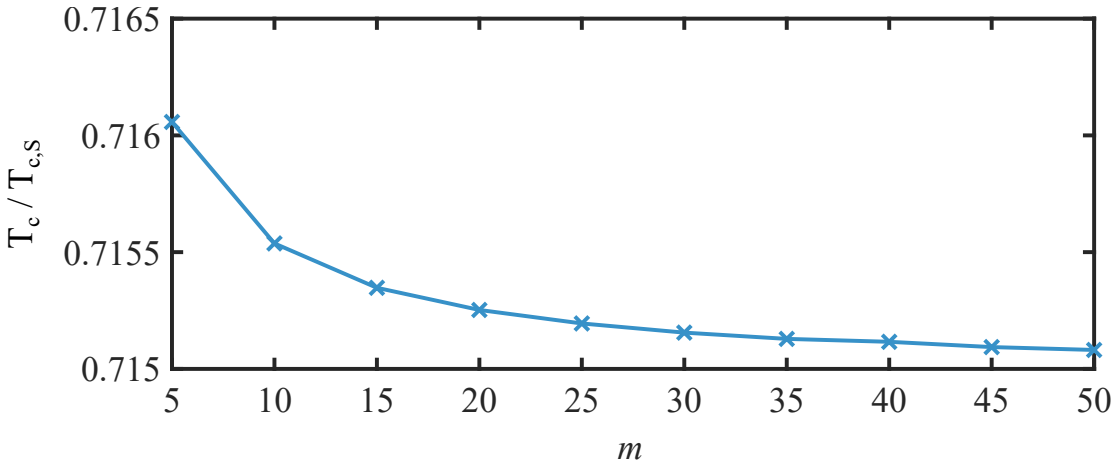

Figure 5.3: The curve shows the calculated value of $T_c/T_{c,S}$ for different choices of m with $\hat{n}$ directed along the z axis for the same set of parameters as in Fig. 5.2. The critical temperature in Fig. 5.2 was calculated using $m = 35$ where $T_c(m)$ has flattened.

along $\hat{y} + \hat{z}$ as in Fig. 5.2(b), or along the cubic axes as in Fig. 5.4(b). We will return to addressing why different parameter choices result in different behaviors of T_c under IP rotations shortly.

The change in the critical temperature when rotating the spin-orbit field can be explained by generation of triplet Cooper pairs that lowers the s-wave singlet amplitude in the superconducting region. The total s-wave singlet amplitude in the superconducting region given by Eq. 2.66 is plotted in Figs. 5.5 and 5.6 for the first and second set of parameters, respectively. We see that the variation in the total singlet amplitude shown in Fig. 5.5 is of the same form as the variation in T_c shown in Fig. 5.2, and that the variation in the total singlet amplitude shown in Fig. 5.6 is of the same form as the variation in T_c shown in Fig. 5.4. The suppression of the critical temperature can therefore be attributed to the suppression of the superconducting gap caused by singlet to triplet generation. If we further investigate the triplet amplitudes present for different orientations of the spin-orbit field, we find that the s-wave odd-frequency anomalous triplet amplitude is absent for $\hat{n} = \hat{x}$, *i.e.* if $\hat{n}$ has no IP component. For all other orientations of the spin-orbit field, the s-wave odd-frequency anomalous triplet amplitude is nonzero. This suggests that the IP to OOP change in the superconducting critical temperature is at least partly caused by the increase in the s-wave triplet amplitude from zero at $\hat{n} = \hat{x}$ to an increasing finite value as the IP component of $\hat{n}$ increases. For the p-wave even-frequency triplet amplitudes, we find that the p_x-wave triplet amplitude is zero for $\hat{n} = \hat{x}$, the p_y-wave triplet amplitude is zero for $\hat{n} = \hat{y}$ and that the p_z-wave triplet amplitude

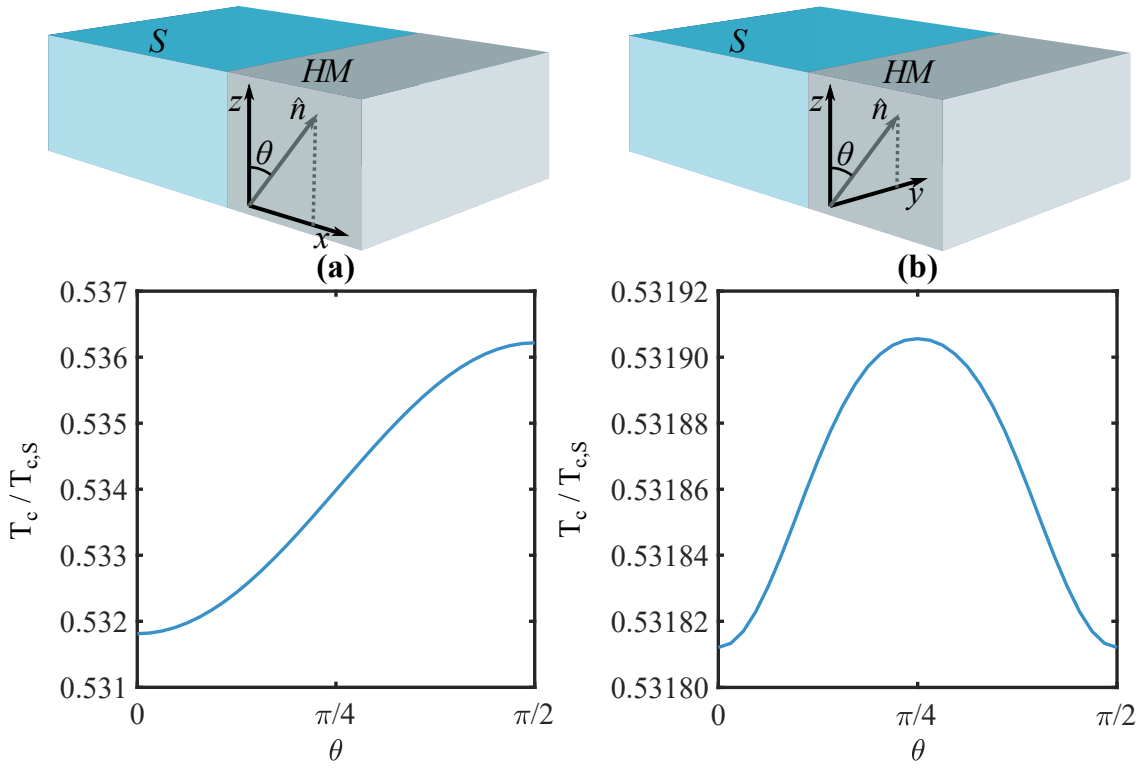

Figure 5.4: Panels (a) and (b) show $T_c/T_{c,S}$ for rotations of $\hat{n}$ in the xz and yz planes respectively. The parameters are specified in the main text. Notice that for the given choice of parameters we have an IP suppression of the critical temperature for $\hat{n}$ along the y and z axes.

is zero for $\hat{n} = \hat{z}$. The remaining p-wave triplet amplitudes are nonzero. This may be explained by the fact that the spin-orbit coupling is only odd in the $\boldsymbol{k}$-component perpendicular to the direction of the spin-orbit field. It is hard to determine how strongly each of the p-wave triplet amplitudes contributes to the variation in T_c under rotations of $\hat{n}$, and also whether the s-wave triplet amplitude contributes to the IP variation in T_c. However, the variation in the s-wave triplet amplitude under IP to OOP rotations is of special importance as the s-wave triplet amplitude is the only triplet amplitude robust with respect to impurity scattering. In diffusive materials, all physical quantities are effectively averaged over all $\boldsymbol{k}$ [56], and the s-wave amplitude is the only amplitude that is even under all inversions in k-space. We may therefore expect an IP suppression of the critical temperature also in diffusive materials.

In order to explain the absence of the s-wave triplet amplitude for $\hat{n} = \hat{x}$, we consider a 2D square lattice and follow the theoretical framework presented in Ch. 3. For $\hat{n} = \hat{x}$, the singlet and opposite-spin triplet anomalous Green's functions are given by Eqs. 3.152 and 3.158, and their symmetries under inversion

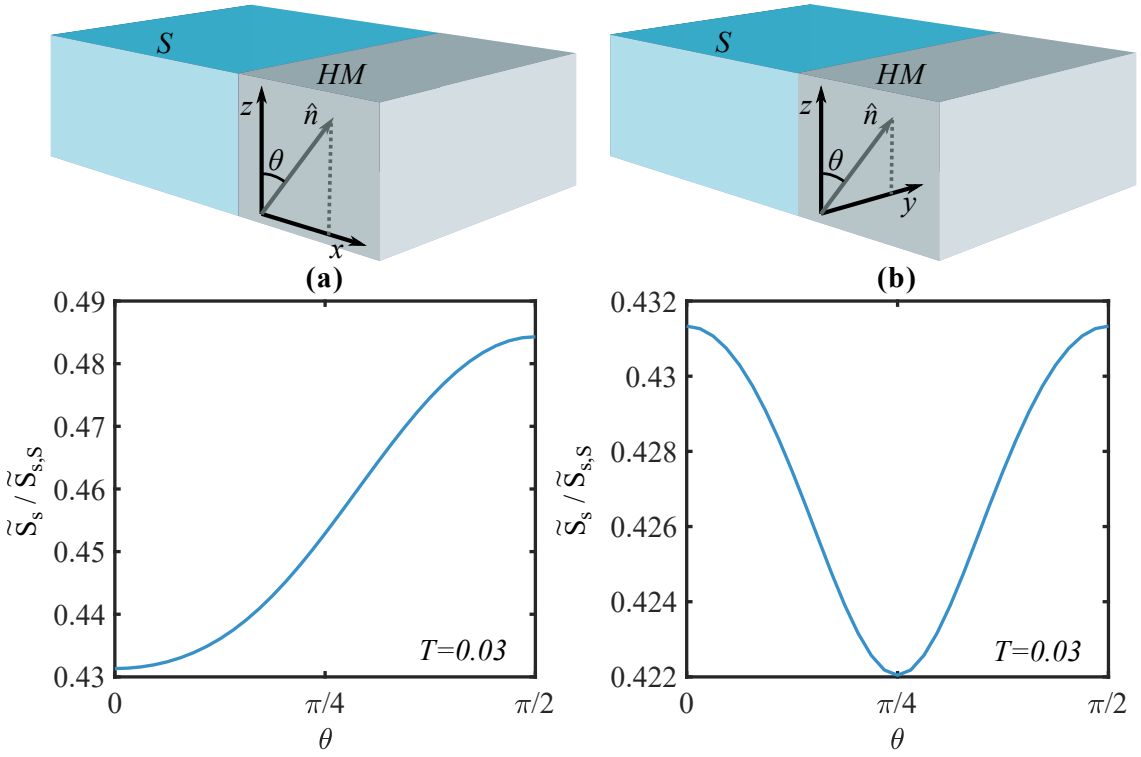

Figure 5.5: Panels (a) and (b) show the singlet amplitude $\tilde{S}_s/\tilde{S}_{s,S}$ for rotations of $\hat{n}$ in the xz and yz planes respectively. $T = 0.03$ is just below the minimum value of the critical temperature, $T_{c,\min} = 0.033$. The choice of parameters is the same as in Fig. 5.2. We see that the singlet amplitude has a similar angular dependence as the critical temperature.

of the spatial x coordinate and the momentum in the y direction are shown in Table 3.2. There are no equal-spin triplet anomalous Green's functions present. The spatial symmetries of the singlet and opposite-spin triplet retarded anomalous Green's functions allows for the s-wave singlet amplitude, the p_x-wave singlet amplitude, the p_y-wave opposite-spin triplet amplitude and the d_{xy}-wave opposite-spin triplet amplitude to be nonzero. There may also be $d_{x^2-y^2}$-wave singlets in the system, but as discussed in Sec. 3.3 their presence is harder to prove. There is no s-wave triplet amplitude present. At the first glance, it might seem strange that the odd-frequency s-wave triplet amplitude is zero, when it is nonzero for a 2D F/S structure with magnetization along the z axis. Although the Hamiltonians of these systems are of a similar form (see Eqs. 3.108 and 3.120), they allow for the existence of different triplet amplitudes. As can be seen from Eqs. 3.169 and 3.175, and from Table 3.4, all singlet and triplet amplitudes in the F/S system are invariant under the inversion of the momentum in the y direction, p_y. In the HM/S system the k_y dependence of the allowed k_x values causes the triplet amplitudes to be odd in p_y. The crucial difference leading to a generation of p_y- and d-wave triplets in the HM/S system rather than s- and p_x-wave triplets

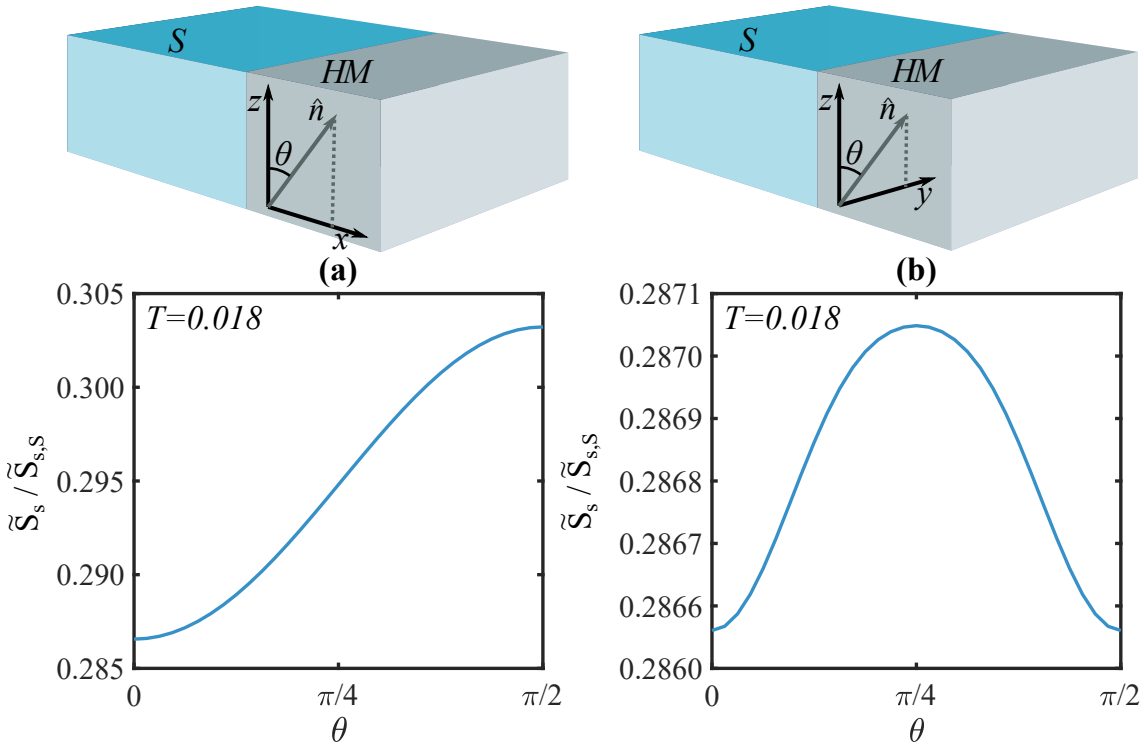

Figure 5.6: Panels (a) and (b) show the singlet amplitude $\tilde{S}_s/\tilde{S}_{s,S}$ for rotations of $\hat{n}$ in the xz and yz planes respectively. $T = 0.018$ is just below the minimum value of the critical temperature, $T_{c,\min} = 0.019$. The choice of parameters is the same as in Fig. 5.4. We see that the singlet amplitude has a similar angular dependence as the critical temperature.

as in the F/S system, is therefore the k_y dependence of the spin-orbit coupling terms in the Hamiltonian. For a HM/S structure with $\hat{n} = \hat{z}$, we compute the singlet and triplet retarded anomalous Green's functions numerically following the theoretical framework in Ch. 3. From Table 3.3, we see that in addition to the singlet and triplet amplitudes present for $\hat{n} = \hat{x}$, there exist nonzero equal-spin triplet amplitudes. These must contain p_x-, p_y-, and d_{xy}-wave triplets and they must also include either s-wave or $d_{x^2-y^2}$-wave triplets, or both. In our ballistic limit calculations, the variations in the singlet amplitude under rotations of $\hat{n}$ is affected by variations in all of these different triplet amplitudes.

In order to connect the above results to those obtained from the theoretical framework in Ch. 2, we follow the theoretical framework presented in Ch. 2 and plot the triplet amplitudes of the 2D S/HM and S/F systems. For our S/HM system, we choose the parameters $N_{x,S} = 7$, $N_{x,HM} = 3$, $N_y = 85$, $\mu_S = 1.9$, $\mu_{HM} = 1.7$, $U = 2.1$ and $\lambda = 0.8$. These are the same parameters that are used in obtaining Figs. 5.2 and 5.5, except that we consider a 2D lattice instead of a 3D lattice. We have considered zero temperature and used the z axis as the projection axis for both $\hat{n} = \hat{x}$ and $\hat{n} = \hat{z}$, so that the triplet amplitudes

can be directly compared to the retarded anomalous Green's functions obtained by instead following the theoretical framework in Ch. 3. The s- and p-wave triplet amplitudes are plotted in Fig. 5.7. From (a), (c) and (e), we see that in

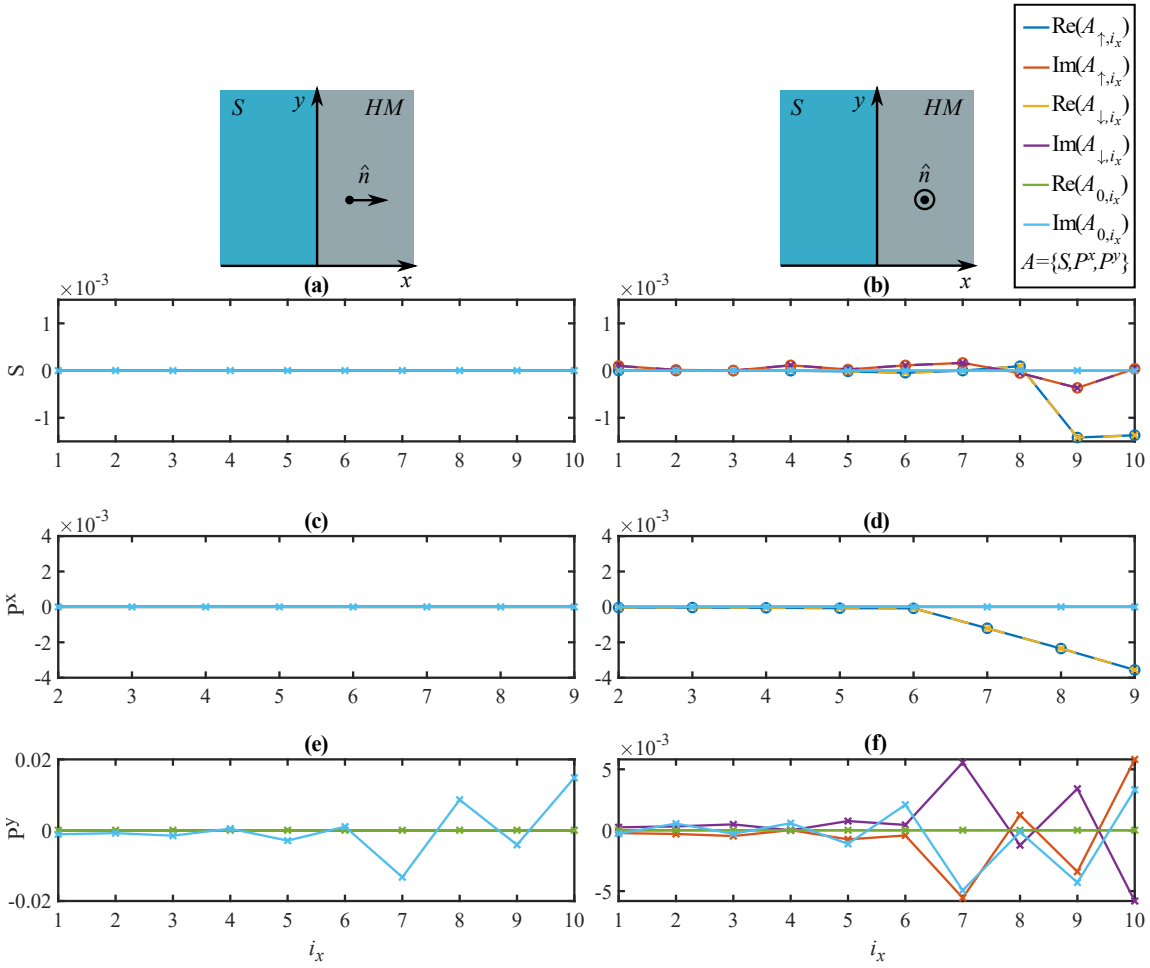

Figure 5.7: Panels (a), (c) and (e) show the triplet amplitudes for $\hat{n} = \hat{x}$. Panels (b), (d) and (f) show the triplet amplitudes for $\hat{n} = \hat{z}$. Panels (a) and (b) show odd-frequency s-wave triplets, panels (c) and (d) show even-frequency p_x-wave triplets, and panels (e) and (f) show even-frequency p_y-wave triplets. When reorienting $\hat{n}$ from the x direction to the z direction, equal-spin s-, p_x- and p_y-wave triplets appear in addition to the opposite-spin p_y-wave triplet, that is the only nonzero triplet for $\hat{n} = \hat{x}$. Note that curves with two colors mark two different types of triplets with the same amplitude. Note also that triplet amplitudes that are not visible in the plots are zero or close to zero. The parameters are given in the main text. The temperature is $T = 0$ and the relative time coordinate is $\tau = 10$.

perfect correspondence with our previous results, the s-wave and p_x-wave triplet amplitudes are absent when $\hat{n} = \hat{x}$. There are also no equal-spin triplets in the system. From (b), (d) and (f), we see that for $\hat{n} = \hat{z}$, we have gained additional s-, p_x-, and p_y-wave equal-spin triplets. In Fig. 5.8, we plot the s- and p-wave

triplet amplitudes of a S/F system with the same parameters as the S/HM system, except that the HM layer is replaced by a ferromagnetic layer with $N_{x,F} = 3$ and $h = 0.8$. For this system, the s-wave and p_x-wave opposite-spin triplet amplitudes

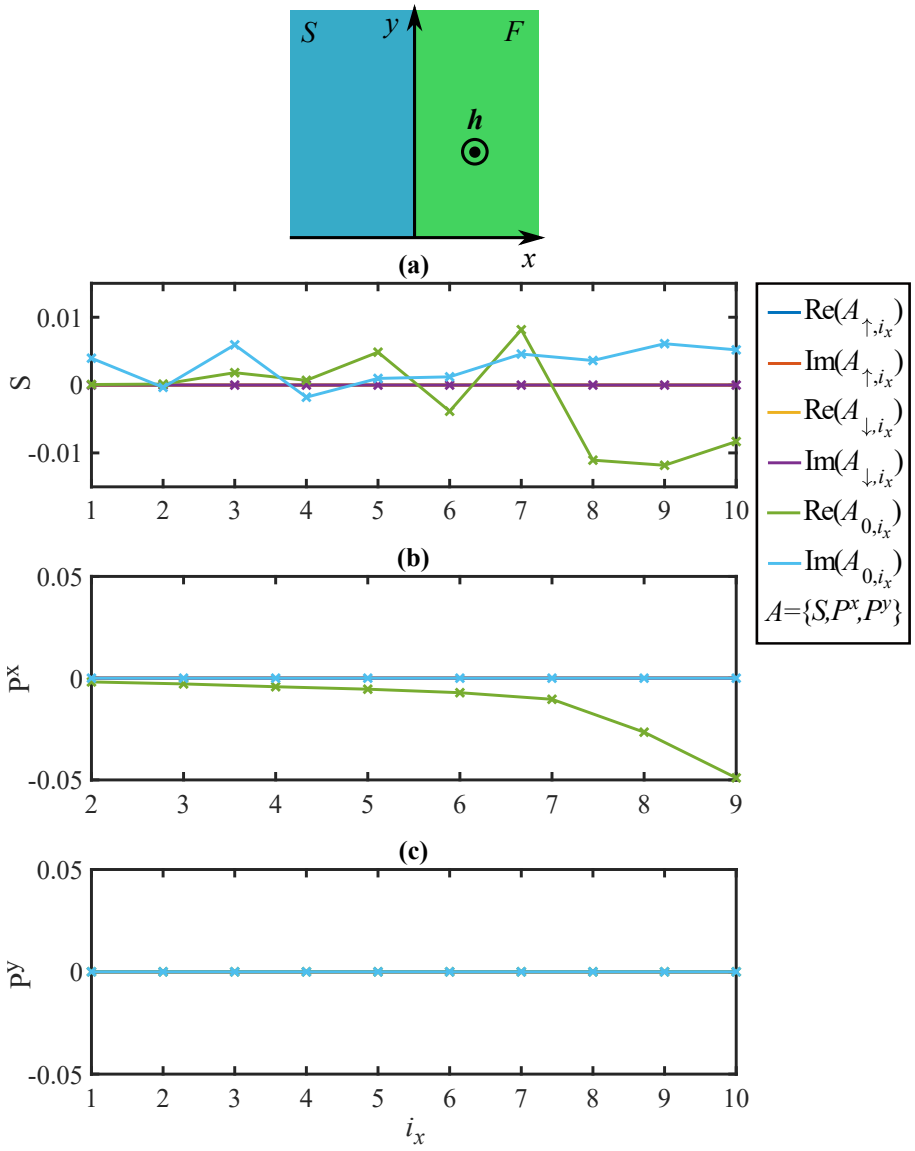

Figure 5.8: (a), (b) and (c) shows the triplet amplitudes for a 2D ferromagnet with $\boldsymbol{h} = h\hat{z}$. (a) shows odd-frequency s-wave triplets, (b) shows even-frequency p_x-wave triplets, and (c) shows even-frequency p_y-wave triplets. Triplet amplitudes that are not visible in the plots are zero or close to zero. The parameters are specified in the main text. The relative time coordinate is $\tau = 10$.

are nonzero, while the p_y-wave triplet amplitude is absent. The triplet generation found by the theoretical framework presented in Ch. 3 therefore correspond well to, and explain, the triplet generation found from the theoretical framework in Ch. 2. By comparing the results obtained from the two theoretical frameworks,

we also find that the equal-spin triplets obtained from the theoretical framework in Ch. 3 for the 2D HM/S system with $\hat{n} = \hat{z}$ must contain s-wave triplets.

Although an analytical expression for the singlet and triplet amplitudes cannot be obtained for a 3D system, it is plausible that the s-wave triplet amplitude is in general zero for $\hat{n} = \hat{x}$ also in 3D. Since the Hamiltonian is dependent on both k_y and k_z for a 3D HM/S system with $\hat{n} = \hat{x}$ (see Eq. 2.49), the allowed k_x values will depend on k_y and k_z. Similarly as in 2D, this may lead to the possibility of triplet amplitudes that are odd under inversion of k_y and k_z, and therefore be the cause of the absence of the s-wave triplet amplitudes.

The fact that we have a variation in the triplet generation under IP rotations, *i.e.* when the IP component of $\hat{n}$ is constant, means that the variations in the triplet generation cannot be solely attributed to the change in the s-wave triplet amplitude under changes in the IP component of $\hat{n}$. The triplet generation, and therefore also T_c, depends on whether $\hat{n}$ points towards the nearest or next-nearest neighbours in the cubic lattice. Since the triplet amplitudes in Eqs. 2.58-2.61 depend on both the eigenvectors and eigenenergies of the system, the triplet concentration must depend on the band structure of the system. From Eq. 2.50, we see that the free energy of the system only depends on the superconducting gap and the band structure. If we consider a N/HM system, a change in the free energy under rotations of $\hat{n}$ must therefore mean that the energy band structure changes. Using the same parameters as in Figs. 5.2 and 5.5 and setting U to zero, we plot the normal state free energy F_N of a N/HM system in Fig. 5.9. We have subtracted the maximum of the free energy within each plane of rotation to make it easier to compare the magnitude of the change in the two rotation planes. From the figure, we see that there is a change in the free energy, and therefore also in the energy band structure, under both IP to OOP rotations and for rotations within the plane of the interface. Note that the change in the normal state free energy of the system under rotations of $\hat{n}$ need not be of the same form as the variation in the free energy of the superconducting system. The fact that the reorientation of the spin-orbit field alone can induce a change in the energy band structure in a N/HM system suggests that reorientations of the spin-orbit field may cause similar changes in the band structure of a S/HM system. These changes in band structure may explain the variation in the singlet amplitude and the critical temperature for IP rotations. They may also contribute to the change in the singlet amplitude and the critical temperature under IP to OOP rotations. Band structure effects are also a likely candidate for explaining the differences in the behavior of the critical temperature under the IP rotations in Figs. 5.2(b)

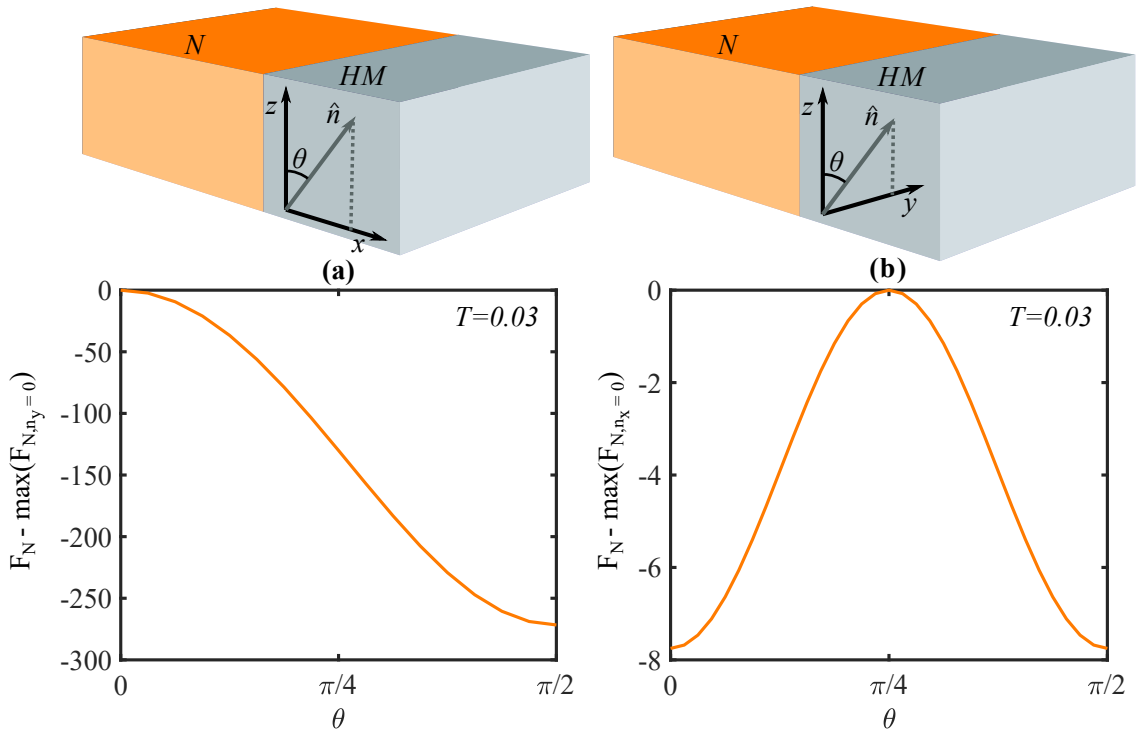

Figure 5.9: (a) shows $F_N - \max(F_{N,n_y=0})$ for rotations in the xz plane. (b) shows $F_N - \max(F_{N,n_x=0})$ for rotations in the yz plane. The calculation is done for a normal-metal with the same choice of parameters and at the same temperature as for the singlet amplitude in Fig. 5.5. In this case the free energy curves have the opposite shape of the singlet amplitude in Fig. 5.5, however this need not be the case. The normal state variation in the free energy suggests band structure effects to be present.

and 5.4(b) provided that the band structure favors an increased triplet generation at different orientations of $\hat{n}$ for different choices of parameters.

We finally comment on the possibilities of the experimental realization of the above discussed T_c-modulation. We suggest cleaving a non-centrosymmetric material in different directions and growing a superconductor on the surface. For this, we suggest Bismuth (Bi), as it is the heaviest non-reactive element and has shown a strong spin-orbit interaction [57]. Experiments [58, 59] have shown that the Rashba-like spin-orbit interactions in Bi can favor a spin polarization with a nonzero out-of-plane component, corresponding to a nonzero in-plane component of the spin-orbit field. This can be explained by the layered structure of Bi, where the spin-orbit field is directed perpendicular to the layers independently of the angle at which the material is cut. This method demands different samples for different orientations of the spin-orbit field. However, if the superconducting critical temperature is systematically lower for one case than the other, this could be taken as evidence for a T_c suppression. Another possibility is to deposit

superconductors on the surface of a curved non-centrosymmetric material. The non-centrosymmetric material, *e.g.* Bi, can be mechanically polished into a cylindrical shape [60]. If the superconductors are deposited in regions with different angles between the Bi layers and the surface, and the curvature is weak so that the surface covered by a superconducting layer is approximately flat, this effectively shows the effects of different orientations of the spin-orbit fields using just one sample. For both of these approaches, the interface quality should be as good as possible in order to maximize the proximity effect.

Another suggestion for the experimental realization of the T_c-modulation is growing transition metal dichalcogenides on superconducting samples. Transition metal dichalcogenides have two competing contributions to the spin-orbit field [61], an in-plane contribution, and an out-of plane contribution induced by Rashba spin-splitting. The strength of the two contributions can be modulated by adding strain [62]. The strain may be modified by growing the transition metal dichalcogenide together with a polar substrate with an intrinsic dipole moment [63]. A tensile strain increasing the in-plane lattice constant increases the out-of-plane contribution to the spin-orbit field compared to the in-plane component. A compressive strain decreasing the in-plane lattice constant on the other hand increases the in-plane contribution to the spin-orbit field compared to the out-of-plane component. Note that the applied strain is restricted to be weak enough to not cause a breaking of inter-atomic bonds [62]. This method require multiple samples.

5.4 CONCLUDING REMARKS

The work presented in this chapter predicts a suppression of the superconducting critical temperature of a superconductor/heavy-metal heterostructure when the Rashba spin-orbit field of the heavy-metal is oriented in the plane of the interface. This suppression may be attributed to the fact that the odd-frequency s-wave triplet amplitude increases from zero when the spin-orbit field gains an increasing in-plane component, but may also be affected by variations in the generation of even-frequency p-wave and odd-frequency d-wave triplets. For a 2D system with the interface normal along the x axis, the absence of s-wave triplets for out-of-plane spin-orbit fields is explained by the k_y dependence of the allowed k_x values. This allows for triplets that are odd under inversion of k_y, rather than the s-wave amplitude, which is even under inversion along all spatial axes. Due to the

robustness of s-wave triplets under impurity scattering, we expect the in-plane suppression of the critical temperature to be observable also in diffusive systems. We have also predicted a variation in T_c under in-plane rotations of the spin-orbit field, that may be attributed to differences in the energy band structure when the spin-orbit field is oriented in different directions in the cubic crystal structure.

6

SUMMARY AND OUTLOOK

In this thesis, we have demonstrated the emergence of new physics upon combining superconducting and non-superconducting materials into hybrid structures, due to the proximity-induced conversion of singlet into triplet Cooper pairs. We have focused on hybrid structures consisting of a single conventional superconducting layer either proximity-coupled to a single homogeneous ferromagnet with an intermediate heavy-metal layer boosting interfacial Rashba spin-orbit coupling, or combined with a single heavy normal-metal layer with Rashba spin-orbit coupling. In particular, we have demonstrated magnetization reorientation driven by the superconducting phase transition and critical temperature modulation under rotations of the magnetization and Rashba spin-orbit field.

For the superconductor/heavy-metal/ferromagnet trilayer, we have predicted a magnetization reorientation upon lowering the temperature below the superconducting critical temperature. This system thus acts as a temperature-driven magnetic switch. For thin-film ferromagnets with a weak magnetic anisotropy, the superconducting phase transition may trigger an in-plane to out-of-plane reorientation of the magnetization. For thicker ferromagnetic layers where shape anisotropy enforces in-plane magnetization, a $\pi/4$ in-plane rotation of the magnetization should be possible upon lowering the temperature below the critical temperature. We also predict an in-plane modulation of the critical temperature present in ballistic systems. This result complements the earlier diffusive-limit calculations that only predict a suppression of the critical temperature independently of the in-plane orientation of the magnetization. Our predictions should be experimentally observable in thin-film heterostructures with good interface quality, strong interfacial Rashba-spin orbit coupling, and with a soft ferromagnet with low switching-energy.

For the superconductor/heavy-metal structure, we have predicted a suppression of the superconducting critical temperature for in-plane Rashba spin-orbit fields dependent upon the in-plane orientation. We have demonstrated that the out-of-plane to in-plane variation in the critical temperature is at least partly caused by

the odd-frequency s-wave triplet concentration increasing from zero when the in-plane component of the spin-orbit field increases from zero. Due to the robustness of s-wave Cooper pairs under impurity scattering, an in-plane suppression of the critical temperature should therefore be observable both in diffusive materials and in the ballistic-limit materials considered in this thesis.

It is likely that future investigations of new combinations of superconducting and non-superconducting materials will lead to the discovery of interesting physics. The exploration of these systems is therefore important from a fundamental physics point of view that focuses on increasing our understanding of these materials, but also with regard to possible future applications. In this, it is of particular importance to urge the experimental realization of theoretical predictions such as those done in this thesis.

BIBLIOGRAPHY

[1] J. Linder, and J. W. A. Robinson,
Superconducting spintronics,
Nat. Phys. **11**, 307 (2015).

[2] H. Kamerlingh-Onnes,
Further experiments with liquid helium. D. On the change of electric resistance of pure metals at very low temperatures, etc. V. The disappearance of the resistance of mercury,
Commun. Phys. Lab. Univ. Leiden **1226**, 264 (1911).

[3] D. van Delft, and P. Kes,
The discovery of superconductivity,
Phys. Today **63**, 38 (2010).

[4] J. Bardeen, L. N. Cooper, and J. R. Schrieffer,
Theory of superconductivity,
Phys. Rev. **108**, 1175 (1957).

[5] N. N. Bogoliubov,
On a new method in the theory of superconductivity,
Il Nuovo Cimento **7**, 794 (1958).

[6] L. P. Gor'kov,
On the energy spectrum of superconductors,
Sov. Phys. JETP **34**, 505 (1958).

[7] L. P. Gor'kov,
Microscopic derivation of the Ginzburg-Landau equations in the theory of superconductivity,
Sov. Phys. JETP **36**, 1364 (1959).

[8] M. Eschrig,
Spin-polarized supercurrents for spintronics,
Phys. Today **64**, 43 (2011).

[9] M. Eschrig,
Spin-ploarized supercurrents for spintronics: A review of current progress,
Rep. Prog. Phys. **78**, 104501 (2015).

[10] P. G. de Gennes, and E. Guyon,
Superconductivity in "normal" metals,
Phys. Lett. **3**, 168 (1963).

[11] P. G. de Gennes,
Boundary effects in superconductors,
Rev. Mod. Phys. **36**, 225 (1964).

[12] N. R. Werthamer,
Theory of the superconducting transition temperature and energy gap function of superposed metal films,
Phys. Rev. **132**, 2440 (1963).

[13] J. J. Hauser, H. C. Theuerer, and N. R. Werthamer,
Superconductivity in Cu and Pt by means of superimposed films with lead,
Phys. Rev. **136**, 637 (1964).

[14] A. F. Andreev,
The thermal conductivity of the intermediate state of superconductors,
Sov. Phys. JETP **19**, 1228 (1964).

[15] P. G. de Gennes, and D. Saint-James,
Elementary excitations in the vicinity of a normal metal-superconducting metal contact,
Phys. Lett. **4**, 151 (1963).

[16] G. E. Blonder, M. Tinkham, and T. M. Klapwijk,
Transition from metallic to tunneling regimes in superconducting microconstrictions: Excess current, charge imbalance, and supercurrent conversion,
Phys. Rev. B **25**, 4515 (1982).

[17] J. Y. Gu, C. Y. You, J. S. Jiang, J. Pearson, Y. B. Bazaliy, and S. D. Bader,
Magnetization-orientation dependence of the superconducting transition temperature in the ferromagnet-superconductor-ferromagnet system : CuNi/Nb/CuNi,
Phys. Rev. Lett. **89**, 267001 (2002).

[18] I. C. Moraru, W. P. Pratt, and N. O. Birge,
Magnetization-dependent T_c shift in ferromagnet/superconductor/ferromagnet trilayers with a strong ferromagnet,
Phys. Rev. Lett. **96**, 037004 (2006).

[19] P. V. Leksin, N. N. Garif'Yanov, I. A. Garifullin, Y. V. Fominov, J. Schumann, Y. Krupskaya, V. Kataev, O. G. Schmidt, and B. Büchner,
Evidence for triplet superconductivity in a superconductor-ferromagnet spin valve,
Phys. Rev. Lett. **109**, 057005 (2012).

[20] N. Banerjee, C. B. Smiet, R. G. J. Smits, A. Ozaeta, F. S. Bergeret, M. G. Blamire, and J. W. A. Robinson,
Evidence for spin selectivity of triplet pairs in superconducting spin valves,
Nat. Commun. **5**, 3048 (2014).

[21] X. L. Wang, A. Di Bernardo, N. Banerjee, A. Wells, F. S. Bergeret, M. G. Blamire, and J. W. A. Robinson,
Giant triplet proximity effect in superconducting pseudo spin valves with engineered anisotropy,
Phys. Rev. B **89**, 140508(R) (2014).

[22] S. H. Jacobsen, J. A. Ouassou, and J. Linder,
Critical temperature and tunneling spectroscopy of superconductor-ferromagnet hybrids with intrinsic Rashba-Dresselhaus spin-orbit coupling,
Phys. Rev. B **92**, 024510 (2015).

[23] J. A. Ouassou, A. D. Bernardo, J. W. A. Robinson, and J. Linder,
Electric control of superconducting transition through a spin-orbit coupled interface,
Sci. Rep. **6**, 29312 (2016).

[24] H. T. Simensen, and J. Linder,
Tunable superconducting critical temperature in ballistic hybrid structures with strong spin-orbit coupling,
Phys. Rev. B **97**, 054518 (2018).

[25] N. Banerjee, J. A. Ouassou, Y. Zhu, N. A. Steimashenko, J. Linder, and M. G. Blamire,
Controlling the superconducting transition by spin-orbit coupling,
Phys. Rev. B **97**, 184521 (2018).

[26] D. Terrade,
Proximity effects and Josephson currents in ferromagnet - spin-triplet superconductors junctions,
Ph.D. thesis, Max-Planck-Institut für Festkörperforschung, Universität Stuttgart (2015) pp. 137-146.

[27] J. Linder, M. Amundsen, and V. Risinggård,
Intrinsic superspin Hall current,
Phys. Rev. B **96**, 094512 (2017).

[28] Y. A. Bychkov, and E. I. Rashba,
Oscillatory effects and the magnetic susceptibility of carriers in inversion layers,
J. Phys. C: Solid State Phys. **17**, 6039 (1984).

[29] H. Bruus, and K. Flensberg,
Many-body quantum theory in condensed matter physics,
(Oxford University Press, Unites States of America, 2004) pp. 27-29, 120-123.

[30] T. Thomson,
Magnetic properties of metallic thin films,
(Elsevier Ltd., 2013) pp. 454-446.

[31] M. T. Johnson, P. J. H. Bloemen, F. J. A. den Broeder, and J. J. de Vries,
Magnetic anisotropy in metallic multilayers,
Rep. Prog. Phys **59**, 1409 (1996).

[32] J. A. Ouassou,
Density of states and critical temperature in superconductor/ferromagnet structures with spin-orbit coupling,
M.Sc. thesis, Norwegian University of Science and Technology (2015) pp. 65-71.

[33] J. Linder, and A. V. Balatsky,
Odd-frequency superconductivity,
arXiv:1709.03986 (2017).

[34] A. L. Fetter, and J. D. Walecka,
Quantum theory of many-particle systems,
(Dover Publications inc., Mineola, New York, 2003) pp. 58-59.

[35] A. M. Black-Schaffer, and J. Linder,
Strongly anharmonic current-phase relation in ballistic graphene Josephson junctions,
Phys. Rev. B **82**, 184522 (2010).

[36] C. English, D. R. Hamilton, C. Chialvo, I. C. Moraru, N. Mason, and D. J. Van Harlingen,
Observation of non-sinusoidal current-phase relation in graphene Josephson junctions,
Phys. Rev. B **94**, 115435 (2013).

[37] W. L. McMillan,
Theory of superconductor-normal-metal interfaces,
Phys. Rev. **175**, 559 (1967).

[38] J. Cayao, and A. M. Black-Schaffer,
Odd-frequency superconducting pairing and subgap density of states at the edge of a two-dimensional topological insulator without magnetism,
Phys. Rev. B **96**, 155426 (2017).

[39] J. Cayao, and A. M. Black-Schaffer,
Odd-frequency superconducting pairing in junctions with Rashba spin-orbit coupling,
Phys. Rev. B **98**, 075425 (2018).

[40] R. T. W. Koperdraad, R. E. S. Otadoy, M. Blaauboer, and A. Lodder,
Multiple-scattering theory for clean superconducting layered structures,
J. Phys.: Condens. Matter **13**, 8707 (2001).

[41] S. Kashiwaya, and Y. Tanaka,
Tunneling effects on surface bound states in unconventional superconductors,
Rep. Prog. Phys. **63**, 1641 (2000).

[42] A. Furusaki, and M. Tsukada,
DC Josephson effect and Andreev reflection,
Solid State Commun. **78**, 299 (1991).

[43] C. Ishii,
Josephson currents through junctions with normal metal barriers,
Prog. Theor. Phys. **44**, 1525 (1970).

[44] B. Lu, and Y. Tanaka,
Study on Green's function on TI surface,
arXiv:1512.00916v3 (2016).

[45] J. P. Morten,
Spin and charge transport in dirty superconductors,
M.Sc. thesis, Norwegian University of Science and Technology (2003) pp. 7-24, 56.

[46] M. M. Odashima, B. G. Prado, and E. Vernek,
Pedagogical introduction to equilibrium Green's functions: condensed-matter examples with numerical implementations,
Rev. Bras. Ensino Fis. **39**, 1303 (2017).

[47] M. G. Flokstra,
Proximity effects in superconducting spin-valve structures,
Ph.D. thesis, Universiteit Leiden (2010) pp. 16-20.

[48] C. R. Reeg, and D. L. Maslov,
Proximity-indused triplet superconductivity in Rashba materials,
Phys. Rev. B **92**, 134512 (2015).

[49] P. C. Hemmer,
Kvantemekanikk,
(Tapir Akademisk Forlag, Trondheim, 2005) pp. 35-37 (norwegian).

[50] B. H. Bransden, and C. J. Joachain,
Quantum mechanics,
(Pearson Education Limited, England, 2000) pp. 86-90.

[51] N. Satchell, and N. O. Birge,
Supercurrent in ferromagnetic Josephson junctions with heavy metal interlayers,
Phys. Rev. B **97**, 214509 (2018).

[52] E. C. Gingrich,
Phase control of the spin triplet state in S/F/S Josephson junctions,
Ph.D. thesis, Michigan State University (2014).

[53] J. D. Donaldson, and D. Beyersmann,
Ullmann's encyclopedia of industrial chemistry - Cobalt and cobalt compounds,
(Wiley VCH, Weinheim, Germany, 2003) p. 431.

[54] K. Fossheim, and A. Sudbø,
Superconductivity - Physics and applications,
(John Wiley & Sons Ltd., Chichester, England, 2004) pp. 10-26.

[55] Y. Zhu, A. Pal, M. G. Blamire, and Z. H. Barber,
Superconducting exchange coupling between ferromagnets,
Nat. Mater. **16**, 195 (2016).

[56] K. D. Usadel,
Generalized diffusion equation for superconducting alloys,
Phys. Rev. Lett. **23**, 507 (1970).

[57] P. Hofmann,
The surfaces of bismuth: Structural and electronic properties,
Prog. Surf. Sci. **81**, 191 (2006).

[58] J. W. Wells, J. H. Dil, F. Meier, J. Lobo-Checa, V. N. Petrov, J. Osterwalder, M. M. Ugeda, I. Fernandez-Torrente, J. I. Pascual, E. D. L. Rienks, M. F. Jensen, and P. Hofmann,
Nondegenerate metallic states on Bi(114): A one-dimensional topological metal,
Phys. Rev. Lett. **120**, 096802 (2009).

[59] M. Bianchi, F. Song, S. Cooil, A. F. Monsen, E. Wahlström, J. A. Miwa, E. D. L. Pienks, D. A. Evans, A. Strozecka, J. I. Pascual, M. Leandersson, T. Balaubramanian, P. Hofmann, and J. W. Wells,
One-dimensional spin texture of Bi(441): Quantum spin Hall properties without a topological insulator,
Phys. Rev. B **91**, 165307 (2015).

[60] J. E. Ortega, M. Corso, Z. M. Abd-el Fattah, E. A. Goiri, and F. Schiller,
Interplay between structure and electronic states in step arrays explored with curved surfaces,
Phys. Rev. B **83**, 085411 (2011).

[61] Y. C. Cheng, Z. Y. Zhu, M. Tahir, and U. Schwingenschlögl,
Spin-orbit–induced spin splittings in polar transition metal dichalcogenide monolayers,
EPL **102**, 57001 (2013).

[62] M. A. U. Absor, I. Santoso, Harsojo, K. Abrasha, H. Kotaka, F. Ishii, and M. Saito,
Polarity tuning of spin-orbit-induced spin splitting in two-dimensional transition metal dichalcogenides,
J. Appl. Phys. **122**, 153905 (2017).

[63] R. K. Defo, S. Fang, S. N. Shirodkar, G. A. Tritsaris, A. Dimoulas, and E. Kaxiras,
Strain dependence of band gaps and exciton energies in pure and mixed transition-metal dichalcogenides,
Phys. Rev. B **94**, 155310 (2016).

Magnetization reorientation due to the superconducting transition in heavy-metal heterostructures

Lina G. Johnsen*
Center for Quantum Spintronics, Department of Physics, Norwegian University of Science and Technology, NO-7491 Trondheim, Norway

Niladri Banerjee
Department of Physics, Loughborough University, Loughborough LE11 3TU, United Kingdom

Jacob Linder
Center for Quantum Spintronics, Department of Physics, Norwegian University of Science and Technology, NO-7491 Trondheim, Norway

(Received 2 January 2019; revised manuscript received 2 April 2019; published 23 April 2019)

Recent theoretical and experimental work has demonstrated how the superconducting critical temperature (T_c) can be modified by rotating the magnetization of a single homogeneous ferromagnet proximity-coupled to the superconducting layer. This occurs when the superconductor and ferromagnet are separated by a thin heavy normal metal that provides an enhanced interfacial Rashba spin-orbit interaction. In the present work, we consider the reciprocal effect: magnetization reorientation driven by the superconducting phase transition. We solve the tight-binding Bogoliubov–de Gennes equations on a lattice self-consistently and compute the free energy of the system. We find that the relative angle between the spin-orbit field and the magnetization gives rise to a contribution in the free energy even in the normal state, $T > T_c$, due to band-structure effects. For temperatures below T_c, superconductivity gives rise to a competing contribution. We demonstrate that by lowering the temperature, in addition to reorientation of the favored magnetization direction from in-plane to out-of-plane, a $\pi/4$ in-plane rotation for thicker ferromagnetic layers is possible. Furthermore, computation of T_c of the structure in the ballistic limit shows a dependence on the in-plane orientation of the magnetization, in contrast to our previous result on the diffusive limit. This finding is relevant with respect to thin-film heterostructures since these are likely to be in the ballistic regime of transport rather than in the diffusive regime. Finally, we discuss the experimental feasibility of observing the magnetic anisotropy induced by the superconducting transition when other magnetic anisotropies, such as the shape anisotropy for a ferromagnetic film, are taken into account. Our work suggests that the superconducting condensation energy in principle can trigger a reorientation of the magnetization of a thin-film ferromagnet upon lowering the temperature below T_c, in particular for ferromagnets with weak magnetic anisotropies.

DOI: 10.1103/PhysRevB.99.134516

I. INTRODUCTION

Recent research within the field of superconducting spintronics has focused on combining superconducting and magnetic materials into hybrid structures to study novel phases arising from proximity effects not found in individual materials [1]. In conventional superconductors (S), Cooper pairs exists as spin-singlet pairs. The two electrons in a pair have opposite spin and are destroyed when they enter a ferromagnet (F) as they quickly lose their coherence due to the magnetic exchange field. At the interface between a superconductor and a ferromagnet, spin-singlet pairs are transformed into spin-zero triplet Cooper pairs that have a short penetration depth into the ferromagnetic region. However, two misoriented ferromagnets breaking spin-rotational symmetry can transform opposite-spin triplets into equal-spin triplets [2]. Due to their equally directed spins along the magnetization direction, these Cooper pairs maintain coherence longer and are instead able to survive for a longer distance inside the ferromagnet. The density of equal-spin triplets in the system depends on the relative orientation of the ferromagnets [2,3]. This has been demonstrated experimentally (see for instance Refs. [4–8]) by showing a variation of T_c in a F1/S/F2 or F1/F2/S system by changing the relative magnetization of the F1 and F2 layers. This variation is attributed to the generation of triplet Cooper pairs with increasing misalignment of the magnetizations of F1 and F2 layer moments. Recent research [9–12] has reported a similar modulation of the critical temperature by changing the orientation of a single homogeneous ferromagnet coupled to a superconductor through a thin heavy normal metal (HM) film with strong Rashba spin-orbit coupling. Measurements [12] performed on a Nb/Pt/Co/Pt system showed a suppression of the critical temperature for an in-plane (IP) magnetization that was attributed to a reduced superconducting gap due to triplet generation. A reduced gap also implies an increase in the free energy since part of the superconducting condensation energy is lost. We may therefore suspect the superconducting contribution to the free energy to favor an out-of-plane (OOP) magnetization direction.

Motivated by this, here we explore the striking possibility of reorienting the magnetization of the ferromagnetic layer in an S/HM/F system by changing the temperature. We discover

*Corresponding author: lina.g.johnsen@ntnu.no

that upon lowering the temperature below T_c, the dependence of the free energy on the magnetization direction changes due to the superconducting phase transition. In turn, this leads to a change in the ground-state magnetization direction, or effectively the magnetization angle that minimizes the free energy. For sufficiently thin ferromagnetic layers, we get a change from IP to OOP magnetization. We also find that there is an IP variation in the free energy and show that it is in principle possible to get an IP $\pi/4$ rotation of the magnetization when lowering the temperature below T_c. This opens the possibility for temperature-induced switching of the magnetization both between the IP and OOP orientation and switching within a plane parallel to the interface.

II. THEORY

To describe our S/HM/F system, we use the tight-binding Bogoliubov–de Gennes (BdG) framework and use conventions similar to those in Refs. [13,14]. The lattice BdG framework is well suited for describing heterostructures, fully accounts for the crystal symmetry of the electronic environment, and can describe atomically thin layers of a material. The Hamiltonian we use is

$$\begin{aligned} H = &-t \sum_{\langle \boldsymbol{i},\boldsymbol{j}\rangle,\sigma} c^\dagger_{\boldsymbol{i},\sigma} c_{\boldsymbol{j},\sigma} - \sum_{\boldsymbol{i},\sigma} \mu_{\boldsymbol{i}} c^\dagger_{\boldsymbol{i},\sigma} c_{\boldsymbol{i},\sigma} - \sum_{\boldsymbol{i}} U_{\boldsymbol{i}} n_{\boldsymbol{i},\uparrow} n_{\boldsymbol{i},\downarrow} \\ &- \frac{i}{2} \sum_{\langle \boldsymbol{i},\boldsymbol{j}\rangle,\alpha,\beta} \lambda_{\boldsymbol{i}} c^\dagger_{\boldsymbol{i},\alpha} \hat{n} \cdot (\boldsymbol{\sigma} \times \boldsymbol{d}_{\boldsymbol{i},\boldsymbol{j}})_{\alpha,\beta} c_{\boldsymbol{j},\beta} \\ &+ \sum_{\boldsymbol{i},\alpha,\beta} c^\dagger_{\boldsymbol{i},\alpha} (\boldsymbol{h}_{\boldsymbol{i}} \cdot \boldsymbol{\sigma})_{\alpha,\beta} c_{\boldsymbol{i},\beta}. \end{aligned} \tag{1}$$

Above, t is the hopping integral, $\mu_{\boldsymbol{i}}$ is the chemical potential at lattice site $\boldsymbol{i}$, $U > 0$ is the attractive on-site interaction that gives rise to superconductivity, $\lambda_{\boldsymbol{i}}$ is the Rashba spin-orbit coupling magnitude at site $\boldsymbol{i}$, $\hat{n}$ is a unit vector normal to the interface, $\boldsymbol{\sigma}$ is the vector of Pauli matrices, $\boldsymbol{d}_{\boldsymbol{i},\boldsymbol{j}}$ is the vector from site $\boldsymbol{i}$ to site $\boldsymbol{j}$, and $\boldsymbol{h}_{\boldsymbol{i}}$ is the local magnetic exchange field. $c^\dagger_{\boldsymbol{i},\sigma}$ and $c_{\boldsymbol{i},\sigma}$ are the second-quantization electron creation and annihilation operators at site $\boldsymbol{i}$ with spin σ, and $n_{\boldsymbol{i},\sigma} \equiv c^\dagger_{\boldsymbol{i},\sigma} c_{\boldsymbol{i},\sigma}$. The superconducting term in the Hamiltonian is treated by a mean-field approach, where we insert $c_{\boldsymbol{i},\uparrow} c_{\boldsymbol{i},\downarrow} = \langle c_{\boldsymbol{i},\uparrow} c_{\boldsymbol{i},\downarrow}\rangle + \delta$ and $c^\dagger_{\boldsymbol{i},\uparrow} c^\dagger_{\boldsymbol{i},\downarrow} = \langle c^\dagger_{\boldsymbol{i},\uparrow} c^\dagger_{\boldsymbol{i},\downarrow}\rangle + \delta^\dagger$ into Eq. (1) and neglect terms of second order in the fluctuations δ and $\delta^\dagger$. $\Delta_{\boldsymbol{i}} \equiv U_{\boldsymbol{i}} \langle c_{\boldsymbol{i},\uparrow} c_{\boldsymbol{i},\downarrow}\rangle$ is the superconducting order parameter, which we solve for self-consistently. We consider a 3D cubic lattice of size $N_x \times N_y \times N_z$, as shown in Fig. 1. The lattice consists of three layers: a superconducting layer, a thin heavy-metal layer with Rashba spin-orbit coupling, and a thin ferromagnetic layer. For enabling experimental observation of the effects considered in this paper, the system should have as good an interface quality as possible to maximize the proximity effect, and heavy-metal interlayers should be used to boost the spin-orbit coupling strength. For concrete material choices, we suggest a Nb superconductor with Pt interlayers, which should give a strong proximity effect and strong spin-orbit coupling (see for instance Ref. [15]). In addition, the ferromagnet should be soft and have as weak an anisotropy as possible. We suggest using a 7% Mo-doped permalloy, which has a very low switching energy [16]. We describe the trilayer system shown in Fig. 1 using the Hamiltonian in Eq. (1), where the terms are only nonzero in their respective regions. The interface normals are parallel to the x axis ($\hat{n} = \hat{x}$). We assume periodic boundary conditions in the y and z directions, so that all quantities depend on the x component of the site index only. In our presentation of the results, we scale all energies to the hopping element, t, and all lengths to the lattice constant, a. For simplicity, we also set the reduced Planck constant $\hbar$ and the Boltzmann constant k_B equal to 1. Therefore, all temperatures are scaled by t/k_B in the presentation of the results. The magnetic exchange field of the ferromagnet is expressed by $\mathbf{h} = h(\cos(\phi)\sin(\theta), \sin(\phi)\sin(\theta), \cos(\theta))$, where θ is the polar angle with respect to the z axis and ϕ is the azimuthal angle. Because of our assumption of periodic boundary conditions along $\hat{y}$ and $\hat{z}$, the Fourier transform

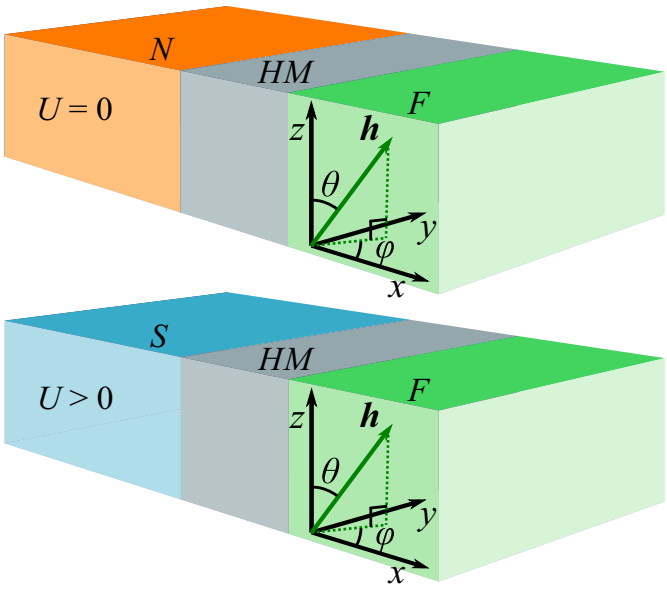

FIG. 1. Suggested experimental setup for demonstrating a magnetization reorientation due to a change in temperature. We have a stack of a normal-metal layer ($T > T_c$, $U = 0$) or a superconducting layer ($T < T_c$, $U > 0$), a heavy-metal layer, and a ferromagnetic layer. We model our system as a 3D cubic lattice with interface normal along the x direction. The exchange field $\boldsymbol{h}$ is described by the polar and azimuthal angles with respect to the z axis, (θ, ϕ). Note that the above model is not to scale.

$$c_{\boldsymbol{i},\sigma} = \frac{1}{\sqrt{N_y N_z}} \sum_{k_y,k_z} c_{i_x,k_y,k_z,\sigma} e^{i(k_y i_y + k_z i_z)} \tag{2}$$

can be used to diagonalize the Hamiltonian. The sum is over the allowed k_y and k_z inside the first Brillouin zone. Also note that

$$\begin{aligned} \frac{1}{\sqrt{N_y}} \sum_{i_y} e^{i(k_y - k'_y) i_y} &= \delta_{k_y,k'_y}, \\ \frac{1}{\sqrt{N_z}} \sum_{i_z} e^{i(k_z - k'_z) i_z} &= \delta_{k_z,k'_z}. \end{aligned} \tag{3}$$

We choose a basis

$$B^{\dagger}_{i_x,k_y,k_z} = \left[c^{\dagger}_{i_x,k_y,k_z,\uparrow} \quad c^{\dagger}_{i_x,k_y,k_z,\downarrow} \quad c_{i_x,-k_y,-k_z,\uparrow} \quad c_{i_x,-k_y,-k_z,\downarrow}\right] \tag{4}$$

and rewrite the Hamiltonian as

$$H = H_0 + \frac{1}{2}\sum_{i_x,j_x,k_y,k_z} B^{\dagger}_{i_x,k_y,k_z} H_{i_x,j_x,k_y,k_z} B_{j_x,k_y,k_z}. \tag{5}$$

By using Eqs. (2) and (3) to rewrite the Hamiltonian in Eq. (1), we can show that

$$\begin{aligned} H_{i_x,j_x,k_y,k_z} &= \epsilon_{i_x,j_x,k_y,k_z}\hat{\tau}_3\hat{\sigma}_0 \\ &\quad + \delta_{i_x,j_x}\left[h^x_{i_x}\hat{\tau}_3\hat{\sigma}_x + h^y_{i_x}\hat{\tau}_0\hat{\sigma}_y + h^z_{i_x}\hat{\tau}_3\hat{\sigma}_z\right. \\ &\quad - \lambda_{i_x}\sin(k_y)\hat{\tau}_0\hat{\sigma}_z + \lambda_{i_x}\sin(k_z)\hat{\tau}_3\hat{\sigma}_y \\ &\quad \left. + \Delta_{i_x} i\hat{\tau}^{+}\hat{\sigma}_y - \Delta^{\star}_{i_x} i\hat{\tau}^{-}\hat{\sigma}_y\right], \end{aligned} \tag{6}$$

where

$$\begin{aligned} \epsilon_{i_x,j_x,k_y,k_z} &\equiv -2t[\cos(k_y)+\cos(k_z)]\delta_{i_x,j_x} \\ &\quad - t\left(\delta_{i_x,j_x+1} + \delta_{i_x,j_x-1}\right) - \mu_{i_x}\delta_{i_x,j_x} \end{aligned} \tag{7}$$

and $\hat{\tau}^{\pm} = (\hat{\tau}_1 \pm i\hat{\tau}_2)/2$. Above, $\hat{\tau}_i\hat{\sigma}_j \equiv \hat{\tau}_i \otimes \hat{\sigma}_j$ is the Kronecker product of the Pauli matrices spanning Nambu and spin space. The constant term is

$$\begin{aligned} H_0 &= N_y N_z \sum_{i_x} \frac{\left|\Delta_{i_x}\right|^2}{U_{i_x}} \\ &\quad - \sum_{i_x,k_y,k_z} \{2t[\cos(k_y)+\cos(k_z)] + \mu_{i_x}\}. \end{aligned} \tag{8}$$

By defining another basis,

$$W^{\dagger}_{k_y,k_z} = \left[B^{\dagger}_{1,k_y,k_z}, \ldots, B^{\dagger}_{i_x,k_y,k_z}, \ldots, B^{\dagger}_{N_x,k_y,k_z}\right], \tag{9}$$

Eq. (5) can be rewritten as

$$H = H_0 + \frac{1}{2}\sum_{k_y,k_z} W^{\dagger}_{k_y,k_z} H_{k_y,k_z} W_{k_y,k_z}, \tag{10}$$

where

$$H_{k_y,k_z} = \begin{bmatrix} H_{1,1,k_y,k_z} & \cdots & H_{1,N_x,k_y,k_z} \\ \vdots & \ddots & \vdots \\ H_{N_x,1,k_y,k_z} & \cdots & H_{N_x,N_x,k_y,k_z} \end{bmatrix}. \tag{11}$$

H_{k_y,k_z} is Hermitian and can be diagonalized numerically with eigenvalues E_{n,k_y,k_z} and eigenvectors Φ_{n,k_y,k_z} given by

$$\begin{aligned} \Phi^{\dagger}_{n,k_y,k_z} &= \left[\phi^{\dagger}_{1,n,k_y,k_z} \cdots \phi^{\dagger}_{N_x,n,k_y,k_z}\right], \\ \phi^{\dagger}_{i_x,n,k_y,k_z} &= \left[u^{\star}_{i_x,n,k_y,k_z}\ v^{\star}_{i_x,n,k_y,k_z}\ w^{\star}_{i_x,n,k_y,k_z}\ x^{\star}_{i_x,n,k_y,k_z}\right]. \end{aligned} \tag{12}$$

The diagonalization is done numerically and gives a Hamiltonian of the form

$$H = H_0 + \frac{1}{2}\sum_{n,k_y,k_z} E_{n,k_y,k_z}\gamma^{\dagger}_{n,k_y,k_z}\gamma_{n,k_y,k_z}, \tag{13}$$

where the new quasiparticle operators are related to the old operators by

$$\begin{aligned} c_{i_x,k_y,k_z,\uparrow} &= \sum_n u_{i_x,n,k_y,k_z}\gamma_{n,k_y,k_z}, \\ c_{i_x,k_y,k_z,\downarrow} &= \sum_n v_{i_x,n,k_y,k_z}\gamma_{n,k_y,k_z}, \\ c_{i_x,-k_y,-k_z,\uparrow} &= \sum_n w_{i_x,n,k_y,k_z}\gamma_{n,k_y,k_z}, \\ c_{i_x,-k_y,-k_z,\downarrow} &= \sum_n x_{i_x,n,k_y,k_z}\gamma_{n,k_y,k_z}. \end{aligned} \tag{14}$$

To find the eigenvectors and eigenvalues the initial guess of the order parameter must be improved by iterative treatment. The expression for the gap can be rewritten by inserting the operators given in Eq. (14) and by using that $\langle\gamma^{\dagger}_{n,k_y,k_z}\gamma_{m,k_y,k_z}\rangle = f(E_{n,k_y,k_z}/2)\delta_{n,m}$. We get

$$\Delta_{i_x} = -\frac{U_{i_x}}{N_y N_z}\sum_{n,k_y,k_z} v_{i_x,n,k_y,k_z} w^{\star}_{i_x,n,k_y,k_z}[1 - f(E_{n,k_y,k_z}/2)]. \tag{15}$$

Here, $f(E_{n,k_y,k_z}/2)$ is the Fermi-Dirac distribution.

Having found E_{n,k_y,k_z} and $\{u, v, w, x\}$, we can compute the physical quantities of interest. The free energy is given by

$$F = H_0 - \frac{1}{\beta}\sum_{n,k_y,k_z} \ln(1 + e^{-\beta E_{n,k_y,k_z}/2}), \tag{16}$$

where $\beta = (k_B T)^{-1}$. Note that if $T \to 0$,

$$F = H_0 + \frac{1}{2}{\sum_{n,k_y,k_z}}' E_{n,k_y,k_z}, \tag{17}$$

where $\sum'$ means that the sum is taken over negative eigenenergies only. The ground state of the system minimizes the free energy. F is therefore used to find the preferred orientation of the ferromagnet. Additional magnetic anisotropy terms may be added to the free energy to take the thickness of the thin ferromagnetic film into account more properly. We model these terms in a simple way and write the additional contribution to the free energy as [17]

$$F_a = -K_{\text{eff}}\cos^2(\theta_p), \tag{18}$$

where θ_p is the polar angle relative to the interface normal. K_{eff} is the effective anisotropy constant. We assume a thin ferromagnetic film with one interface to another material and one free surface, and approximate K_{eff} by [17]

$$K_{\text{eff}} = K_v + \frac{K_s + K_i}{t_F}. \tag{19}$$

Above, $K_v < 0$ is the bulk anisotropy of the ferromagnet, K_s is the surface anisotropy, and $K_i > 0$ is the anisotropy of the interface between the ferromagnet and the other material. K_{eff} may be positive or negative depending on the thickness of the ferromagnetic layer, t_F. If $K_{\text{eff}} < 0$, the magnetic anisotropy contribution F_a to the free energy favors IP magnetization and shape anisotropy dominates. For $K_{\text{eff}} > 0$, OOP magnetization is favored and perpendicular anisotropy dominates. To model a noncubic ferromagnet, we use the average lattice constant, $a = (a_x + a_y + a_z)/3$. By doing this we obtain a rather rough estimate of F_a, but since we are comparing F_a to the superconducting contribution to the free energy, the order of magnitude of the change in F_a is more interesting than the details.

The physical mechanism leading to a variation in the superconducting condensation energy when the magnetization direction changes is the conversion of singlet Cooper pairs to triplet ones. To reveal the types of triplet Cooper pairs in our system, we compute the triplet anomalous Green's function amplitudes. The on-site odd-frequency s-wave anomalous triplet amplitudes are defined as

$$\begin{aligned} S_{0,\boldsymbol{i}}(\tau) &= \langle c_{i,\uparrow}(\tau)c_{\boldsymbol{i},\downarrow}(0)\rangle + \langle c_{i,\downarrow}(\tau)c_{\boldsymbol{i},\uparrow}(0)\rangle, \\ S_{\sigma,\boldsymbol{i}}(\tau) &= \langle c_{i,\sigma}(\tau)c_{\boldsymbol{i},\sigma}(0)\rangle, \end{aligned} \tag{20}$$

where we have defined the time-dependent electron annihilation operator $c_{i,\sigma}(\tau) \equiv e^{iH\tau}c_{i,\sigma}e^{-iH\tau}$. By differentiating $c_{i,\sigma}(\tau)$ with respect to τ we obtain the Heisenberg equation,

$$\frac{dc_{i,\sigma}(\tau)}{d\tau} = i[H, c_{i,\sigma}(\tau)], \tag{21}$$

from which we can obtain expressions for $c_{\boldsymbol{i},\uparrow}(\tau)$ and $c_{\boldsymbol{i},\downarrow}(\tau)$ by inserting Eq. (14). Here, τ is the relative time coordinate between the electron operators. τ is scaled by $\hbar/t$. The even-frequency p-wave anomalous triplet amplitudes are defined

$$\begin{aligned} P^{n}_{0,\boldsymbol{i}} &= \sum_{\pm} \pm(\langle c_{i,\uparrow}c_{\boldsymbol{i}\pm\hat{n},\downarrow}\rangle + \langle c_{i,\downarrow}c_{\boldsymbol{i}\pm\hat{n},\uparrow}\rangle), \\ P^{n}_{\sigma,\boldsymbol{i}} &= \sum_{\pm} \pm\langle c_{\boldsymbol{i},\sigma}c_{\boldsymbol{i}\pm\hat{n},\sigma}\rangle, \end{aligned} \tag{22}$$

where $n = \{x, y, z\}$. The spins in these triplet amplitudes are defined with respect to the z axis. If we want to compute the triplet amplitudes for a specific direction of $\boldsymbol{h}$ such that $(\uparrow\uparrow)_{\boldsymbol{h}}$ and $(\downarrow\downarrow)_{\boldsymbol{h}}$ represent the long-range triplets, the triplet amplitudes must be transformed so that the spins are defined with respect to the vector $\boldsymbol{h}$. This is done by inserting $(c_{\boldsymbol{i},\uparrow})_{\theta,\phi} = \cos(\theta/2)e^{-i\phi/2}(c_{\boldsymbol{i},\uparrow})_z + \sin(\theta/2)e^{i\phi/2}(c_{\boldsymbol{i},\downarrow})_z$ and $(c_{\boldsymbol{i},\downarrow})_{\theta,\phi} = -\sin(\theta/2)e^{-i\phi/2}(c_{\boldsymbol{i},\uparrow})_z + \cos(\theta/2)e^{i\phi/2}(c_{\boldsymbol{i},\downarrow})_z$ [2] into Eqs. (20) and (22). The even-frequency s-wave singlet amplitude is proportional to the gap and given by

$$S_{s,\boldsymbol{i}} = \langle c_{\boldsymbol{i},\uparrow}c_{\boldsymbol{i},\downarrow}\rangle - \langle c_{i,\downarrow}c_{\boldsymbol{i},\uparrow}\rangle. \tag{23}$$

The singlet amplitude is rotationally invariant with respect to the choice of quantization axis, and the quantity

$$\tilde{S}_s = \frac{1}{N_{x,S}}\sum_{i_x}\left|S_{s,i_x}\right| \tag{24}$$

is a measure of the singlet amplitude of the system for a given magnetization direction. The sum is taken over the superconducting region only, as we are primarily interested in describing how the superconducting condensation energy depends on the magnetization direction.

We find T_c numerically by a binomial search within temperatures below the bulk critical temperature of the superconductor. In each of the n iterations, we determine whether T_c is above or below the temperature in the middle of the current temperature interval. This is done by choosing an initial guess for Δ_{i_x} very close to zero and checking whether $\Delta_{i_x}(T)$ close to $N_{x,S}/2$ increases or decreases from the initial guess after recalculating Δ_{i_x} m times by Eq. (15). The gap decreases in the normal state and increases in the superconducting state.

The superconducting coherence length (ξ) of the superconducting layer is an important length scale in our system. The effects of the HM/F layer can be expected to be strongest when ξ is the same length or slightly longer than the thickness of the superconductor. In the ballistic limit the superconducting coherence length is given by $\xi = \hbar v_F/\pi\Delta_0$ [18]. The normal-state Fermi velocity, v_F, is obtained by the dispersion relation $v_F = \frac{1}{\hbar}\frac{dE_{\boldsymbol{k}}}{dk}|_{k=k_F}$ [18]. $E_{\boldsymbol{k}} = -2t[\cos(k_x) + \cos(k_y) + \cos(k_z)] - \mu_N$ is the normal-state eigenenergies obtained from Eq. (1) if we use periodic boundary conditions in all three directions. The Fermi momentum k_F corresponds to the Fermi energy, which is the highest occupied energy level at $T = 0$. Δ_0 is the zero-temperature superconducting gap. In our lattice model we round ξ down to the closest integer number of lattice points.

In our calculations, we have used a 3D cubic lattice model with periodic boundary conditions in both the y and z directions. It is worth noting that this gives qualitatively different results than if we use a 2D square lattice model with periodic boundary conditions only in the y direction. Since the 2D model does not have periodic boundary conditions in the z direction, we do not get the $\sin(k_z)$ terms in Eq. (6) when considering a 2D square lattice. This makes the system invariant under ϕ rotations of $\boldsymbol{h}$. This implies that physical quantities such as T_c and F have the same angular dependence in the xz and yz plane, so that the system is not invariant under $\pi/2$ rotations in the yz plane as is expected for a 3D cubic lattice. It should therefore be cautioned against simplifying the numerical simulations of a 3D cubic lattice by using a 2D square lattice model. In our calculations we use $N_y = N_z$ so that we get an equal number of k_y and k_z values, thereby obtaining a $\pi/2$-rotational invariance in the yz plane even when N_y and N_z are not much larger than the film thicknesses. It should also be noted that the thickness of the sample parallel to the interfaces is important for the physical results obtained in an experiment. In our paper, we have modeled a thin-film structure in which the width of the sample in the y and z directions is much larger than the thickness of the sample.

Before presenting our results, we finally also comment on the relevance of the BdG-lattice framework used here with respect to making predictions for experimentally realistic systems. The lattice framework has several advantages, such as capturing the crystal symmetry and its influence on physical quantities in addition to the fact that that the energy scales in the system can be varied across a large range. The main weakness with the present theoretical framework is that only relatively small sample sizes are computationally manageable, especially with periodic boundary conditions in two directions used here. When considering a thin superconducting layer, the superconducting coherence length must be short in order to be comparable to the thickness of the superconducting layer. ξ is proportional to the inverse of the zero-temperature gap of the superconducting layer. Considering a thin superconducting layer therefore results in a large value for the superconducting order parameter, and also a large critical temperature. However, the present framework can still be used to make qualitative and quantitative predictions for experimentally realistic systems, so long as the spatial dimensions are scaled by the superconducting coherence length. An example that illustrates that this method gives good agreement with experimental

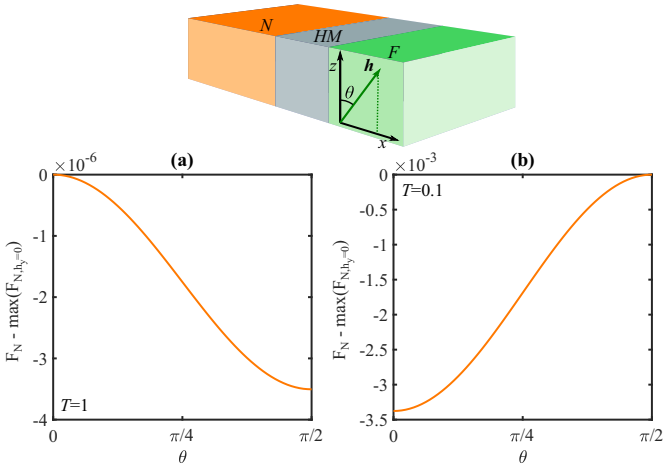

FIG. 2. Panels (a) and (b) show $F_N(\theta) - \max(F_{N,h_y=0})$ in the xz plane for $T = 1$ and $T = 0.1$. The parameters used are specified in the main text. In (a) OOP magnetization is favored. In (b) IP magnetization is favored.

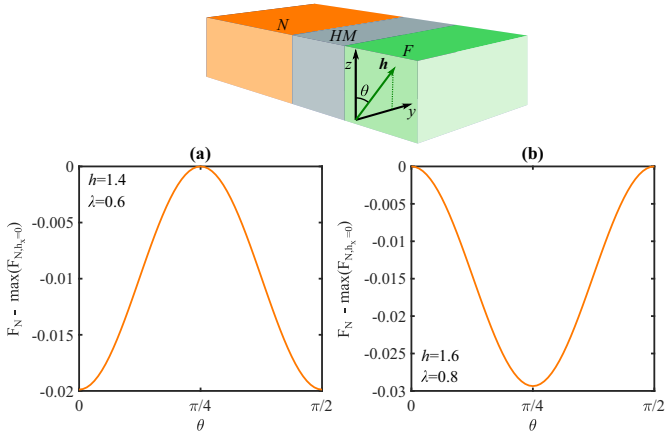

FIG. 3. Panels (a) and (b) show $F_N(\theta) - \max(F_{N,h_x=0})$ in the yz plane for $h = 1.4$, $\lambda = 0.6$ and for $h = 1.6$, $\lambda = 0.8$. The other parameters used are given in the main text. $T = 0.01$. We see a $\pi/4$ rotation of the minimum from (a) to (b).

results when scaled in this way is Ref. [19]. This paper utilized the same theoretical formalism as we do here and the predictions made therein were later found to correspond very well to experimental measurements done in Ref. [20]. Thus, there is good reason to expect that the results obtained in the present framework for system parameters corresponding to a certain ratio between the system size N_x/ξ should correspond well to experimental measurements on a system that has the same ratio between its length and the superconducting coherence length. This is the approach we will take below.

III. RESULTS AND DISCUSSION

A. The nonsuperconducting contribution to the free energy

We first look at a system as shown in Fig. 1, where we have a normal metal (N) rather than a superconductor, i.e., $U = 0$. This is important in order to later distinguish the influence of the superconducting phase on the preferred magnetization orientation compared to the normal-state phase. We diagonalize the Hamiltonian described in Eqs. (1) and (6) numerically using the parameters $N_{x,N} = 9$, $N_{x,HM} = N_{x,F} = 3$, $N_y = N_z = 50$, $\mu_N = 1.8$, $\mu_{HM} = 1.7$, $\mu_F = 1.6$, $h = 1.4$, and $\lambda = 0.6$. We then plot the free energy for the N/HM/F trilayer, $F_N(\theta)$, to find the preferred direction of $\mathbf{h}$ for a given T. In all free-energy plots we subtract the maximal free energy within the plane of rotation we are considering, i.e., $\max(F_{N,h_y=0})$ when considering the xz plane and $\max(F_{N,h_x=0})$ when considering the yz plane. We do this to make it easier to compare the change in free energy for different parameter choices. Figure 2 shows $F_N(\theta)$ in the xz plane for $T = 1$ and $T = 0.1$. We see that the preferred magnetization direction may change as the temperature is increased. The preferred direction may also change when changing h, λ, or the layer thicknesses. The angular dependence of F is the same for the xy and xz planes. Figure 3 shows $F_N(\theta)$ in the yz plane at $T = 0.01$ for different choices of h and λ. We see that the preferred direction of $\boldsymbol{h}$ is rotated by $\pi/4$ when changing the parameters from $h = 1.4$, $\lambda = 0.6$ to $h = 1.6$, $\lambda = 0.8$. A similar rotation may also happen when changing T or the layer thicknesses. Note that the free energy is invariant under a $\pi/2$ rotation in the yz plane. This is reasonable, because a $\pi/2$ rotation of the cubic system around the interface normal should leave the system invariant independently of the magnetization direction. For sufficiently high temperatures, F_N becomes constant. We underline that the effective magnetization anisotropy that arises here is distinct from the anisotropy terms described in Eqs. (18) and (19), the latter not being included in the analysis yet. We will shortly come back to the physical origin of the magnetic anisotropy in the present case. It is evident that the preferred direction of $\mathbf{h}$ is highly dependent on the choice of parameters. To make a superconducting switch, we must therefore make sure that the nonsuperconducting contribution to the free energy favors a different magnetization direction than the superconducting contribution so that the superconducting and nonsuperconducting contributions compete. We must also check whether a change in the preferred magnetization direction is actually caused by the superconducting contribution to F and not by the nonsuperconducting contribution.

Before turning to the superconducting case, we examine the energy band structure of the system in order to explain the change in free energy of the N/HM/F trilayer. If we consider small temperatures so that F_N can be approximated by Eq. (17), the free energy is determined by the sum over negative eigenenergies. If eigenenergies are shifted from above to below zero when some parameter is changed or if the eigenenergies below zero shift closer or farther away from zero, $F_N(\theta)$ will change. When increasing the temperature from zero, the smallest of the positive eigenenergies will give a contribution to the free energy. The band structure close to zero energy (relative the chemical potential) should therefore be of great importance to the free energy at low temperatures. In Fig. 4 we have plotted the energy bands, $E_{n,k_y,k_z=0}(k_y)$, for three different magnetization directions. We consider the out-of-plane case $(\theta, \phi) = (\pi/2, 0)$ and two in-plane cases $(\theta, \phi) = (\pi/4, \pi/2)$ and (0,0), respectively. We have used the same parameters as in Fig. 2. In Fig. 4, panels (a)–(c)

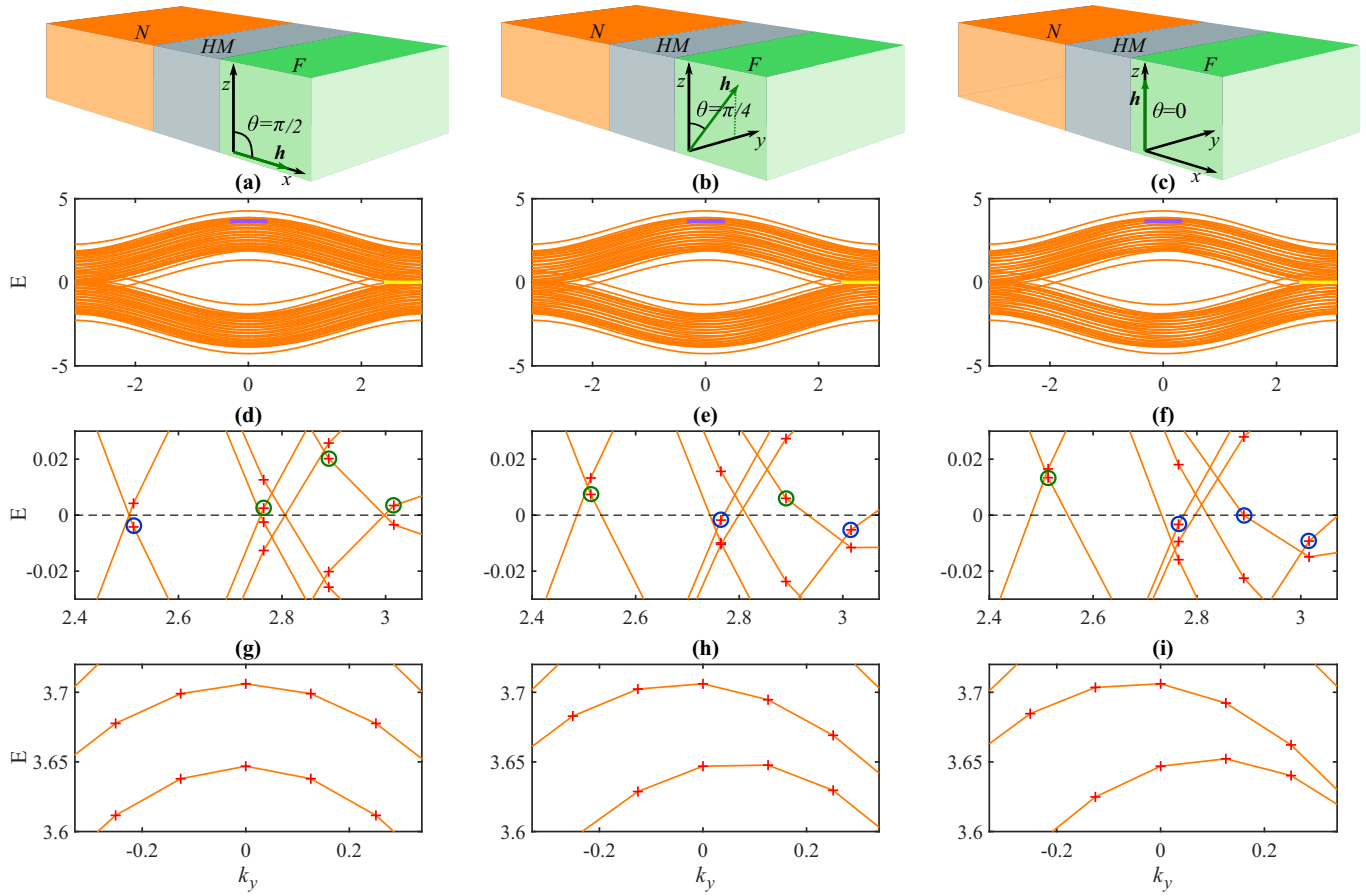

FIG. 4. Panels (a)–(i) show the energy band structure, $E_{n,k_y,k_z=0}(k_y)$, of the N/HM/S system. The parameters used are given in the main text. In (a), (d), and (g) we have OOP magnetization corresponding to the maximum of F_N for low T. In (b), (e), and (h) we have IP magnetization with $\theta = \pi/4$ corresponding to the maximum IP value of F_N for low T. In (c), (f), and (i) we have IP magnetization with $\theta = 0$ corresponding to the minimum of F_N for low T. Panels (d)–(f) show the band structure in the region marked in yellow in (a)–(c). The crosses mark the discrete eigenenergies. The encircled eigenenergies are shifted from above zero energy (green circle) to below zero energy (blue circle) or vice versa when rotating $\boldsymbol{h}$. At $T = 0$ only eigenenergies below zero energy contribute to F_N. Panels (g)–(i) show the band structure in the region marked in purple in (a)–(c). Also for these higher-energy bands that contribute to F at finite temperatures, there is a shift in the energy bands when rotating $\boldsymbol{h}$.

show the overall band structure of the three magnetization directions. Panels (d)–(f) correspond to the region marked in yellow in (a)–(c) and show some of the eigenenergies close to zero energy. We see a variation in band structure between the different directions of $\boldsymbol{h}$. As a result some eigenenergies are shifted from above to below zero energy and vice versa. For $T \to 0$ it is therefore likely that the differences in band structure cause the variation in F_N for different magnetization directions. Note that this effective anisotropy is not caused by the discreteness of k_y and k_z. In the limit where we have continuous energy bands, $N_y, N_z \to \infty$, the shifting of the energy bands should cause the same effect since finite sections of the continuous energy bands are shifted from above to below zero energy and vice versa. Panels (g)–(i) correspond to the purple region in (a)–(c) and show higher energy bands that only contribute to the free energy at finite temperatures. We see that the band structure has an angular dependence also at finite temperatures. It is therefore reasonable that F_N has a temperature-dependent angular dependence also for low, finite temperatures. For temperatures that are sufficiently high to make all energy eigenvalues partially occupied, $F_N(\theta)$ becomes gradually more independent of the magnetization direction. Since $F_N(\theta)$ becomes constant for high temperatures, this indicates that the relative shift between the energy bands is such that it leaves the sum over all eigenenergies constant.

B. The superconducting contribution to the free energy

We now look at a system as shown in Fig. 1, where we have a superconductor, i.e., $U > 0$. The basic question we seek to address is, is it possible to trigger a reorientation of the preferred magnetization direction in the system via a superconducting phase transition, i.e., by adjusting the temperature from above to below T_c? We diagonalize the Hamiltonian described in Eqs. (1) and (6) numerically using the parameters $N_{x,S} = 9$, $N_{x,HM} = N_{x,F} = 3$, $N_y = N_z = 50$, $\mu_S = 1.8$, $\mu_{HM} = 1.7$, $\mu_F = 1.6$, $U = 1.9$, $h = 1.4$, and $\lambda = 0.6$. For this parameter set the superconducting coherence length is $\xi = 5$. We expect that our results can be generalized to systems with thicker layers as long as the relative thicknesses of the layers compared to the coherence length stay constant, as explained previously in this paper.

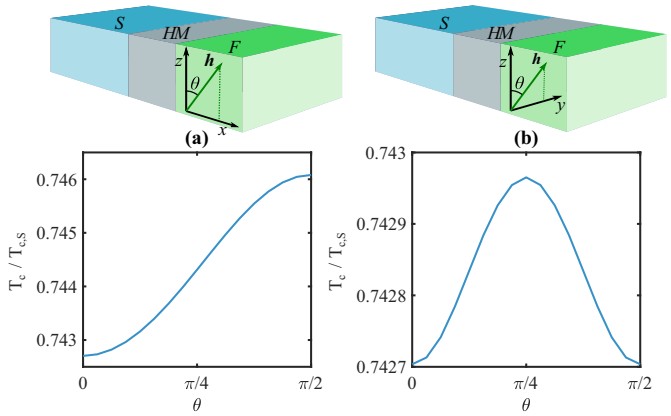

FIG. 5. Panel (a) shows $T_c/T_{c,S}$ when rotating the magnetization from IP to OOP. Panel (b) shows $T_c/T_{c,S}$ for an IP rotation. The parameters used are specified in the main text.

We begin by considering the dependence of the superconducting critical temperature on the magnetization direction. Since we have chosen a size of the superconductor larger than the coherence length, the magnitude of the change in critical temperature is rather small. $T_c(\theta)/T_{c,S}$ is plotted in Fig. 5. $T_{c,S}$ is the critical temperature of the superconducting layer without the heavy-metal layer and the ferromagnetic layer. In (a) we see a suppression of T_c for IP magnetization as found by experiments [12] on a similar system. Panel (b) shows an additional IP variation in T_c, where T_c is suppressed along the cubic axes. In our system, where the thickness of the superconductor is less than twice the coherence length, we do not obtain a substantial bulk region with a constant gap. When calculating T_c we measure the change in the gap in the middle of the superconducting region when recalculating the gap m times. This means that for superconducting layers that are not much longer than the coherence length, our method for calculating T_c is not entirely accurate unless m is chosen to be very large. Therefore, we set $m = 150$. The change in T_c when increasing m by 10 is then $10^{-4}T_{c,S}$, which is a small change compared to the total change in T_c when rotating $\boldsymbol{h}$. We have checked that we get a qualitatively similar behavior of T_c to that in Fig. 5 for thicker superconducting layers. $T_{c,S}$ was calculated with $m = 200$. The number of times we divided our temperature interval is $n = 20$, making m the parameter that restricts the accuracy of our T_c calculation. The reason we chose a superconductor of only 9 lattice points is that a long superconducting layer requires a low U to obtain a coherence length that is comparable to the thickness of the superconducting layer. This results in a very low critical temperature. At very low temperatures only the eigenenergies below zero contribute to the free energy as shown in Eq. (17). If we have few k_y and k_z values, the shifting of eigenenergies from above to below zero energy will have a great impact on the free energy. This is especially a problem when computing the nonsuperconducting contribution to the free energy, where we have no gap and many eigenenergies are close to $E = 0$. We therefore do not get a smooth curve when plotting $F_N(\theta)$. To avoid this problem we must either choose a short superconductor such that we can look at higher temperatures, or let N_y and N_z be very large. The latter option makes the free-energy calculations computationally expensive, which is why we chose the former. Note that we would expect a stronger variation in T_c if we made our superconductor comparable to the coherence length rather than almost two times larger.

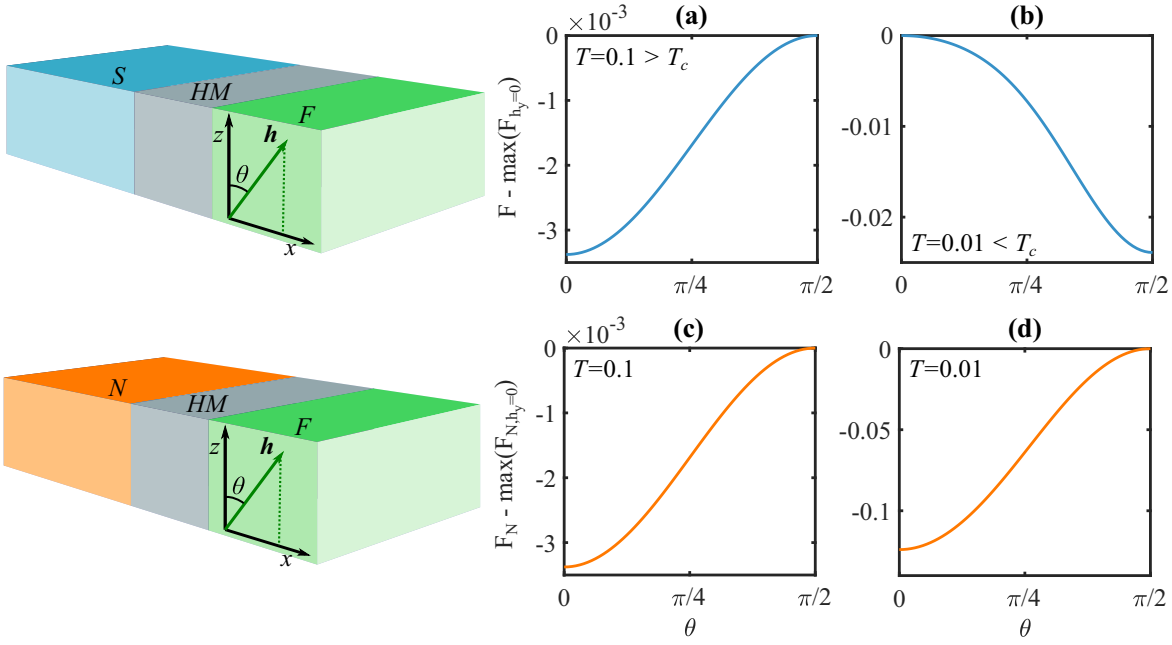

FIG. 6. Panels (a) and (b) show $F(\theta) - \max(F_{h_y=0})$ in the xz plane for $T = 0.1 > T_c = 0.017$ and $T = 0.01 < T_c$, respectively. Panels (c) and (d) show the normal-state contribution to the free energy at the same temperatures. The parameters used are specified in the main text. From (a) and (b) we see that by decreasing the temperature below T_c the preferred magnetization direction of the ferromagnet changes from IP to OOP. Since the normal-state contribution shown in (c) and (d) favors IP magnetization, the change in the preferred magnetization direction must be due to superconductivity.

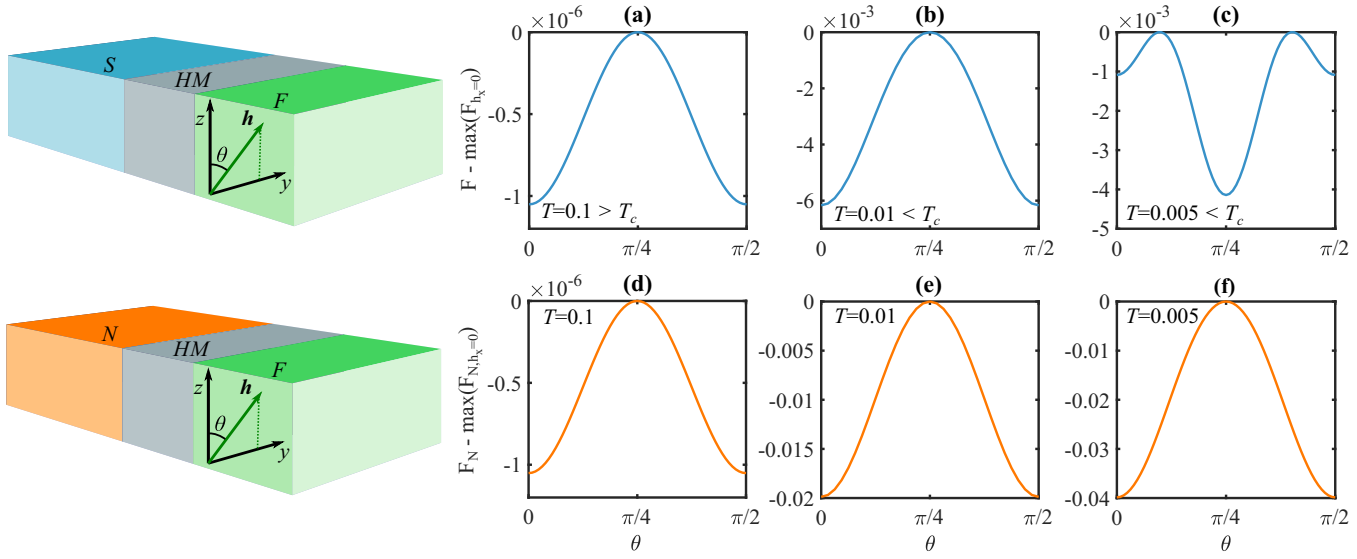

FIG. 7. Panels (a), (b), and (c) show $F(\theta) - \max(F_{h_x=0})$ in the yz plane for $T = 0.1 > T_c = 0.017$, $T = 0.01 < T_c$, and $T = 0.005 < T_c$, respectively. Panels (d), (e), and (f) show the normal-state contribution to the free energy at the same temperatures. The parameters used are specified in the main text. From (a), (b), and (c) we see that the IP minimum of the free energy rotates by $\pi/4$ at some temperature between 0.01 and 0.005, which are both below T_c. Since the normal-state contribution shown in (d), (e), and (f) favors magnetization along the crystal axes at all of these three temperatures, the change in the preferred magnetization direction must be due to superconductivity.

From the angular dependence of T_c we may expect a superconducting contribution to the free energy in which F is increased for the IP orientation, especially along the cubic axes. Figure 6 shows the free energy in the xz plane for $T = 0.1 > T_c$, $T = 0.01 < T_c$, and $T = 0.005 < T_c$. As expected, we see a change in the preferred magnetization direction due to the fact that the superconducting contribution to F favors OOP magnetization while the nonsuperconducting contribution to F favors IP magnetization. Figure 7 shows the free energy in the yz plane for the same temperatures. For sufficiently low T, the superconducting contribution to the free energy starts to dominate, and we have an IP $\pi/4$ rotation of the minimum of free energy. Notice however that the IP variation in the free energy is weaker than the IP-OOP variation. Therefore OOP magnetization is favored as the ground state of the system despite the fact that the free energy also varies when the magnetization is rotated IP. For both the xz and yz planes the change in preferred magnetization direction will generally occur at lower temperatures than T_c, meaning that the superconducting contribution does not necessarily start to dominate exactly at the critical temperature. When increasing T the preferred magnetization direction at some point changes from IP to OOP without any involvement of superconductivity. This is exemplified by the behavior of $F_N(\theta)$ in Fig. 2, which was plotted for a temperature $T > T_c$. The superconducting switch must therefore be operated over a limited temperature range around the temperature at which the change in the preferred magnetization direction occurs. However, we discuss toward the end of this paper how the superconducting contribution to the free energy, causing an effective magnetic anisotropy, can be experimentally detected even in the cases in which the superconducting contribution is not sufficiently strong to change the preferred magnetization orientation.

The angular dependence of T_c and of the superconducting contribution to F can be explained by the generation of triplet Cooper pairs. At an S/F interface, the spin splitting of the energy bands of the ferromagnet causes transformation of singlet Cooper pairs into opposite-spin triplets. The Rashba spin-orbit coupling terms in the Hamiltonian in Eqs. (1) and (6) are proportional to $\sin(k_y)$ and $\sin(k_z)$. Therefore, electrons experience different energies if the sign of (k_y, k_z) is changed. This symmetry-breaking causes triplet generation at the S/HM interface, and enables equal-spin triplet generation, depending on the relative orientation of the magnetization and the spin-orbit field. In Fig. 8 we have plotted the triplet amplitudes corresponding to OOP magnetization and the IP magnetization directions $(\theta, \phi) = (\pi/2, \pi/4)$ and (0,0), respectively. The relative time used in the computation of the s-wave odd-frequency triplet amplitudes is $\tau = 5$. We see that there is a generation of short-range and long-range triplet amplitudes depending on the magnetization direction. The generation of triplet amplitudes lowers the singlet amplitude in the superconductor, since singlet Cooper pairs are converted into triplet Cooper pairs. In Fig. 9 we have plotted $\tilde{S}_s/\tilde{S}_{s,S}$, where $\tilde{S}_s$ is defined in Eq. (20). $\tilde{S}_{s,S}$ is the singlet amplitude in the superconducting layer without the heavy-metal layer and the ferromagnetic layer. We see that the singlet amplitude is suppressed for IP magnetization, especially along the cubic axes. Since the singlet amplitude is proportional to the superconducting order parameter, a suppression of the singlet amplitude should lead to a decrease in T_c and an increase in F. This is exactly what we have seen from Figs. 5, 6, and 7. We may therefore explain the variation in T_c and F by the generation of triplet amplitudes depending on the relative orientations of the spin-orbit field and the magnetization.

The diffusive limit calculations in Ref. [12] found an IP suppression of T_c as in our calculations. However, in the

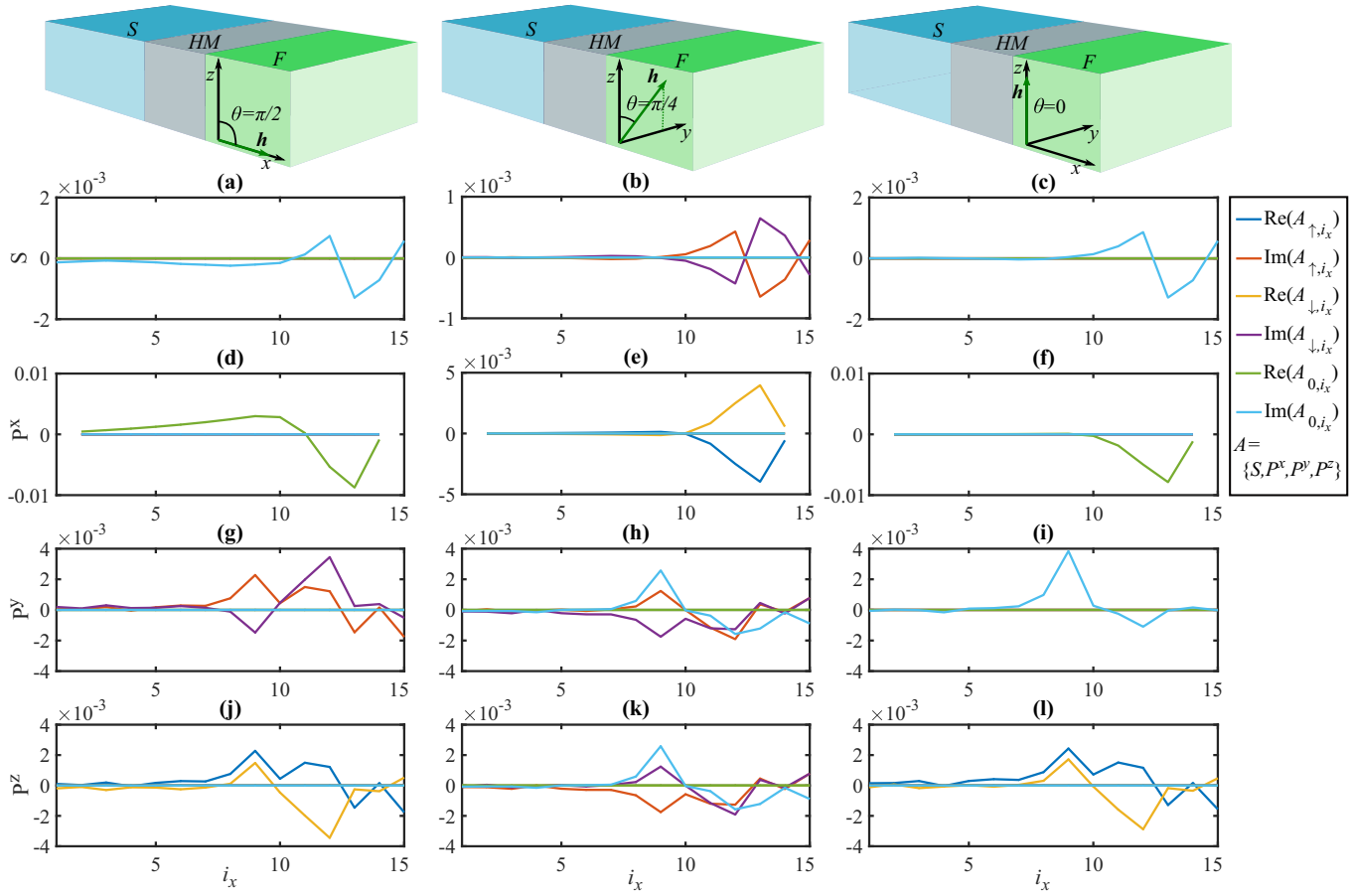

FIG. 8. Panels (a)–(l) show the triplet amplitudes generated in the S/HM/F system at $T = 0.01 < T_c = 0.017$. The parameters are given in the main text. Panels (a)–(c) show the s-wave triplet amplitudes, (d)–(f) show the p_x-wave triplet amplitudes, (g)–(i) show the p_y-wave triplet amplitudes, and (j)–(l) show the p_z-wave triplet amplitudes. The first column corresponds to OOP magnetization, the second column corresponds to IP magnetization with $\theta = \pi/4$, and the third column corresponds to IP magnetization with $\theta = 0$. Note that all amplitudes that are not visible in the plots are either zero or close to zero.

diffusive limit T_c was found to be invariant under IP rotations of the magnetization. In Ref. [12] the HM/F layer is modeled as a single layer with the exchange field and the spin-orbit coupling as homogeneous background fields, which similarly to what occurs in the ballistic limit results in a generation of both short-range and long-range triplets close to the interface. The IP suppression of T_c compared to T_c at OOP magnetization is both for the ballistic and the diffusive limit a result of differences in the triplet generation when the exchange field is parallel and perpendicular to the interface between the superconductor and the HM/F layer. The change in T_c under IP rotations of the magnetization found in the present paper is a result of differences in the triplet generation at different IP magnetization directions due to the crystal structure of the lattice in the HM region. This is the reason why these variations are not found in the diffusive limit calculations in Ref. [12], which does not model the S/HM/F system by a lattice model. For very thin films, like the ones considered experimentally in Ref. [12], we expect the sample to approach the ballistic limit such that a variation in T_c for IP rotations of the magnetization should be observable.

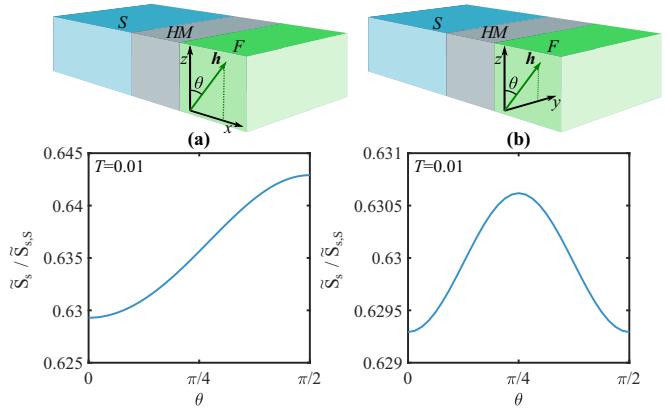

FIG. 9. Panels (a) and (b) show the singlet amplitude $\tilde{S}_s/\tilde{S}_{s,S}$ in the xz and yz plane. The parameters are given in the main text. $T = 0.01 < T_c = 0.017$.

C. The shape anisotropy contribution to the free energy

Until now, we have disregarded the intrinsic magnetic anisotropy of the thin ferromagnetic film, which does not depend on the coupling to itinerant electrons $\{c, c^\dagger\}$ in our model. For concreteness, we will now consider the case of a Pt heavy-metal layer and a Co(111) ferromagnetic layer. In this

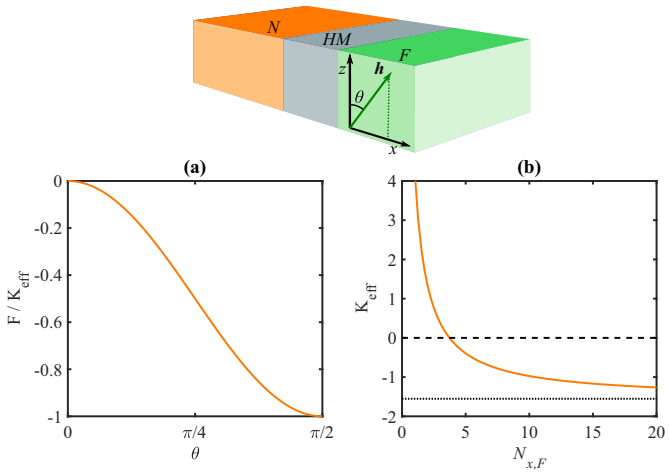

FIG. 10. Panel (a) shows the perpendicular/shape anisotropy contribution to F. Panel (b) shows the effective anisotropy constant, K_{eff}, as a function of the ferromagnet thickness.

case, the anisotropy constants are [17] $K_v = -0.77$ MJ/m^3, $K_i = 1.15$ mJ/m^2, and $K_s = -0.28$ mJ/m^2. The lattice constants of Co are [21] $a_x = a_y = 251$ pm and $a_z = 407$ pm. The anisotropy contribution to the free energy is plotted in Fig. 10(a) for this choice of parameters. The effective anisotropy constant defined in Eq. (19) is plotted in Fig. 10(b) as a function of $N_{x,F}$. By solving $K_{\text{eff}} = 0$, we find that the anisotropy contribution to the free energy favors an OOP magnetization for $N_{x,F} \leqslant 3$ and an IP magnetization for $N_{x,F} \geqslant 4$. Since we may generalize our results to any system size as long as the layer thickness relative to ξ stays constant, we may consider a system with any $N_{x,F}$. By making the ferromagnetic layer thick enough to give a contribution to $F(\theta)$ favoring an IP magnetization, but thin enough that K_{eff} is small, it is in principle possible to get an IP-OOP superconducting switch despite the fact that the nonsuperconducting contribution to F has gained an extra term. We may also make the ferromagnetic layer so thick that the nonsuperconducting contribution to the free energy enforces IP magnetization. Since the shape anisotropy contribution to the free energy is invariant under rotations in the yz plane, we may get a $\pi/4$ rotation in the magnetization as shown in Fig. 7. This means that an IP superconducting switch in the magnetization direction is in principle possible, even if the preferred magnetization direction is OOP when disregarding shape anisotropy. The possibility of changing the preferred direction in the yz plane is interesting as the magnetic field of the ferromagnet in such a case is not perpendicular to the superconducting layer. We therefore avoid demagnetizing currents close to the interface in the superconducting region as well as vortex formation inside the superconductor [22]. For magnetization with an OOP component, demagnetization effects may be of greater importance.

It is worth noting that even if the ferromagnetic layer is so thick that the nonsuperconducting contribution dominates, it may still be possible to measure the superconducting contribution to the free energy. The superconducting contribution to the free energy in an F1/S/F2 system can be measured [23] by applying an external magnetic field and measuring the critical field needed to flip the magnetization from an antiparallel to a parallel alignment. It should be possible to do similar measurements on the S/HM/F-system. For instance, one could apply an external field to flip the magnetization of the ferromagnet between the IP and the OOP direction. The superconducting contribution favors OOP magnetization and would therefore reduce the critical field needed to flip the magnetization from IP to OOP orientation. Such a reduction of the critical field would thus be evidence of a superconductivity-induced anisotropy term for the ferromagnet.

IV. CONCLUDING REMARKS

This work predicts a possible reorientation of the magnetization direction of a thin-film ferromagnet upon lowering the temperature below the superconducting critical temperature T_c when the ferromagnet is separated from a superconductor by a thin heavy-metal film. Especially for a thin ferromagnetic film with weak shape anisotropy, the superconducting phase transition should induce an in-plane to out-of-plane rotation of the magnetization. We have also found that if the shape anisotropy is strong enough to enforce an in-plane magnetization direction, a $\pi/4$ in-plane rotation of the magnetization can occur upon lowering the temperature below T_c. In addition, we have considered the dependence of T_c on the magnetization direction. Here, we find that our lattice-model calculations predict an additional in-plane variation in T_c compared to the previous diffusive-limit calculations, which only show an in-plane suppression of T_c independently of the in-plane magnetization orientation. Both the T_c suppression and the magnetization reorientation can be explained by the generation of short-range and long-range triplet Cooper pairs close to the interfaces depending on the relative orientations of the exchange field of the ferromagnet and the spin-orbit field of the heavy metal. Our results should be reproducible experimentally for systems with the same ratio between the layer thicknesses and the superconducting coherence length.

ACKNOWLEDGMENTS

We thank J. A. Ouassou, V. Risinggård, M. Amundsen, and M. G. Blamire for helpful discussions. This work was supported by the Research Council of Norway through its Centres of Excellence funding scheme grant 262633 QuSpin. N.B. was supported by the UKIERI grant from the British Council.

[1] J. Linder and J. W. A. Robinson, Nat. Phys. **11**, 307 (2015).
[2] M. Eschrig, Rep. Prog. Phys. **78**, 104501 (2015).
[3] M. Eschrig, Phys. Today **64(1)**, 43 (2011).
[4] J. Y. Gu, C.-Y. You, J. S. Jiang, J. Pearson, Y. B. Bazaliy, and S. D. Bader, Phys. Rev. Lett. **89**, 267001 (2002).

[5] I. C. Moraru, W. P. Pratt, and N. O. Birge, Phys. Rev. Lett. **96**, 037004 (2006).
[6] P. V. Leksin, N. N. Garif'Yanov, I. A. Garifullin, Y. V. Fominov, J. Schumann, Y. Krupskaya, V. Kataev, O. G. Schmidt, and B. Büchner, Phys. Rev. Lett. **109**, 057005 (2012).
[7] N. Banerjee, C. B. Smiet, R. G. J. Smits, A. Ozaeta, F. S. Bergeret, M. G. Blamire, and J. W. A. Robinson, Nat. Commun. **5**, 3048 (2014).
[8] X. L. Wang, A. Di Bernardo, N. Banerjee, A. Wells, F. S. Bergeret, M. G. Blamire, and J. W. A. Robinson, Phys. Rev. B **89**, 140508(R) (2014).
[9] S. H. Jacobsen, J. A. Ouassou, and J. Linder, Phys. Rev. B **92**, 024510 (2015).
[10] J. A. Ouassou, A. D. Bernardo, J. W. A. Robinson, and J. Linder, Sci. Rep. **6**, 29312 (2016).
[11] H. T. Simensen and J. Linder, Phys. Rev. B **97**, 054518 (2018).
[12] N. Banerjee, J. A. Ouassou, Y. Zhu, N. A. Stelmashenko, J. Linder, and M. G. Blamire, Phys. Rev. B **97**, 184521 (2018).
[13] D. Terrade, Proximity effects and Josephson currents in ferromagnet - spin-triplet superconductors junctions, Ph.D. thesis, Max-Planck-Institut für Festkörperforschung, Universität Stuttgart, 2015, pp. 137–146.
[14] J. Linder, M. Amundsen, and V. Risinggård, Phys. Rev. B **96**, 094512 (2017).
[15] N. Satchell and N. O. Birge, Phys. Rev. B **97**, 214509 (2018).
[16] E. C. Gingrich, Phase control of the spin triplet state in S/F/S Josephson junctions, Ph.D. thesis, Michigan State University, 2014.
[17] M. T. Johnson, P. J. H. Bloemen, F. J. A. den Broeder, and J. J. de Vries, Rep. Prog. Phys. **59**, 1409 (1996).
[18] J. Bardeen, L. N. Cooper, and J. R. Schrieffer, Phys. Rev. **108**, 1175 (1957).
[19] A. M. Black-Schaffer and J. Linder, Phys. Rev. B **82**, 184522 (2010).
[20] C. D. English, D. R. Hamilton, C. Chialvo, I. C. Moraru, N. Mason, and D. J. Van Harlingen, Phys. Rev. B **94**, 115435 (2016).
[21] J. D. Donaldson and D. Beyersmann, *Ullmann's Encyclopedia of Industrial Chemistry: Cobalt and Cobalt Compounds* (Wiley VCH, Weinheim, Germany, 2003), p. 431.
[22] K. Fossheim and A. Sudbø, *Superconductivity: Physics and Applications* (John Wiley & Sons Ltd., Chichester, UK, 2004), pp. 10–26.
[23] Y. Zhu, A. Pal, M. G. Blamire, and Z. H. Barber, Nat. Mater. **16**, 195 (2016).

Lina Grøvan Johnsen

Controllable Superconducting Phase Transition and Magnetization Reorientation due to Spin-Orbit Interactions

NTNU
Kunnskap for en bedre verden